UNIVERSITY OF EXETER

Understanding climate feedbacks with idealized models

Submitted by **Qun Liu**, to the University of Exeter
as a thesis for the degree of
Doctor of Philosophy in Mathematics,
August 2021.

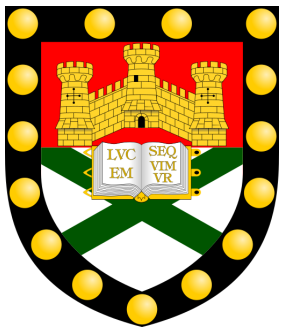

I certify that all material in this thesis which is not my own work has been identified and that no material has previously been submitted and approved for the award of a degree by this or any other University.

(Signature) Qun Liu .....

Abstract

The global mean surface air temperature change in response to global warming, namely climate sensitivity, plays a central role in climate change studies, and the estimates of climate sensitivity depend critically on the climate feedbacks, the processes that can either amplify or dampen the responses of the climate system to external perturbations. The goal of this thesis is to understand climate feedbacks through idealized climate models.

The first part explores the roles of climate feedbacks in polar amplification of surface temperature change. By running idealized aquaplanet simulations with a hierarchy of radiation schemes (without sea ice and clouds), and by decomposing the total surface temperature responses into different components through the radiative kernel method, we find the poleward heat transport, the lapse rate and Planck feedbacks contribute to amplified surface temperature changes in the polar region, while the forcing and water vapor feedback dominates the tropical temperature change.

The second part investigates the underlying causes of cloud feedback uncertainty with a simple cloud scheme. The scheme diagnoses the cloud fraction from relative humidity and other variables such as inversion strength, and its optical properties such as effective radius and cloud water content are prescribed as simple functions of temperature. The simulations show this scheme can capture the basic feature of cloud climatology. Through a series of perturbed parameter ensemble global warming simulations, part of the inter-model spread of cloud feedbacks among general circulation models can be reproduced. In addition, the low cloud amount feedback, especially over the low-latitude subsidence regions, is the largest contributor to the net cloud feedback uncertainty. The cloud controlling factor analysis suggests that the sea surface temperature (SST) and estimated inversion strength (EIS) have opposite impacts on marine low cloud amounts, but their responses to SST rather than EIS seem to bring larger uncertainty. Finally, the equilibrium climate sensitivity and cloud feedback over tropical subsidence regimes show a robust linear relationship, implying a possible constraint for climate sensitivity.

Acknowledgements

First and foremost, I would like to express my sincerest thanks to my supervisors, Prof. Mat Collins and Prof. Geoff Vallis, for their generous guidance, support and endless patience throughout my PhD. The discussions with them (mostly) on Fridays have greatly shaped my research. They always encourage me to think big pictures of scientific problems, which I will benefit in the rest of my life. I would also like to thank the SPOOKIE II project for providing the initial version of the simple cloud scheme used in Chapter 4, and thank Dr. Penelope Maher and Dr. Stephen Thomson for coding the initial version of the scheme, all of which form the basis of Chapter 4. My gratitude is also due to Neil Lewis for developing the column version of Isca model, which makes the tests of parameterization scheme much easier.

I am thankful to Prof. James Screen for working as an assessor for my annual report and for his advice and suggestions during every mini-viva. Many thanks to everyone who has helped me along the way in Exeter, especially those in my office on Laver level 9 and the members of the 'Isca group'. I would also like to extend my thanks to the Exeter Climate Systems (XCS) group for organizing so many excellent seminars, although all the discussions have to be online during the COVID-19 pandemic.

I would like to acknowledge the joint PhD scholarship from University of Exeter and China Scholarship Council (NO. 201706210070), as I could not finish my study in the UK without their support.

Finally, I am incredibly grateful to my family and friends for their continuous care and support over the past four years. Every week's chats with my parents and brother, also with my sister sometimes, have given me lots of support, especially during the COVID-19 lockdown period. My twin brother, who has obtained his PhD degree two years ago, sets a good example for me to follow. I also owe many thanks to my housemates and friends for their support and help.

Contents

List of Tables

List of Figures

Acronyms, Abbreviations and Symbols

Acronyms and abbreviations

AMIP	Atmospheric Model Intercomparison Project
BOG	Byrne & O'Gorman (Radiation Scheme)
CALIPSO	Cloud-Aerosol Lidar and Infrared Pathfinder Satellite Observations
CERES	Clouds and Earth's Radiant Energy System
CFMIP	Cloud Feedback Model Intercomparison Project
CMIP5/6	The Fifth / Sixth Coupled Model Intercomparison Project
COSP	CFMIP Observational Simulator Package
CRE (CRF)	Cloud Radiative Effect (Forcing)
CWP	Cloud Water Path
ECMWF	European Centre for Medium-Range Weather Forecasts
EIS	Estimated Inversion Strength
ELF	Estimated Low-level Cloud Fraction
ERA5	ECMWF Reanalysis version 5
GCM	General Circulation Model
GFDL	Geophysical Fluid Dynamics Laboratory
GOCCP	GCM-Oriented CALIPSO Cloud Observations Product
IPCC	Intergovernmental Panel on Climate Change
IPCC AR5	The Fifth Assessment Report of the IPCC
ISCCP	International Satellite Cloud Climatology Project
ITCZ	Intertropical Convergence Zone
LCL	Lifting Condensation Level
LTS	Low Tropospheric Stability
LW	Longwave
OLR	Outgoing Longwave Radiation
PDF	Probability Density Function
PPE	Perturbed Parameter (or Physics) Ensemble
RH	Relative Humidity

RRTM	Rapid Radiative Transfer Model
SOCRATES	Suite Of Community RAdiative Transfer codes based on Edwards & Slingo
SPOOKIE	Selected Process On/Off Klima Intercomparison Experiment
SST	Sea Surface Temperature
SW	Shortwave
TOA	Top of the Atmosphere

Greek

α	Surface albedo
δ, Δ	Change of a variable
ϵ	Surface emissivity
θ	Potential temperature (K)
θ_s, θ_{700}	Potential temperature at surface or 700 hPa (K)
λ	Climate feedback parameter
ρ, ρ_w	Density; density of water (kg m^{-3})
σ	Stefan–Boltzmann constant (5.67×10^{-8} W m^{-2} K^{-4})
τ	Optical depth
φ	Latitude
ω	Vertical pressure velocity (Pa s^{-1} or hPa day^{-1})
ω_{500}, ω_{700}	Vertical pressure velocity at 500 hPa or 700 hPa (Pa s^{-1} or hPa day^{-1})

Roman

a	Earth radius in Chapter 3; linear coefficient in Chapter 4
C	Cloud fraction
c_p	Dry air specific heat capacity at constant pressure (1006 J kg^{-1} K^{-1})
C_w	Specific heat capacity of ocean water (J kg^{-1} K^{-1})
D	Depth of mixed-layer (m)
e_s	Saturated water vapor pressure
e_{s0}	Reference saturation vapor pressure (6.1078 hPa) at 273.16 K
F, $F_{2\times}$	Radiative forcing; radiative forcing from a doubling of CO_2 (W m^{-2})
f_l	Liquid cloud fraction
F_s, F_Q	Surface flux or Q-Flux (W m^{-2})
g	Gravitational acceleration (9.8 m s^{-2})
Γ_m	Moist-adiabatic potential temperature gradient (K m^{-1})
H	Relative humidity in Chapter 4; heat transport in Chapter 3
H_c	Critical relative humidity
K	Radiative kernel (W m^{-2} K^{-1})
L_v	Latent heat of vaporization (2.47×10^6 J kg^{-1})
p	Pressure (hPa)

p_0, p_s	Reference pressure or sea level pressure (hPa)
q	Specific humidity (kg kg^{-1})
q_s	Saturation mixing ratio or specific humidity (kg kg^{-1})
q_0, q_{700}	Specific humidity at surface or 700 hPa (kg kg^{-1})
q_t, q_c	Total water or cloud water mixing ratio (kg kg^{-1})
R	Radiative flux at top of the atmosphere (W m^{-2})
R_a	Dry air gas constant (287.04 J kg^{-1} K^{-1})
r_e	Effective radius of cloud condensate (μm)
R_v	Gas constant for water vapor (461.50 J kg^{-1} K^{-1})
S_0	Solar constant (W m^{-2})
T	Temperature (K)
T_s, T_0	Surface temperature or reference temperature (K)
w_l	In-cloud liquid water mixing ratio (g kg^{-1})
z_{700}, z_{LCL}, z_{inv}	Heights of 700 hPa, lifting condensation level (LCL) or inversion layer (m)

Chapter 1

Introduction

1.1 Motivation

Climate feedbacks are the processes in the climate system that can either amplify or dampen its responses to the external perturbations (Bony et al., 2006; Soden and Held, 2006). Understanding these feedbacks is key to demystifying the unresolved problems in the climate system. For example, the climate sensitivity, i.e., how the global mean surface temperature changes in response to increased greenhouse gas, is one of the central problems in climate change studies (e.g., Bony et al., 2006; Stocker et al., 2013; Sherwood et al., 2020), and narrowing down the range of climate feedbacks, especially the range of cloud feedbacks, is crucial to constraining the climate sensitivity (e.g. Cess et al., 1990; Webb et al., 2006; Vial et al., 2013; Zelinka et al., 2020; Myers et al., 2021). Despite the efforts payed by the climate communities, the general circulation models (GCMs) still do not have consensus on the sign of global mean cloud feedback (Zelinka et al., 2020), whose uncertainty is still the leading cause of intermodel spread of climate sensitivity (Ceppi et al., 2017; Zelinka et al., 2020). Therefore, to understand the underlying causes for cloud feedback uncertainty (e.g., Bony and Dufresne, 2005; Vial et al., 2013; Qu et al., 2014; Webb et al., 2015; Zelinka et al., 2016; Geoffroy et al., 2017) and to find the potential constraints to it (e.g., Qu et al., 2015b; Klein et al., 2017; Myers and Norris, 2016; Scott et al., 2020; Myers et al., 2021; Ceppi and Nowack, 2021) are key tasks in current climate research.

In addition, it should be noted that the temperature changes under global warming are not uniform across the globe, with amplified warming in polar regions ('polar amplification'; e.g., Manabe and Wetherald, 1975; Pithan and Mauritsen, 2014). It is believed that diminishing sea ice plays a leading role in recent Arctic temperature amplification (Screen and Simmonds, 2010). Nevertheless, polar amplification can also occur in simulations even without sea ice (e.g., Alexeev et al., 2005; Cai, 2005, 2006; Langen et al., 2012). In this case, the roles of climate feedbacks are important to understand the temperature changes in polar

regions (e.g., Pithan and Mauritsen, 2014; Kim et al., 2018).

Therefore, understanding the roles of climate feedbacks is essential to comprehend the possible changes of the climate system under global warming, and the goal of this thesis is to understand these radiative feedbacks through idealized climate models. In doing so, the Isca model (Vallis et al., 2018), an intermediate modelling framework developed at the University of Exeter, is employed throughout this thesis. Currently there is no sea ice scheme in Isca, so it is impossible to explore the surface albedo feedback with it. But we still can revisit the polar amplification problem with it, only focusing on the roles of other climate feedback processes. Another problem of Isca is that it had no cloud scheme at the beginning of this study, meaning the questions related to cloud feedbacks are not able to be investigated within the framework of Isca. But as the cloud feedbacks are vital for calculating climate sensitivity, one of the central problems of current climate change research, we plan to construct a simple diagnostic cloud scheme first so that we can examine cloud feedbacks under the same framework. Thereby, the following scientific questions are to be addressed in this thesis:

1. What roles do the climate feedback processes play in the polar amplification of surface temperature change in idealized aquaplanet simulations without sea ice and clouds?

2. Could we build a cloud scheme for idealized GCMs that is simple enough but could grasp the key features of cloud fields?

3. If so, could the scheme be used to probe the underlying causes of the inter-model spread of cloud feedback in climate models?

The first question intends to understand the roles of climate feedbacks (except surface albedo and cloud feedbacks) in the climate system, while other questions focus on the clouds, cloud feedback and its uncertainty through a potential simple cloud scheme.

In this chapter, the background knowledge to understand climate feedback is briefly introduced. Section 1.2 describes the Earth's radiation budget, which is the basis for us to understand the energy balance of climate system. In Section 1.3, the framework to understand climate feedback is presented, including its definition and the key individual feedbacks in the climate system. In addition, the basic mechanisms of these feedbacks are also summarized in short. As the cloud feedback has the largest uncertainty among all the climate feedbacks in current climate models, the necessary knowledge to understand the cloud feedback is presented in Section 1.4, including the essential features of cloud radiative effect (Section 1.4.1) and the major mechanisms for cloud feedbacks (Section 1.4.2). Section 1.5 briefly reviews the development of cloud parameterization schemes,

as this study intends to understand the cloud feedback through a simple cloud scheme. Finally, the outline of whole thesis is described in Section 1.6.

1.2 The Earth's radiation budget

The Earth's climate is driven by the energy flow into and out of the system. The incoming solar radiation (yellow fluxes in Figure 1.1) reaches the Earth at the top of the atmosphere (TOA), then goes through the atmosphere and arrives at the Earth's surface. During this process, approximately two thirds of the shortwave (SW) radiation is absorbed by the Earth's surface and atmosphere, and roughly one third of this energy is reflected back to space. The surface and atmosphere are heated by this incoming solar radiation, and they also re-emit the longwave (LW) radiation (purple fluxes in Figure 1.1) to keep a relatively stable temperature. Globally, the annual mean incoming solar radiation flux is about 340 Wm^{-2}, the reflected solar radiation flux is around 100 Wm^{-2} and the outgoing longwave radiation (OLR) is close to 240 Wm^{-2} at the TOA for period 2000–2010 (Stephens et al., 2012). These three components balance with each other, with a small positive imbalance (about 0.6 Wm^{-2}) at the TOA. A more recent estimate from Wild et al. (2015) (see their Fig. 1) indicates that the global mean OLR is about 239 Wm^{-2}, and the TOA energy imbalance is about 1 Wm^{-2}.

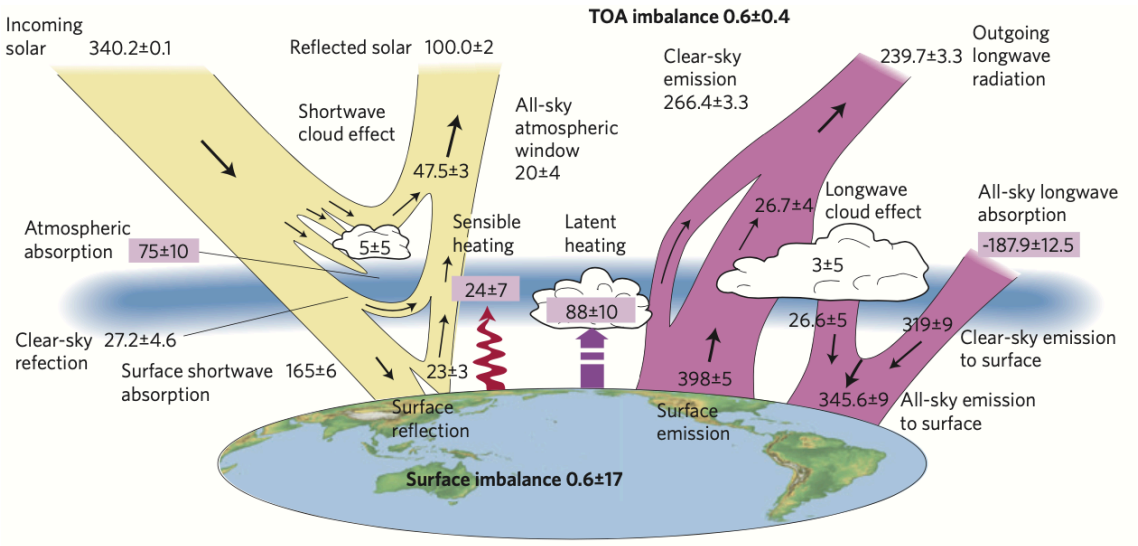

Figure 1.1 The global annual mean energy budget of Earth for the approximate period 2000–2010. All fluxes are in Wm^{-2}. Solar fluxes are in yellow and infrared fluxes in purple. The four flux quantities in purple-shaded boxes represent the principal components of the atmospheric energy balance. Adapted from Fig. B1 of Stephens et al. (2012). Reproduced with permission of the Springer Nature.

As shown in Figure 1.1, the energy budget at the Earth's surface is more complicated than at the TOA. When the incoming solar radiation reaches the surface,

the majority (about 165 Wm^{-2}) of this solar radiation is absorbed by the surface and only a small portion (about 23 Wm^{-2}) is reflected back to space. Of course, these are global mean results and it would be different over certain areas such as Arctic where the surface albedo is large. The global annual mean LW radiation emitted from the surface is about 398 Wm^{-2}. Much of this is absorbed by the atmosphere (such as greenhouse gases, aerosols and clouds), and only a small part (about 20 Wm^{-2}) can pass through the atmospheric window region (a portion of the infrared spectrum where there is almost no atmospheric absorption) reaching the TOA directly. The atmosphere can re-emit the absorbed LW radiation both upward and downward, and the downward part (about 346 Wm^{-2}) can reheat the surface. In addition, due to the temperature and moisture difference between the surface and atmosphere, the surface is also cooled by the latent heat flux (about 88 Wm^{-2}) and sensible heat flux (about 24 Wm^{-2}) through the turbulent movement of the atmosphere. In total, the surface energy budget is balanced by the downward/upward SW and LW radiation, the sensible and latent heat fluxes, but it has much larger uncertainty than at the TOA.

1.3 Climate feedback

1.3.1 Definition

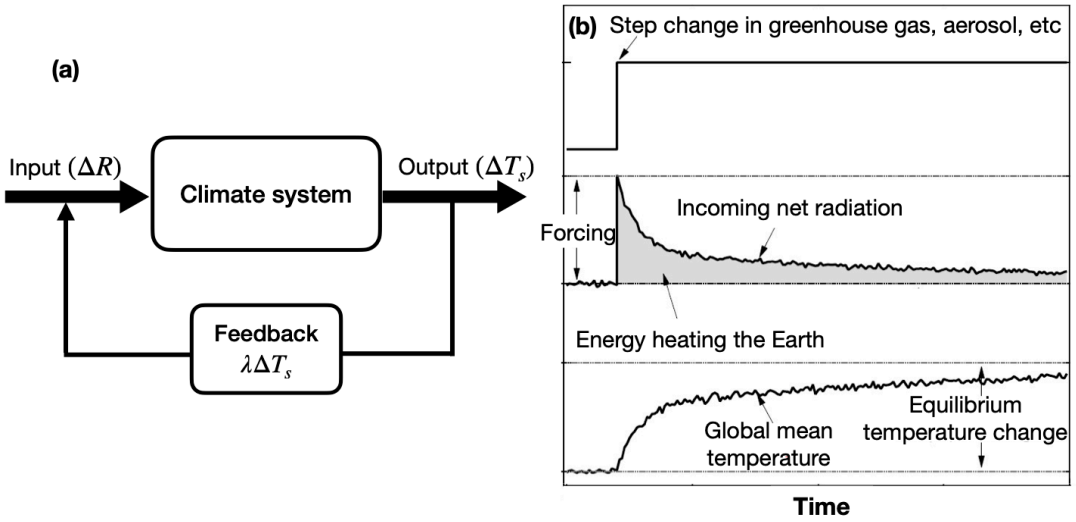

Figure 1.2 (a) Schematic of feedback in the climate system. ΔR is the input disturbance to the climate system, ΔT_s is the change of surface temperature and λ denotes the climate feedback parameter. (b) The illustration of forcing (middle) and global mean temperature (bottom) change with time due to a step change (top) in greenhouse gas, aerosol, etc. Modified from Fig. 1 of Murphy et al. (2009) with permission of the John Wiley and Sons.

As introduced in Section 1.2, the energy budget at the TOA is balanced by the incoming solar radiation and the OLR (the imbalance is usually small). Another

problem is how to understand the way in which the climate system responds to perturbations. In this section, a framework to understand such characters of climate system, including the forcing, feedback, and climate sensitivity will be presented.

In the energy balance model, any disturbance imposed on the system is regarded as the forcing (ΔF), which can arise from the perturbation of greenhouse gas concentration (e.g., CO_2, CH_4), aerosol (Ramanathan et al., 2001), and change in solar cycle (Fröhlich and Lean, 2004) or volcanic eruption (Figure 1.2). Then the climate system will response to this radiative imbalance (ΔR) at the TOA by changing the surface temperature (T_s). As shown in Figure 1.2a, the change in surface temperature (i.e. ΔT_s) can in turn impact the radiative balance at the TOA. That is to say the output response is fed back to the system. ΔR goes to zero when the climate system adjusts towards a new equilibrium (Figure 1.2b). Using the idea of feedback, which is taken from the control system and used to understand the system response to different forcings (Stephens, 2005), ΔR can be linked to the change of surface temperature (ΔT_s) as follows:

$$\Delta R = \Delta F + \lambda \Delta T_s, \tag{1.1}$$

which can be viewed as a Taylor expansion in surface temperature change (ΔT_s), but neglecting the high order terms (Feldl and Roe, 2013b). The second term, $\lambda \Delta T_s$, on the right hand side reflects the radiative flux change that depends linearly on the surface temperature change, and λ is called the *feedback parameter* (Gregory, 2004). At the equilibrium state (i.e., $\Delta R = 0$), the total climate feedback is expressed as

$$\lambda = -\frac{\Delta F}{\Delta T_s}. \tag{1.2}$$

Thus, λ is in units of $Wm^{-2}K^{-1}$ and is a measure of the TOA radiative flux change per degree of surface air temperature change.

Based on the forcing and feedback analysis framework, the equilibrium climate sensitivity (ECS) , i.e., the equilibrium response of global mean surface air temperature to the radiative forcing from a doubling of CO_2 ($F_{2\times}$), can be estimated as:

$$\text{ECS} = \Delta T_{s\_2\times} = -\frac{F_{2\times}}{\lambda}. \tag{1.3}$$

ECS is a measure of the climate sensitivity of the GCM to the forcing, and has quite a large range (~1.5–4.5K) among the fifth phase of the Coupled Model Intercomparison Project (CMIP5; Taylor et al., 2012) models (e.g., Andrews et al., 2012b; Ceppi et al., 2017). In addition, such spread (see the first panel in Figure 1.3) does not reduce in recent sixth phase of the Coupled Model Intercomparison Project (CMIP6; Eyring et al., 2016) models (Zelinka et al., 2020). Evidence from historical and paleoclimate records can perhaps help narrow down the uncertainty of ECS (Sherwood et al., 2020), but more work is still needed to understand the

underlying causes of the uncertainty.

1.3.2 Individual feedbacks

In the climate system, climate feedbacks are the processes that can either amplify or dampen the effects of climate forcings (Hansen et al., 1984). A feedback that amplifies the initial perturbation is called a "positive feedback", while a "negative feedback" reduces the initial perturbation. In general, λ can be decomposed into feedbacks from different physical processes, such as temperature (Planck and lapse rate), water vapor, surface albedo, clouds, etc. These climate feedback parameters can be evaluated as follows

$$\lambda = \frac{\partial R}{\partial T_s} = \sum_x \frac{\partial R}{\partial x}\frac{\partial x}{\partial T_s} + \mathrm{Re}, \tag{1.4}$$

where x represents the climate variable such as temperature, water vapor, surface albedo and cloud properties. $\frac{\partial R}{\partial x}$ can be treated as the feedback parameter due to climate variable x. When neglecting the nonlinearities and interactions among different feedbacks, the high-order residual term (Re) is usually neglected in analysis.

The temperature feedback in the climate system can be decomposed into Planck and lapse rate feedback (Soden and Held, 2006). The Planck feedback assumes that the tropospheric temperature change is vertically uniform and equals the surface temperature change (Bony et al., 2006; Soden and Held, 2006). In other words, there is no vertical temperature change in the troposphere. The Planck feedback is named due to Planck's blackbody radiation law, which is the basic and the strongest negative feedback in the climate system. According to the Stefan–Boltzmann law, the longwave radiation emitted by the Earth's surface rises with temperature following $\mathrm{OLR} = \epsilon\sigma T_s^4$, where ϵ is the surface emissivity close to unity and σ ($5.67 \times 10^{-8}\,\mathrm{W\,m^{-2}\,K^{-4}}$) is the Stefan–Boltzmann constant (Pithan and Mauritsen, 2014). Thus, the Planck feedback can be expressed as $\lambda_P = \frac{\partial R}{\partial T_s} = -4\epsilon\sigma T_s^3 = -4\frac{\mathrm{OLR}}{T_s}$ (assuming R downward positive). As shown in Figure 1.1, the OLR is closed to 240 $\mathrm{Wm^{-2}}$, and the observed global mean surface temperature of Earth is about 288K, thus the estimated Planck feedback is about $\lambda_P = -4 \times 240/288 \approx -3.3\ \mathrm{Wm^{-2}K^{-1}}$, closed to the multi-model mean results from CMIP models (see Planck column in Figure 1.3). As the physical law to control the Planck feedback is quite solid, its intermodel spread is the smallest among all the climate feedback parameters in models from the CMIP5 and CMIP6 (see Figure 1.3).

The lapse rate feedback is associated with the vertical temperature change in troposphere that deviates from the surface temperature change (Bony et al., 2006; Soden and Held, 2006; Feldl et al., 2017a). As we know, the atmosphere's

temperature decreases with height in the troposphere (the rate of such a change is termed lapse rate), and the emission of longwave radiation varies with temperature, thus the emitted longwave radiation from inhomogenous warming profiles would be different from the uniform warming cases. For example, if there is an enhanced warming at the upper troposphere in response to the radiative forcing at the tropopause, more OLR will be emitted than in a uniform temperature change over the vertical. Therefore, the lapse rate decreases and the system loses more energy, so inducing a negative feedback. This is usually the case in tropical regions (see Fig. 5 of Armour et al., 2013). In contrast, if the warming is trapped near the surface, the lapse rate feedback can be positive due to the strong inversion, the infrared cooling is less efficient than the homogeneous warming, thus providing a positive feedback. This usually occurs in high latitude regions (Armour et al., 2013; Pithan and Mauritsen, 2014; Goosse et al., 2018). Therefore, the global mean lapse rate feedback depends on the relative magnitude of those two opposite effects. On average, the influence of the tropics dominates, so the global mean lapse rate feedback is relatively negative and the multi-model mean value is about -0.5 $Wm^{-2}K^{-1}$ in CMIP5/6 models, as shown in Figure 1.3 (LR column).

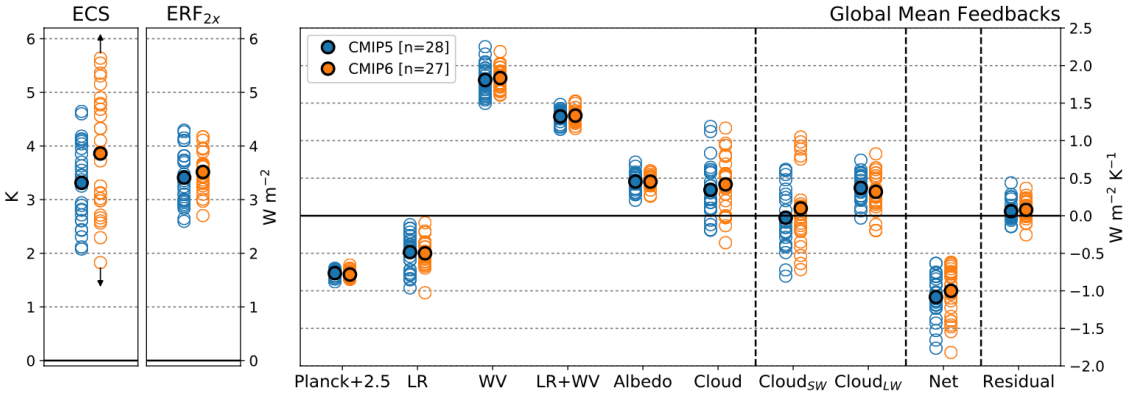

Figure 1.3 Estimates of (left) equilibrium climate sensitivity (ECS), (middle) effective radiative forcing ($ERF_{2\times}$), and (right) global mean climate feedbacks, derived from coupled experiments with abrupt quadrupling of CO_2 concentration experiments in CMIP5 (blue dots) and CMIP6 (orange dots) models. The black circles indicate the multi-model ensemble mean values. For display purpose, the Planck feedbacks have been added 2.5 $Wm^{-2}K^{-1}$ before plotting. LR and WV are lapse-rate and water vapor feedbacks, respectively. Taken from Fig. S3 of Zelinka et al. (2020) with permission of the John Wiley and Sons.

According to the Clausius–Clapeyron relation, the saturated vapor pressure is a quasi-exponential function of temperature. In addition, observations and numerical experiments consistently show that the relative humidity tends to remain more or less constant in response to climate change (Held and Soden, 2000; Soden and Held, 2006; Goosse et al., 2010). Thus the warming will cause a significant increase in the amount of water vapor in the atmosphere. Since water vapor is

the dominant greenhouse gas in the atmosphere (Held and Soden, 2000), the increase in water vapor content warms the atmosphere further, which in turn makes the atmosphere hold more water vapor. Thereby, water vapor feedback is a very strong positive feedback and the multi-model mean value of global mean water vapor feedback in CMIP5/6 models is about 1.8 $Wm^{-2}K^{-1}$ (see WV column in Figure 1.3).

Despite the large intermodel differences in lapse rate and water vapor feedbacks, the spread in net contribution of both feedbacks is much smaller compared to their individual spread (see LR+WV column in Figure 1.3). As pointed by previous studies, the lapse rate feedback and water vapor feedback are closely anti-correlated with each other (Soden and Held, 2006; Po-Chedley et al., 2018). Soden and Held (2006) have shown that the models exhibit a nearly constant relative humidity behavior under global warming, suggesting that most of the intermodel spread in water vapor feedback does not stem from the various responses of the relative humidity field, but from differences in the lapse rate response between models. As temperature and water vapor changes are tightly coupled in models, it is better to combine the lapse rate and water vapor feedbacks together when considering sources of intermodel spread in feedback strength (Soden and Held, 2006; Po-Chedley et al., 2018). Another option, proposed by Held and Shell (2012), is to compute Planck and lapse rate feedbacks assuming relative rather than absolute humidity is constant, and a small feedback from changes in relative humidity quantified separately. This method can remove the cancellation between water and lapse rate feedbacks in models, so that the individual feedbacks have less scatter than in the traditional decomposition (see their Fig. 1 in Held and Shell 2012; also see their Fig. 1 and Fig. S3 in Zelinka et al. 2020).

Surface albedo feedback is related to the regions with snow and ice, which is a positive feedback that enhances climate change (Winton, 2006b; Goosse et al., 2018). The mechanism is easy to understand: Warmer temperatures lead to the retreat of snow and ice, which makes the surfaces be less reflective than previous ones. This further causes an increase in the absorbed solar radiation and thus leads to more warming. The global mean surface albedo feedback is weakly positive, and the multi-model mean of globally averaged value in CMIP5/6 models is about 0.5 $Wm^{-2}K^{-1}$ (see Albedo column in Figure 1.3).

Cloud feedback is the variation of cloud radiative effect at the TOA in response to global warming. In the fifth assessment report (AR5) of the Intergovernmental Panel on Climate Change (IPCC), the sign of net cloud radiative feedback is likely positive with an estimate of 0.6 $Wm^{-2}K^{-1}$, which, however, has a lot of uncertainties (-0.2 to 2 $Wm^{-2}K^{-1}$) (Stocker et al., 2013). A recent estimate of net cloud feedback from CMIP6 models is 0.45 $Wm^{-2}K^{-1}$ (Zelinka et al., 2020; Sherwood et al., 2020), but the intermodel spread has no clear reduction from CMIP5 models

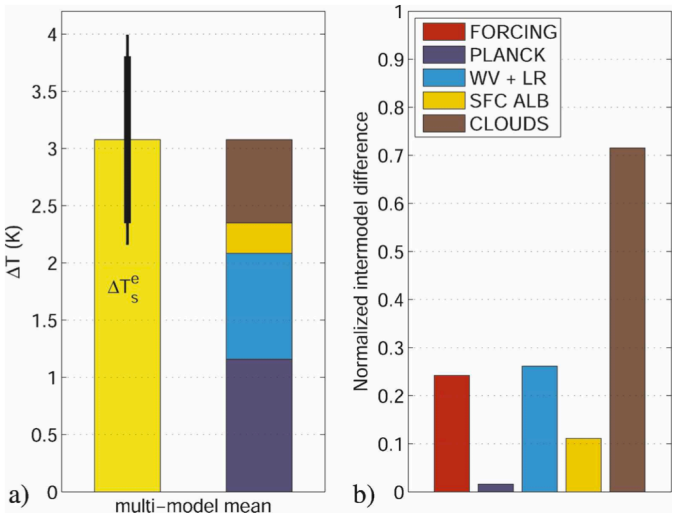

Figure 1.4 For a CO2 doubling, (a) multi-model mean ±1 standard deviation (thick line) and 5%–95% interval (thin line) of the equilibrium temperature change (ΔT_s^e), and contributions to this temperature change associated with the Planck response, combined water vapor and lapse rate (WV+LR) feedback, surface albedo feedback, and cloud feedback. (b) Intermodel standard deviation of the temperature change estimates associated with the radiative forcing, the Planck response, and the various feedbacks normalized by the intermodel standard deviation of the equilibrium temperature change ΔT_s^e reported in (a). Taken from Fig. 1 of Dufresne and Bony (2008). ©American Meteorological Society. Used with permission.

(see Cloud column in Figure 1.3). Nevertheless, there is still no agreement on the signs of global mean net cloud feedbacks in CMIP5/6 models, and several models show negative global mean values. Furthermore, sign disagreements also exist in the shortwave and longwave components of cloud feedback, and such a disagreement is more evident in the cloud shortwave component (see Cloud_{SW} and Cloud_{LW} columns in Figure 1.3). Cloud feedback is the single largest contributor to the uncertainty in the global mean net climate feedback parameters, and also contributes most to the intermodel spread of ECS (Bony and Dufresne, 2005; Soden and Held, 2006; Dufresne and Bony, 2008; Colman and McAvaney, 2011; Vial et al., 2013; Ceppi et al., 2017; Zelinka et al., 2020; Sherwood et al., 2020). For instance, Figure 1.4b, taken from Dufresne and Bony (2008), quantified the contributions to intermodel difference of ECS from various factors, and found the cloud feedback (brown bar) to be the largest source (including forcing) of such uncertainty, although it is not the largest contributor to the multi-model mean of ECS (Figure 1.4a). Recently, a lot of efforts have been paid trying to narrow down the range of ECS by finding possible observational constraints on cloud feedbacks (e.g., Cesana and Del Genio, 2021; Myers et al., 2021). The next questions are why the intermodel spread of cloud feedback is so large, and what mechanisms control the cloud response to global warming, as to be reviewed in next section.

1.4 Cloud radiative effect and cloud feedback

1.4.1 Cloud radiative effect

To answer the questions proposed at the end of last section, basic knowledge about clouds and their roles in the climate system is briefly introduced first.

Table 1.1 Statistics of the annually averaged total cloud amount (%) for various regions, which are from the ISCCP H-series data sets (Young et al., 2018) from 1984 to 2014.

Region	Ocean	Land	Total
Global	71.7	54.8	66.1
15°S – 15°N	62.4	63.5	62.6
15°N – 35°N	60.1	46.6	55.2
15°S – 35°S	65.0	48.3	61.4
35°N – 60°N	80.9	64.6	72.5
35°S – 60°S	84.0	65.0	83.5
60°N – 90°N	68.9	62.0	66.5
60°S – 90°S	80.1	44.3	60.1

Clouds usually cover more than half the area of the Earth at any given time (Houze, 2014; Ramanathan et al., 1989), which is supported by recent International Satellite Cloud Climatology Project (ISCCP) H-series products (Young et al., 2018), as shown in Table 1.1. Although the cloudiness varies among different regions, the annual mean cloud amount is usually larger than or close to 50% at any selected region. Also, the cloud amounts are usually larger over ocean regions than over land (Table 1.1 and Figure 1.5d), as the ocean provides an abundance of water vapor. The spatial pattern of cloud climatology is shown in Figure 1.5, and its features are to be discussed in detail in comparison with the spatial patterns of cloud radiative effect. Clouds play important roles in Earth's radiation budget and hydrological cycle, and this thesis will focus on their effect on radiation.

As shown in Figure 1.1, clouds can exert competing influences on the energy budget of the Earth. Specifically, clouds cool the Earth by reflecting the incoming shortwave radiation emitted by the sun, and warm the planet by trapping the longwave radiation emitted by the Earth. In general, we quantify the impact of clouds on planet's radiation budget using cloud radiative effect (CRE), which is defined as the differences in TOA net radiative fluxes between all-sky and clear-sky conditions, or the upward radiative fluxes at TOA between clear-sky and all-sky conditions (e.g., Ramanathan et al., 1989; Soden et al., 2004, 2008; Li et al., 2017). Note that the CRE is also called cloud radiative forcing (CRF) in some literatures (e.g., Ramanathan et al., 1989), but CRE is more commonly used currently, so we prefer using CRE in this study. According to the definition, the shortwave and

longwave CREs at TOA can be computed as follows:

$$\text{SWCRE} = \text{SW}^{\uparrow}_{\text{clr}} - \text{SW}^{\uparrow}_{\text{all}}, \tag{1.5}$$

$$\text{LWCRE} = \text{LW}^{\uparrow}_{\text{clr}} - \text{LW}^{\uparrow}_{\text{all}}, \tag{1.6}$$

in which the subscripts clr and all mean clear-sky and all-sky, respectively, and the arrows indicate the direction of radiation flux. Of course, $\text{SW}^{\uparrow}$ and $\text{LW}^{\uparrow}$ are reflected solar radiation and OLR at the TOA, respectively. The net CRE is the sum of shortwave and longwave CREs, that is:

$$\text{Net CRE} = \text{SWCRE} + \text{LWCRE} \tag{1.7}$$

The global mean shortwave CRE is approximately -50 Wm^{-2}, and global mean longwave CRE is around 30 Wm^{-2}. As the shortwave CRE dominates over the longwave CRE, the net impact of clouds on Earth's energy budget is a cooling effect with a global mean value about -20 Wm^{-2}, as shown in Figure 1.1 and Figure 1.6.

The distribution of annual-mean shortwave, longwave and net CREs at TOA is displayed in Figure 1.6, adapted from the IPCC AR5 (Stocker et al., 2013). To better understand the spatial pattern of the CRE climatology, the CRE equations are derived in further following Ramanathan et al. (1989). First, all-sky radiation (R_{all}; R can be SW or LW) is rewritten as

$$R_{\text{all}} = (1 - C_{\text{tot}})R_{\text{clr}} + C_{\text{tot}}R_{\text{cld}} = C_{\text{tot}}(R_{\text{cld}} - R_{\text{clr}}) + R_{\text{clr}}, \tag{1.8}$$

in which C_{tot} is the total cloud fraction and the upward arrows in R are neglected for simplicity. If we replace R_{all} in Equation (1.5) or Equation (1.6) with Equation (1.8), then CRE can be expressed as follows

$$\text{CRE} = R^{\uparrow}_{\text{clr}} - R^{\uparrow}_{\text{all}} = C_{\text{tot}}(R_{\text{clr}} - R_{\text{cld}}). \tag{1.9}$$

For shortwave CRE , we can write $R_{\text{clr}} = S_0\alpha_{\text{clr}}$ and $R_{\text{cld}} = S_0\alpha_{\text{cld}}$, such that Equation (1.9) becomes

$$\text{SWCRE} = S_0 C_{\text{tot}}(\alpha_{\text{clr}} - \alpha_{\text{cld}}), \tag{1.10}$$

where S_0 is solar constant, and α_{clr} and α_{cld} are clear-sky and all-sky albedo respectively. As the clear-sky albedo usually smaller than that in all-sky (i.e. $\alpha_{\text{clr}} < \alpha_{\text{cld}}$), the shortwave CRE is negative everywhere (Figure 1.6a). This means clouds reflect more sunlight back to space than clear-sky conditions, and thus the shortwave effect of clouds is to cool the Earth. In addition, the magnitude of shortwave CRE increases with cloud fraction and albedo contrast between cloudy and

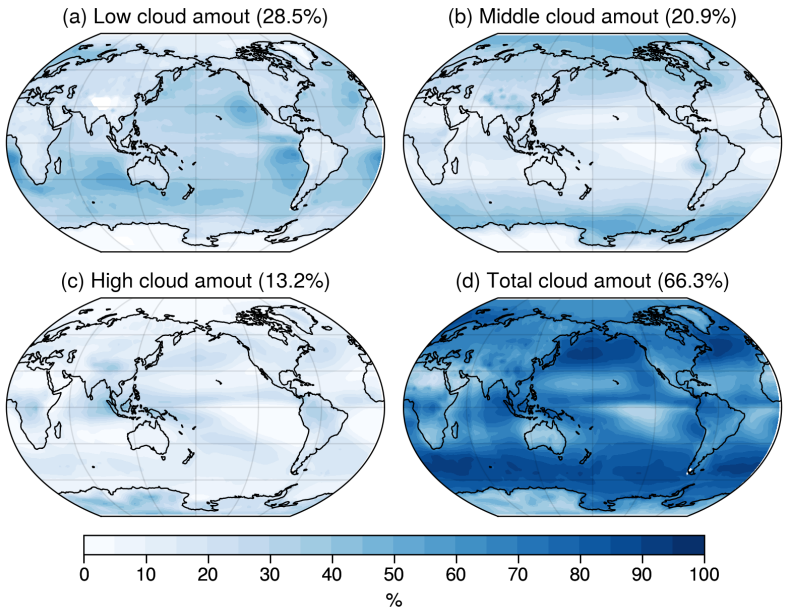

Figure 1.5 Distribution of annual-mean (a) low cloud amount (below 680 hPa), (b) middle cloud amount (440-680 hPa), (c) high cloud amount (above 440 hPa) and (d) total cloud amount from ISCCP H-series data set from 1984 to 2014. The global mean amounts are shown in titles.

clear conditions, as indicated by Equation (1.10). For example, when comparing the distribution of total cloud amount (Figure 1.5d) and shortwave CRE (Figure 1.6a), we can find that the magnitude of shortwave CRE is large over regions of persistent cloudiness such as Southern Ocean, and is small over the regions where there is little cloud cover such as subtropical trade cumulus regions. In addition, the shortwave CRE generally has more negative values over ocean than over land, as the surface albedo over land is larger than ocean, thus the contrast between clear and cloudy albedo is smaller. The albedo of clouds can be derived from its optical depth (see Figure 4.6; Liou et al. 1990), a value determined by the combination of cloud macro-physical (e.g., cloud fraction and cloud water content) and micro-physical properties such as cloud droplet shape and size and cloud thermodynamic phase (Stephens, 1978). This could bring lots of uncertainties and could be one possible reason that the shortwave cloud feedback is more uncertain than the longwave component (see 'Cloud_{SW}' and 'Cloud_{LW}' columns in Figure 1.3; Zelinka et al. 2020).

For longwave CRE, we can write $R_{\text{clr}} \approx \sigma T_{\text{clr}}^4$ and $R_{\text{cld}} \approx \epsilon_{\text{cld}} \sigma T_{\text{cld}}^4 + (1 - \epsilon_{\text{cld}}) \sigma T_{\text{clr}}^4$ based on Stefan–Boltzmann law, and after putting them into Equation (1.9), the longwave CRE becomes

$$\text{LWCRE} \approx \epsilon_{\text{cld}} \sigma C_{\text{tot}} \left(T_{\text{clr}}^4 - T_{\text{cld}}^4 \right), \tag{1.11}$$

where ϵ_{cld} is the emissivity of clouds, σ is Stefan–Boltzmann constant, and T_{cld} and

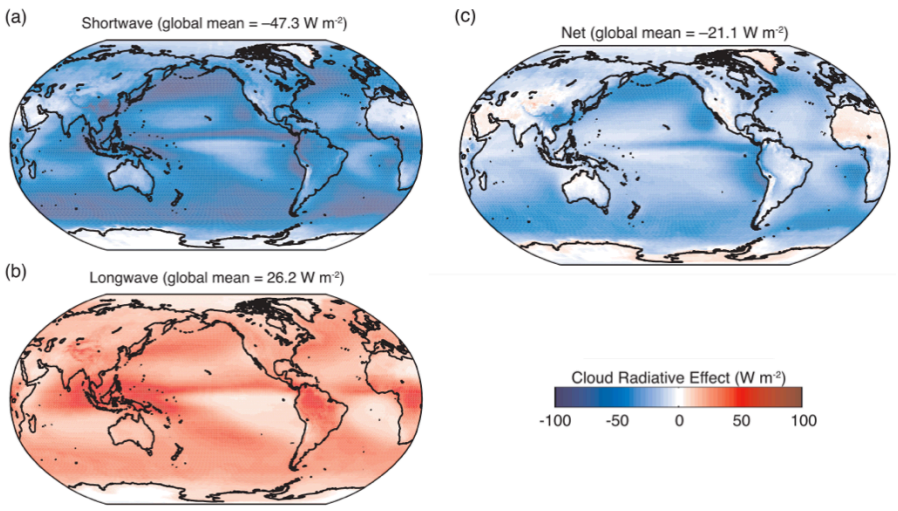

Figure 1.6 Distribution of annual-mean top of the atmosphere (a) shortwave, (b) longwave, (c) net cloud radiative effects averaged over the period 2001–2011 from the Clouds and the Earth's Radiant Energy System (CERES) Energy Balanced and Filled (EBAF) Ed2.6r data set. Adapted from Fig. 7.7 of the Fifth Assessment Report (AR5) of the Intergovernmental Panel on Climate Change (IPCC) (Stocker et al., 2013).

T_{clr} are emission temperature at cloudy and clear conditions, respectively. From Equation (1.11) we can judge that longwave CRE is positive (see Figure 1.6b) as $T_{clr} > T_{cld}$. This indicates that clouds emit less longwave radiation to space than the clear-sky atmosphere, and thus can heat Earth. Additionally, the longwave CRE increases with cloud fraction, emissivity and the emission temperature contrast between clouds and clear-sky atmosphere, in which the last depends on the cloud top temperature. In fact, we can find the spatial patterns of longwave CRE (Figure 1.6b) and high cloud amount (Figure 1.5c) are similar. For instance, the longwave CREs are large over the areas with much high clouds, such as the Intertropical Convergence Zone (ITCZ); The longwave CRE is smaller where high clouds are rare, such as over the subtropical trade-wind cumulus region.

The net CRE is the competing result of shortwave and longwave CREs, with the spatial pattern shown in Figure 1.6c. Clearly, the large negative values over the regions with persistent low clouds (see Figure 1.5a), such as Southern Ocean and subtropical eastern Pacific regions, as the shortwave CRE dominates over the longwave CRE in these regions. The net CRE over deep convective regions is near-zero due to the cancellation between shortwave and longwave components (e.g., Wall et al., 2019).

In summary, different factors have impact on shortwave and longwave CREs, including both macrophysical (e.g., cloud fraction, cloud water content) and microphysical properties (e.g., cloud condensate shape and size). The net effect depends on its shortwave and longwave components, which have opposite signs and different magnitudes. For shortwave CRE, cloud amount and cloud albedo (or

optical depth) are important factors to determine its strength; while for longwave CRE, the cloud amount (especially high cloud amount), cloud emissivity and the contrast of cloud top temperature with clear-sky atmosphere are important contributors to its magnitude. To better understand how cloud radiative properties change in response to the increase of greenhouse gas concentration, we need to investigate how these factors might change under global warming.

1.4.2 Mechanisms of cloud feedback

To fully understand cloud feedback is a challenging job, partly due to the diversity of clouds in the climate system (Ceppi et al., 2017; Zelinka et al., 2017). For example, the clouds are located at different locations (e.g., low, middle and high clouds) and the cloud condensates are in different shapes or forms (such as liquid, ice or mixed phase), so they can affect the radiation in different ways. In addition, these clouds are usually controlled by different meteorological factors, therefore it is hard to predict the responses of clouds under climate change. Nevertheless, lots of efforts have been paid by previous studies to pin down the intermodel spread of cloud feedbacks (e.g., Bony et al., 2004; Bony and Dufresne, 2005; Bony et al., 2006; Vial et al., 2013; Webb et al., 2015; Geoffroy et al., 2017; Zelinka et al., 2016; Myers et al., 2021; Ceppi and Nowack, 2021).

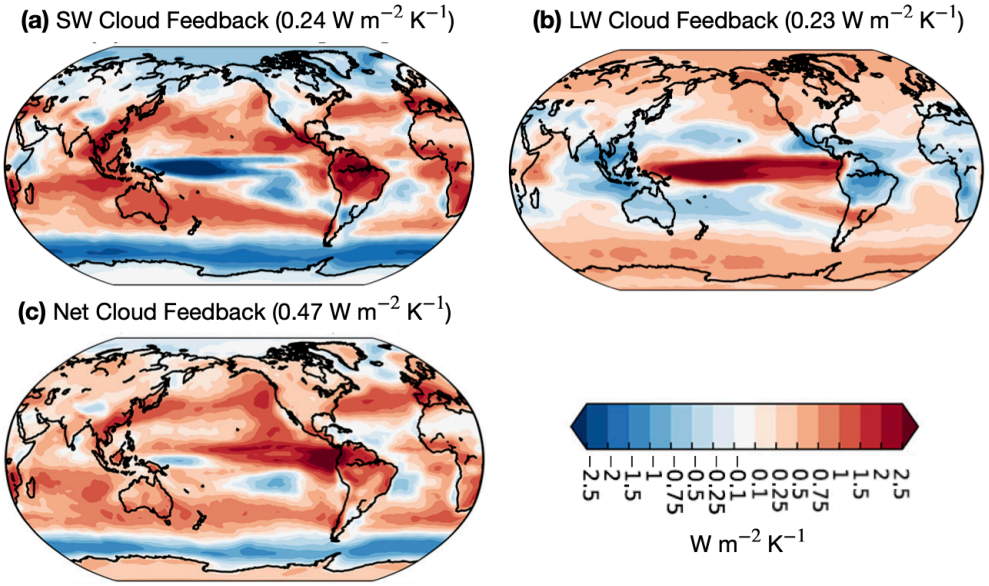

Figure 1.7 Multi-model ensemble mean (a) shortwave, (b) longwave and (c) net cloud feedbacks for the first and second phases of the Cloud Feedback Model Intercomparison Project (CFMIP; Webb et al., 2017) models, which are computed through the cloud radiative kernel technique. Adapted from Figs. 2, S5 and S6 of Zelinka et al. (2016) with permission of the John Wiley and Sons.

The shortwave, longwave and net cloud feedbacks have been introduced in Section 1.3.2, and their spatial patterns simulated in the first and second phases

of Cloud Feedback Model Intercomparison Project (CFMIP; Webb et al., 2017) models are shown in Figure 1.7. The net cloud feedback is positive at nearly every location equatorward of 50°, and negative in high latitudes such as the Southern Ocean and Arctic region (Figure 1.7c). When decomposing the net cloud feedback into shortwave and longwave components, we find that the shortwave cloud feedback is negative in lower and high latitudes, but positive over the subtropics. For instance, the shortwave cloud feedback is negative in Southern Ocean region (Figure 1.7a). The longwave cloud feedback is positive in tropical and high-latitude regions, and especially pronounced over tropical deep convection regions (Figure 1.7b). The possible mechanisms for these feedbacks can be understood by further breaking down the cloud feedback into three categories (i.e., cloud amount, cloud altitude and cloud opacity feedbacks; Zelinka et al. 2012b) due to their different radiative properties. The features of net cloud feedback can be understood through the sum of these three different components (Ceppi et al., 2017; Zelinka et al., 2017), as we will explain below.

Altitude feedback

As introduced in Section 1.4.1, high clouds have much larger longwave cloud radiative effect due to their colder cloud top temperature. As clouds get higher, they will have lower temperature and emit less infrared radiation to space. Therefore, the increase in cloud altitude has a warming effect on climate by reducing the outgoing longwave radiation.

One robust cloud change under global warming is the positive longwave cloud feedback in tropical regions (Figure 1.7b), which is believed to be related to the rising of high clouds (e.g., Wetherald and Manabe 1988). The positive longwave cloud altitude feedback can be explained by the fixed anvil temperature (FAT) hypothesis, which is first proposed by Hartmann and Larson (2002), and used by lots of later studies (e.g., Kuang and Hartmann, 2007; Zelinka and Hartmann, 2010; Yoshimori et al., 2020). The FAT theory holds that the isotherms move up and convection deepens in tropical region as climate warms, but the cloud-top temperature of anvils remains approximately constant. In this case, according to Equation (1.11), the cloud-top temperature does not warm in step with the surface warming and the OLR keeps relatively constant, so the tropics become less efficient at radiating the heat away and more heat would be trapped within the Earth, indicating that high clouds act as a positive feedback on climate under global warming.

Optical depth feedback

Another robust cloud change in response to increasing concentrations of CO_2 is the cloud phase change from the middle to high latitudes (e.g., Storelvmo et al., 2015; Ceppi et al., 2016; Tan et al., 2016; McCoy et al., 2016). As the melting level shifts upward and poleward in response to warming, the ice condensate in mixed-phase clouds (i.e., containing both liquid and ice condensates) melts into liquid water. That is to say, the occurrence of liquid water in clouds should increase relative to ice. Therefore, for a fixed cloud condensate amount, this leads to the increase of cloud optical depth (Stephens, 1978), due to the smaller effective radius of liquid droplets (Stubenrauch et al., 2013). In addition, given the ice cloud droplets are larger than liquid cloud droplets, ice clouds tend to precipitate more efficiently. That is to say, the cloud life time is longer after cloud phase changing from ice to liquid, making the liquid clouds persist longer than ice clouds and a further optical thickening of the cloud (Storelvmo et al., 2015; Ceppi et al., 2016). Therefore, more shortwave radiation would be reflected back to space due to this optical depth change, resulting in a negative shortwave feedback (e.g., Zelinka et al., 2012a,b, 2013b; Ceppi et al., 2016; Tan et al., 2016; McCoy et al., 2016; Zelinka et al., 2020; Bjordal et al., 2020). As this phase change mechanism can only operate below freezing, its occurrence in low clouds is evident in middle and high latitudes as shown in Figure 1.7a (Ceppi et al., 2017).

However, this negative optical depth feedback from hydrometeor phase change is perhaps overestimated in CMIP5 models due to the poor representation of supercooled liquid cloud in mixed-phase clouds (Tan et al., 2016; Frey and Kay, 2018). Too much present-day ice in mixed-phase clouds leads to stronger negative optical depth feedback under global warming. This bias is partly mitigated in CMIP6 models, and thus the negative optical depth feedback over middle to high latitudes weakens, which leads to the increase in net cloud feedback and in ECS in CMIP6 models (e.g., Zelinka et al., 2020; Bjordal et al., 2020). But we should also notice that this cloud phase change would make the precipitation less likely (e.g., Korolev et al., 2017), hence increasing the cloud lifetime and bringing a negative feedback. But as the warm clouds precipitate too readily in CMIP models, this negative cloud lifetime feedback is underestimated in current GCMs and the simulated ECS might be higher than it should be (Mülmenstädt et al., 2021).

Cloud amount feedback

The feedback induced by the cloud amount change is different for different cloud types. Specifically, the warming induced by increase of high, thin clouds usually leads to a positive feedback. The reason is that the optical depth of these high, thin clouds is typically small, thus having little impact on the shortwave radiation.

However, such clouds can absorb the longwave radiation and thus constitute a strong greenhouse effect. This can also be inferred from Equation (1.11): the increase of high cloud amount leads to the rise of longwave CRE, which has a heating effect on climate. In contrast, the warming induced increase in the amount of low clouds (especially the opaque ones) brings a negative feedback as less sunlight can reach the surface, thus a cooling effect. As shown in Equation (1.10), the increase of cloud amount (especially the low opaque clouds) strengthens the magnitude of shortwave CRE, which has a cooling effect on climate. Currently, there is still lack of a well-accepted theoretical basis for the possible changes of low cloud amount, and the GCMs have low confidence in simulating their changes under global warming (Stocker et al., 2013).

The low cloud amount feedback in GCMs is dominated by the response of boundary-layer cloud types at low latitudes: stratus, stratocumulus, and cumulus clouds (Ceppi et al., 2017). Although they cover a relatively small fraction of Earth, the low clouds such as stratus and stratocumulus have relatively large shortwave CREs, so that even small changes in their coverage may have significant regional and global impacts (e.g., Schneider et al., 2019). The formation and dissipation of low clouds are controlled by the differences between the supply of moisture from the surface and the mixing of relatively dry air in the free troposphere. Observations have shown a strong relationship between inversion strength at the top of the planetary boundary layer and cloud amount (Gordon, 1992; Klein and Hartmann, 1993; Wood and Bretherton, 2006). Stronger inversion weakens the mixing between the moisture boundary layer and the dry free troposphere aloft, so more moisture is trapped below the inversion layer, thereby favoring more low-level clouds (e.g., Qu et al., 2014, 2015b; Scott et al., 2020). In contrast, the increase in sea surface temperature (SST) leads to higher temperature and saturation water vapor pressure in the boundary layer, which can weaken the inversion strength if the temperature in the free troposphere remains constant. In this case, the in-cloud latent heating enhances the turbulance and entrainment of the drier air from aloft into the boundary layer, thus resulting in the reduction of cloudiness in low level (e.g., Rieck et al., 2012; Webb and Lock, 2013; Qu et al., 2014; Bretherton, 2015; Brient et al., 2016; Myers and Norris, 2016; Ceppi and Gregory, 2017; Scott et al., 2020). This mechanism is not only found in large-eddy simulations (Bretherton, 2015), but also supported by some GCM simulations (e.g., Zhang et al., 2013; Myers and Norris, 2016) and recent low cloud constraints constructed from satellite observations (Scott et al., 2020; Myers et al., 2021). The inversion strength and SST are two major meteorological factors to determine the observed natural variability of low cloud amount (e.g., Zhou et al., 2016; Cesana and Del Genio, 2021). In addition, other factors such as the relative humidity in the free troposphere, the strength of large-scale subsidence,

warm/cold temperature advection and surface wind speed also have impacts on cloudiness at low troposphere, but their contributions are relatively small (e.g., Bretherton, 2015; Myers and Norris, 2016; Scott et al., 2020).

Moreover, previous studies also find that low cloud changes depend not only on local SST changes, but also on some remote effects (e.g., Zhou et al., 2015, 2016, 2017; Mauritsen, 2016; Andrews and Webb, 2018). For example, Zhou et al. (2017) analyzed the dependence of global cloud feedback on the spatial pattern of SST change with a Green's function approach, and found that warming in tropical ascent regions increases the free-tropospheric temperature throughout the tropics, thereby enhancing the inversion strength over remote regions and inducing positive change in global low cloud amount and negative CRE anomalies; while the warming in the tropical subsidence or extratropical regions only causes local decrease in low cloud amount and positive change in CRE. These results suggest that the low cloud amount feedbacks could be different due to the differences in SST warming patterns, the so called 'pattern effect' (e.g., Dong et al., 2020).

In CMIP models, the low cloud amount feedback is the largest single contributor to the intermodel spread of net cloud feedback (Bony and Dufresne, 2005; Caldwell et al., 2016; Zelinka et al., 2016). It has been suggested that the different convective parametrizations play important roles in driving the spread of low cloud amount feedback and climate sensitivity (e.g., Gettelman et al., 2012; Zhao, 2014; Sherwood et al., 2014), but Webb et al. (2015) found that the range in cloud feedbacks among the CFMIP models did not change substantially when convective parametrizations were switched off, implying that some non-convective processes must also contribute substantially to the overall intermodel spread of cloud feedback. Also, previous studies such as Qu et al. (2014) have suggested that models with different type of cloud schemes may predict opposite cloud cover changes under global warming in several marine stratocumulus regions in subtropical ocean region off the west coasts of continents. Subsequently, Geoffroy et al. (2017) implemented six different diagnostic cloud schemes found in CMIP models into two test-bed climate models, and found that roughly half of the multi-model spread in the cloud feedback in stratocumulus regions could be reproduced by changing the stratiform cloud scheme alone, suggesting that different stratiform cloud schemes play an important part in the spread of cloud feedback, both in stratocumulus cloud regions and globally. From these studies we can find that the intermodel spread in cloud feedback in GCMs depends not only on cloud scheme (i.e., how clouds are represented in GCMs) itself (e.g., Qu et al., 2014; Geoffroy et al., 2017), but also on the interaction between clouds and various physical process such as shallow convective mixing, turbulence and radiation (e.g., Vial et al., 2016).

1.5 Cloud scheme

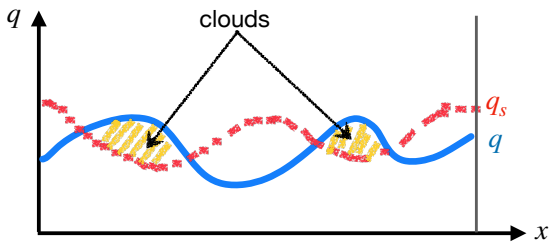

Figure 1.8 Schematic showing partial cloud cover in a grid box (1D) when temperature or humidity fluctuations exist. The blue line shows humidity and the red dashed line indicates saturation mixing ratio of the grid box. The shaded regions are cloudy parts as the humidity exceeds the saturation mixing ratio.

At present the typical horizontal resolution of the GCMs is 50-200km, but clouds usually involve the air motions in mesoscale and convective scale (Houze, 2014), which are usually in sub-grid scale both horizontally and vertically, implying that cloud processes are hard to resolve explicitly by the GCMs. In this case, the "parameterization" becomes a practical way to build cloud schemes. The parameterization is to represent the effects of the smaller-scale processes (turbulence, cloud microphysics, convection, etc.) in terms of the large-scale states (such as velocity, temperature, pressure, humidity) (Randall et al., 2003), which could be seen as a way to find potential relationships between the unknown and known variables (Randall, 1989).

1.5.1 Relative humidity schemes

Previous studies have investigated various ways to represent clouds in climate models. For example, Holloway and Manabe (1971) prescribed the clouds externally with climatological data without dynamic interplay with the other components of the model. Some early modelling studies made the assumption that a grid box in the model is either fully saturated or totally unsaturated. However, this assumption is not reasonable as the humidity can distribute unevenly within a grid box, suggesting that condensation can occur even if the relative humidity is less than 100%, as shown in Figure 1.8. A general idea is to link the cloud cover with the relative humidity (RH), as one can expect that the amount of condensation would increase with the increase of mean humidity of the model grid box, which is the basis for some diagnostic methods.

Diagnostic schemes predict the cloudiness based on the model variables empirically or statistically. In these schemes, the clouds can be linked to atmospheric outputs such as relative humidity, vertical velocity and static stability, among which a linear relationship between cloud fraction and RH might be simplest one. For ex-

ample, Smagorinsky (1960) found empirically that non-convective cloud amount correlated with the average relative humidity in the respective layers, arguing that the non-precipitating condensation depends only on the accumulated history of vertical motion, which can be reflected by the humidity. Ricketts (1973) obtained a roughly linear relationship between cloud amount and observed relative humidity but commented that the relationship is somewhat indefinite.

Water vapor generally distributes heterogeneously in the grid box, so the averaged RH within a box should be less than 1 for a partial coverage of clouds (Figure 1.8). Previous studies usually adopt the critical relative humidity RH_{crit} as the minimum threshold for clouds to form, which is often left as a free parameter that can be tuned during model development (e.g., Hourdin et al., 2017; Kay et al., 2012; Mauritsen et al., 2012). For example, Sundqvist (1978) and Sundqvist et al. (1989) find that cloud fraction can be rewritten as a function of critical RH by assuming the water vapor is uniform distributed within the grid box. In general, RH_{crit} decreases with height, but will vary according to different types of clouds. Although RH_{crit} does not have clear physical meaning, it can be used to modify the cloud amounts in different locations. For example, one can increase RH_{crit} asymptotically to nearly unity to prevent the unrealistic circus clouds (Sundqvist et al., 1989).

As a unique predictor, RH is very simple and useful to diagnose the cloudiness, and it is still widely used in GCMs (e.g., Gordon, 1992; Park et al., 2014; Pope et al., 2000). However, it is not valid for all the cases. As we can see, some studies also made use of other variables to diagnose the cloudiness. For instance, Xu and Randall (1996) developed a semi-empirical scheme to determine the stratiform cloud fraction based on grid-averaged mixing ratio of condensate (cloud water and cloud ice) and RH. As for the scheme provided by Slingo (1987), both the RH and vertical velocity were taken into account, in which different empirical relations were used for different clouds including low, middle, high and convective clouds.

In summary, the methods based on relative humidity and other predictors are useful to diagnose the cloudiness, which ensures that the clouds can form before the grid box get saturated. One problem for the diagnostic methods is that in most cases the cloud condensate has to be diagnosed or prognosed via other methods (e.g., Zhang et al., 2003; Park et al., 2014), which could lead to some inconsistencies between cloud fraction and cloud condensate (e.g. Gregory et al., 2002; Tompkins, 2005).

1.5.2 Statistical schemes

In contrast, the prognostic approach (e.g., Tiedtke, 1993) is to explicitly calculate the cloud-related variables, such as cloud water content, in order to pursue a unification of all clouds processes, which is more realistic in some degree and

requires more physical basis and interactions with other parts of the models. Another widely used cloud prediction method is a statistical scheme, in which the cloud fraction and in-cloud liquid water/ice are determined based on the assumed probability distributions of subgrid variability of thermodynamic properties. As the cloud related variables such as moisture and temperature are not the same everywhere but distributed randomly within the grid box, it is natural to assume that the cloud cover depends on the distribution of moisture, sometimes on the joint distribution of moisture and temperature. As shown in a very early work, Sommeria and Deardorff (1977) gave up the assumption that a grid is either entirely saturated or unsaturated in the climate models and proposed to use the statistical distribution of moisture within the grid box. In this case, given the probability distribution function (PDF) of the total water (q_t is the mixing ratio) in grid box, the cloud fraction (C) can be calculated as

$$C = \int_{q_s}^{\infty} \mathrm{PDF}(q_t)\,\mathrm{d}\,q_t, \tag{1.12}$$

and the cloud water content (q_c is the mixing ratio of cloud water) is

$$q_c = \int_{q_s}^{\infty} (q_t - q_s)\mathrm{PDF}(q_t)\,\mathrm{d}\,q_t, \tag{1.13}$$

where q_s is the saturation mixing ratio in both formulations.

However, the shapes of subgrid-scale PDF of total water specific humidity, saturation deficit, or a combined variable of liquid water and potential temperature are difficult to determine due to limitation of observational data, so sometimes the model data are also used (Bony and Emanuel, 2001). Additionally, many different PDF forms have been proposed in the previous studies. For example, Le Treut and Li (1991) made use of the uniform distribution of total water in the grid box to calculate the cloud cover and liquid water content. Other symmetrical distributions, such as the Gaussian distribution (Sommeria and Deardorff, 1977), triangular distribution (Smith, 1990) and skewed distributions, such as lognormal distribution (Bony and Emanuel, 2001) and beta distribution (Tompkins, 2002), have also been employed in numerical models. However, there are also some problems in the distributions. For example, the Gaussian distribution is unbounded, indicating that the maximum cloud condensate mixing ratio might approach infinity, and cloud cover is always large than zero (Tompkins, 2002). In general, complicated forms of the PDF need more parameters to fit. But due to the limitation of the data, it is possibly hard to validate the distributions. Linking the statistical cloud scheme to other physical processes seems a promising way to improve cloud simulations. For example, Qin et al. (2018) developed a Gaussian PDF cloud scheme with the PDF variance diagnosed from the turbulent and shallow convective processes,

which could improve the simulation of low marine clouds and alleviate the double ITCZ problem (Qin and Lin, 2018).

1.5.3 Relationship between relative humidity and statistical schemes

As discussed in the previous section, one has to determine the expression of subgrid variance (i.e. second order moment) or other higher-order moments in the statistical schemes. In doing so there are two general practices in current studies. The simple case is to use time-invariant variance (e.g., Sundqvist, 1978; Smith, 1990), and the other approach is to employ time varying variance, which is usually obtained from other physical processes such as a boundary layer scheme or shallow convection scheme (e.g., Qin et al., 2018). The second case usually provides a more realistic link between clouds and other physical processes (Tompkins, 2002).

Note that there is no distinction between the RH schemes and statistical schemes, although they seem different in form. As a matter of fact, if the subgrid variance in a statistical scheme is assumed to be time-invariant, it can be reduced to a RH scheme (Tompkins, 2002, 2005). The key is to link the variance with the critical relative humidity. That is to say, the critical RH value can reflect the level of sub-grid variance in RH schemes (Quaas, 2012). A larger critical RH value means a lower subgrid variability and vice versa. For example, the RH scheme from Sundqvist (1978) can be derived by assuming a uniform distribution of total water mixing ratio within a grid box, in which the variance is assumed a constant fraction of the saturation water vapor mixing ratio, and this constant is associated with critical RH value (see Appendix A of Quaas (2012) for a full derivation). Another example is the triangular distribution used by Smith (1990) and Park et al. (2014), they also obtain the equivalent RH formulation by assuming the variance is related to critical RH. As pointed out by Tompkins (2002), the parameterizations such as Xu and Randall (1996), in which cloud fraction is related to RH and cloud condensate, can be viewed as manifestations of the statistical schemes although the actual PDFs of total water are not known.

1.6 Thesis outline

The goal of this thesis is to understand the climate feedbacks with simple models, and the thesis is arranged as follows:

Chapter 1 introduces the motivation, background and outline of this study. The background includes the basic ideas of Earth's radiation budget, climate feed-

backs, cloud radiative effects and their feedback mechanisms, and a brief introduction to cloud parameterization schemes.

The data and methods used in the thesis are presented in Chapter 2. The data sets include the satellite observations relating to clouds and radiation, and other climate variables, such as temperature, relative humidity and vertical velocity, from the reanalysis. The methodology part first gives a brief introduction to the Isca model, then presents the methods used in the thesis to calculate and decompose the cloud feedbacks. Finally, several low cloud proxies used in Chapter 4 are listed for reference.

Chapter 3 mainly presents the results from polar amplification of surface temperature change in aquaplanet simulations. In this chapter, the contributions from different climate feedbacks, forcing and heat transport are quantified through the decomposition method. The major conclusion is that the local lapse rate feedback and Planck feedback (plus heat transport) play important roles in determining the warming structure in the polar region.

Chapter 4 focuses on the parameterization of a simple cloud scheme and the evaluation of its simulation of cloud climatology. These include the parameterization of the cloud fraction and cloud optical properties, simulation setup and the comparison of the simulated cloud fraction, radiative flux and cloud radiative effect with observations and CMIP5 models. The comparison consists of the spatial pattern, zonal mean structure and seasonal cycle.

The topics of Chapter 5 are cloud feedback and its uncertainty. First, the cloud feedback simulated from the simple cloud scheme is evaluated. The spatial patterns of longwave, shortwave and net cloud feedbacks, as well as their components such as cloud amount, altitude and optical depth feedbacks, will be investigated and compared with the CMIP models. The possible reasons for the feedback features are to be explored. Then the results from perturbed parameter ensemble (PPE) will be analysed. The cloud feedback spread from the PPE simulations will be checked to see if it reproduces the spread in the CMIP models. The causes of the cloud feedback spread in Isca PPE will be investigated. Based on these results, which parameter or process is more sensitive would be analysed. Finally, the implications for equilibrium climate sensitivity will be discussed.

Finally, Chapter 6 summarizes the major contents and conclusions of the thesis, and discusses possible future work.

Chapter 2

Data and Methods

In this thesis, several different observational and reanalysis data sets, as well as model simulations, are used. For example, the reanalysis data sets are employed in Chapter 4 to derive the linear formula between cloud fraction and relative humidity, and to evaluate the relationship between low cloud amount and its possible proxies. The satellite products relating to clouds and radiation fields are used in Chapter 4 to evaluate the performance of the simple cloud scheme. To make it clear, these data sets are briefly summarized in this chapter. One major topic of this thesis is the cloud feedback, and the main tool used to simulate it is the idealized climate model, Isca (Vallis et al., 2018). Therefore, the features of this climate model and the advantages of using the idealized models are discussed here. However, how to calculate or estimate cloud feedback in climate models is not so evident, and the direct estimate from the change of cloud radiative effect might be impacted by the cloud masking effect. Therefore, it is necessary to discuss the pros and cons of the several different methods to estimate cloud feedback in this chapter.

The chapter is organized as follows: The satellite data sets related to radiation and cloud fields are introduced in Section 2.1. The idealized general circulation model employed throughout this thesis is described briefly in Section 2.2. In Section 2.3, how the cloud observation simulator package is implemented in Isca is documented. Section 2.4 summarizes the possible methods to calculate the cloud feedback. The low cloud amount proxies used in Chapter 4 are listed in Section 2.5 for reference.

2.1 Observational and reanalysis data sets

2.1.1 Clouds and radiation data sets

Satellites have played an important role in observing the Earth over recent decades, and these satellite retrievals are essential data sets for us to understand the

weather and climate on Earth. The observation of clouds and radiation at the top of the atmosphere (TOA) depends particularly on the satellites. In general, the satellite products can be categorized into different groups according to their processing levels ranging from Level 0 to Level 4 (Parkinson et al., 2006). Specifically, Level 0 is the raw and unprocessed instrument data. Level 1 is annotated with ancillary information (1A) and processed to sensor units (1B). Level 2 is derived geophysical variables, Level 3 is mapped to a space-time grid, and Level 4 are modeled outputs or variables derived from multiple measurements. It is usually easier for users to use these satellite retrievals when they have higher processing levels. In this thesis, most satellite data sets used are at Level 3 or 4, and only one at Level 2, as to be introduced below.

Clouds and the Earth's Radiant Energy System Top-of-Atmosphere (TOA) data product

The Clouds and the Earth's Radiant Energy System (CERES) project (https://ceres.larc.nasa.gov) provides satellite-based observations of Earth's radiation budget and clouds (Wielicki et al., 1996). It uses measurements from CERES instruments flying on several satellites (TRMM[1], Terra, Aqua, S-NPP[2], NOAA-20[3]), along with measurements from higher-resolution imagers on polar orbiting and geostationary satellites and other input data source, to produce a comprehensive set of Earth's radiation budget data products for weather, climate and applied science research. The goal of CERES is to produce a long-term, integrated global climate data record for detecting the possible changes in the Earth's radiation budget from the surface to the top of the atmosphere, so as to improve our understanding of how Earth's radiation budget varies in time and space and of the role that clouds and other atmospheric properties play.

The main CERES product used in this thesis is the Energy Balanced and Filled (EBAF) product (CERES-EBAF hereafter; Loeb et al., 2009), especially the latest version Ed4.1 (Loeb et al., 2018). The CERES-EBAF product involves the CERES and Moderate Resolution Imaging Spectroradiometer (MODIS) instruments flying on the Terra (descending sun-synchronous orbit with an equator crossing time of 10:30 A.M. local time) and Aqua (ascending sun-synchronous orbit with an equator crossing time of 1:30 P.M. local time) as well as geostationary imagers that provide hourly diurnal information between 60°S–60°N (Loeb et al., 2018). The EBAF data set is designed to solve the existing imbalance issue in the average global net radiation at the TOA from the CERES satellite observations. It uses an objective constraint algorithm to adjust shortwave and longwave TOA

[1]TRMM: Tropical Rainfall Measuring Mission, a research satellite in operation from 1997 to 2015

[2]S-NPP: Suomi National Polar-orbiting Partnership

[3]NOAA-20: National Oceanic and Atmospheric Administration-20

fluxes within their ranges of uncertainty to remove the inconsistency between average global net TOA flux and heat storage in the Earth-atmosphere system. The EBAF product consists of monthly mean shortwave, longwave, and net TOA all-sky and clear-sky radiative fluxes over 1°×1° latitude–longitude regions, as well as the MODIS-based cloud properties such as cloud amount, optical depth, effective pressure, and temperature at cloud top. In Chapter 4, this CERES-EBAF Ed4.1 product is used to evaluate the cloud radiative effect simulated from the simple cloud scheme.

International Satellite Cloud Climatology Project (ISCCP) – H Series

The International Satellite Cloud Climatology Project (ISCCP) began in early 1980s as part of the World Climate Research Program (WCRP) (Schiffer and Rossow, 1983; Rossow and Schiffer, 1991), and is probably the longest-running international satellite-based global environmental data project. Its goal is to collect weather satellite radiance measurements and to analyze them to infer the global distribution of clouds, their properties, and their diurnal, seasonal and interannual variations. This project has accumulated cloud observation for almost four decades and has therefore been widely used in cloud related research.

Several series of the ISCCP products have been publised previously. However, the widely used ISCCP D-series product (Rossow and Schiffer, 1999) has not been updated since December 2009. Recently, a new H-series product was published (Young et al., 2018), spanning from 1982 to 2015 (see `https://isccp.giss.nasa.gov/products/onlineData.html`, last accessed: April 28, 2021). Comparing to the previous ISCCP D-series product, the H-series has improved the low-level cloud sensitivity over snow and ice in polar regions. More importantly, based on ISCCP's legacy and in light of the technological advancements that include active spaceborne sensors (e.g., Cloud–Aerosol Lidar and Infrared Pathfinder Satellite Observations and CloudSat) and cloud data sets that rely on newer passive imagers with higher spectral, spatial, radiometric, and temporal resolutions, the H-series has exploited to produce cloud products with much higher resolutions (Young et al., 2018).

In this study, the high-resolution global monthly (HGM) product (at Level 3) with 1°×1° resolution is used for analysis (e.g., in Chapter 1). Of course, gridded hourly high-resolution output (HGH) is also available. In ISCCP H-series product, it has provided many cloud related variables, such as (but not limited to) cloud amount (low, middle, high and total), cloud-top temperature, cloud-top pressure, cloud optical thickness, cloud water path, cloud phase and cloud type.

CloudSat Radar-Only Cloud Water Content (2B-CWC-RO) product

The CloudSat Radar-Only Cloud Water Content (2B-CWC-RO) product contains retrievals of cloud liquid and ice water content, effective radius of the ice and liquid particles, number concentration, and the size distribution width parameter using radar and auxiliary temperature data (Austin et al., 2009). The latest release P1_05 is used in this study. Retrievals are performed separately for the liquid and ice phases assuming liquid only and ice only, then the two sets combined in a simple way to obtain a composite profile that is consistent with the input measurements. The partition of ice and liquid is based purely on temperature, and the solutions of ice and liquid are scaled linearly with temperature to obtain a smooth transition from all ice at −20°C to all liquid at 0°C. The retrieval uses a temperature dependent a priori of lognormal (a modified gamma distribution) size distribution parameters, which are fitted from in situ particle size spectra.

In this study, we choose to use the CloudSat 2B-CWC-RO product for cloud water path rather than the CERES-EBAF data set, because previous study has shown that the CloudSat 2B-CWC-RO product can better represent cloud liquid and ice water path over high latitudes than CERES-EBAF data set, owing to its explicit determination of cloud phase (Lenaerts et al., 2017). But we should notice that the CloudSat 2B-CWC-RO product also has some potential problems. For example, Barker et al. (2008) has shown the temperature-partitioned profiles could not capture the mixed phased cloud structure accurately. In this thesis, the CloudSat 2B-CWC-RO product is used in Chapter 4.

GCM-Oriented CALIPSO Cloud Product

The General Circulation Model (GCM)-Oriented Cloud-Aerosol Lidar and Infrared Pathfinder Satellite Observation (CALIPSO) Cloud Product (GOCCP) (CALIPSO-GOCCP hereafter; Chepfer et al., 2010) is designed to evaluate the cloudiness simulated by GCMs. It contains observational cloud diagnostics fully consistent with the ones simulated by the GCM plus the lidar simulator, that is they have similar spatial resolution, the same criteria used for cloud detection and the same statistical cloud diagnostics. In doing so, the Cloud-Aerosol Lidar with Orthogonal Polarization (CALIOP) Level 1 data (raw data but annotated with ancillary information) are processed following the steps in a lidar simulator to diagnose the model cloud cover that CALIPSO would observe from space if the satellite were flying above an atmosphere similar to that predicted by the GCM.

The CALIPSO-GOCCP products include the vertical distribution of cloud fraction, horizontal distribution of low, middle, high, and total cloud fractions, instantaneous lidar scattering ratio profiles, and scattering ratio histograms as a function of height. Hence, the cloud cover outputs from GCM can be compared directly with

this product when the cloud simulator was not implemented. More importantly, the CALIPSO-GOCCP data can be used to evaluate the cloud fraction profiles simulated from climate models. In this thesis, the CALIPSO-GOCCP is used in Chapter 4.

2.1.2 Other climatology variables

In this thesis, the basic climate state variables such as temperature, specific humidity, relative humidity and dynamical fields such as zonal and meridional winds, pressure velocity (e.g., ω_{500}) and mean sea level pressure are taken from the reanalysis data sets. The reanalysis is produced by combining the past short-range weather forecasts with observations through data assimilation, which can provide multi-variate, globally complete, consistent record of the atmosphere. The reanalysis has some advantages over the observation. For example, the observations are not always evenly distributed, and even in the satellite era, observations alone cannot provide a complete picture of the state of the Earth system across the globe at a given point in time. Also, the reanalysis is usually the best choice currently when there is no complete observation of a certain variable, or when data sets which are consistent with each other are required.

In this thesis, the European Centre for Medium-Range Weather Forecasting (ECMWF) Interim Reanalysis (ERA-Interim; Dee et al., 2011) and the latest ERA5 (Copernicus Climate Change Service (C3S), 2017) reanalysis are used. The ERA-Interim is produced by the data assimilation system based on Cy31r2 of the Integrated Forecasting System (IFS), which includes a 4-dimensional variational analysis (4D-Var) with a 12-hour analysis window. The spatial resolution of the data set is approximately 80 km (T255 spectral) on 60 levels in the vertical from the surface up to 0.1 hPa (Dee et al., 2011). This ERA-Interim is available from 1 January 1979 to 31 August 2019, and now is replaced by the ERA5. ERA5 is the latest reanalysis product from ECMWF, which is based on the IFS Cy41r2 and covers the period from 1950 to present. The atmospheric variables from ERA5 has a regular latitude-longitude grid ($0.25^\circ \times 0.25^\circ$) with 37 pressure levels from 1000 to 1 hPa (Hersbach et al., 2020).

In Chapter 4, the hourly outputs from ERA5 reanalysis are used to derive the relationship between the cloud fraction and relative humidity. The monthly outputs from ERA-Interim are used to assess the relationship between low cloud amount and its proxy. In Chapter 4, the monthly pressure velocity from ERA-Interim reanalysis is used to distinguish the dynamical regimes over tropical region.

2.2 Idealized climate model - Isca

2.2.1 Overview

In this section, the idealized climate model, Isca[1] (Vallis et al., 2018), is introduced, which is the model employed for all the simulations in this thesis. Isca is an open-source framework for the idealized modeling of global circulation of atmospheres developed at the University of Exeter (Vallis et al., 2018), which uses the dynamical core and the Flexible Modeling System (FMS, see https://www.gfdl.noaa.gov/fms/) software infrastructure from the Geophysical Fluid Dynamics Laboratory (GFDL), and the physical parameterizations from Frierson et al. (2006) and Frierson (2007). Isca is coded in Fortran and the scripts to configure and run the experiments are written in Python. The code is public available at https://github.com/ExeClim/Isca.

Isca provides various options for users to set up experiments for their own interests, so that they can explore the models with different levels of complexity under the same framework. These options include the dry and moist models, various convection and radiation schemes, a variety of land/sea configurations and different parameters for other planetary atmospheres.

2.2.2 Several parameterization schemes

Convection and large-scale condensation

Isca includes various convective parameterization schemes, specifically a simple dry scheme following Walker and Schneider (2006), the original Bettts–Miller scheme (a covective relaxation scheme; Betts, 1986; Betts and Miller, 1986), a simplified Betts–Miller scheme (SBM; Frierson, 2007), and the relaxed Arakawa–Schubert (RAS) scheme (a mass-flux based scheme; Moorthi and Suarez, 1992).

The SBM scheme used in this thesis is a moist adjustment convection scheme developed by Frierson (2007) and the modifications described in O'Gorman and Schneider (2008). In the SBM scheme, the convection acts to relax the temperature and humidity to the post-convective reference profiles. Based on the first-guessed reference profiles, the next step is to determine whether there will be deep, shallow, or no convection based on some criteria, then to relax towards the reference profiles. Also, the scheme will do some corrections if the enthalpy is not conserved during the relaxation. In this convection scheme, deep convection and non-precipitating shallow convection are both included, and the convective precipitation can be derived from the deep convection. In addition, the precipita-

[1] Isca is the ancient name of the city Exeter in Roman times and is also an ancient word for running water; see more at https://execlim.github.io/IscaWebsite/ (last access: May 1, 2021)

tion can be partitioned into rain and snow simply by the temperature, but this is not enabled in this study.

The large-scale condensation scheme used in Isca is from Frierson et al. (2006), which is accomplished by adjusting the humidity in super-saturated regions to the saturated values immediately, with temperatures adjusted to reflect this condensation. The precipitation falls out immediately, but is re-evaporated below. The precipitation diagnosed from this scheme is regarded as large-scale precipitation.

Radiation scheme

For the radiation scheme in Isca, the choices include two gray radiation schemes (gray means that radiation in different wavelength is treated equally), which we call Frierson (Frierson et al., 2006) and Byrne & O'Gorman (BOG; Byrne and O'Gorman, 2013); an intermediate scheme with two infrared bands and one solar band, similar to Geen et al. (2016); and two full radiation schemes, the multiband correlated-k Rapid Radiative Transfer Model (RRTM; Clough et al., 2005) and the SOCRATES (Suite Of Community RAdiative Transfer codes based on Edwards and Slingo) radiation scheme (Edwards and Slingo, 1996; Manners et al., 2015).

In the clouds related simulations in this thesis, Isca uses the SOCRATES radiation scheme, as implemented in Thomson and Vallis (2019). It is the radiation scheme used by UK Met Office for Earth and planetary science (Manners et al., 2015). Compared to RRTM radiation scheme, SOCRATES is more flexible in terms of atmospheric composition and the spectral properties of the radiation scheme (e.g. number of bands for longwave and shortwave), as these properties can be specified by the spectral files separately. More bands in spectral files have more accurate simulation results, but they will make the model run much more slowly. Currently, the default spectral files used in Isca are from the Met Office Unified Model's Global Atmosphere version 7 (GA7), which have 9 longwave bands and 6 shortwave bands (Walters et al., 2019).

Land/sea configuration

For Earth-like simulations, Isca can use land/sea configurations with various complexities. For example, Isca can run with slab ocean without land (aquaplanet setup; e.g., Geen et al., 2018, 2019), or run with idealized continent shapes (e.g., Pietschnig et al., 2019), or run with realistic continents and topography (e.g., Geen et al., 2018). In the model, the land is treated the same with the slab ocean, except that the physical properties such as mixed layer depth, albedo, roughness length seen by the boundary-layer scheme, and moisture availability over prescribed areas are different.

In general, the prescribed mixed layer depth for land is smaller than that for

ocean, and thus the land has lower heat capacity compared to the ocean. In this thesis, the mixed layer depth of land is 1/10 of ocean's mixed layer depth, so the mixed layer depth for ocean and land are 20 m and 2 m, respectively. In addition, the albedo of the land is 1.3 times that of the ocean in setups, so that land can reflect more shortwave radiation than ocean. The moisture availability is controlled by introducing the "evaporative resistance" parameters into the equation for surface evaporation (E):

$$E = \rho_a C |\mathbf{v}_a| \beta (\alpha q_s - q_a), \tag{2.1}$$

where ρ_a, $|\mathbf{v}_a|$ and q_a are the density, wind speed, and specific humidity at the lowest model level, respectively; C is the drag coefficient; and q_s is the saturation specific humidity at the surface temperature (Frierson et al., 2006). Evaporative resistance parameters (α and β) are used to adjust the surface evaporation flux and their values can be chosen by the users. Typically, one of them might be 1 and the other is between 0 and 1, and such values will reduce evaporation from land regions. As recommended in Vallis et al. (2018), using $\alpha = 1$ and $0 < \beta < 1$ has the advantage of not allowing E to change sign. In this study, the default values are $\alpha = 1$ and $\beta = 0.6$. Currently, there is no dynamical ocean in Isca and the slab ocean with prescribed mixed layer depth is adopted in the model. In this way, a closed atmospheric energy budget can be achieved, as the slab ocean responds to the incident fluxes at the sea surface, with no dynamic heat transport. In fact, the horizontal heat transport in the ocean can be achieved in Isca by prescribing the Q-flux, which is the topic of Section 2.2.4.

2.2.3 Boundary conditions for Isca

For the Atmospheric Model Intercomparison Project (AMIP)-type simulations (Gates et al., 1999) in Isca, the boundary conditions such as sea surface temperature (SST) and sea ice concentration are specified by the files. In this thesis, the monthly sea surface temperature (SST) and sea ice concentration are fixed at their climatology, which are derived from the input4MIPs data sets (input data sets for Model Intercomparison Projects) (Durack et al., 2018) over the period from 1979 to 2008, and the scripts to process the input data set are available at `https://github.com/lqxyz/input4MIPs`. The annual mean spatial patterns of the derived SST and sea ice concentration are shown in Figure 2.1. The SST over the tropical and subtropical Southeast Pacific is cooler than the West Pacific.

The topography and land/sea mask are from the ERA-Interim reanalysis (Dee et al., 2011). The original topography is smoothed to reduce the Gibbs ripples arising from the truncated spherical harmonic expansion (The method is provided by Greg Colyer and Ruth Geen). The final topography over land is displayed in

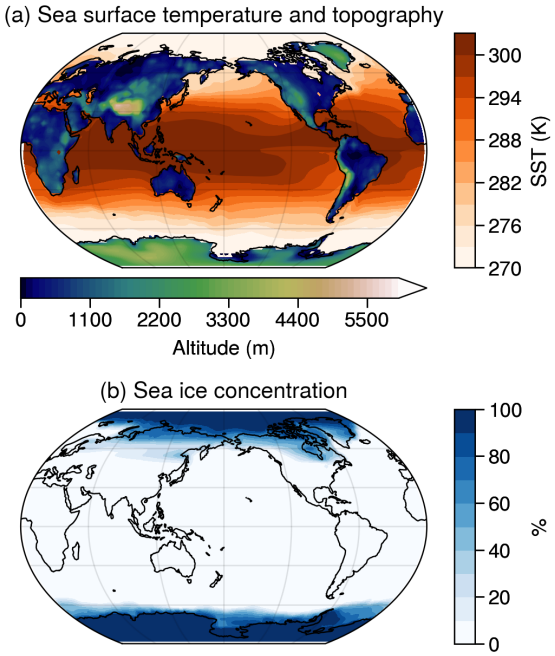

Figure 2.1 Boundary conditions for Isca, including (a) the annual mean sea surface temperature (SST, units: K; orange) and topography over land (altitude, units: m), and (b) annual mean sea ice concentration (SIC; units: %). The SST and SIC are derived from input4MIPs data sets (Durack et al., 2018) over the period from 1979 to 2008, and the topography is derived from ERA-Interim reanalysis (Dee et al., 2011).

Figure 2.1a.

2.2.4 Ocean heat transport (Q-flux)

Another feature in Isca is that it can include ocean heat transport (the 'Q-flux') from a given distribution of SSTs (Vallis et al., 2018). Here we repeat how to derive the Q-flux following the method from Russell et al. (1985). After prescribing the Q-flux in simulations, the SST can respond freely to the CO_2 forcing. The observed SST climatology is from the input4MIPs data set (Durack et al., 2018) over the period from 1979 to 2008 (see Section 2.2.3 for details). To derive the Q-flux, the aforementioned SST climatology is prescribed in a simulation with the realistic continents, topography and a slab ocean (mixed layer depth is 20 m). The energy balance model is applied as follows:

$$F_Q = C_w \rho_w D \frac{\partial T}{\partial t} - F_s, \tag{2.2}$$

$$F_s = \mathrm{SW} - \mathrm{LH} - \mathrm{SH} - \mathrm{LW}, \tag{2.3}$$

where F_Q is the Q-flux to be derived, which distributes energy globally to match the prescribed SST distribution. The C_w (3989.24 J kg^{-1} K^{-1}) and ρ_w (1035 kg

m^{-3}) are the specific heat capacity and density of ocean water, respectively. D is the depth of mixed layer. The rate of change of mixed layer temperature ($\frac{\partial T}{\partial t}$, in units of K s^{-1}) is calculated by the prescribed SST. The surface flux (F_s, positive downward, units Wm^{-2}) in Equation (2.2) is calculated from the upward latent and sensible heat fluxes (LH and SH, respectively), the net longwave radiation (LW, positive upward) and net shortwave radiation (SW, positive downward), as indicated by Equation (2.3).

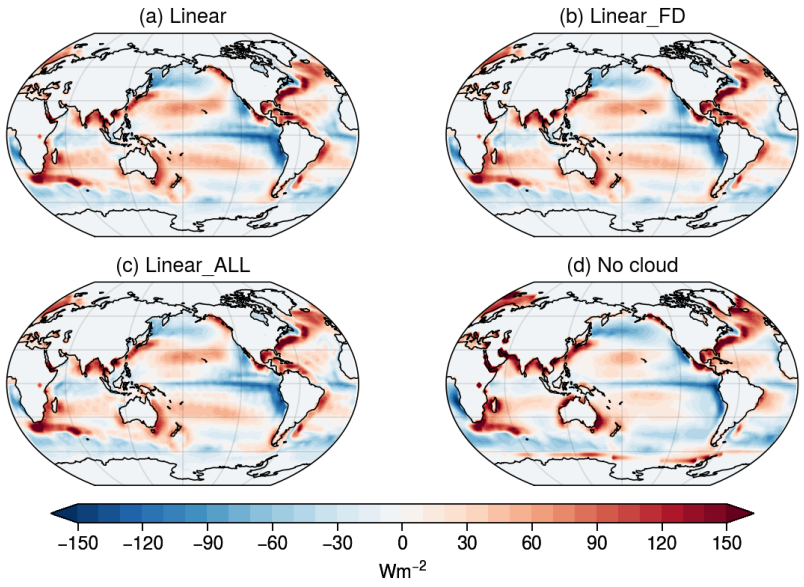

Figure 2.2 Annual mean Q-flux pattern (in W m^{-2}) derived from AMIP fixed-SST experiments with realistic continents and topography. The cloud schemes used are (a) linear, (b) linear_FD and (c) linear_ALL as in Table 4.2 and (d) no cloud scheme.

The AMIP fixed-SST experiments with linear cloud scheme described in Table 4.2 and a new fixed-SST simulation without clouds are used to derived the Q-flux, and the results are shown in Figure 2.2. The spatial patterns of Q-flux from different cloud schemes are similar, and have some differences from the simulation without cloud in subtropical and Southern Ocean regions. Q-flux can capture the ocean currents such as the Gulf Stream and cold tongue in the eastern tropical Pacific (Figure 2.2), and the positive value compensates for too little heating to the slab ocean by the surface flux from the 'prescribed-SST' run compared to the SST climatology. In this case, the Q-flux obtained from the run with the linear cloud scheme only is used in the following simulations. In addition, the Q-flux remains the same in the control and perturbed experiments, but it is noted that the SST can change freely in response to different CO_2 forcing.

2.3 CFMIP Observation Simulator Package

This section records how the Cloud Feedback Model Intercomparison Project (CFMIP) Observational Simulator Package (COSP) was implemented in Isca. Note that the COSP was not included in Isca simulations in Chapter 4, but as to be introduced in Section 2.4, it is useful to calculate cloud feedback and to decompose the cloud feedback into different components. The outputs from the COSP are employed in Chapter 5.

In this study, the latest version (version 2) of COSP (Swales et al., 2018) is implemented in Isca, which is publicly available at `https://github.com/CFMIP/COSPv2.0`. COSP was originally developed as a satellite simulator package whose aim is to produce virtual satellite observations from atmospheric model fields for a better comparison of model output with observations (Bodas-Salcedo et al., 2011). This approach is needed because the satellite retrievals generally do not directly correspond to the numerical model fields due to the mismatch between their definitions of certain fields. COSP accounts for the limited view of the satellite instrument by calculating radiative transfer through the atmosphere, i.e. attenuation by hydrometeors and air molecules and backscattering (Kuma et al., 2020). Note that multiple instrument simulators, such as MODIS, CALIPSO, CloudSat and ISCCP, have been incorporated in COSP, and it is flexible for users to decide which one to use based on their research purposes. Specifically, several modules have been written in Isca to call COSP, in which the outputs from simple cloud scheme and SOCRATES radiation schemes, such as cloud fraction, effective radius, cloud water content and cloud optical depth, are provided through the interfaces. However, as the cloud scheme is simple and there is no microphysics scheme in Isca, we could not provide some properties about convective clouds and cloud condensate such as ice and graupel. Although this may bring some problems, the outputs from ISCCP simulator are relatively reasonable.

2.4 The calculation of cloud feedback

As introduced in Chapter 1, the concept of climate feedback is used to characterize the response to the climate system to external radiative forcing. If we assume the climate system is at an equilibrium state, then when an external forcing ΔF is imposed to it, the system will response to this perturbation by a series of feedback processes. When the climate system adjusts towards a new equilibrium, the relationship among the radiation imbalance (ΔR) at the top of the atmosphere (TOA), the forcing and surface temperature change (ΔT_s) can be expressed in Equation (1.1), with climate feedback (λ) in Equation (1.4).

2.4.1 Short summary of three approaches

Several different methods have been proposed to diagnose climate feedbacks in GCMs. Three main approaches are summarized below, and readers may refer to Appendix B of Bony et al. (2006) for a clear summary of the first two methods.

(1) **The PRP approach**

The partial radiative perturbation (PRP) method (Wetherald and Manabe, 1988) evaluates partial derivatives of model TOA radiation with respect to changes in model parameters by re-running the model radiation code offline. For example, to calculate the climate feedback parameter associated with x, the radiative response that results from the perturbation of x is calculated as follows:

$$\delta_x R = R(a, b, ..., x') - R(a, b, ..., x), \tag{2.4}$$

where a, b etc are climate variables except x and they are kept unchanged during calculation. x' is the value of x from perturbed climate state. In doing so, $\frac{\partial R}{\partial x}$ in Equation (1.4) can be obtained from this offline calculation. The feedback parameter associated with x is finally computed from $\lambda_x = \frac{\partial R}{\partial x}\frac{\mathrm{d}x}{\mathrm{d}T_s}$, and $\frac{\mathrm{d}x}{\mathrm{d}T_s}$ is calculated by differencing the simulation outputs from two experiments or from different time periods. Note that a more accurate two-sided PRP method (Colman and McAvaney, 1997) is also used to estimate the partial radiative responses at TOA, so Equation (2.4) can be rewritten as

$$\delta_x R = \frac{1}{2}\left[R(a, b, ..., x') - R(a, b, ..., x) + R(a', b', ..., x') - R(a', b', ..., x)\right]. \tag{2.5}$$

The advantage of PRP method is that it can separate different climate feedbacks, including ones related to clouds. But the procedure can be computationally expensive (Soden et al., 2008), and the calculation must be repeated for every simulation and climate model versions.

(2) **The CRE approach**

The 'cloud radiative effect' (CRE) approach (or CRF in Cess et al., 1990, 1996) decomposes the climate feedback into clear-sky and cloudy components. They do so by decompose the total TOA radiation budget R as the sum clear-sky component (R_{clear}) and CRE (CRE $= R - R_{\mathrm{clear}}$), so Equation (1.1) can be written as

$$\lambda = \frac{\Delta R - \Delta F}{\Delta T_s} = \underbrace{\frac{\Delta R_{\mathrm{clear}} - \Delta F}{\Delta T_s}}_{\text{clear-sky climate feedback}} + \underbrace{\frac{\Delta \mathrm{CRE}}{\Delta T_s}}_{\text{cloud feedback}}. \tag{2.6}$$

It is clear that this method can not separate the clear-sky climate feedback components into temperature, water vapor and surface albedo ones in fur-

ther. As we will discuss in Section 2.4.2, the cloud feedback parameter (second term in Equation (2.6)) obtained from this approach depends on changes in both clear-sky and cloudy properties, which in fact can not separate the cloud feedback completely from the clear-sky components. Nevertheless, the calculation of this method is straightforward and still valuable in GCM evaluations.

(3) **The radiative kernel method**
The radiative kernel method (e.g., Soden and Held, 2006; Soden et al., 2008; Shell et al., 2008) decompose each climate feedback into two parts. The first is the 'radiative kernel' ($\partial R/\partial x$), which describes the change of TOA fluxes in response to a standard change in property x and depends on the radiative properties and base state of the model. The second term is the climate response of feedback variable normalized by surface temperature change ($\mathrm{d}x/\mathrm{d}T_s$). Most importantly, Soden et al. (2008) has shown the climate feedbacks calculated from three different radiative kernels are quite similar, although the radiative transfer code is different, indicating that a single kernel can be used to perform a first-order comparison of feedbacks across multiple models (Shell et al., 2008). One problem is that the kernel calculation is also computationally expensive as it requires running the offline radiative transfer code for perturbation at each model level and time step, but luckily it just needs one-time calculation and the kernel can be applied for different experiments and models.

As for the cloud feedback, Zelinka et al. (2012a,b) proposed a new method combing the cloud radiative kernel and the ISCCP-type histogram of cloud fraction partitioned into cloud-top pressure (CTP) and optical depth (τ) bins, which can quantify the cloud feedbacks from different components such as cloud amount, height and optical depth, as further discussed in Section 2.4.4.

2.4.2 Using ΔCRE to estimate cloud feedback?

In this section, we try to answer the question whether we could use the change of CRE between perturbed and control climate states to estimate the cloud feedback. According to Soden et al. (2004), in the PRP method the change of radiation flux at TOA due to clouds ($\delta_C R$) is calculated as follows:

$$\delta_C R = R(T, C', w, \alpha_s) - R(T, C, w, \alpha_s), \tag{2.7}$$

where T, C, w and α_s are temperature, cloud properties (e.g., cloud fraction, cloud water content), water vapor and surface albedo, respectively. C' represents the altered cloud properties in perturbed climate; that is $C' = C + \Delta C$, and so forth for

other variables. In contrast, the change in net CRE at TOA between control and perturbed simulations is defined as

$$\Delta \mathrm{CRE}_{\mathrm{net}} = \underbrace{\left[\, R(T', C', w', \alpha_s') - R(T', 0, w', \alpha_s') \,\right]}_{\text{Net CRE in perturbed climate}} - \underbrace{\left[\, R(T, C, w, \alpha_s) - R(T, 0, w, \alpha_s) \,\right]}_{\text{Net CRE in control climate}}, \tag{2.8}$$

as the CRE at TOA is computed from the radiation flux difference between total- and clear-sky conditions. For the case where there is no cloud feedback $\Delta C = 0$, thus $C' = C$ and $\delta_C R = 0$ in Equation (2.7). The change in net CRE in Equation (2.8) becomes

$$\begin{aligned} \Delta \mathrm{CRE}_{\mathrm{net}} &= \left[\, R(T', C, w', \alpha_s') - R(T', 0, w', \alpha_s') \,\right] - \left[\, R(T, C, w, \alpha_s) - R(T, 0, w, \alpha_s) \,\right] \\ &= \underbrace{\left[\, R(T', C, w', \alpha_s') - R(T, C, w, \alpha_s) \,\right]}_{\text{Change in total-sky flux}} - \underbrace{\left[\, R(T', 0, w', \alpha_s') - R(T, 0, w, \alpha_s) \,\right]}_{\text{Change in clear-sky flux}}. \end{aligned} \tag{2.9}$$

If we assume that ΔT, Δw, and $\Delta \alpha_s$ are not zero (i.e. $T' \neq T$, $w' \neq w$, and $\alpha_s' \neq \alpha_s$), the only way to get $\Delta \mathrm{CRE}_{\mathrm{net}} = 0$ would be for the changes in total-sky flux (term within first bracket in Equation (2.9)) and clear-sky flux (term within second bracket in Equation (2.9)) due to non-cloud feedbacks to be equal. However, this is not always the case. An explanation with a simple model is presented in Section 2.4.3.

Soden and Held (2006) found that all the models from IPCC Fourth Assessment (AR4) have a positive cloud feedback in 21$^{\mathrm{st}}$ century climate change experiments, but roughly half the models show a reduction in net CRE (or CRF; and normalized by surface temperature change) in response to climate change. In their study the cloud feedback is estimated by the radiative kernel method. This apparent discrepancy is possibly due to the influence of noncloud feedbacks on the CRE term (Zhang et al., 1994; Soden et al., 2004). Therefore, the change of net CRE is not a reliable measure of cloud feedback, as the signs of them are sometimes different. However, it is noted that the cloud feedback is correlated with the change in net CRE, indicating that intermodel differences in cloud feedback can be estimated by the intermodel differences in the changes of CRE (Soden and Held, 2006; Bony et al., 2006; Vial et al., 2013).

2.4.3 Cloud masking effect

A modified simple thought experiment from Soden et al. (2008) is adopted here to explain what the cloud masking effect is and why the two right-hand terms in Equation (2.9) are usually not equal with each other. As illustrated in Figure 2.3, we assume part of the grid is covered by high clouds (cloud fraction is f), and the water vapor contents are q_1 and q_2 for clear and cloudy subgrid regions,

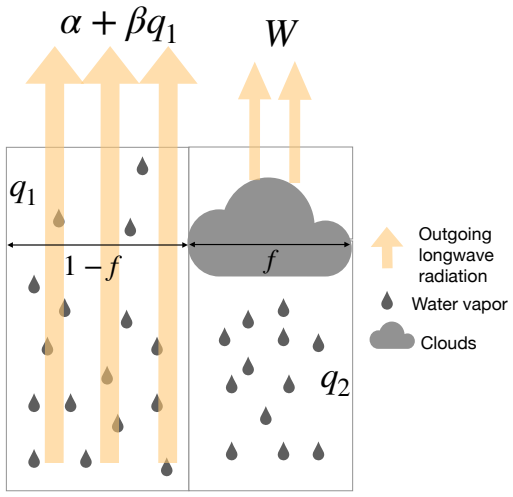

Figure 2.3 Illustration of cloud masking effect on noncloud feedbacks in a grid box.

respectively. Here we focus on longwave radiation only and assume the longwave radiation emitted by water vapor is a linear function of its content, that is $\alpha + \beta q$, where α and β are assumed linear coefficients and β is negative so that the outgoing longwave radiation decreases with the increase of water vapor. The outgoing longwave radiation emitted from clouds is regarded as a constant W.

If there is no clouds in this grid (i.e. $f = 0$), the net longwave radiation flux at TOA (downward positive) is $-[\alpha + \beta(q_1 + q_2)]$. When clouds are present, the grid averaged net longwave flux at TOA becomes

$$R = -(\alpha + \beta q_1)(1 - f) - Wf, \tag{2.10}$$

as the longwave raditation emitted from water vapor q_2 is masked by clouds. Consider a climate change case in which the water vapor and cloud fraction change a bit, and the change in R can be written as follows by differencing Equation (2.10):

$$\delta R = \delta R_f + \delta R_q, \tag{2.11}$$

where

$$\delta R_f = (\alpha + \beta q_1 - W)\ \delta f, \tag{2.12}$$

and

$$\delta R_q = -(1 - f)\beta\ \delta q_1. \tag{2.13}$$

Now reconsider the situation in Equation (2.9), in which there is no cloud feedback ($\delta f = 0$), so the longwave radiation change at TOA due to clouds is also zero, namely $\delta R_f = 0$ in Equation (2.12). However, as for the longwave radiation flux change due to water vapor perturbation, the cloud fraction f is also included as in Equation (2.13), indicating that clouds have masking effect on the water vapor feedback and the δR_q under clear-sky should be different from the one under

cloudy conditions.

This simple thought experiment has illustrated that the presence of clouds can have an impact on the radiation associated with noncloud variables. That is why the two right-hand terms in Equation (2.9) are usually not equal with each other, and it also implies that estimating cloud feedback from changes of cloud radiative effect is probably not a good option due to the cloud masking effect.

2.4.4 Cloud radiative kernel method

In general, previous methods introduced in Section 2.4.1 can give us an estimate of integrated quantity of cloud feedback. Of course, methods such as the PRP and radiative kernel can also generate other types of cloud feedbacks by perturbing the corresponding properties, but it is usually hard to do so. To solve this problem, Zelinka et al. (2012a,b) proposed a new technique based on cloud radiative kernel and the histograms of cloud fraction partitioned by CTP and τ, which can easily attribute the contributions of specific types of cloud changes to cloud feedback.

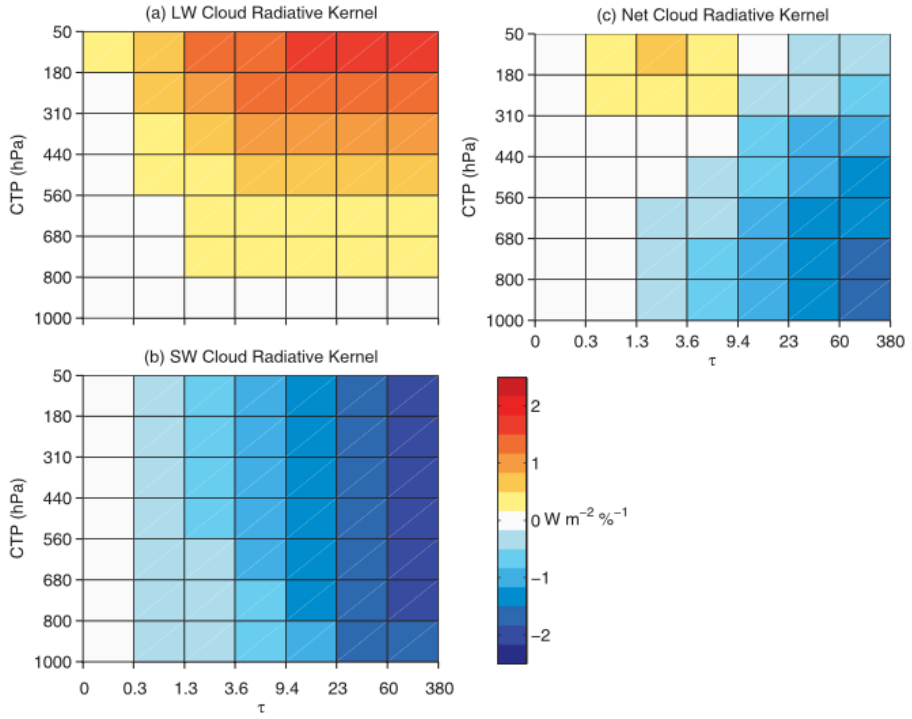

Figure 2.4 Global, annual, and ensemble mean (a) longwave, (b) shortwave and (c) net cloud radiative kernels. Adapted from Fig. 1 of Zelinka et al. (2012a). ©American Meteorological Society. Used with permission.

In this method, the cloud radiative kernel K in each histogram bin of Figure 2.4 is defined as

$$K = \frac{\partial R}{\partial C}, \tag{2.14}$$

which quantifies the sensitivity of TOA radiative flux to cloud fraction changes (ΔC), and is estimated offline from radiation transfer code for each CTP-τ bin.

The process is complicated and a detailed description can be found from Zelinka et al. (2012a). The longwave, shortwave and net cloud radiative kernel results are shown in Figure 2.4, and the major features are:

1. The longwave cloud radiative kernel is positive for all bins, as the longwave CRE is positive. It increases dramatically with cloud top height, and is small near surface as the cloud top temperature contrast with surface is small.

2. The shortwave cloud radiative kernel is negative for all bins, as the shortwave CRE is negative. Its magnitude increases dramatically with optical depth, and almost insensitive to cloud top height.

3. The net cloud radiative kernels for the lower and thicker clouds are negative, as the shortwave reflection exceeds longwave trapping; while for higher and thinner clouds, the net cloud radiative kernel are positive, as longwave trapping exceeds shortwave reflection.

Multiplying the cloud radiative kernel K by the change in cloud fraction histogram (ΔC, differencing the histogram outputs from cloud simulator), one can estimate the contribution of each cloud type to the change in TOA radiation associated with climate change:

$$\Delta R = K \Delta C \tag{2.15}$$

and hence the cloud feedback is calculated as follows:

$$\lambda_c = K \frac{\Delta C}{\Delta T_s} = \frac{\Delta R}{\Delta T_s}. \tag{2.16}$$

Note that the ΔR and cloud feedback parameter λ_c are function of CTP, τ, latitude, longitude and time, so it can be used to estimate cloud feedback from certain cloud types (according to CTP and τ). The cloud radiative method, combining with the ISCCP histogram outputs from COSP, will be used in Chapter 5.

2.5 Low cloud amount proxy

Several low cloud amount proxies have been proposed in previous studies and used for low cloud amount predictions (e.g., Kawai and Inoue, 2006; Joshi et al., 2015; Collins et al., 2004; Guo and Zhou, 2014; Kawai et al., 2019). Here we list the expressions of these proxies for reference, as they are used in Chapter 4.

Low-tropospheric stability

Klein and Hartmann (1993) studied the seasonal cycle of low stratiform clouds with data from the Earth Radiation Budget Experiment and found that the low-tropospheric stability (LTS) has a good linear relationship with the low stratus

amount, which is applied in the Community Atmosphere Model (Collins et al., 2004). In the scheme, LTS can be seen as a measure of the inversion strength and is defined as the potential temperature difference between 700 hPa (θ_{700}) and surface (θ_s),

$$LTS = \Delta\theta \equiv \theta_{700} - \theta_s. \tag{2.17}$$

Estimate inversion strength

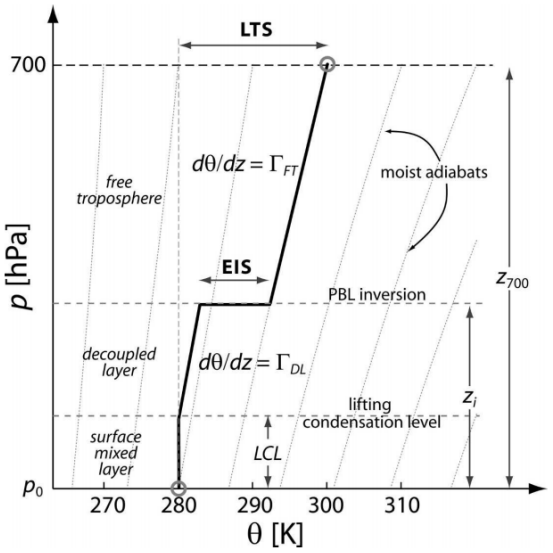

Figure 2.5 Idealized profile (thick solid line) of lower-tropospheric structure during periods of undisturbed flow. Moist adiabats are shown as light dotted lines. Adapted from Wood and Bretherton (2006). ©American Meteorological Society. Used with permission.

Despite the wide use of LTS in climate models, Wood and Bretherton (2006) argued that it has yet to be demonstrated whether the observationally derived LTS-CF relationships will hold in a changed climate. They proposed a new proxy called estimate inversion strength (EIS) to represent the planetary boundary layer inversion strength and proved that it is better to indicate the low stratiform cloud cover. An idealized profile of lower-tropospheric structure is shown by a thick solid line in Figure 2.5, where the atmospheric conditions roughly follow a dry adiabat below the lifting condensation level (LCL), and then a moist adiabat above. The EIS is defined as

$$\mathrm{EIS} = \mathrm{LTS} - \Gamma_m^{700} z_{700} + \Gamma_m^{\mathrm{LCL}} z_{\mathrm{LCL}}, \tag{2.18}$$

or simplified as

$$\mathrm{EIS} = \mathrm{LTS} - \Gamma_m^{850} \left(z_{700} - z_{\mathrm{LCL}}\right), \tag{2.19}$$

where

$$\Gamma_m(T,p) = \frac{g}{c_p}\left(1 - \frac{1 + \frac{L_v q_s(T,p)}{R_a T}}{1 + \frac{L_v^2 q_s(T,p)}{c_p R_v T^2}}\right), \tag{2.20}$$

$$z_{700} = \frac{R_a T_0}{g} \ln\left(\frac{p_0}{700\ \text{hPa}}\right). \tag{2.21}$$

In Equation (2.18), Γ_m is the moist-adiabatic potential temperature gradient, z_{700} is the height of 700 hPa, z_{LCL} is the height of the lifting condensation level. In Equation (2.20), $L_v = 2.47 \times 10^6$ J kg^{-1} is the latent heat of vaporization. $q_s(T, p)$ is the saturation mixing ratio, and is a function of temperature and pressure derived from the Clausius-Clapeyron equation. $R_a = 287.04$ J kg^{-1} K^{-1} and $R_v = 461.50$ J kg^{-1} K^{-1} are the gas constants for dry and water vapor, respectively, $g = 9.8$ m s^{-2} is the gravitational acceleration, and $c_p = 1006$ J kg^{-1} K^{-1} is the specific heat of air at constant pressure. In Equation (2.21), T_0 and p_0 (in units of hPa) are the surface temperature and pressure respectively.

Estimated cloud-top entrainment index

Recently proposed predictors of low cloud amount are also considered in this study: one is the estimated cloud-top entrainment index (ECTEI) by Kawai et al. (2017) and the other is the estimated low-level cloud fraction (ELF) by Park and Shin (2019) (see Equation (4.7) in Chapter 4). The ECTEI is a modification of estimated inversion strength (EIS) and takes into account a cloud-top entrainment criterion and is defined as

$$\text{ECTEI} \equiv \text{EIS} - \beta \left(L_v / c_p\right) \left(q_0 - q_{700}\right), \tag{2.22}$$

where

$$\beta = (1 - k) C_{\text{q\_gap}}. \tag{2.23}$$

In Equation (2.22), L_v is latent heat of vaporization, and c_p is the specific heat of air at constant pressure. The values of both parameters are the same as the ones in Equation (2.20). q_0 and q_{700} are the specific humidity at surface and 700 hPa respectively. The coefficient $C_{\text{q\_gap}}$ is the ratio of the total water specific humidity (q_t) gap at the inversion and the q difference between the surface and 700 hPa. Kawai et al. (2017) estimated the $C_{\text{q\_gap}} = 0.76$, $k = 0.70$ and $\beta = 0.23$ based on radiosonde observation data off the coast of Peru.

Chapter 3

The Role of Climate Feedbacks in Polar Amplification

3.1 Introduction

Polar amplification is the phenomenon where surface temperature in the polar regions rises faster than the global average (IPCC, 2007; Stocker et al., 2013), which exists not only in observation where Arctic warming is evident (Johannessen et al., 2004; Polyakov et al., 2002), but is also confirmed by models at varying levels of complexity (e.g., Winton, 2006a; Langen and Alexeev, 2007; Merlis and Henry, 2018; Alexeev et al., 2005).

Many discussions have focused on the sea ice and surface albedo feedback when discussing the mechanisms of polar amplification under global warming, as it is obvious that initial warming will melt the sea ice in Arctic region, leading to the decrease of surface albedo, which in turn will lead to the absorption of more solar radiation and cause the further retreat of sea ice cover (Serreze and Barry, 2011). In fact, diminishing sea ice does play a leading role in recent Arctic temperature amplification (Screen and Simmonds, 2010). Nevertheless, polar amplification also occurs in simulations even without sea ice and surface albedo feedbacks (e.g., Alexeev et al., 2005; Langen et al., 2012; Cai, 2005, 2006). Different physical mechanisms have been proposed to explain polar amplification, including increasing northward heat transport (Alexeev et al., 2005) and climate feedbacks such as Planck feedback, lapse rate feedback, cloud feedback and water vapor feedback (Pithan and Mauritsen, 2014; Screen and Simmonds, 2010; Vavrus, 2004). In addition, these mechanisms will interact with each other in the climate system, making the quantification of the contributions to polar amplification more complicated. For instance, Graversen and Wang (2009) found that an increase of water vapor and total cloud cover is favorable for a stronger greenhouse effect in the Arctic than at lower latitudes with fixed albedo under doubled CO_2 forcing. However, Screen and Simmonds (2010) find no evidence of changes

in cloud cover contributing to recent near-surface Arctic warming.

Goosse et al. (2018) categorized the feedbacks in the polar regions into radiative and non-radiative feedbacks, in which the first is linked the surface temperature change to the perturbation of top of the atmosphere (TOA) energy budget and the latter one is associated with sea ice, the ocean and other components of the climate system. In fact, radiative feedback analysis can provide clear insights into the mechanisms of surface temperature change at high latitudes, and thus we focus on radiative feedback analysis only in this study. Besides surface albedo feedback, various feedback processes in the climate system can also contribute to polar amplification. Compared to regions with higher background temperature, a given increase in emitted radiation requires a larger temperature increase at colder regions according to the Stefan-Boltzman law, indicating that Planck feedback (i.e., feedback related to uniform warming in surface and tropsphere) supports polar amplification naturally (Pithan and Mauritsen, 2014).

The lapse rate feedback, associated with vertically non-uniform warming of the atmosphere, is negative in tropical region as the vertical temperature profile is close to moist adiabatic. It is positive in the polar regions due to the larger static stability, leading to 'top-heavy' and 'bottom-heavy' warming profiles in tropical and polar regions respectively (Graversen and Wang, 2009; Pithan and Mauritsen, 2014; Manabe and Wetherald, 1975; Kim et al., 2018). As for the water vapor feedback, the increased water vapor will amplify the greenhouse effect and cause further warming, and is bigger in tropical regions as the increase of water vapor is greater there (Taylor et al., 2013; Pithan and Mauritsen, 2014). In fact, the quantification of the relative importance of these contributions is difficult. For example, Pithan and Mauritsen (2014) pointed out that temperature feedback is the largest contribution and surface albedo feedback is the second main contributor to Arctic amplification, which is, conversely, cited as the largest contributor in some studies (e.g., Manabe and Wetherald, 1975; Winton, 2006a; Hall, 2004).

In this chapter, we will revisit the polar amplification problem with a hierarchy of radiation schemes provided in the Isca model (Vallis et al., 2018), in order to investigate the roles of different climate feedbacks. As introduced in Chapter 2, the radiation scheme choices include two gray radiation schemes, Frierson (Frierson et al., 2006) and Byrne & O'Gorman (BOG hereafter; Byrne and O'Gorman, 2013), and the multiband correlated-k Rapid Radiative Transfer Model (RRTM; Clough et al., 2005). In fact, the plentiful options in the Isca offer users an opportunity to explore the models with different levels of complexity under the same framework. For instance, the role of water vapor can be examined closely, as the Frierson and BOG schemes are similar except there is no water vapor feedback in the first scheme (see details in Section 3.2.3).

This chapter is structured as follows. Section 3.2 describes the experimental

setups and lists the details and differences of the two gray radiation schemes used in the simulations. Section 3.3 quantifies the Planck, lapse rate and water vapor feedbacks from three radiaiton schemes in the Isca through the radiative kernel method, in which the radiative kernels are derived from the offline calculation of radiation codes. In Section 3.4, we investigate the roles of heat transport and various climate feedbacks in polar amplification of surface temperature change in the Isca simulations. The conclusions are summarized and discussed in Section 3.5.

3.2 Experimental setup

3.2.1 Basic setup

The Isca model is employed for the simulations. The configuration has 25 vertical levels and is run with a spectral dynamical core at T42 horizontal resolution, roughly equivalent to 2.8 degrees in latitude and longitude. The atmosphere is coupled to a slab ocean with a depth of 10m. The insolation conditions for all the experiments are perpetual equinox without seasonal change but with diurnal variations, because the perpetual equinox insolation can cause the most evident polar amplification compared to the seasonal and annual-mean insolations (Kim et al., 2018). Three radiation schemes (i.e. BOG, Frierson and RRTM schemes) are applied in our experiments to calculate the radiative transfer, as BOG and Frierson schemes are relatively simple gray radiation schemes and RRTM is a widely used full radiation scheme, which can provide a good reference for the results. The sea ice formation is not enabled in the model even if the surface temperature is below the freezing point. Furthermore, the global uniform albedo is adopted in the model, and thus the surface albedo feedback is disabled. The default CO_2 concentration is 360 ppm. All the experiments are run for 20 years following 10 years of spinup.

3.2.2 Changing forcing through varying albedos

The general way to investigate climate sensitivity is to evaluate the degree of warming in response to a doubling of the CO_2 concentration in the climate system. Actually, the external forcing can be introduced into the climate system through other ways such as adding a ghost forcing arbitrarily at the TOA (Hansen et al., 1997; Alexeev et al., 2005). Given the fact that there is no sea ice in our experiments, changes of albedo will not introduce albedo feedbacks to the climate system. Instead, it provides an simple way to perturb the radiation balance at the TOA without doubling CO_2 concentration. Therefore, we will first examine the

zonal mean surface temperature change when varying the albedo. Specifically, four albedos, α =0.27, 0.3, 0.33 and 0.38, are selected for each radiation scheme in this study, where $\alpha = 0.3$ is roughly the Earth's global averaged albedo and used in the control run for each radiation scheme. $\alpha = 0.27$ (0.33) decreases (increases) 10% from the control run value, which will cause the warming (cooling) response to the climate system. $\alpha = 0.38$ increases even more than the albedo in the control run, leading to a much colder climate state. The experiments for the BOG, Frierson and RRTM radiation schemes with different albedos are shown in Table 3.1.

Table 3.1 The experiments for the BOG, Frierson and RRTM radiation schemes with four different albedos, where 1× indicates the CO_2 concentration is not doubled.

Scheme \ Albedo	0.38	0.33	0.3*	0.27
Frierson	1×	1×	1×	1×
BOG	1×	1×	1×	1×
RRTM	1×	1×	1×	1×

* indicates the control run for each radiation scheme.

To estimate the external forcing after changing the albedos, the fixed sea surface temperature (SST) forcing method is applied in this study (Hansen et al., 2005; Andrews et al., 2012a; Feldl and Roe, 2013a; Kim et al., 2018), which has included the adjustment throughout the atmosphere. For each radiation scheme, the radiative forcing for experiments after changing albedos ($\alpha = 0.27,\ 0.33$ and 0.38) is calculated from radiation imbalance at TOA when prescribed with the monthly mean SST profiles from control experiment.

3.2.3 Water vapor feedback in radiation scheme

To examine the roles of water vapor feedback in polar amplification, the BOG and Frierson radiation schemes are employed in this study, as only one of the schemes provides moisture feedback. According to Byrne and O'Gorman (2013) and Frierson et al. (2006), the same shortwave radiation schemes are adopted in both schemes, but the ways to calculate the longwave radiative transfer are different. Specifically, the longwave optical thickness (τ) for the BOG scheme in the Isca is

$$\frac{\mathrm{d}\tau}{\mathrm{d}\sigma} = a\mu + bq + c\,\log(\mathrm{CO}_2/360), \tag{3.1}$$

where $\sigma = p/p_0$, and p_0 is 10^3 hPa; q is the specific humidity and $\mu = 1$ is a scaling parameter intended to represent absorption by well-mixed gases; $a = 0.1627$,

$b = 1997.9$ and $c = 0.17$ are values recommended in Vallis et al. (2018). $CO_2 = 360$ ppm is the default CO_2 concentration, which has no effect on changes in longwave optical thickness at this default level. It is evident that water vapor feedback can have an impact on the optical depth in the BOG radiation scheme. However, long-wave optical depth in the Frierson scheme is a function of latitude (θ) and pressure (p) (Frierson et al., 2006), which is specified to approximate the effects of atmospheric water vapor. The surface value of optical depth (τ_0) is given in the form of

$$\tau_0 = \tau_{0e} + (\tau_{0e} - \tau_{0p}) \sin^2 \theta, \tag{3.2}$$

where τ_{0e} and τ_{0p} are the surface optical depth at equator and pole separately. The vertical structure of optical depth (τ) is a combination of a linear term, which is included to reduce stratospheric relaxation times, and a quartic term, which is used to approximate the structure of water vapor in the atmosphere as it is an absorber with a scale height that is one quarter of the density-scale height, and thus is given by

$$\tau = \tau_0 \left[f_l \frac{p}{p_s} + (1 - f_l) \left(\frac{p}{p_s} \right)^4 \right], \tag{3.3}$$

where p_s is sea level pressure and coefficient f_l is set to 0.1 in the equation. Note that moisture is held fixed in the Frierson scheme, which implies that the comparison between simulation results from BOG and Frierson schemes can demonstrate the role of water vapor feedback in polar amplification. To investigate that role in further, we re-run the experiments for the BOG scheme without allowing water vapor feedback by prescribing the annual and zonal mean specific humidity profiles from the control run. In this case, the processes such as water vapor advection and convection will carry on as usual, but the moisture feedback is turned off. All the associated results will be shown in Section 3.4.

3.3 Quantify climate feedbacks in Isca

3.3.1 Introduction

In order to quantify the relative importance of various contributions to polar amplification, the radiative kernel technique (Soden et al., 2008; Shell et al., 2008) is used to calculate various climate feedbacks (see Section 3.3.2). In general, climate feedback is used to characterize the response of the climate system to an external radiative forcing, which can either amplify or diminish the effect of the forcings (Hansen et al., 1984). The change of net radiative flux at TOA between two different climate states, ΔR, can be represented by

$$\Delta R = \Delta F + \lambda \Delta T_s + O\left(\Delta T_s^2\right), \tag{3.4}$$

which can be viewed as a Taylor expansion in surface temperature change (ΔT_s) (Feldl and Roe, 2013b). The first term, ΔF, in Equation (3.4) is the climate forcing, which is estimated by the fixed-SST method (Hansen et al., 2005; Feldl and Roe, 2013b; Kim et al., 2018). The second term, $\lambda \Delta T_s$, reflects the radiative flux change that is linearly dependent on the surface temperature change, and λ is the total *feedback parameter*. The third term (or residual term) $O\left(\Delta T_s^2\right)$ represents the high-order components, reflecting the non-linear interactions among different processes, which we consider to be neglected in our analysis. It should be pointed out that variables in Equation (3.4) can be a global mean value or a function of the latitude (Feldl and Roe, 2013b). When neglecting the nonlinearities and interactions among the feedbacks, the feedback parameter λ can be decomposed into the sum of different components:

$$\lambda = \lambda_T + \lambda_w + \lambda_\alpha + \lambda_C, \tag{3.5}$$

where λ_T, λ_w, λ_α and λ_C are the feedback parameters related to temperature, water vapor, surface albedo and cloud, respectively. Further, the temperature feedback can be divided into Planck feedback (λ_P) and lapse rate feedback (λ_L) (Soden and Held, 2006), that is $\lambda_T = \lambda_P + \lambda_L$, where the Planck feedback assumes that the tropospheric temperature change is vertically uniform and equals the surface temperature change (in other words, there is no vertical temperature change in the troposphere) and the lapse rate feedback is associated with the vertical temperature change in troposphere that deviates from the surface temperature change (Bony et al., 2006; Soden and Held, 2006; Feldl et al., 2017b). In our analysis, the surface albedo feedback (λ_α) and cloud feedback (λ_C) are automatically neglected as there are no sea ice and cloud schemes in the Isca model currently. The calculation of these feedbacks for Isca model is described in Section 3.3.2 and the analysis of the contributions to polar amplification from these feedbacks will be presented in Section 3.4.

3.3.2 Radiative kernel method

In this study, we apply the radiative kernel technique (Soden et al., 2008; Shell et al., 2008) to calculate the climate feedbacks of Isca model. It should be mentioned that the radiative kernel technique is not the only approach to quantify climate feedbacks, other methods such as partial radiative perturbation (PRP) method (Wetherald and Manabe, 1988), regression method of Gregory (2004) are also used by other studies. Nevertheless, the PRP method is time consuming and the calculations have to be repeated for different simulations (Shell et al., 2008). Furthermore, interpretation of results must then take account of the possible problem associated with correlated variables as pointed by Bony et al. (2006).

In contrast, the radiative kernels are calculated from the offline version of radiative codes and can be used for different experiments and models. For instance, Soden et al. (2008) compare the climate feedbacks in 14 different coupled ocean-atmosphere models from the Fourth Assessment of the Intergovernmental Panel on Climate Change (IPCC AR4) with radiative kernels from three different general circulation models (GCMs) respectively, demonstrating that the strength of global feedbacks is relatively insensitive to the choice of kernels.

To get the radiative kernels for one model, the model should produce high-frequency (typically either every time step or every 3 hours) output in order to get the instantaneous fields for the various variables that are needed. Initially, the model run is performed with profiles without perturbation in order to get the original TOA radiation fluxes, then run with profiles where a certain variable is perturbed at each level and each time step (e.g. 3 hours) to obtain the new TOA radiation fluxes corresponding to that perturbation. Specifically, the small perturbations are applied to surface temperature (+1 K), atmospheric temperature (+1 K) and specific humidity (the change amount is determined when temperature increases by 1 K but assuming relative humidity is constant) at each vertical level at each time step (e.g. 3 hours), respectively. In particular, the change of specific humidity Δq for one layer is given by

$$\Delta q = q \left(\frac{e_s(T+1)}{e_s(T)} - 1 \right), \tag{3.6}$$

where q, e_s, and T are specific humidity, saturation pressure of water vapor and temperature, respectively. e_s satisfies Clausius–Clapeyron relation, i.e. $\frac{\mathrm{d}e_s}{\mathrm{d}T} = \frac{L_v e_s}{R_v T^2}$, where L_v is the specific latent heat of evaporation of water, taken to as a constant value of 2.47×10^6 J kg^{-1} K^{-1}; R_v, with value of 461.5 J kg^{-1} K^{-1}, is the gas constant of water vapor. The simple method used in this study to estimate the saturated water vapor pressure is

$$e_s(T) = e_{s0} \exp\left[\frac{L_v}{R_v} \left(\frac{1}{T_0} - \frac{1}{T} \right) \right], \tag{3.7}$$

where e_{s0} is a reference value of 6.1078 hPa for this at a reference temperature $T_0 = 273.16$ K. After each perturbation, the changes of radiation flux at TOA are recorded and then averaged over each month to get the kernels. In fact, the traditional kernels are supposed to compute under total-sky and clear-sky conditions separately so as to obtain the radiative effect of clouds, but only the clear-sky case will be calculated for the Isca model at present due to the lack of cloud schemes.

If ΔR represents the TOA radiation flux change due to the perturbation of variable x, then the radiative kernel for each level is defined as $K_x^i = \partial R / \partial x_i$, which is a function of space and time. In general, the resulting kernels are weighted

relative to 100-hPa thick layer in order to make it easier to compare with other different kernels, that is $\mathbb{K}_x^i = K_x^i / \Delta p_i \times 100$ hPa, where Δp_i is the thickness of layer i in units of hPa. The total radiation flux change at TOA due to x perturbation is obtained by integrating from the surface to the tropopause, that is

$$\Delta R = \sum_{i=1}^{nlev} \frac{\partial R}{\partial x_i} \Delta x_i, \tag{3.8}$$

where $nlev$ denotes the number of vertical levels. The tropopause height is determined following the approach developed by Soden and Held (2006), which defines the tropopause (H) at 100 hPa at the equator and 300 hPa at the poles and varies by cosine of latitude (ϕ) in between, that is $H = 300 - 200 \cos \phi$. After getting the radiation response, the climate feedback parameter is defined as

$$\lambda = \frac{\Delta R}{\Delta T_s} = \frac{1}{\Delta T_s} \sum_{i=1}^{n} \frac{\partial R}{\partial x_i} \Delta x_i, \tag{3.9}$$

where ΔT_s is the surface temperature change and the units of λ is Watt per meter squared per Kelvin ($\mathrm{Wm^{-2}\ K^{-1}}$). Note that zonal-mean variables, not the global-mean values, will be applied in Equation (3.9) so we can analyze local or regional feedback, as it offers some advantages such as spatial pattern of changes (Feldl and Roe, 2013a; Feldl et al., 2017a).

In calculation of different climate feedbacks, different variables (x) will be employed in Equation (3.9). As for Planck feedback, the temperature change is vertically uniform in atmosphere, meaning that the air temperature change equals to the surface temperature change, so we have $x = T_s$ in Equation (3.9). Similarly, the lapse rate feedback is associated with the warming/cooling that deviates from surface temperature change, indicating that $x = T_a - T_s$ (T_a denotes the atmospheric temperature) is utilized in Equation (3.9). Regarding the water vapor feedbacks, the natural logarithm of atmospheric specific humidity (i.e. $x = \ln q$) is applied in Equation (3.9), since the absorption of radiation by water vapor is approximately proportional to the natural logarithm of water vapor content (Shell et al., 2008; Feldl and Bordoni, 2016; Liu et al., 2018). Similarly, Huang et al. (2017) employ another way to calculate the water vapor feedback:

$$\lambda_w = \sum_{i}^{nlev} K_q^i \frac{\Delta \ln q_i}{(\delta \ln e_s / \delta T)_i} \frac{1}{\Delta T_s}, \tag{3.10}$$

and $(\delta \ln e_s)_i$ is estimated by $\left(e_s(T_i + 1) - e_s(T_i)\right) / e_s(T_i)$, which is similar to the method that Pendergrass et al. (2018) used to calculate the water vapor kernel, and hence we use Equation (3.10) to calculate the water vapor kernel in this study.

3.3.3 Radiative kernels in Isca

To calculate the radiative kernels for Isca , a 10-year control experiment ($\alpha = 0.3$) is re-run for each radiation scheme to get the corresponding model outputs (e.g. temperature, specific humidity) at 3-hour frequency. Then 1-year climatology computed from the last 5-year period is taken as the basic profiles for the offline radiation codes. Then the perturbation procedure will be carried out for different variables such as surface temperature, atmospheric temperature and specific humidity to obtain the surface temperature, temperature and water vapor kernels respectively. The radiative kernel results for each radiation scheme are shown below and the data sets are available at Zenodo (http://doi.org/10.5281/zenodo.4282681).

Frierson and BOG scheme

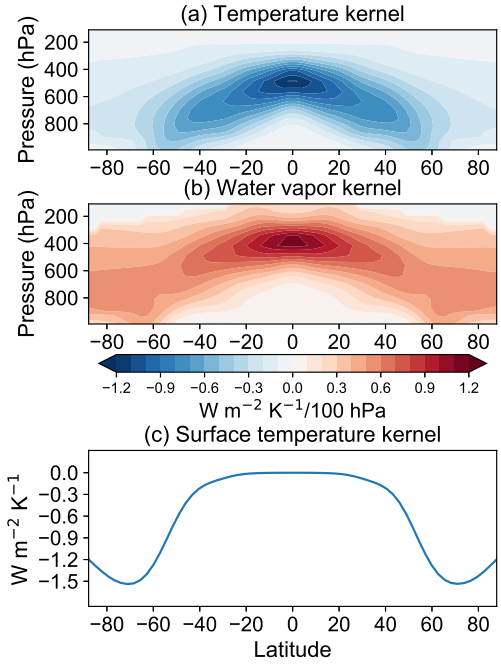

Figure 3.1 Annual-mean and zonal-mean radiative kernel for the Byrne and O'Gorman (BOG) radiation scheme: (a) temperature kernel with respect to 1-K increase in atmospheric temperature, (b) water vapor kernel for a specific humidity perturbation corresponding to a 1-K temperature increase with relative humidity unchanged, (c) surface temperature kernel for 1-K perturbation in surface temperature.

The radiative kernels for temperature, water vapor and surface temperature in the BOG schemes are shown in Figure 3.1. There is no water vapor kernel in the Frierson scheme (Figure 3.2). The temperature kernel illustrates the contribution of different latitudes and levels to the change of TOA longwave fluxes. The numerical values are generally negative, indicating that an increase in temperature increases the outgoing longwave radiation (negative feedback). As shown in

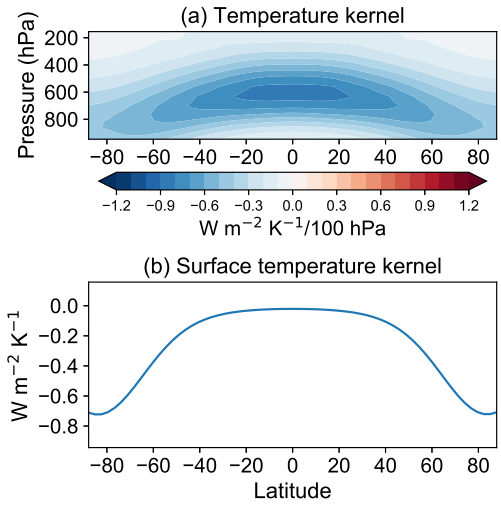

Figure 3.2 As in Figure 3.1, but only for temperature and surface temperature kernels in the Frierson radiation scheme.

Figure 3.1a and Figure 3.2a, the values of temperature kernels are more negative in tropical atmosphere owing to the larger sensitivity according to the Stefan-Boltzmann law, but the location of largest sensitivity is somewhat different from the temperature kernel in the RRTM scheme (Figure 3.3a), where the largest sensitivity appears near the surface in tropical regions. Low sensitivity occurs near the tropopause and polar region in the BOG's and Frierson's temperature kernel, reflecting the regional differences in lapse rate and emissivity (Soden et al., 2008). The vertically integrated global, annual mean of temperature kernel for the BOG and Frierson radiation schemes are -3.45 and -3.65 W m^{-2} K^{-1} respectively, which are similar to clear-sky temperature kernel for Geophysical Fluid Dynamics Laboratory (GFDL) atmospheric model (version AM2p12b), which is 3.6 W m^{-2} K^{-1} estimated by Soden et al. (2008).

The water vapor kernel for the BOG scheme (Figure 3.1b) demonstrates the relative importance of different level and latitudes to the strength of longwave water vapor feedback when temperature increases uniformly but the relative humidity keeps unchanged. In contrast, the values for water vapor feedback are positive almost everywhere, as the increase in the content of water vapor in atmosphere can help to increase the net incoming longwave radiation at TOA. Clearly, the water vapor kernel is largest in the deep tropics and decreases in the poleward direction. The vertically integrated global and annual mean for water vapor kernel in the BOG scheme is 3.61 W m^{-2} K^{-1}, which is more than twice the clear-sky water vapor kernel (1.62 W m^{-2} K^{-1}) of GFDL AM2p12b (Soden et al., 2008), suggesting that the water vapor feedback is much stronger in the BOG scheme.

The surface temperature kernel also contributes partially to the temperature feedback (the Planck feedback), and the warming of surface temperature increases the outgoing longwave radiation, so the surface temperature kernel is negative in

all the latitudes as displayed in Figure 3.1c and Figure 3.2b. But the scales of surface temperature kernel in the BOG and Frierson radiation schemes are different, and the possible reason for that is the surface temperature came from their own control runs rather than the same ones.

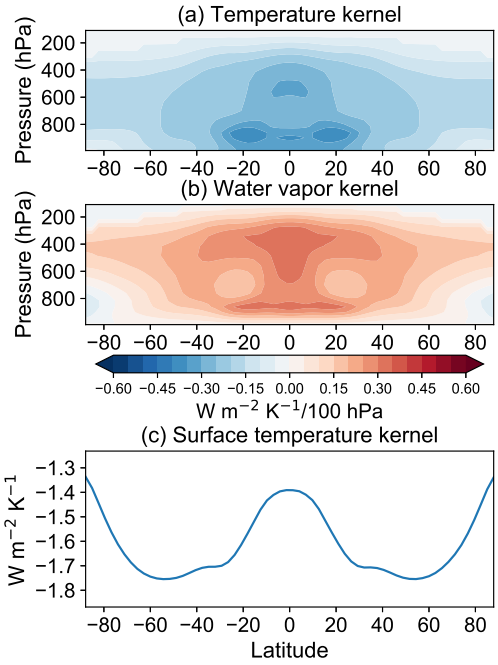

Figure 3.3 As in Figure 3.1, but for the RRTM radiation scheme.

RRTM scheme

The offline version of RRTM code is from *pyrrtm* (https://github.com/tomflannaghan/pyrrtm), which provides a user-friendly python wrapper for the single-column version of RRTM scheme. The input profiles for *pyrrtm* are from the Isca outputs in which the albedo is 0.3. Nevertheless, one frustrating fact is that the single-column version of RRTM will consume too much time if we perturb each level and each position every 3 hours. In order to get over this drawback, we employ zonal-mean and monthly mean profiles as the input for the *pyrrtm* to calculate the radiative kernels. As shown in Figure 3.3a, the temperature kernel for the RRTM is weaker compared to the results of GFDL AM2.1 (see their Fig. A1 of Feldl et al., 2017b), and the vertical integration of global and annual mean result is -1.79 W m^{-2} K^{-1}, which is almost a half of the clear-sky results (-3.6 W m^{-2} K^{-1}) of GFDL AM2p12b (Soden et al., 2008), suggesting that the feedbacks depending on this kernel would be small than other GCM's. However, the RRTM surface temperature kernel makes the situation different. It has a similar shape but the strength is much stronger compared to the surface temperature kernel of GFDL AM2.1 (see their Fig. A1 of Feldl et al., 2017b), making the Planck feedback for the RRTM comparable (Figure 3.4c). With respect to the water vapor kernel for

the RRTM, the vertical integration of global and annual mean value is 1.65 W m^{-2} K^{-1}, which is close to the longwave water vapor kernel results (1.62 W m^{-2} K^{-1}) of GFDL AM2p12b, meaning that the water vapor kernel is similar to other models. Although the positive values dominate the water vapor kernels, some negative values appear in the polar regions, as there are temperature inversions near the surface at high latitudes, which will decrease, rather than increase, the net longwave flux in response an increase of water vapor (Soden et al., 2008). However, this does not occur in water vapor kernel for the BOG radiation scheme (Figure 3.1b).

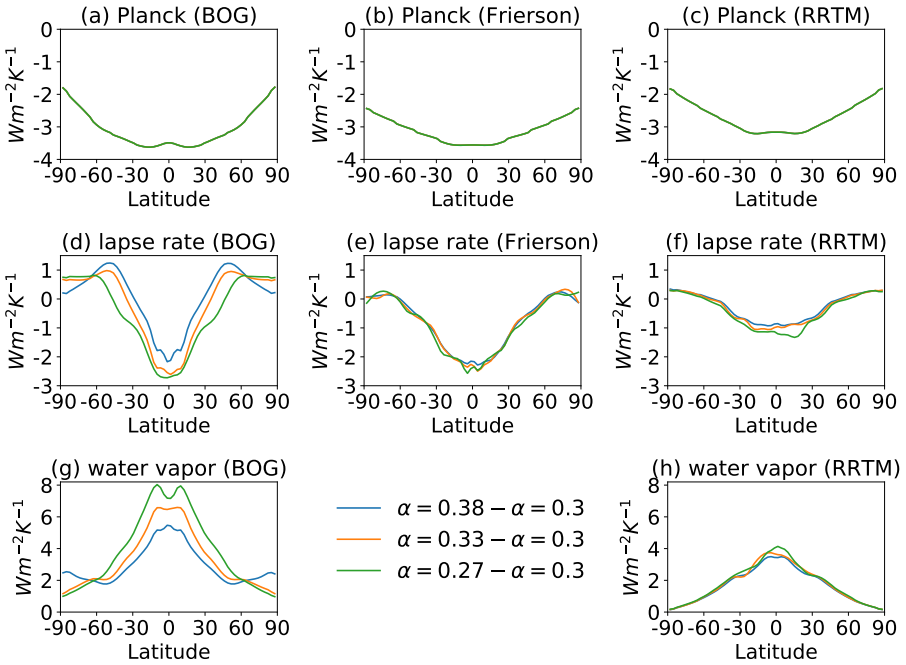

Figure 3.4 The zonal and annual mean climate feedback parameters for all the experiments in the BOG, Frierson and RRTM radiation schemes, where (a)-(c) are for the Planck feedbacks, (d)-(f) for the lapse rate feedbacks and (g)-(h) for the water vapor feedbacks. Blue, orange and green lines represent the experiments when albedo (α) is changed from 0.3 to 0.38, 0.33 and 0.27 respectively.

3.3.4 Climate feedbacks in the Isca

For each radiation scheme, the albedo parameter is changed from 0.3 to 0.27, 0.33 and 0.38 to provide an external forcing to the simulation respectively, leading to different degree of climate responses in the experiments. Thus in this section, we will use the radiative kernel technique to analyze the feedbacks for these experiments when changing albedos. The resulting Planck feedback, lapse rate feedback and water vapor feedback for each experiment are displayed in Figure 3.4.

The Planck feedback is negative at all latitudes (Figures 3.4a-c), meaning that

Table 3.2 Global mean lapse rate and water vapor feedback parameters (Units: W m^{-2} K^{-1}).

Experiment	Lapse rate			Water vapor	
	BOG	Frierson	RRTM	BOG	RRTM
$\alpha = 0.38 - \alpha = 0.3$	-0.33	-1.23	-0.51	3.38	2.14
$\alpha = 0.33 - \alpha = 0.3$	-0.84	-1.28	-0.61	4.21	2.23
$\alpha = 0.27 - \alpha = 0.3$	-1.15	-1.32	-0.72	5.03	2.41

an increase in temperature can increase the outgoing longwave radiation. In addition, the strength of the Planck feedback in the polar regions is weaker than the tropical region due to smaller blackbody emissions per unit warming at lower temperatures according to the Stefan-Boltzmann law (Goosse et al., 2018). The global mean Planck feedback parameters are -3.82, -3.79 and -3.41 W m^{-2} K^{-1} for the BOG, Frierson and RRTM radiation schemes respectively, showing that the differences of the Planck feedbacks in different radiation schemes are small. Regarding the lapse rate feedbacks, they are negative in low latitudes but positive in high latitudes, which is due to the different vertical distribution of temperature change in the polar regions compared to the tropics, as the temperature change is bottom heavy in the polar regions (Pithan and Mauritsen, 2014). The global mean lapse rate feedback parameters for all experiments and all radiation schemes are listed in Table 3.2. It is clear that the difference of global mean lapse rate feedbacks among different radiation schemes is large, but is small within the experiments with the same radiation schemes, except the one where the albedo is 0.38 in the BOG radiation scheme. As for water vapor feedback, it is positive in all experiments, implying that the net incoming longwave radiation increases in response to temperature warming. However, the spatial distribution of water vapor feedback is nonuniform, with high feedback in the tropics and small values in the polar regions (Figures 3.4g and 3.4h). This is because of the nonlinear effect of water vapor in response to warming. In addition, the global mean water vapor feedback parameters are displayed in Table 3.2, where the water vapor feedback in the BOG schemes is almost twice of feedbacks in the RRTM scheme and the later is close to the water vapor feedback (2.01 W m^{-2} K^{-1}) estimated by Soden et al. (2008) in GFDL AM2p12b, indicating that the water vapor feedback is much stronger in the BOG radiation scheme.

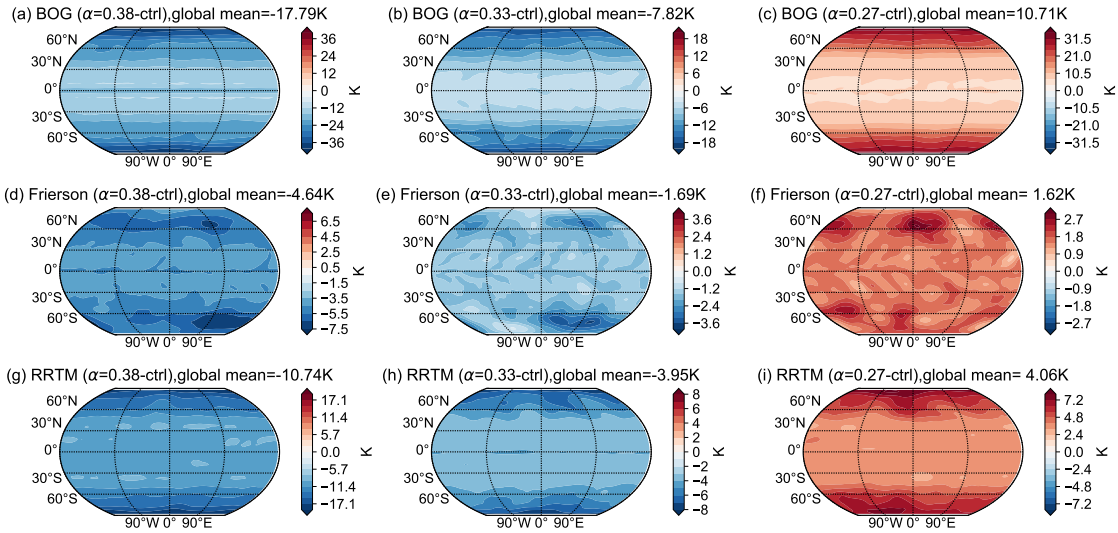

Figure 3.5 The global patterns of annual-mean surface temperature differences between the runs after changing albedos and the control run (i.e. $\alpha = 0.3$) for the (a-c) BOG, (d-f) Frierson and (g-i) RRTM radiation schemes respectively, where the (a, d, g) left, (b, e, h) middle and (c, f, i) right panels represent the runs in which albedos are changed from 0.3 to 0.38, 0.33 and 0.27 respectively.

3.4 Results

3.4.1 Surface temperature response

The global patterns of annual mean surface temperature differences after changing albedos for the BOG, Frierson and RRTM radiation schemes are displayed in Figure 3.5. The BOG scheme produces the largest surface temperate changes compared to the other two radiation schemes and Frierson scheme produces the weakest responses. For example, the annual and global mean surface temperature difference is 10.71K in the experiment where the albedo decreased 10% from control run (i.e. from 0.3 to 0.27) for the BOG scheme. Global mean values are only 4.06K and 1.62K for the RRTM and Frierson schemes. Despite the fact that the responses are in relatively wide ranges, all simulation results from the three radiation schemes show polar amplified patterns either in the cooling or warming situations, which are clearly shown in the annual and zonal mean patterns (Figures 3.6a-c). The striking feature is that the strongest polar amplification pattern appears in the BOG scheme. However, the zonal mean surface temperature change in the Frierson scheme is almost flat with slight amplified cooling or warming at high latitudes but not exactly at the poles. Like the global mean surface temperature changes, the zonal mean patterns and the polar amplification are also moderate in the RRTM scheme among the three schemes.

To make the feature more evident, the zonal mean surface temperature responses are also normalized by the change in global mean surface temperature

(Figures 3.6d-f), showing that results from the Frierson scheme also have a slight polar amplification. Generally, the Arctic warming is almost twice as large as the global average in recent decades (Serreze and Francis, 2006). For example, the Arctic has a warming 1.9 times that of the globe on average in twelve IPCC AR4 models in CO_2 doubling experiments (Winton, 2006b). As for the observed Arctic warming in the last half century, the zonal-mean Arctic warming is roughly 3 times greater than the tropical warming (Merlis and Henry, 2018). All results suggest that the ratios between polar and global temperature response seem a little surprising due to the lack of some feedback mechanisms such as surface albedo feedback in our experiments.

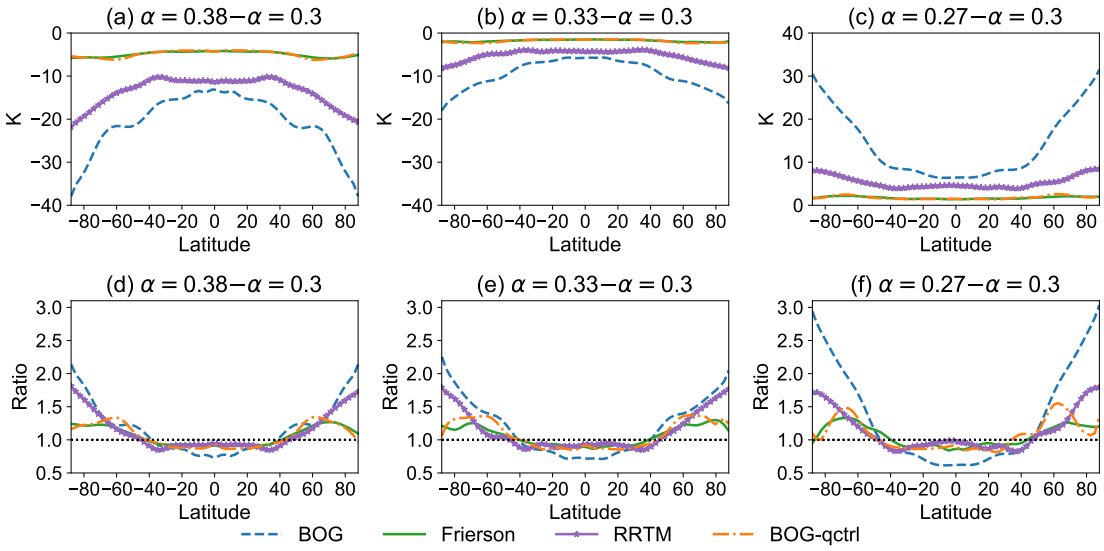

Figure 3.6 The zonal mean and annual mean surface temperature changes for experiments where the albedo is changed from 0.3 to (a) 0.38, (b) 0.33 and (c) 0.3 respectively. Correspondingly, (d)-(f) show the ratios of surface temperature change at each latitude to the global mean surface temperature change for different simulations. Each experiment has been run in the BOG (blue dashed line), Frierson (green solid line) and RRTM (purple solid-starred line) radiation schemes respectively. The orange dash-dotted lines denote the experiments in the BOG scheme without moisture feedback.

To better understand the surface temperature responses, the structures of vertical atmospheric temperature changes are also investigated. As shown in Figure 3.7, it is obvious that bottom-heavy cooling or warming profiles appear in the polar regions (Figures 3.8a-c) in all the experiments, but top-heavy cooling or warming profiles appear in tropical upper troposphere (Figures 3.8d-f). Many studies have found that this bottom-heavy structure is associated with polar amplification (Screen et al., 2012; Pithan and Mauritsen, 2014; Kim et al., 2018; Park et al., 2018), as the stability in the polar region can trap more heat at the surface in the warming case, which hence leads to the positive lapse rate feedback in the polar region (Figures 3.4d-f). In contrast, the lapse rate feedback is negative in the tropics, which means that in a warming climate, more latent heat will be released in

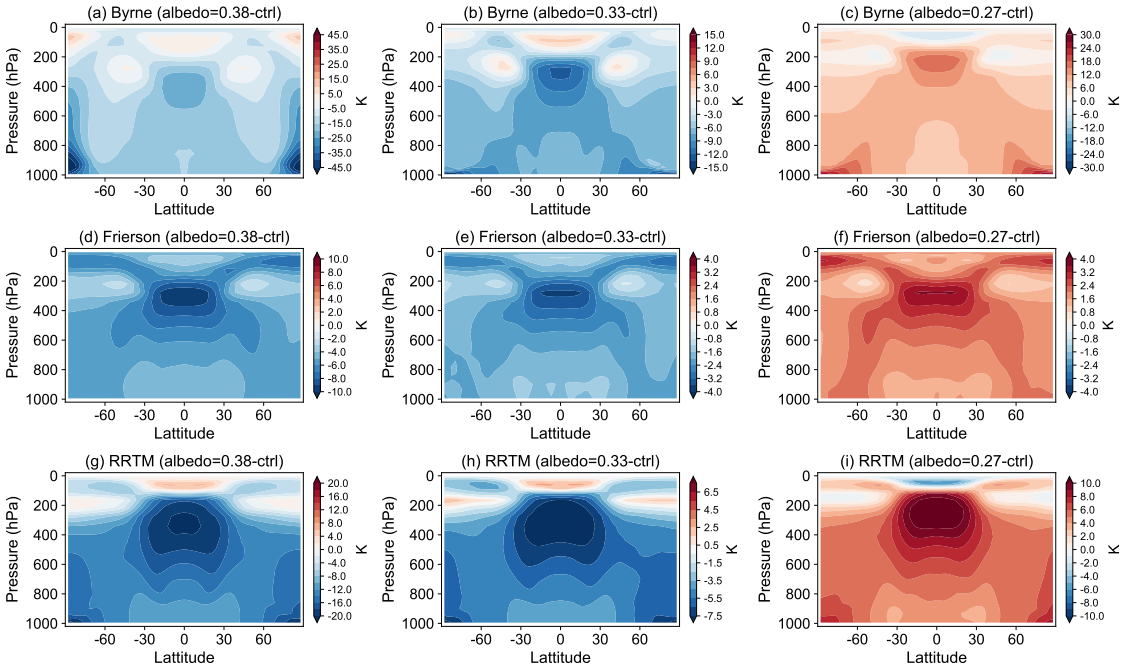

Figure 3.7 The annual mean atmospheric temperature change profiles for experiments in (a)-(c) BOG, (d)-(f) Frierson and (g)-(i) RRTM radiation schemes. The (a, d, g) left, (b, e, h) middle and (c, f, i) right panels are for the experiments where albedos are altered from 0.3 (control run) to 0.38, 0.33 and 0.27 respectively.

the upper troposphere and thus cause greater warming in the upper troposphere than at the surface (Pithan and Mauritsen, 2014).

It is worth noted that sea ice is responsible for the stable atmospheric structure in the polar region in the real world, but the stability of the polar region in our study is due to the equinox solar radiation. Kim et al. (2018) studied the sensitivity of polar amplification to insolation conditions and found that the equinox insolation brings larger static stability than seasonal or annual mean conditions due to the year-round near zero solar radiation reaching the polar region. Taking the warming case as an example, the active convection in the tropics induces a tight coupling between surface and upper troposphere, and a rising air parcel in warming climate will release more latent heat in the upper troposphere, decreasing the moist lapse rate (Graversen et al., 2014). Instead, the polar region is more stable and mixing with air aloft is harder than in the tropics, so that more heat is trapped near the surface, leaving a bottom heavy temperature structure and positive lapse rate feedback (Pithan and Mauritsen, 2014). What is more, if we check closely the bottom heavy profile in the Frierson scheme, the largest warming or cooling near the surface occurs at about 70 degree not the poles (Figures 3.7d-f), which explains largest value of the zonal mean surface temperature change in the Frierson scheme in Figure 3.6.

In summary, polar amplification can exist in the aquaplanet model even without the sea ice and surface albedo feedback. Regarding the three radiation schemes

we used in this study, the polar amplification of surface temperature is strongest in the BOG scheme, moderate in the RRTM and weakest in the Frierson scheme. As mentioned in Section 3.2.3, the crucial distinction between BOG and Frierson is whether there is moisture feedback in their longwave radiation schemes, which will be discussed further in Section 3.4.2. On the mechanisms about polar amplification, the bottom heavy structure of temperature difference provides some reasonable explanations for the polar amplification via lapse rate feedback, which will be investigated further in Section 3.4.4.

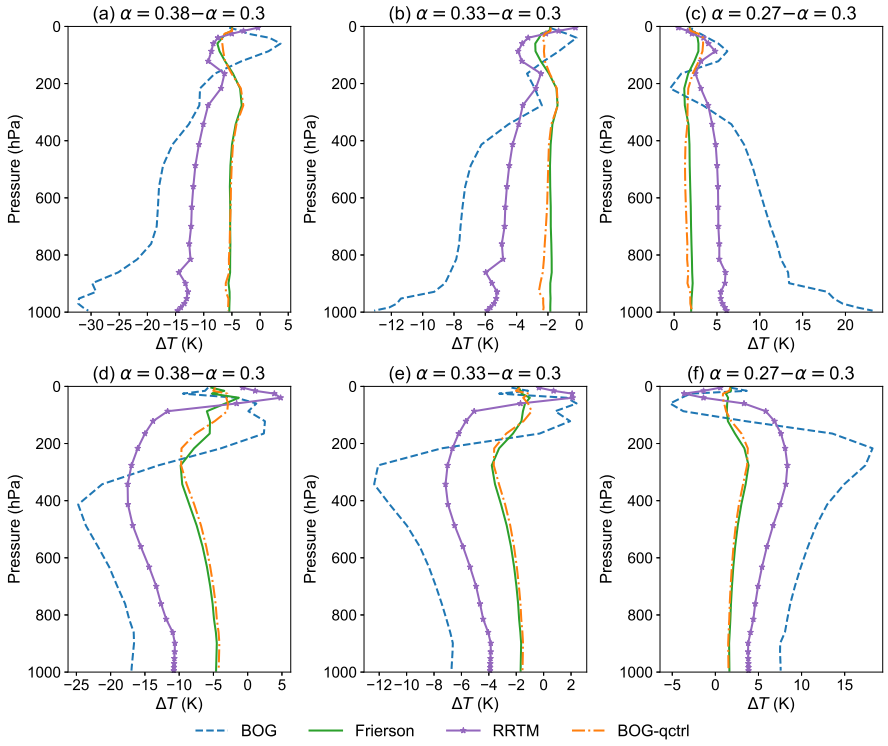

Figure 3.8 The annual mean profiles of atmospheric temperature change in (a-c) polar (60°N northward) and (d-f) tropical (10°S-10°N) regions, where the left (a and d), middle (b and e) and right (c and f) panels are for the experiments where albedo is changed from 0.3 to 0.38, 0.33 and 0.27 respectively. The blue dashed, green solid and purple solid-starred lines denote BOG, Frierson and RRTM radiation schemes respectively. The orange dash-dotted lines denote the experiments in the BOG scheme without moisture feedback.

3.4.2 Water vapor feedback

The annual and zonal mean changes in moisture profiles from different radiation schemes are shown in Figure 3.9. It is clear that the change of specific humidity profile is strongest in the BOG scheme and weakest in the Frierson scheme, both in the cooling and warming cases. Note that the specific humidity increases (decreases) in the warming (cooling) cases almost everywhere but most strongly near the surface at low latitudes, this indicates that the radiative effect of water

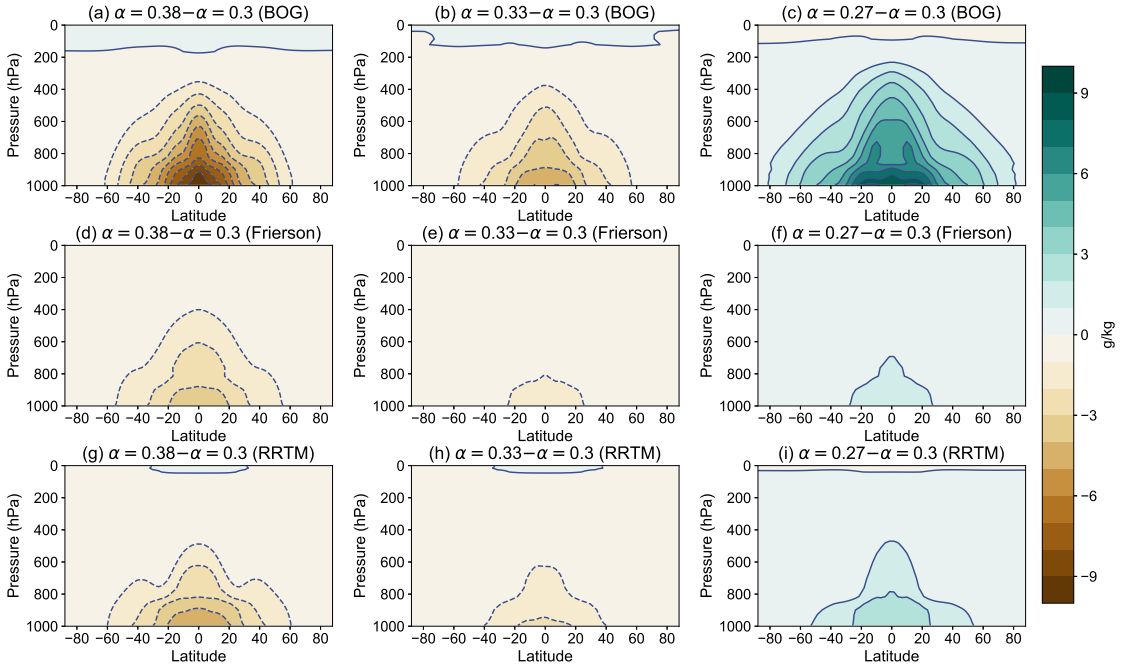

Figure 3.9 As Figure 3.7, but for the specific humidity change in the experiments with the BOG, Frierson and RRTM radiation schemes.

vapor is strongly amplified at low latitudes (Langen et al., 2012; Pithan and Mauritsen, 2014). However, the previous results show that even if the only difference between the BOG and Frierson radiation schemes lies in whether moisture feedback exists in longwave radiation transfer, the polar amplification of surface temperature change is evident in the BOG scheme rather than in the Frierson scheme (Figures 3.6 and 3.7), which implies that water vapor feedback is possibly associated with the contrast of surface temperature responses. As demonstrated in previous studies (e.g. Schneider et al., 1999), the variability of clouds and water vapor fields is significant in the simulation of the radiation field. It is for this reason that we perform the runs without moisture feedback in the BOG scheme.

To identify the role of moisture feedback in the BOG radiation scheme, we read the specific humidity (q) profile from the control run (i.e. $\alpha = 0.3$) into other experiments (i.e. $\alpha = 0.38$, 0.33 and 0.27) to make the moisture feedback fixed in the longwave radiation transfer. The longwave optical depths are examined first before analyzing the simulation results. For instance, the original optical depth profiles from the two runs where albedos are 0.3 (Figure 3.10a) and 0.38 (Figure 3.10b) show great differences when the moisture feedback is freely performed in radiation schemes, but they are almost identical to each other after the specific humidity profile for the run where albedo is 0.38 has been specified by the profile from control experiment (Figure 3.10c and 3.10d). Compared to the original optical depths, the runs with increased albedos (e.g. $\alpha = 0.38$) have thicker optical depths as they have been prescribed with specific humidity profiles from a warmer control state ($\alpha = 0.3$), where the atmospheric water vapor content is

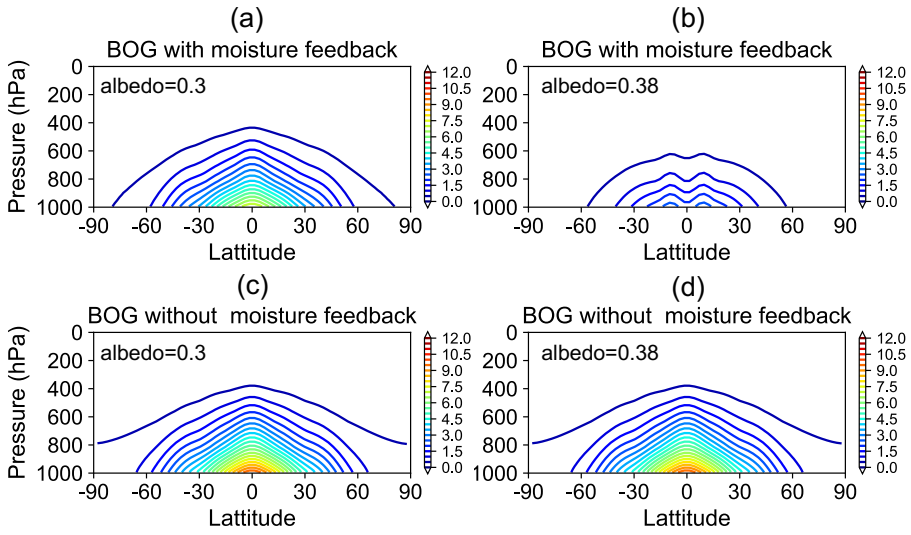

Figure 3.10 Annual and zonal mean longwave optical depth in the BOG radiation scheme before and after reading the q profile. (a) and (b) are the averaged longwave optical depth from the experiments with moisture feedback where albedo is 0.3 and 0.38. (c) and (d) are similar to (a) and (b), but the q profiles are fixed by reading annual and zonal mean q profile from control experiment (aledo is 0.3), so (c) and (d) are identical with each other.

much larger due to the non-linear effect of saturation water vapor pressure with respect to temperature according to Clausius-Clapeyron relation. Similarly, the runs with decreased albedos will have a thinner optical depth as they are specified with moisture profiles from relative cold control state.

The surface temperature change for the BOG radiation scheme without moisture feedback (BOG-qctrl, orange dash-dotted lines in Figure 3.6) shows different behaviors from the runs with water vapor feedback, where the zonal mean surface temperature changes are much smaller and polar amplification becomes much weaker compared to the original runs. This indicates that the moisture feedback plays an important role in the surface temperature change as well as polar amplification at least in the BOG scheme. Note that the surface temperature changes in the runs without moisture feedback in the BOG scheme are close to those in the Frierson scheme, which is reasonable as the moisture feedback is also missing in the Frierson scheme. In addition, the vertical temperature profiles in polar and tropical regions also change a lot when there is no water vapor feedback in the BOG scheme. Specifically, the bottom-heavy cooling or warming profiles become less evident in polar region (see the orange dash-dotted lines in Figures 3.8a-c) and the top-heavy cooling or warming profiles get weaker in tropical region (orange dash-dotted lines in Figures 3.8d-f), implying the positive lapse rate feedback is weakened in polar region.

As remarked by Pithan and Mauritsen (2014), the water vapor feedback contributes more to the tropical warming than to polar warming, which corresponds to our findings for the BOG radiation scheme (Section 3.4.4). But we should also no-

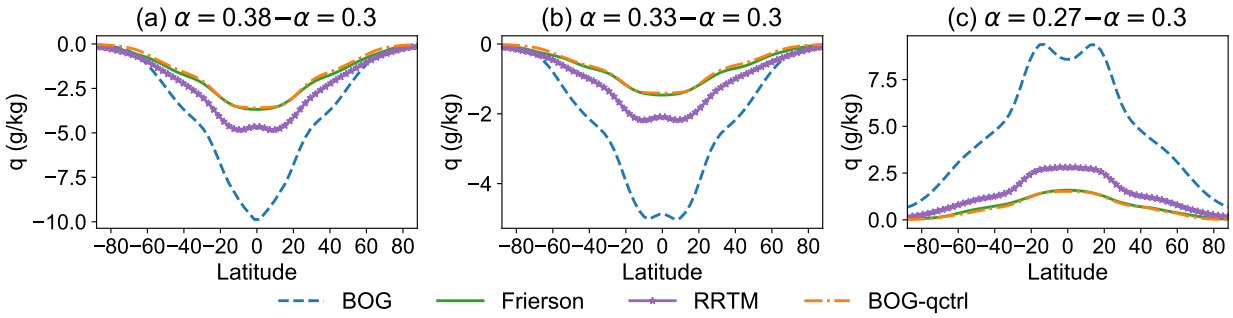

Figure 3.11 As in Figure 3.6, but for the specific humidity at surface.

tice that while water vapor feedback does not result in polar amplification by itself, it could approximately double the climate sensitivity both at low and high latitudes (Langen et al., 2012). However, we find the polar amplification of surface temperature decreases remarkably after turning off the water vapor feedback, which as illustrated in Figure 3.11 (blue dashed and orange dash-dotted lines). This is due to the water vapor content and its meridional gradient, which have both changed when the moisture feedback is turned off. In addition, the zonal mean profile from BOG scheme with moisture feedback is quite different from the RRTM scheme, suggesting that the moisture feedback prescribed in the BOG radiation scheme is possibly too strong compared to a more realistic radiation scheme. Although the water vapor is only specified in radiation code, other processes associated with the advection and latent heat release are still retained in the BOG experiment, that is why the runs without moisture feedback (BOG-qctrl) behave so similarly to Frierson scheme. As illustrated in Figure 3.5, there is still slight amplified surface temperature change at high latitudes even if no moisture feedback is included in radiation schemes, and therefore other mechanisms need to be investigated.

3.4.3 Heat transport

The total northward energy transport H across each latitude (φ) is calculated by the energy budget balance in an atmospheric column,

$$H(\varphi) = \int_{-\frac{\pi}{2}}^{\varphi} 2\pi a^2 (\mathrm{ASR} - \mathrm{OLR}) \cos\varphi \, \mathrm{d}\varphi, \tag{3.11}$$

where a is the radius of Earth, ASR is the absorbed solar radiation flux and OLR is outward longwave radiation flux at latitude band, and hence ASR – OLR is the net TOA radiation. The total northward energy transport can be decomposed into energy transport by atmosphere and ocean. In our aquaplanet experiments, there is no Q-flux to represent the ocean heat transport, so the total energy transport is contributed from atmospheric energy transport (H_a, AET) only:

$$H_a(\varphi) = H(\varphi). \tag{3.12}$$

In addition, the northward AET can be decomposed further into latent heat transport (H_{LH}), which is related to latent heat release, and dry static energy transport (H_{dry}) associated with the motion of dry air, which are given by

$$H_{LH}(\varphi) = 2\pi a^2 \int_{-\frac{\pi}{2}}^{\varphi} \cos\varphi L_v (E - P)\, \mathrm{d}\varphi, \tag{3.13}$$

and

$$H_{dry} = H_a - H_{LH}, \tag{3.14}$$

where E and P denote evaporation and precipitation respectively, and L_v is the specific latent heat capacity. The meridional energy transports mentioned above in all experiments for the BOG, Frierson and RRTM radiation schemes are shown in the Figure 3.12 and the changes of energy transport after changing albedos are displayed in Figure 3.13.

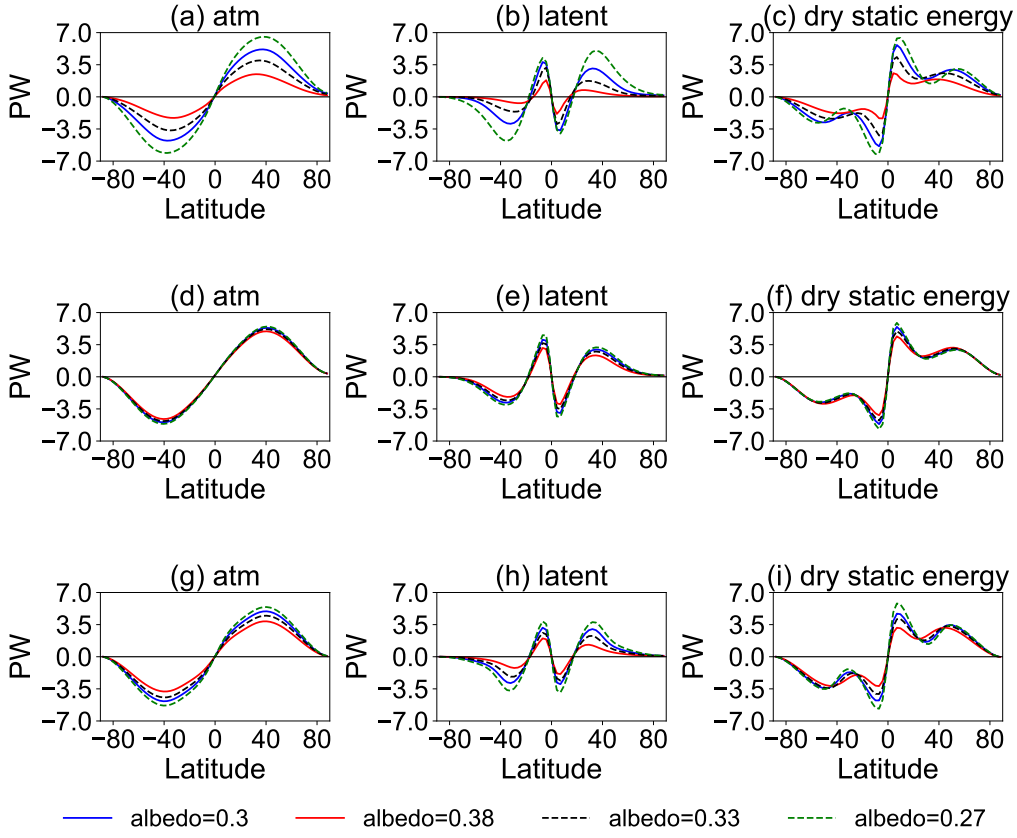

Figure 3.12 Heat transport in the experiments with different radiation schemes and various albedos. The top, middle and bottom panels are for the BOG, Frierson and RRTM radiation schemes respectively. The atmospheric heat transports are presented in (a), (d) and (g), the latent heat transport are illustrated in (b), (e) and (h), and the dry static energy transport are depicted in (c), (f) and (i). Blue solid, red solid, blue dash and green dash lines indicate the experiments where albedos are 0.3, 0.38, 0.33 and 0.27 respectively.

The changes of the surface albedo do have influence on the atmopspheric energy transports in these experiments, although the degree of influence is differ-

ent. The experiments performed with the BOG radiation scheme have the largest changes after varying the albedo, the runs with the RRTM radiation schemes have moderate changes, while the ones with Frierson schemes have the least effect (Figures 3.12a, d and g), which are much clearer when checking the differences of the experiments in Figures 3.13. Compared to the dry static energy transport, the latent heat transport contributes a larger portion to the total atmospheric at 40° poleward (Figures 3.12 and 3.13). Previous studies have shown that an increase in atmospheric heat transport can cause midtropospheric warming in polar region (e.g., Screen et al., 2012), which can explain indirectly the polar amplification in the experiments under seasonal or annual mean insolations (Kim et al., 2018). Here we also examined the temperature change in polar region (70° northward) both at surface and mid-troposphere (450-700hPa) (Figure 3.14). The results show strong linear relationships between the total AET change across 70° and either the surface temperature change and (R^2 = 0.97, Figure 3.14a) or mid-troposphere temperature change (R^2 = 0.90, Figure 3.14b), implying that the heat transport is associated with the polar amplification both at surface and mid-troposphere under insolation conditions.

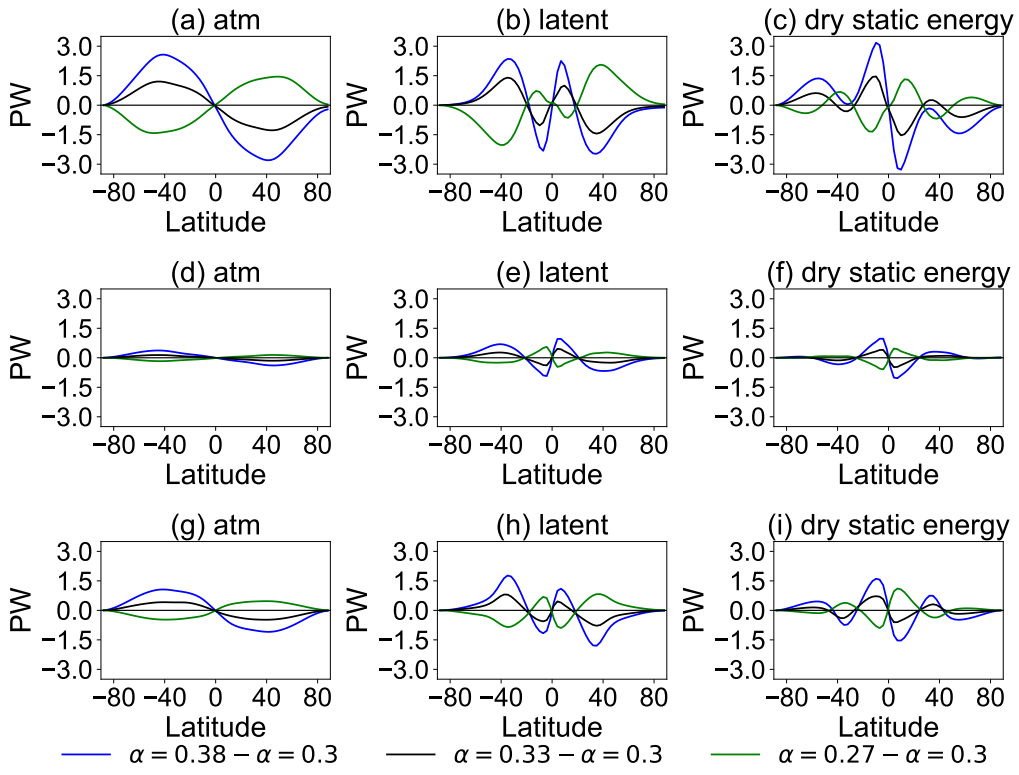

Figure 3.13 As in Figure 3.12, but for the difference in heat transport between the experiments with different radiation schemes and various albedos. Blue, black and green solid lines indicates the difference between experiments where albedo is 0.38, 0.33 and 0.27 and the control experiment respectively.

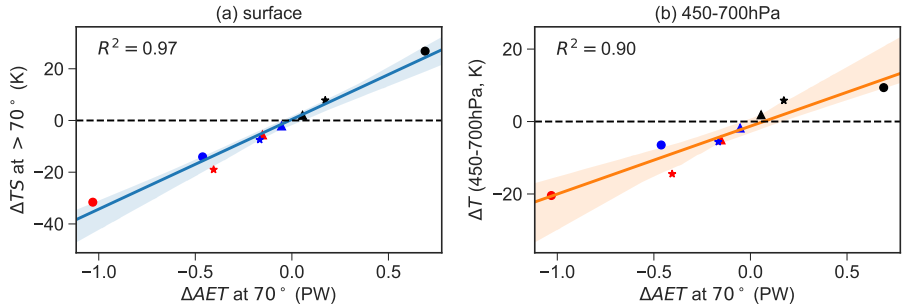

Figure 3.14 (a) Changes of surface temperature poleward of 70° versus changes in atmospheric energy transport (AET) at 70° and the blue line is the linear regression of the two variables with the shading area indicating the 95% confidence interval. The solid circles, stars and triangles denote the BOG, Frierson and RRTM schemes respectively, and red, blue and black markers represent the runs in which the albedos are changed from 0.3 to 0.38, 0.33 and 0.27 respectively. (b) Same as (a), but for temperature change in middle troposphere (450–700 hPa).

3.4.4 Decomposition of surface temperature response

In Section 3.3, with the aid of the radiative kernel method, we have obtained the zonal mean radiative feedback parameters for the BOG, Frierson and RRTM radiation schemes in the Isca model (Figure 3.4), which enables us to investigate the relative importance of each feedback to zonal mean surface temperature change. Following Feldl and Roe (2013a) and Kim et al. (2018), we decompose the surface temperature change into various components after rearranging the Equation (3.4):

$$\Delta T_s = \frac{1}{\overline{\lambda_P}} \left[\Delta R - \left(\lambda'_P + \sum_i \lambda_{NP_i} \right) \Delta T_s - \Delta F \right], \tag{3.15}$$

where $\overline{\lambda_P}$ designates the global mean Planck feedback, by which all the feedbacks will be normalized, including the local deviation of the Planck feedback (λ'_P) from its global mean and all the other non-Planck feedbacks (λ_{NP_i}). As mentioned earlier, the cloud feedback and albedo feedback are not included in the experiments and thus lapse rate and water vapor feedback are the only two non-Planck feedbacks in Equation (3.15). ΔR is the net TOA radiative flux and it should be equal to the change in the convergence of horizontal atmospheric heat flux, referred to as the heat transport term. ΔF is the forcing after changing albedos estimated by fixed-SST method.

The contributions to the zonal mean surface temperature change in the BOG, Frierson and RRTM radiation schemes are displayed in Figure 3.15. We first look at the results from the RRTM radiation scheme as it provides a more realistic radiation scheme. As shown in Figures 3.15g-i, the sum of the different components (red thick dash-dotted line) reproduces the actual surface temperature change

(blue thick solid line) in the RRTM scheme either in the cooling (Figures 3.15g, h) or warming (Figure 3.15i) cases, which implies we can analyze the relative importance of various components. As analyzed by Pithan and Mauritsen (2014), the Planck feedback itself will automatically cause greater temperature change in high latitudes. In fact, according to the Stefan-Boltzmann law, the longwave radiation emitted by the Earth's surface (R_s) is

$$R_s = \epsilon \sigma T^4, \tag{3.16}$$

where ϵ is surface emissivity, which is close to 1, and σ the Stefan-Boltzmann constant with value of 5.67×10^{-8} $\mathrm{Wm^{-2}K^{-4}}$. Assuming there is a uniform radiation disturbance (ΔR) at TOA, the surface temperature has to change by ΔT to balance ΔR, and ΔT given by

$$\Delta T = \frac{\Delta R_s}{4\epsilon\sigma T^3} = \frac{\Delta R}{4\epsilon\sigma T^3}, \tag{3.17}$$

in which ΔR_s is the radiation change at the surface. It is clear that the temperature response (ΔT) is large when the temperature (T) is low (e.g. polar region) and ΔT is small when T is relative high (e.g. tropical region). Therefore, the temperature response from Planck feedbacks (orange lines in Figures 3.15g-i) is large at high latitudes and small at low latitudes. It should be pointed out that the Planck feedback is a negative feedback, but here Figure 3.15 shows the local deviation of the Planck feedback from its global mean value and that is why the temperature response is negative in Figures 3.15g, h, and positive in Figure 3.15i. For the temperature response caused by lapse rate feedback (green solid lines in Figures 3.15g-i), it is positive in the polar region and negative in tropical region in the warming case and the signs are opposite in the cooling case, indicating that the lapse rate feedback will amplify the temperature response in high latitudes. The positive lapse rate feedback in the polar region is due to the bottom-heavy warming/cooling vertical structure (Figure 3.7). Our finding in the warming case is consistent with the result under equinox insolation in Kim et al. (2018), but they show that things are different under seasonal and annual mean insolation conditions in which the lapse rate feedback is globally negative (see Fig. S1 of Kim et al., 2018). This is because the induced temperature change is not enough to form an inversion layer near the surface (Kim et al., 2018).

The heat transport contributes most to the surface temperature change in the polar region both in the cooling and warming cases in our study, but it is different from the calculation of Pithan and Mauritsen (2014), where they find that the temperature related feedbacks contribute most to the Arctic warming when there is a surface albedo feedback. When there is a lack of surface albedo feedback, the heat transport is also the largest contributor to polar amplification under seasonal

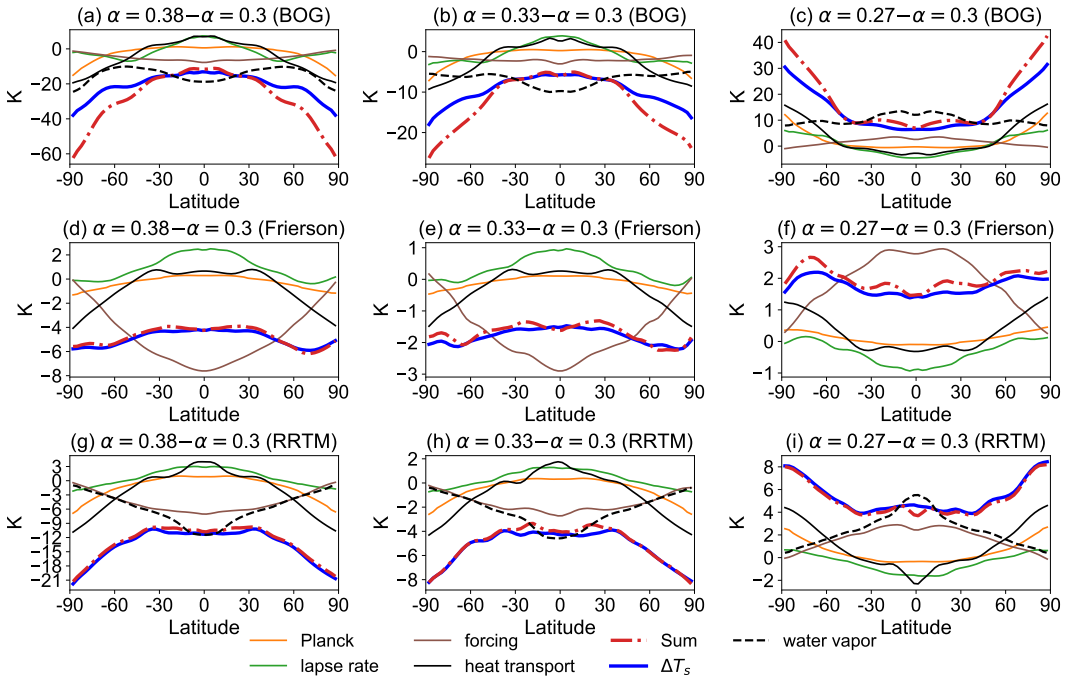

Figure 3.15 Zonal and annual mean contributions of surface temperature changes for (a)-(c) BOG scheme, (d)-(f) Frierson scheme, (g)-(i) RRTM schemes and (j)-(l) BOG scheme without moisture feedback respectively. The components include Planck feedback (orange), lapse rate feedback (green), forcing (brown), water vapor feedback (black dashed) and heat transport (black solid), all of which are weighted by global and annual mean of the Planck feedback following Feldl and Roe (2013b) and Kim et al. (2018). The sum of the different components is shown in thick red dash-dotted lines and the surface temperature change in the experiments is indicated by thick blue lines. The first, second and third columns are for experiments when albedo is changed from 0.3 to 0.38, 0.33 and 0.27 respectively.

solar radiation according to Kim et al. (2018). In the warming case (Figure 3.15i), the heat transport cools the low latitudes and warms the high latitudes, which decreases the large meridional temperature and energy imbalance gradients. As illustrated in Figures 3.15g-i, the water vapor feedbacks contribute more to the tropical warming or cooling rather than to polar regions, which is consistent with the conclusion of Pithan and Mauritsen (2014). But water vapor does have an effect on the temperature change due to the enlarged climate sensitivity (Langen et al., 2012). In fact, the temperature responses due to water vapor feedbacks in the BOG scheme (black dashed lines in Figures 3.15a-c) are different from that in the RRTM schemes. They do not tend to zero as latitude increases. Instead, they are relative flat at high latitudes, which could possibly be used to explain the abnormal surface temperature response in the BOG scheme. Regarding the forcing (brown lines in Figures 3.15g-i) due to the change of albedos, it is larger in low latitudes than in high latitudes as the solar radiation is strong at low latitudes, and hence it will amplify the temperature change at low latitudes.

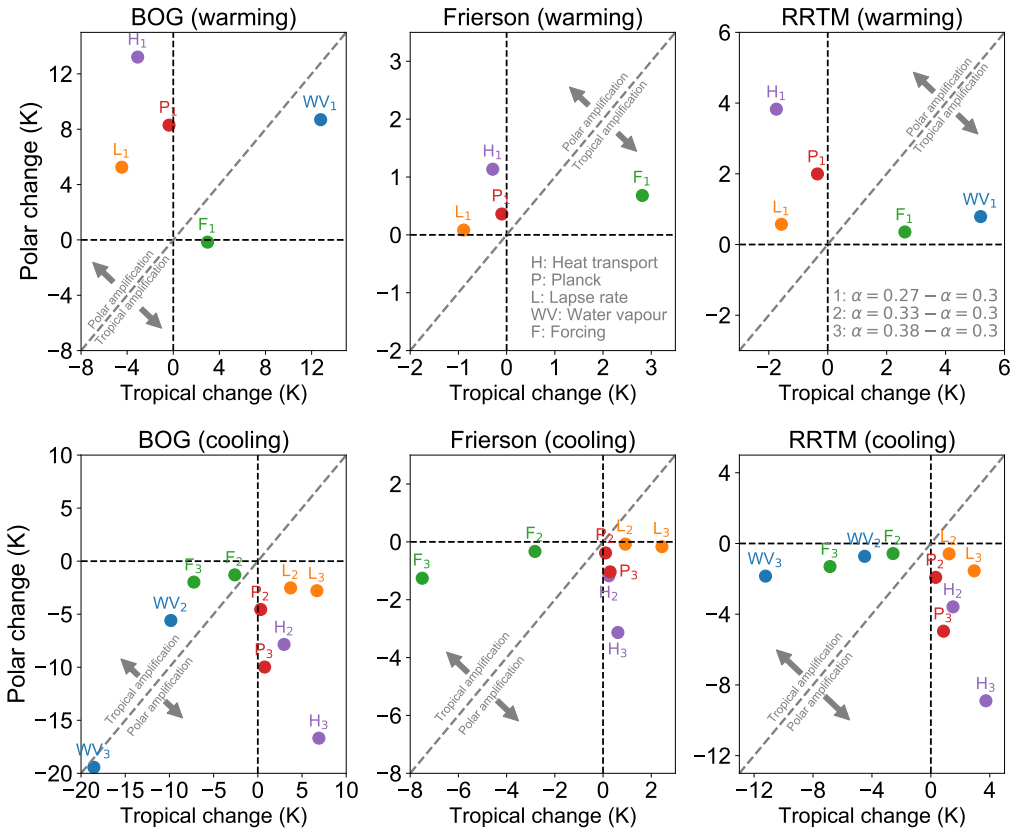

Figure 3.16 The contributions of various factors to polar versus tropical temperature changes from a TOA perspective. The factors are shown in the legend, and those above the 1:1 line contribute to polar amplification, whereas feedbacks below the line oppose polar amplification. The upper and bottom panels are for the warming (subscript 1) and cooling (subscripts 2 and 3) cases respectively. The titles of each figure indicate the radiation schemes used in the runs.

The roles of lapse rate feedback, Planck feedback and heat transport in the BOG (Figures 3.15a-c) and Frierson (Figures 3.15d-f) schemes are similar to those in the RRTM scheme, except the role of water vapor feedback in the BOG scheme, which is much larger at high latitudes compared to others. One strange thing is the sum of these contributions is greater than the actual temperature response at high latitude in the BOG scheme, for which a possible reason is that the decomposition of the surface temperature change is linear and some non-linear factors may have an influence at high latitudes. We can see that after the water vapor feedback is disabled in the BOG scheme, the sum of these various components is close to ΔT_s (Figures 3.15j-l), indicating that the non-linear effect is possibly associated with water vapor.

3.5 Discussion and summary

In this chapter, we employ the Isca model to study the surface temperature changes in aquaplanet simulations with various radiation schemes and albedos in order to quantify the different mechanisms that could lead to polar amplification under equinox insolation. Two gray radiation schemes, BOG and Frierson, and one full radiation scheme, RRTM, are used in the simulations. The BOG scheme shows the largest surface temperature change and polar amplification, while the Frierson scheme shows the weakest surface temperature change when changing albedos.

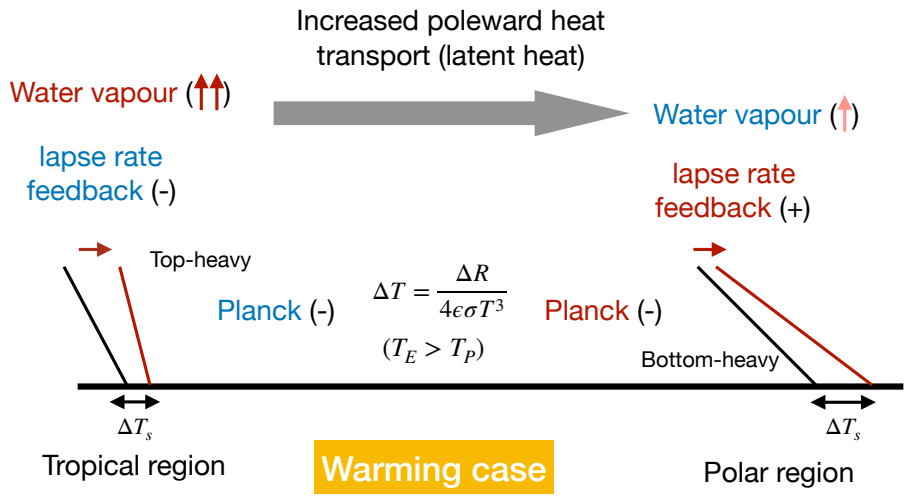

Figure 3.17 A schematic diagram to illustrate the various factors that contribute to polar amplification.

To examine why the temperature responses in the three radiation schemes (Frierson, BOG and RRTM) of Isca are different, the climate feedback processes within these three radiation schemes are analyzed. The feedbacks for each radiation scheme of Isca are computed from the radiative method (Soden et al., 2008; Shell et al., 2008), with the kernels derived from the offline calculation of the radiative transfer codes. The radiative kernels can be used among different simulations, which provides a solid basis for the feedback analysis.

The comparison of results from BOG and Frierson gives us some insights about the role of water vapor feedback in surface temperature change. After turning off the water vapor feedback in the BOG scheme, the surface temperature responses are much smaller and become close to the simulation results from the Frierson scheme. However, there is still the amplified surface temperature change at high latitudes, which is associated with the poleward atmospheric energy transport. Following Feldl and Roe (2013a) and Kim et al. (2018), the decomposition of the surface temperature change illustrates the relative importance of various contributions to surface temperature change at high latitudes. Specifically, heat transport, Planck feedback and the positive lapse rate feedback at polar region are all sup-

portive to polar amplification. However, water vapor feedback and the forcing induced by altering albedo contribute more to the surface temperature change at low latitudes than at high latitudes (Figure 3.16). In spite of that, the water vapor feedback is very strong at high latitudes in the BOG scheme, which could explain the large temperature response in the experiments. A schematic of the mechanisms that contribute to polar temperature changes is illustrated in Figure 3.17, which uses the warming case as an example. Due to the nonlinearity of the Planck feedback, the temperature change in response to the same radiative imbalance at TOA is larger in polar regions than in the tropical region, as the mean temperature is lower at high latitudes ($T_P < T_E$). That is to say, the Planck feedback supports polar amplification naturally. In addition, as illustrated in Figure 3.17, the polar region exhibits a bottom-heavy warming profile because of the stability at the lower troposphere, leading to a positive lapse rate feedback and less infrared radiation to be emitted to space. In contrast, deep convection is active in the tropical region, releasing more latent heat in the upper troposphere and thus favoring a top-heavy warming profile. Such a top-heavy profile brings a negative lapse rate feedback at low latitudes, which is more efficient at emitting the longwave radiation to space. Therefore, lapse rate feedback is favorable to polar amplification as well. However, the water vapor increases more in tropical regions than over polar regions in the warming case, and thus this positive feedback favors tropical warming.

In summary, our findings have confirmed that polar amplification could exist even without sea ice and surface albedo feedback in aquaplanet simulations, which is consistent with previous results (Langen and Alexeev, 2007; Kim et al., 2018; Alexeev et al., 2005). However, we have not explored the role of surface albedo feedback and cloud feedback in polar amplification, due to lack of sea ice and cloud schemes in the Isca model currently.

Chapter 4

The Simple Diagnostic Cloud Scheme

This chapter is mainly based on our publication in *Geoscientific Model Development* (Liu et al., 2021), and modifications have been made to minimize repetition.

4.1 Introduction

As introduced in Chapter 1, cloud feedbacks still have large uncertainties in current CMIP5/6 models (Zelinka et al., 2020). One possible reason for intermodel spread of cloud feedback is the cloud scheme itself. As our understanding of cloud feedback is still limited, the cloud parameterization scheme might not have a solid physical background. For example, Qu et al. (2014) found that models with different types of cloud schemes may predict opposite cloud cover changes under global warming in several marine stratocumulus regions. Another possible reason is that the cloud scheme is coupled with other physical processes and circulation in GCMs, which makes it harder to understand the physical mechanisms behind the possible changes of cloud fields. Therefore it is perhaps not surprising that results can differ considerably.

The proliferation of different cloud schemes, and their interaction with other parameterization schemes and the resolved dynamical flow, means that it is often very difficult to isolate the role of clouds in studies of climate variability and change. For this reason, we take a step back toward simplicity: our intent is to construct a relatively simple cloud scheme that can capture the key processes giving rise to clouds, and that enables us to better understand both their present-day geographical distribution and their possible future change. We also seek to understand what might be a minimal recipe for reproducing cloud effects and their variation in the atmosphere, and just what the limitations are of a scheme based solely on relative humidity. A complementary goal of this chapter is to develop a cloud scheme that can be used in GCMs, without the full complexity of a prognostic or statistical

scheme, for more general climate studies.

For representing the clouds in climate models, perhaps the simplest recipe of representing clouds is to prescribe them with climatological data, without dynamic interplay with the other components of the model, as in Holloway and Manabe (1971). A slightly more complicated step can be constructed by noting that total water within a grid box follows some distribution, so that partial regions within it are saturated even when the grid box, on average, is not. Since clouds normally form on saturation it follows that, depending on the form of the distribution, the cloud amount will be some function of mean relative humidity. A linear relationship between the non-precipitating cloud amount and relative humidity was adopted in early studies (e.g., Smagorinsky, 1960; Ricketts, 1973), and remains of considerable value, although it certainly has its limitations (e.g., Ming and Held, 2018). More recent relative humidity schemes usually assume the cloud forms only when the grid mean relative humidity is larger than a critical relative humidity (e.g., Sundqvist et al., 1989; Slingo, 1980, 1987). In these schemes the critical relative humidity is usually determined empirically and may be a function of grid box size, and the cloud fraction and feedback can be rather sensitive to these threshold values (Quaas, 2012). Relatively simple diagnostic schemes are in fact still used in some comprehensive GCMs (e.g., Giorgetta et al., 2018). In an attempt to move beyond such schemes, various more-or-less complicated prognostic and/or statistical cloud schemes have recently been widely employed in GCMs. The prognostic approach is to explicitly calculate the cloud-related variables (e.g. cloud water content) based on associated physical processes that correspond to the source and sink terms in the prognostic equations (e.g., Tiedtke, 1993). Statistical cloud schemes calculate the cloud fraction and condensate content consistently once the sub-grid probability density functions (PDFs) of certain variables, such as total water specific humidity, are determined (e.g., Sommeria and Deardorff, 1977; Smith, 1990; Tompkins, 2002; Park et al., 2014; Qin et al., 2018; Tsang and Vallis, 2018).

The question then arises as to what a ‘simple’ scheme is. One option would be to specify the PDF of total water within a grid box. Then, supposing that cloud formation occurs on saturation, one may be able derive a functional relation between mean cloud amount and mean relative humidity, supposing that the latter is what is predicted by the GCM from its predictions of specific humidity and temperature. The scheme of Sundqvist et al. (1989) was motivated this way, where the uniform distribution is adopted and the variance of the distribution is assumed to be time-invariant (Tompkins, 2005). Although such a procedure is physically motivated it has two potential drawbacks. First, deciding on a distribution of humidity is somewhat arbitrary, or involves turbulence closure assumptions used in the stochastic model (Sommeria and Deardorff, 1977; Tsang and Vallis, 2018). Second, translat-

ing the prediction of a probability distribution into a practical cloud model may be problematic, for there is in general no straightforward translation from a humidity probability distribution to an analytic formula connecting fractional cloud cover to relative humidity. Thus, here we chose another course by linking the cloud cover with the relative humidity directly with simple forms, as to be introduced in Section 4.2.

In this chapter, the scheme is used in an idealized GCM, Isca (Vallis et al., 2018), configured with a realistic distribution of continents to explore the simulated cloud properties. Idealized models have a number of advantages in investigating physical processes, especially when set within a hierarchy connecting them to more comprehensive models (e.g., Maher et al., 2019; Thomson and Vallis, 2019). We find that a relative-humidity scheme alone is unable to capture the subtropical low cloud distribution, but this issue can be readily improved by the addition of a scheme that takes into account inversion strength. Similarly, we find that in high-latitudes the cloud radiative effect is improved by the addition of a 'freeze-dry' adjustment. In its most complete form, the scheme is able to capture the key features (in both geographical and seasonal variability) of observed clouds without the complexity of contemporary cloud schemes. It does so in a very transparent fashion and the dependence on parameters can be made explicit.

The chapter is organized as follows. Section 4.2 provides a description of the simple cloud scheme, including the methods to parameterize the cloud fraction and specify other needed physical parameters, such as the effective radius of cloud droplets and in-cloud condensate content. Some of the choices and parameters used come from the experiments and observations described in later sections, but for clarity the cloud scheme is described first. Section 4.3 describes the model and experimental configurations as well as the data sets used in this study. In Section 4.4 we compare the simulated cloud properties with observations, with an emphasis on the CRE. The discussion and conclusions are presented in Section 4.5.

4.2 Cloud parameterization scheme

4.2.1 Cloud fraction

In order to have a cloud scheme that interacts with the radiation, we need to predict not only the cloud amount but also its radiative properties. We focus mainly on the former, for the latter we require effective radius of the cloud droplets, and in-cloud liquid water content. In the following subsections we describe how these are specified; an encapsulation of the cloud scheme is also given in Figure 4.1.

The large-scale clouds are parameterized as a function of relative humidity

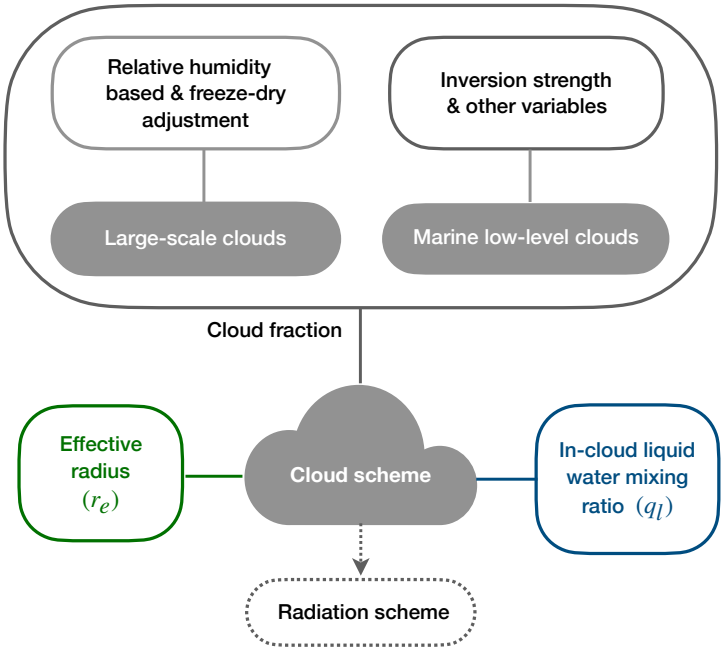

Figure 4.1 A sketch of the simple cloud scheme components, which include the cloud fraction, effective radius of cloud droplet and in-cloud liquid water mixing ratio. At any given location, the maximum of the cloud fractions from large-scale cloud scheme and marine low stratocumulus cloud scheme is applied if both of them are used.

and this provides the majority of the cloud cover. However, this scheme alone is found to be inadequate and two additional effects are needed. First, a 'freeze-dry' method based on the specific humidity is used to reduce the large-scale cloud cover over polar regions to more realistic levels. Second, a separate marine low stratus cloud scheme is used to represent the stratiform clouds (which have a large shortwave radiative effect), and this has a particularly large effect in sub-tropical regions off the west coast of continents. These two additional components are optional and users can decide whether to use them according to their research interest. Although these clouds have different physical properties (e.g., cloud top temperature), all of them are treated essentially as liquid clouds in our scheme. The effective radius of the cloud droplets is allowed to change with temperature, and this affects the radiative transfer. Some tuning of the cloud scheme is performed in order to fit the observations. Nevertheless, the values of certain parameters used in the scheme are not necessarily definitive and may be varied in order to examine the sensitivity of clouds to perturbations such as CO_2 increase.

Relative humidity-based cloud fraction

The use of a relative humidity scheme is based on the notion that over a grid box the humidity varies, and that condensation will occur and clouds will form even when the grid cell is not saturated (Tompkins, 2005; Quaas, 2012), and one such

scheme is that of Sundqvist et al. (1989), discussed more below. Such schemes do not account for variations in dynamical conditions except in so far as they are reflected in the relative humidity field, but they form a simple rational basis for cloud prediction. Here we implement a large-scale cloud scheme in which the cloud fraction (C_s) is a piecewise linear function of grid-mean relative humidity (H), namely

$$C_s = \min\left(1,\ \max\left(0,\ a \cdot (H - 1) + 1\right)\right). \tag{4.1}$$

The diagnosed cloud fraction is therefore unity when the mean relative humidity is equal to one (i.e. grid-box is saturated). The value of a determines the critical value of relative humidity, H_c, above which clouds form, so that $a = 1/(1 - H_c)$ and $H_c = (a - 1)/a$. The coefficient a (and hence H_c) is taken to be a function of height (or pressure) but not latitude or longitude. We have also implemented the Sundqvist et al. (1989) scheme, and that is available for users, but we do not describe it here.

We derive the coefficient profile, the vertical values of the coefficient a, of the linear relationship between C_s and relative humidity based on reanalysis data sets. Specifically, the hourly relative humidity and cloud fraction data sets in the year 2017 from the European Centre for Medium-Range Weather Forecasts (ECMWF) Reanalysis version 5 (ERA5) (Copernicus Climate Change Service (C3S), 2017) are used to derive the coefficient profile. Note that the saturated water vapor pressure is calculated over liquid and ice in the ERA5 data set, while it is calculated over liquid only in the Isca simulations (see Sect.4.3). The ERA5 has $1^\circ \times 1^\circ$ horizontal resolution and 37 vertical levels. For each vertical level, the piecewise linear relationship (as cloud fraction is not allowed to be smaller than 0 or larger than 1) is used to fit the cloud fraction against relative humidity with a least squares method, then the coefficient a of that level is obtained. In addition, data sets with three different horizontal resolutions, including $0.75^\circ \times 0.75^\circ$, $1.4^\circ \times 1.4^\circ$ (T85) and $2.8^\circ \times 2.8^\circ$ (T42), are used to test whether the derived coefficient profile is sensitive to horizontal resolution. The derived profiles with different resolutions are shown in Figure 4.2a, and the corresponding critical relative humidity (H_c) profiles are shown in Figure 4.2b for reference. At very high resolution we would expect the humidity distribution in a given grid box to be narrower, and hence the critical value of relative humidity to increase, however we find that the horizontal resolution has a relatively small influence on the coefficient profiles at the resolutions we consider here.

To apply the coefficient profile of a in the model, a profile similar to the Eq. (3) from Quaas (2012) is used:

$$a = a_t + (a_s - a_t) \exp\left[1 - \left(\frac{p_s}{p}\right)^n\right], \tag{4.2}$$

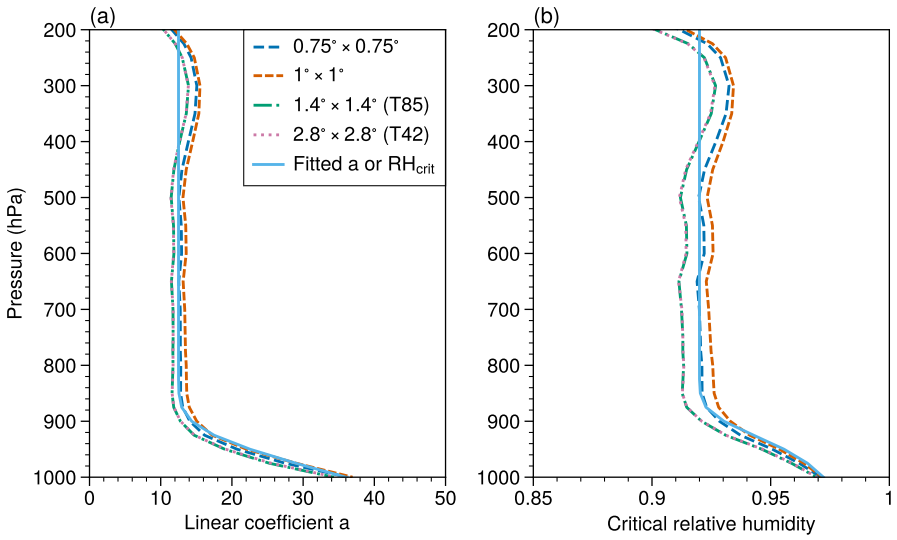

Figure 4.2 (a) Vertical profiles of the linear coefficient for the relative humidity-based cloud diagnostic scheme, with cloud fraction as a piecewise linear function of relative humidity as shown in Equation (4.1). The dashed lines with different colors are profiles of a obtained from ERA5 data with various horizontal resolutions. The solid pale blue line denotes the fitted profile used in the model based on the form of Equation (4.2). (b) is the same as (a), but for the critical relative humidity (H_c) profiles.

where p is the pressure, p_s is the surface pressure, a_s and a_t are the values of coefficient a at surface and free troposphere respectively. Such a functional form fits the observations fairly well with only a small number of tunable parameters. We use $a_s = 36$, $a_t = 13$ and $n = 12$, which determines the shape of the profile. The fitted profile for a, as indicated by the solid pale blue line in Figure 4.2, follows the reanalysis (dashed/dotted lines) quite well at low and middle levels but with some discrepancies at higher levels. The actual cloud fraction for each level is determined by Equation (4.1)with the coefficient for that level determined by Equation (4.2).

We also provide the Sundqvist et al. (1989) scheme as another option for the relative-humidity schemes, namely

$$C_s = 1 - \sqrt{\frac{1 - H}{1 - H_c}}, \tag{4.3}$$

where the H_c is the critical relative humidity. Here we specify H_c as a simple function of height, which is determined by critical relative humidity at three different levels: 0.95 at the surface, 0.85 at 700 hPa, and 0.99 at 200 hPa, which are determined by running sensitivity tests. Between these levels, the critical relative humidity is linearly interpolated with height. To test the performance of the aforementioned schemes, we compare them with another linear scheme with different

form from Equation (4.1), which is defined as

$$C_s = \min\left(1,\ \max\left(0,\ a \cdot H + b\right)\right), \tag{4.4}$$

where a and b vary with height and are determined from the least squares fitting of hourly cloud fraction and relative humidity data from ERA5 reanalysis. The cloud fraction in Figure 4.3a is from ERA5 reanalysis at 450 hPa on 12:00 January 01, 2017, while the cloud fractions from three schemes (Figures 4.3b-4.3d) are diagnosed from the ERA5 relative humidity field at the same time and level. The linear scheme defined in Equation (4.4) has two tunable parameters, so one might expect it to perform better than the others. However, the cloud cover cannot reach 1 when the grid box is saturated (Figure 4.3c), even though the spatial pattern of cloud cover resembles the ERA5 reanalysis and the global mean value is much closer to the ERA5 compared to the other two schemes. In contrast, the diagnosed cloud amount patterns from the Sundqvist scheme (Figure 4.3b) and the linear scheme in the form of Equation (4.1) (Figure 4.3d) are quite similar to the reanalysis (Figure 4.3a), although the cloud cover is a little overestimated in these two schemes. These offline tests suggest that the linear scheme in the form of Equation (4.1) is promising to be applied in GCMs.

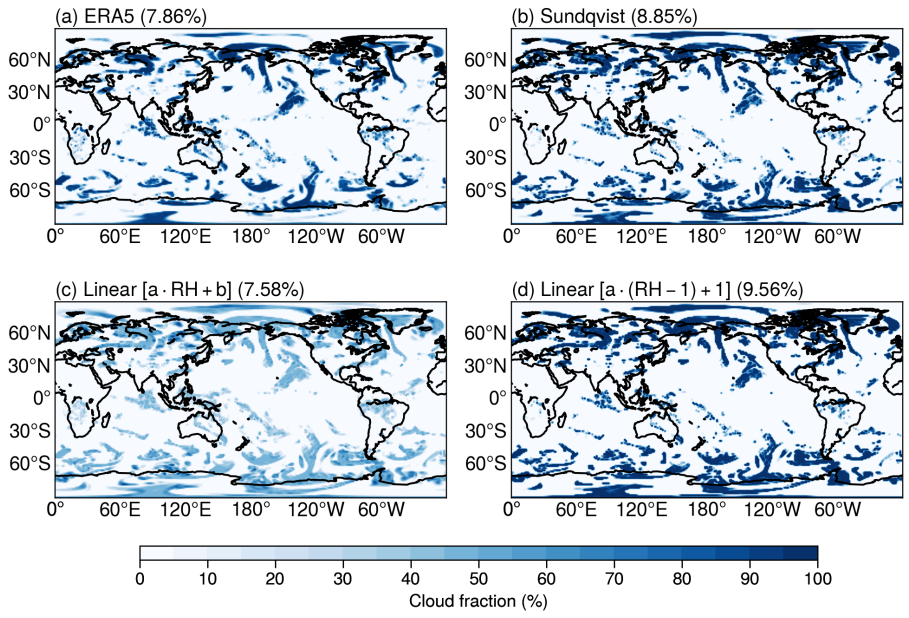

Figure 4.3 (a) A snapshot of cloud fraction from ERA5 reanalysis at 450 hPa on 12:00 January 01, 2017. Diagnosed cloud fraction from ERA5 relative humidity field at the same time and level based on the (b) Sundqvist formula, and two linear formulas (c) using Equation (4.4) and (d) using Equation (4.1). Note that Equation (4.1) is the form used to determine the large-scale clouds in this study. The global mean cloud fractions are given in the titles.

Freeze-dry adjustment

As we will show in Section 4.4.1, the cloud fraction and LW cloud radiative effect from the large scale cloud scheme are overestimated in polar regions, especially during winter. The relative humidity-based cloud fraction scheme assumes there are subgrid-scale fluctuations of humidity and/or temperature, so the partial cloudiness is possible even under subsaturated conditions averaged over a grid box. However, this assumption might not be well suited for the extremely cold and dry atmospheric conditions in polar winter (Jones et al., 2004). The stable boundary layer condition in polar winter leads to little subgrid-scale spatial variability in humidity fields, and there should be less cloudiness than the turbulent environment for a given relative humidity. To alleviate this problem we implement a 'freeze-dry' adjustment, a simple adjustment formula based on specific humidity from Vavrus and Waliser (2008) (see their Eq. (2)). The freeze-dry adjustment is applied to reduce the cloud fraction under very dry conditions in polar regions. Specifically, if grid mean specific humidity (q) is below a threshold (q_v), the cloud fraction (C) decreases linearly according to the water vapor content:

$$C = C \cdot f = C \times \max\left(0.15, \min\left(1.0, \frac{q}{q_v}\right)\right), \tag{4.5}$$

in which the second term is called the freeze-dry factor (f). Although the formula is applied globally, the threshold value in Equation (4.5) ensures that only polar regions will be affected and even there the cloud fraction is adjusted only under very dry conditions.

In the original freeze-dry method, Equation (4.5) was only applied in the lower troposphere (Vavrus and Waliser, 2008). In this study, the freeze-dry formula is applied through the whole atmospheric column, finding that the cloud radiative effect in polar regions is thereby improved. In order to do so, we prescribe the specific humidity threshold q_v in Equation (4.5) to be a function of pressure with the threshold decreasing exponentially with height as

$$q_v = q_0 \left(\frac{p}{p_s}\right)^n. \tag{4.6}$$

Here q_0 is the surface specific humidity, p_s is the sea level pressure ($p_s = 1000$ hPa) and n is the power to describe how quickly the specific humidity decreases with height. In Figure 4.4, different profiles of q_v are shown for the two tunable parameters n and q_0. These two parameters are selected to ensure that the freeze-dry adjustment only has effects on polar regions when the q_v profile is applied in Equation (4.5). In doing so, the specific humidity profiles from several different regions are plotted in Figure 4.4. In particular, the profiles at 60°N and 60°S are used to show the specific humidity boundary values of polar regions, and thus the

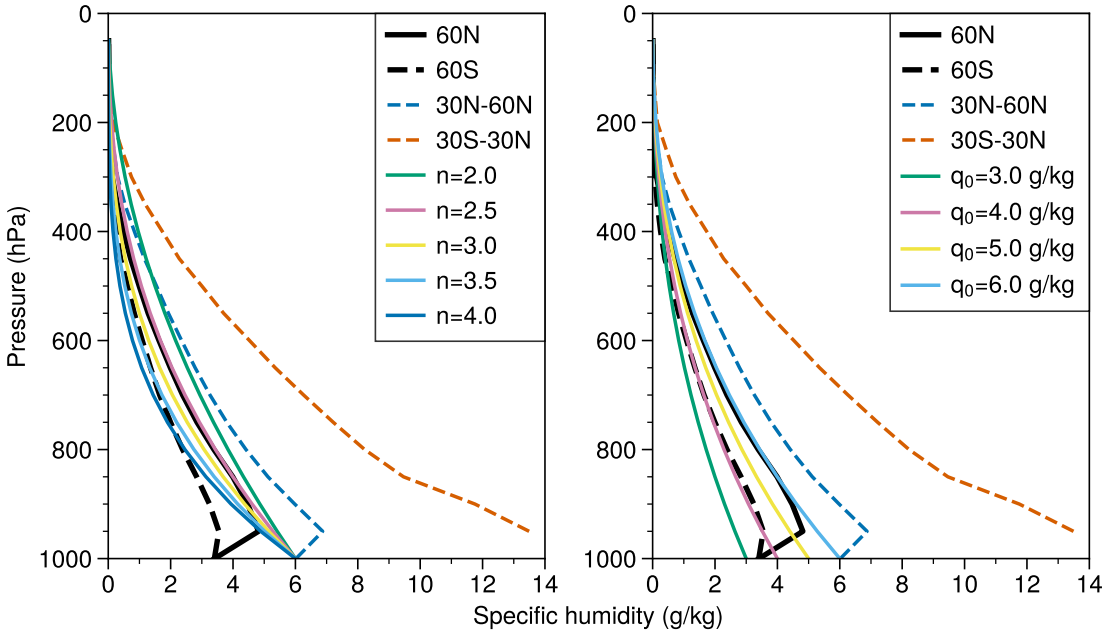

Figure 4.4 The q_v vertical profiles with different n and q_0. The thick solid and dashed black lines are annual mean specific humidity profiles from Isca simulation averaged over latitude circles, 60N and 60S, as boundary values of polar regions in Northern and Southern hemispheres, respectively. The thin dashed blue and orange lines are averaged specific humidity profiles over subtropical (30°-60°N) and tropical (30°S-30°N) regions in Isca simulation. The remaining solid lines are from Equation (4.6) with different parameters. In the left, q_0 in Equation (4.6) is 0.006 kg kg^{-1} but n varies from 2 to 4. In the right, $n = 2.5$ but q_0 varies from 0.003 to 0.006 kg kg^{-1}.

two parameters q_0 and n are tuned to follow the boundary profiles. As shown in Figure 4.4, the q_v profile follows the 60°N profile well when the $q_0 = 0.006$ kg kg^{-1} and $n = 2.5$, which can also cover the specific humidity range poleward of 60°S. Therefore in this study the parameters q_0 and n are chosen as 0.006 kg kg^{-1} and 2.5, respectively. This threshold works well in a current climate setup (see Section 4.4.1), but whether it holds under global warming situation still needs further investigation.

Low cloud fraction

Low clouds, especially the subtropical marine stratocumulus clouds, are characterized by high albedo and a cooling effect on climate (Hartmann, 2016). Because these clouds cover about 20% of the subtropical regions even a small change in stratocumulus cloud amount can exert a large radiative forcing at the top of the atmosphere (TOA) (Slingo, 1990). However, marine stratocumulus amounts off the west coast of continents have commonly been underestimated and has been an issue in climate models for some time (e.g., Nam et al., 2012; Lauer and Hamilton, 2013; Dolinar et al., 2015).

Several proxies or indices for low cloud fraction have been used as predictors for the stratocumulus clouds to try to remedy this (e.g., Kawai and Inoue, 2006; Joshi et al., 2015; Collins et al., 2004; Guo and Zhou, 2014; Kawai et al., 2019), including potential temperature lapse rate ($d\theta/dp$) of the most stable layer below 750hPa (Slingo, 1987); lower tropospheric stability (LTS; Klein and Hartmann, 1993); estimated inversion strength (EIS; Wood and Bretherton, 2006); and the estimated cloud-top entrainment index (ECTEI; Kawai et al., 2017). Recently, Park and Shin (2019) proposed a new index, the estimated low-level cloud fraction (ELF), as a predictor for low cloud fraction. ELF (which is a proxy and not necessarily a cloud amount itself) is defined as

$$\mathrm{ELF} \equiv f \cdot \left[1 - \frac{\sqrt{z_{\mathrm{inv}} \cdot z_{\mathrm{LCL}}}}{\Delta z_s}\right], \tag{4.7}$$

where f is the freeze-dry factor defined in Equation (4.5) with $q_v = 0.003$ kg kg^{-1} and q is the surface water vapor specific humidity, z_{inv} is the inversion height, z_{LCL} is the lifting condensation level of near-surface air, and Δz_s is a constant scale height ($\Delta z_s = 2750$m). As pointed by Park and Shin (2019), $\sqrt{z_{\mathrm{inv}} \cdot z_{\mathrm{LCL}}}/\Delta z_s$ can be rewritten as $z_{\mathrm{LCL}}/\Delta z_s \cdot \sqrt{1 + (z_{\mathrm{inv}} - z_{\mathrm{LCL}})/z_{\mathrm{LCL}}}$, in which $z_{\mathrm{LCL}}/\Delta z_s$ is a simple but practical proxy of surface moisture, and $(z_{\mathrm{inv}} - z_{\mathrm{LCL}})/z_{\mathrm{LCL}}$ quantifies the strength of the vertical decoupling of the inversion base air from the surface. The ELF predicts that low-level cloud fraction increases as the near-surface air gets more wet (smaller z_{LCL}) and as the planetary boundary layer becomes more vertically coupled (smaller z_{inv}).

We have examined the relationship between the seasonal mean low cloud fraction and the various proxies (i.e., $d\theta/dp$, LTS, EIS, ECTEI and ELF) using the ERA-Interim reanalysis data set (Dee et al., 2011). These proxies are derived from the five-year monthly data from 2013 to 2017, including air temperature, surface pressure, surface temperature and low cloud fraction. As shown in Figure 4.5, the regions with typical stratus clouds are selected for the calculation (Klein and Hartmann, 1993). The results indicate that the low cloud fraction is linearly related to each indicator in stratus cloud regions, and the ELF tends to have very high correlation with the low-level cloud cover, judging from the fraction of variance (R^2) explained by the regression equation. We thus choose to use ELF to construct the diagnostic low cloud fraction formula, that is:

$$C_{\mathrm{sc}} = \min(1,\ \max(0,\ b \times \mathrm{ELF} + c)), \tag{4.8}$$

where C_{sc} is the low stratus cloud fraction, and the two coefficients b and c are treated as tunable parameters. The linear regression formula displayed in Figure 4.5e provides a good starting point for tuning b and c in Equation (4.8). After a sensitivity test performed with Isca (the setups will be introduced in Section 4.3),

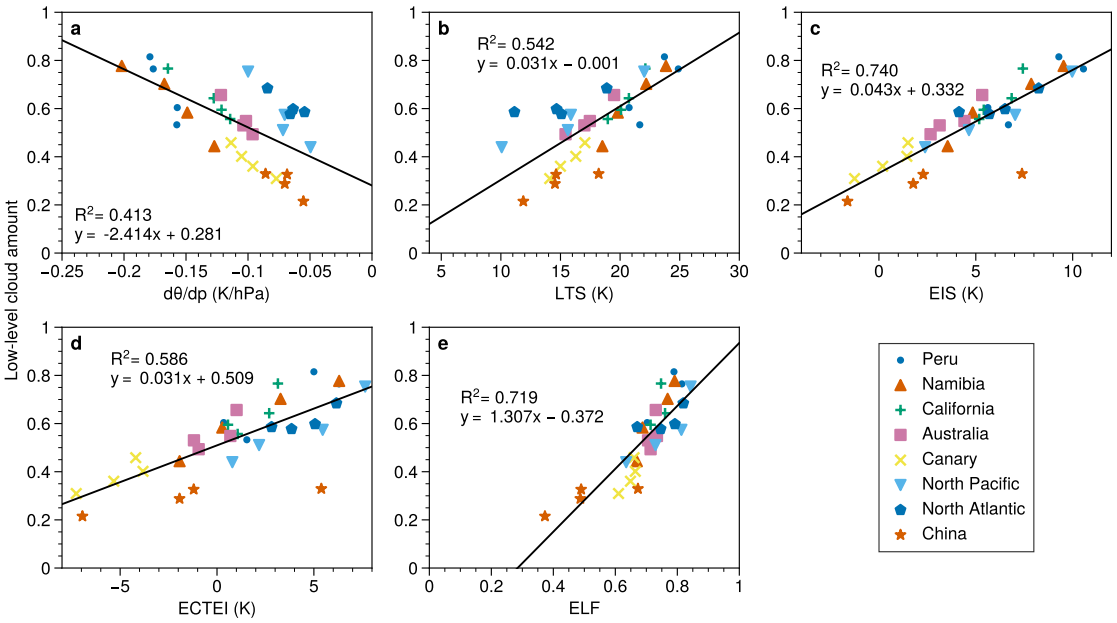

Figure 4.5 The relationship between low-level cloud amount and (a) minimum $d\theta/dp$ below 750 hPa, (b) lower tropospheric stability (LTS), (c) estimated inversion strength (EIS), (d) estimated cloud-top entrainment index (ECTEI) and (e) estimated low cloud fraction (ELF) over stratiform cloud regions, including Peru (20°S-5°N, 80°-90°W), Namibia (10°-30°S, 0°-15°E), California (15°-30°N, 110°-150°W), Australia (15°-35°S, 90°-110°E), Canary (15°-25°N, 25°-35°W), North Pacific (40°-5°0N, 170°-180°E), North Atlantic (50°-60°N, 35°-45°W) and China (20°-30°N, 105°-120°E), which are selected based on Klein and Hartmann (1993). The data sets are from ERA-Interim reanalysis covering the period from 2013 to 2017. The four points in each region denote the average for different seasons. Linear regression lines and the corresponding fraction of variance (R^2) explained by the equation are shown at the top of each plot.

we find that if c is specified as the value shown in Figure 4.5e, the shortwave cloud radiative effect is still weak compared to observations. Therefore the parameters b and c are chosen as 1.3 and -0.1 respectively.

In addition, the stratocumulus clouds usually form at the top of the planetary boundary layer (Wood, 2012), where a strong inversion layer usually exists (Wood and Bretherton, 2006; Park and Shin, 2019). However, it is hard for a global model to capture the exact position of the inversion layer due to the limitation of vertical resolution (Kawai et al., 2019). Care thus needs to be taken to diagnose the marine stratocumulus clouds. First we find the most stable layer below 750 hPa, which is determined by the most negative $d\theta/dp$ (Slingo, 1987). Then within the most stable layer, if the lapse rate and vertical velocity satisfy $d\theta/dp < -0.08$ K hPa^{-1} and $\omega > 0$ Pa s^{-1} respectively, then we diagnose stratocumulus clouds at that location. Note that the $d\theta/dp$ threshold is tuneable in our scheme, and it is -0.125 K hPa^{-1}, as in Collins et al. (2004).

Cloud fraction diagnosis

The cloud fraction of a grid box (C_{total}) is simply defined as the largest fraction of all the clouds within that grid box for simplicity, without separate consideration of their different optical properties:

$$C_{\text{total}} = \max(C_s,\ C_{\text{sc}}), \tag{4.9}$$

assuming a horizontal maximum overlap hypothesis (e.g., Collins et al., 2004; Roehrig et al., 2020). C_s and C_{sc} in Equation (4.9) are determined by Equation (4.1) and Equation (4.8) respectively. To assess the performance of the cloud scheme, it is useful to evaluate the total cloud amount and cloud amounts at different levels. In our scheme, the cloud height is determined by cloud top pressures, where those located above 400 hPa are treated as high clouds, those below 700 hPa are defined as low clouds, and in between are middle clouds (Collins et al., 2004). Then, the total, high, middle or low cloud amounts are diagnosed from the maximum-random overlap assumption (Morcrette and Jakob, 2000), which assumes maximum overlap for consecutive cloudy model levels and random overlap for cloud layers that are separated by clear-sky levels.

4.2.2 Cloud optical property

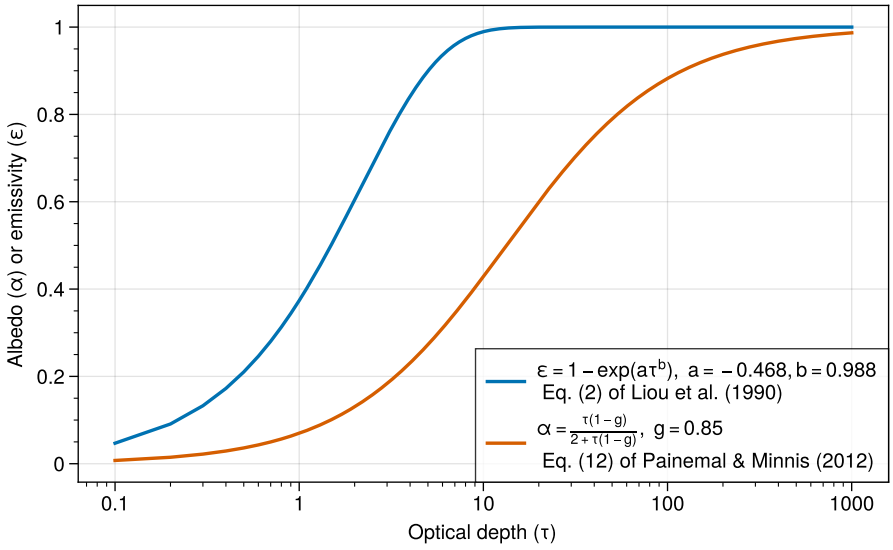

Figure 4.6 The relationship between cloud emissivity (ϵ), albedo (α) and optical depth (τ). The $\epsilon - \tau$ relationship (blue line) is based on Eq. (2) of Liou et al. (1990), and the $\alpha - \tau$ relationship (orange line) is from Eq. (12) of Painemal and Minnis (2012) after Bohren (1987).

To calculate the radiation transfer with clouds properly, it is important to represent the cloud radiative property reasonably. In general, the emissivity (ϵ) and

albedo (α) are important properties for longwave and shortwave radiation transfer respectively. As displayed in Figure 4.6, the emissivity increases quickly towards 1 as the increase of optical depth (see Eq. (2) in Liou et al., 1990). The cloud albedo also increases with optical depth (see Eq. (12) of Painemal and Minnis, 2012), but at a slower rate than emissivity. Thus, both cloud emssivity and albedo are related to cloud optical depth, which is in fact determined by the cloud water path and effective radius as derived by Stephens (1978). Here we re-write the formula as follows:

$$\tau = \frac{3\mathrm{LWP}}{2r_e}, \tag{4.10}$$

where LWP is the liquid water path (g m^{-2}, defined in Equation (4.14)) and r_e is effective radius in units of micrometers (μm). Therefore in this study, the cloud optical properties are parameterized by effective radius (Section 4.2.2) and in-cloud water content (Section 4.2.2), as the cloud water path can be derived from the in-cloud water mixing ratio and cloud fraction based on hydrostatic balance assumption (Eq. 9.30 in Stensrud, 2007).

Effective radius

Cloud particles, including liquid droplets and ice crystals, usually have different sizes, shapes and optical properties. In order not to introduce complicated microphysical processes, we do not distinguish them and assume that all particles seen by the radiation scheme are spherical liquid droplets, and ice clouds have a different effective radius from the liquid ones. In this study, the liquid cloud fraction varies with temperature, which only has an influence on the effective radius.

Following Ose (1993) and Boville et al. (2006), a very simple approach is used to represent the liquid cloud fraction (f_l) within a grid box. Specifically, all clouds are assumed to be in liquid form if temperature is warmer than T_{max}, and all the condensate is considered as ice if temperature is colder than T_{min}. The cloud droplets are in mixed-phase at temperatures between T_{min} and T_{max}, and the proportion of liquid cloud in a grid box is defined as a linear function of temperature:

$$f_l = \max\left(0,\ \min\left(1,\ \frac{T - T_{\mathrm{min}}}{T_{\mathrm{max}} - T_{\mathrm{min}}}\right)\right). \tag{4.11}$$

The bounds T_{min} and T_{max} are different in different models. For example, the lower bound (T_{min}) is -40°C in Ose (1993) and Boville et al. (2006), while it is -15°C in Smith (1990). Observations have shown that cloud liquid water can exist at temperature as low as -40°C (Heymsfield and Miloshevich, 1993), although the incidence of liquid water in stratiform clouds is quite low at temperatures below -15°C (Ryan, 1996). The upper bounds (T_{max}) are -5°C for stratiform clouds in Ose (1993), -10°C in Boville et al. (2006), and 0°C in Smith (1990). Based on

the choices in previous studies, $T_{\min}$ and $T_{\max}$ in Equation (4.11) are chosen to use $-40°C$ and $-5°C$ respectively in this study, but they are to be regarded as adjustable parameters.

The effective radius (r_e) is a weighted mean of the size distribution of cloud droplets as defined in Eq. (2.53) of Hansen and Travis (1974). But in this study the microphysical properties such as number density of cloud droplets are not included, so the effective radius of droplets within a grid box is simply defined as a weighted mean of liquid and ice effective particle radii, with the weights given by the liquid and ice cloud fraction respectively. The radii of liquid and ice particles are selected based on observations. Stubenrauch et al. (2013) assessed cloud properties derived from various satellite data sets, finding that the global mean effective particle radii are about 14 (±1) and 25 (±2) μm for the tops of liquid clouds and for high-level ice clouds, respectively. Therefore these two values are selected to calculate r_e,

$$r_e = 14 f_l + 25(1 - f_l), \tag{4.12}$$

which is applied globally in the model, although the effective radius of cloud droplets is found a little larger over ocean than over continents in observations (Stubenrauch et al., 2013).

In-cloud water mixing ratio

The in-cloud liquid water mixing ratio (w_l) is specified as a linear function of the atmospheric temperature, with values of 3×10^{-4} g kg^{-1} at 220 K and $w_{l0} = 0.18$ g kg^{-1} at 280 K:

$$w_l = \max\left(3 \times 10^{-4},\ w_{l0} \times \min\left(1,\ \frac{T - 220}{280 - 220}\right)\right), \tag{4.13}$$

where the atmospheric temperature T is in units of K. The temperature thresholds, 280 and 220 K, are selected close to the global averages of liquid and ice cloud top temperature in observations, respectively (Fig. 4 in Stubenrauch et al., 2013). Then the grid mean liquid water specific humidity can be obtained from the product of w_l and cloud fraction. Note that Equation (4.13) is modified from the SPOOKIE II project (see https://www.cfmip.org/experiments/informal-experiments for detail, last accessed: 12 March, 2021). At first, the in-cloud water content is specified as a function of height, but in the second version of the protocol, it has been updated as a function of temperature.

4.2.3 Summary and discussions

This section presents how the simple cloud scheme was built. It has a modest level of complexity and is transparent in describing its dependence on tunable pa-

Table 4.1 Summary of the diagnostic cloud scheme.

Symbol	Range / Units	Definition	Diagnostic formula	Tunable parameters
C_s	[0, 1]	Large-scale cloud fraction	$\min(1,\ \max(0,\ a\cdot(H-1)+1))$, $a = a_t + (a_s - a_t)\exp\left[1-\left(\frac{p_s}{p}\right)^n\right]$	a_s=36, a_t=13, n=12
			$\min\left(1,\ \max\left(0,\ 1-\sqrt{\frac{1-H}{1-H_c}}\right)\right)$	H_c: function of height
f	[0.15, 1]	Freeze-dry adjustment factor	$\max\left(0.15, \min\left(1.0,\ \frac{q}{q_v}\right)\right)$, $q_v = q_0\left(\frac{p}{p_s}\right)^n$	q_0=6 g kg^{-1}, n=2.5
C_{sc}	[0, 1]	Low cloud fraction	$\min(1,\ \max(0,\ b\times \mathrm{ELF} + c))$, $\mathrm{ELF} = f\cdot\left[1-\sqrt{z_{\mathrm{inv}}\cdot z_{\mathrm{LCL}}}/\Delta z_s\right]$	b=1.3, c= −0.1 q_v=3 g kg^{-1} in f
f_l	[0, 1]	Liquid cloud fraction	$\max\left(0,\ \min\left(1,\ \frac{T-T_{\min}}{T_{\max}-T_{\min}}\right)\right)$, ($T$ in units of °C)	$T_{\min}$=−40, $T_{\max}$=−5°C
r_e	$[r_{e\_\mathrm{liq}},\ r_{e\_\mathrm{ice}}]$ μm	Effective radius	$r_{e\_\mathrm{liq}} f_l + r_{e\_\mathrm{ice}}(1-f_l)$	r_{e_liq}=14, r_{e_ice}=25 μm
w_l	$[3\times10^{-4},\ w_{l0}]$ g kg^{-1}	In-cloud liquid water mixing ratio	$\max\left(3\times10^{-4},\ w_{l0}\times\min\left(1,\ \frac{T-220}{280-220}\right)\right)$, ($T$ in units of K)	w_{l0}=0.18 g kg^{-1}

rameters. All of the features in the scheme are user-configurable. For reference, the equations and parameters used in the cloud scheme are summarized in Table 4.1.

The large-scale clouds, which form the core of the scheme, are diagnosed from relative humidity. We explore two schemes, one with a piecewise linear relationship between cloud cover and relative humidity and the other with a square-root relationship, as in Sundqvist et al. (1989). The various coefficients entering into these schemes are obtained empirically, comparing results with observations. In addition, the marine low stratus clouds, typically found off the west coast of continents over subtropical oceans, are determined largely as a function of inversion strength. A 'freeze-dry' adjustment based on a simple function of specific humidity is also available to reduce an excessive clouds bias in polar regions. Cloud optical properties, such as the effective radius of cloud droplet and cloud liquid water content, are specified as simple functions. Specifically, the effective radius of cloud droplets is calculated as a weighted mean of liquid cloud droplet and ice cloud crystal, with the weight specified by the liquid cloud fraction, which is defined as a linear function of temperature. The in-cloud liquid water content is also determined as a function of temperature, where the temperature threshold is deduced from the observed liquid and ice cloud top temperature.

It is noted that the present version does not include a separate scheme for convective clouds, and the convection scheme in the model has no effect on cloudiness except in so far as it may change the relative humidity or, possibly, the low-level inversion. We find that the vertical structure of clouds can be simulated relatively well without explicit diagnosis of convective clouds (see Figure 4.7), and we leave the possible explicit representation of convective clouds to a future study.

Moreover, this simple diagnostic scheme is not meant as a replacement for more complicated schemes that are based on microphysical properties and/or explicitly on liquid and solid phases of the condensate. Rather, it is intended to be used in models which may require a level of complexity commensurate with other parameterizations, and/or in situations where particular processes are to be investigated. Cloud schemes in many comprehensive GCMs have become very complicated and differ considerably in detail from each other, and there is value in providing a simpler scheme, but one that also has a number of realistic features and that captures the observed cloud climatology with some verisimilitude. In the next chapter, the performance of this simple cloud scheme is to be examined in Isca. But it could easily be ported to other GCMs, either by a straightforward implementation or by porting the code itself.

4.3 Data and methods

4.3.1 Experiment setup

The simple cloud scheme described in Chapter 4 was implemented into Isca (Vallis et al., 2018) to examine its performance, as there was no cloud scheme in Isca before this implementation. The simulations used in this chapter are AMIP-type, that is they follow those used in the Atmospheric Model Intercomparison Project . They are performed with a realistic Earth-continental configuration following Thomson and Vallis (2018) (which is derived from the ERA-Interim land mask and topography, Dee et al. 2011) and at a horizontal resolution of T42 (roughly $2.8^\circ \times 2.8^\circ$) with 25 vertical levels. Note that here the land topography file is filtered to remove the Gibbs effect (thanks to Greg Colyer and Ruth Geen for providing this).

The monthly sea surface temperature and sea ice concentration are fixed at AMIP climatology (Taylor et al., 2000), which are derived from the input4MIPs data set (Durack et al., 2018) over the period from 1979 to 2008, and the scripts to process the input data set are available at `https://github.com/lqxyz/input4MIPs`. The albedo in sea ice regions increases linearly with the sea ice concentration with a maximum of 0.7. The ocean surface albedo of the other parts except the sea ice is fixed as 0.11, and the land surface albedo prefactor is set to 1.3. The insolation includes a seasonal and diurnal cycle, with a solar constant of 1365 Wm^{-2}. The convection parameterization used in this study is the simplified Betts–Miller scheme from Frierson (2007), from which the convective precipitation is diagnosed. The large-scale precipitation is obtained from the large-scale condensation scheme (Frierson, 2007), which is accomplished by adjusting the humidity in super-saturated regions to the saturated values immediately, with temperatures adjusted to reflect this condensation.

The SOCRATES (Suite Of Community RAdiative Transfer codes based on Edwards and Slingo) radiation scheme (Edwards and Slingo, 1996; Manners et al., 2015) is employed for the radiation transfer calculation as in Thomson and Vallis (2019). Spectral files with 9 longwave bands and 6 shortwave bands are used, which are those used in the Unified Model's Global Atmosphere version 7 (Walters et al., 2019). The cloud fraction, effective radius of cloud particle and liquid water mixing ratio in each grid are passed to it, then the radiation fluxes under all-sky and clear-sky conditions are obtained, which are used to analyze the energy balance and to calculate the cloud radiative effect (Ramanathan et al., 1989; Li et al., 2017) at the TOA.

In order to compare the roles of different cloud parameterization schemes, simulations are performed with the combination of different clouds or different adjustment methods as shown in Table 4.2. The simulation with large-scale clouds only is denoted as the LS simulation. The run with large-scale clouds and freeze-

Table 4.2 Summary of the Isca fixed-SST simulations

Experiment	Description
LS	Run with large-scale clouds only.
FD	Based on the LS run, with freeze-dry adjustment also applied.
ALL	The marine low-level clouds are also included on top of the FD run.
Linear_X	X is one of the LS, FD and ALL runs, in which the large-scale clouds are diagnosed from a linear function of RH as defined in Equation (4.1).
Sundqvist_X	As in Linear_X, but with the Sundqvist et al. (1989) scheme as defined in Equation (4.3).

dry adjustment is called the FD simulation. The run performed with large-scale clouds, freeze-dry adjustment and marine low stratiform clouds is referred as the ALL simulation. The simulations are all run for 20 years, with the first 10 years treated as spin-up and discarded. The outputs are archived at Zenodo: https://doi.org/10.5281/zenodo.4573610.

4.3.2 Data sets

To evaluate the performance of the cloud scheme, several observations and re-analysis data sets are employed. Specifically, the cloud fraction from Isca simulations is compared to retrieved cloud fraction from GCM-Oriented Cloud-Aerosol Lidar and Infrared Pathfinder Satellite Observations Cloud Product (CALIPSO-GOCCP hereafter; Chepfer et al., 2010) over the period 2007-2015. To examine the radiative flux simulated in Isca, monthly data from January 2001 to December 2018 from Clouds and Earth's Radiant Energy System (CERES) Energy Balanced and Filled (EBAF) Edition 4.1 product (CERES-EBAF hereafter; Loeb et al., 2018) are used for comparison.

The cloud water path is from the CloudSat 2B-CWC-RO Release P1_R05 data product (Austin et al., 2009) from 2012 to 2016, which can better represent cloud liquid and ice water path over high latitudes than CERES-EBAF data set, owing to its explicit determination of cloud phase (Lenaerts et al., 2017). The original CloudSat cloud water path data set has some missing data for certain dates, and is not in the T42 resolution we are going to use. To get the annual mean product we desired, the original data set is processed as follows: For the area each grid point covers, the total number of times that the satellite has visited over the 5 years and the sum of the cloud water path that has been retrieved over same period are recorded, from which the annual mean cloud water path is derived. The scripts to

do this can be accessed at https://github.com/lqxyz/cloudsat_cloud_water_path. In addition, monthly vertical pressure velocity from ERA-Interim reanalysis and radiative flux data from CERES-EBAF data sets covering the period 2008-2017 are also adopted to quantify the longwave CRE over the tropics.

In order to demonstrate how this cloud scheme performs with respect to more comprehensive models, the monthly mean radiative fluxes at clear-sky and all-sky conditions in historical simulation (1996 to 2005) from various CMIP5 models are also shown for the names of models). All the data sets are remapped to T42 resolution when necessary for a direct comparison with Isca simulations.

4.4 Evaluation of the simple cloud scheme

4.4.1 Simulated cloud amount

The global mean cloud amount and radiative components for the observations and Isca simulations are summarized in Table 4.3.

The global mean cloud fraction profiles from CALIPSO-GOCCP, ERA-Interim reanalysis and Isca simulations are displayed in Figure 4.7a. The cloud fractions from all the Isca simulations are higher than observations, especially in the middle and high levels. The FD simulations are closer to observations than the LS simulations, which is true for both the linear and Sundqvist schemes. Regarding the annual and zonal mean profiles, a striking feature is that the LS simulations from both linear and Sundqvist schemes overestimate the cloud fraction at high latitudes (Figures 4.7d and 4.7g) compared to the observation (Figure 4.7b) and reanalysis (Figure 4.7c). These biases are mitigated in the FD simulations (Figures 4.7e and 4.7h), as the cloud fractions are limited due to insufficient water vapor content at high latitudes. Despite more clouds being diagnosed at low levels over the eastern subtropical ocean regions, the zonal mean cloud fraction profiles in the ALL simulations (Figures 4.7f and 4.7i) are generally similar to those from the FD simulations. In summary, the cloud fraction profiles have been improved from the LS to ALL simulations due to the freeze-dry adjustment and the extra low clouds. However, the cloud fractions are still overestimated in high levels over the subtropics, which could possibly explain the CRE biases over these regions.

In addition to the cloud fraction profiles, the geographic patterns of cloud amount, diagnosed from the random-maximum overlap assumption (Section 4.2.1), are also compared with observations. For example, the annual mean spatial patterns of low cloud amount from three different simulations (LS, FD and ALL) with linear RH cloud scheme, CALIPSO-GOCCP data set, and the differences between them are shown in Figure 4.8. It should be pointed out that in this chapter we do not compare the simulated cloud amount with satellite retrievals directly, as the cloud

Table 4.3 Global and annual mean climatological properties of observations and different Isca simulations, which are summarized in Table 4.2. The net fluxes in the table are positive downward.

	Obs	Linear_LS	Linear_FD	Linear_ALL	Sundqvist_LS	Sundqvist_FD	Sundqvist_ALL
Low cloud amount (%)	40.4[a]	54.9	49.3	48.8	53.8	48.6	47.7
Middle cloud amount (%)	20.3[a]	25.6	20.6	20.7	25.2	20.2	20.0
High cloud amount (%)	31.6[a]	43.7	31.0	31.1	36.8	26.0	26.0
Total cloud amount (%)	68.9[a]	76.4	66.8	66.5	73.0	63.8	63.2
TOA net SW flux (Wm^{-2})	241.3[b]	228.0	230.7	230.6	232.6	235.0	235.2
TOA net LW flux (Wm^{-2})	240.3[b]	222.7	227.3	227.1	226.2	230.5	230.4
TOA net flux (Wm^{-2})	1.0[b]	5.3	3.4	3.6	6.4	4.5	4.8
TOA SW CRE (Wm^{-2})	-45.8[b]	-60.0	-57.3	-57.3	-55.4	-53.0	-52.8
TOA LW CRE (Wm^{-2})	28.0[b]	36.8	31.7	31.6	33.3	28.5	28.3
TOA net CRE (Wm^{-2})	-17.8[b]	-23.2	-25.5	-25.7	-22.1	-24.5	-24.4
Cloud water path (gm^{-2})	119.3[c]	142.1	126.0	127.8	123.4	109.8	110.4

[a] The observed cloud amounts are from CALIPSO-GOCCP (Chepfer et al., 2010) product (2007–2015)

[b] The radiative fluxes and cloud radiative effects (CREs) at the TOA are from CERES-EBAF (Loeb et al., 2018) data set (2001–2018)

[c] The cloud water path (sum of liquid and ice) is from CloudSat 2B-CWC-RO Release P1_R05 (Austin et al., 2009) data product (2012–2016)

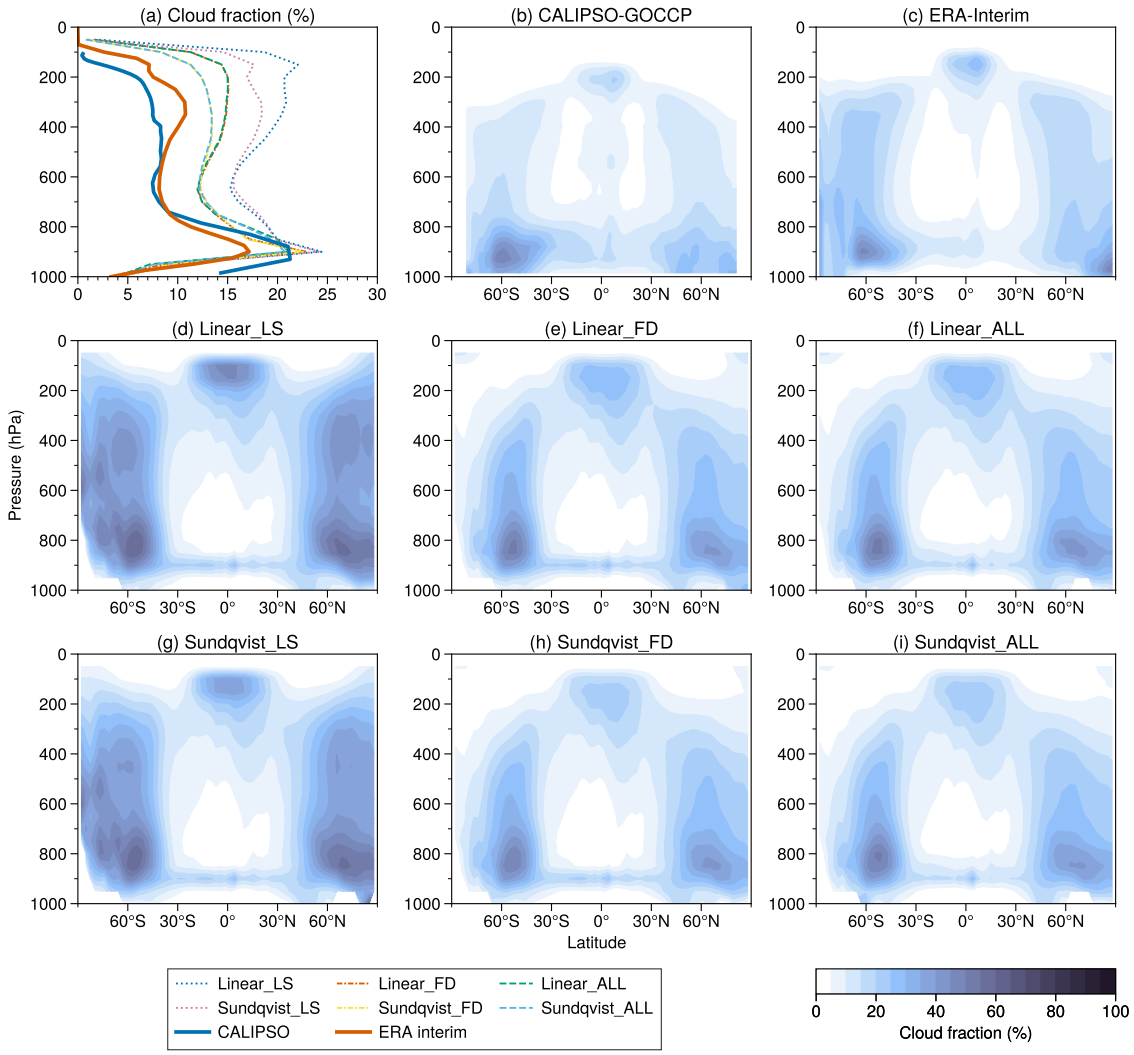

Figure 4.7 (a) The annual and global mean of cloud fraction profiles from the CALIPSO-GOCCP (thick blue solid line), ERA-Interim reanalysis (thick orange solid line) and different Isca simulations, including linear_LS (blue dotted), linear_FD (orange dash-dotted), linear_ALL (green dashed), Sundqvist_LS (pink dotted), Sundqvist_FD (yellow dash-dotted) and Sundqvist_ALL (azure dashed). (b-i) As in in (a), but for annual and zonal mean of cloud fraction profiles.

simulator (e.g., Bodas-Salcedo et al., 2011) has not been implemented in Isca.

One evident feature of the low cloud amount in observations is that marine stratocumulus clouds dominate the areas off the west coast of continents (Figure 4.8d), related to the subsiding branch of the Hadley cell (Wood, 2012). The predominantly downward motion in these regions generally suppresses cloud formation in the middle and upper troposphere, but due to the abundance of water vapor near the ocean surface, clouds form at the top of convective boundary layers. However, these marine low clouds are too far from the coasts in the LS simulation compared to the observations (Figure 4.8a). Looking at the differences between LS simulation and observations (Figure 4.8g), the low cloud amount is underestimated by about 20% off the west coast of Peru. In fact, these are well-

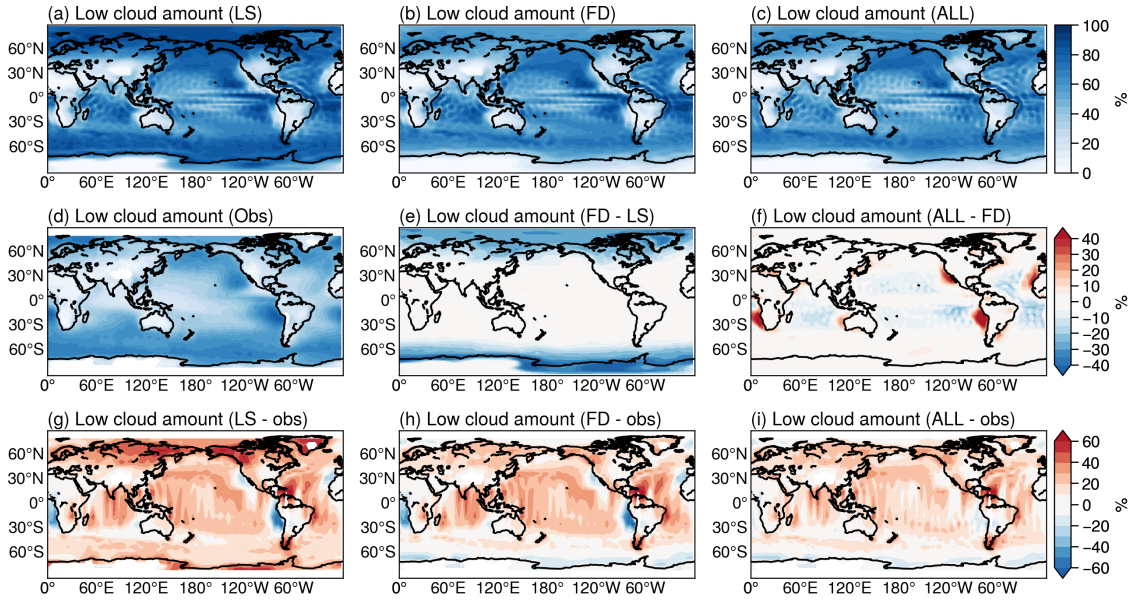

Figure 4.8 The annual mean geographic patterns of low cloud amount (%) from the (a) LS, (b) FD, (c) ALL simulations with the linear scheme as well as (d) observation (CALIPSO-GOCCP), and the differences between the (e) FD and LS, (f) ALL and FD, (g) LS and observation, (h) FD and observation, and (i) ALL and observation. Note that (a-d) use the upper color scale, (e-f) use the middle one, and (g-i) use the one at the bottom.

known biases in CMIP5 models (Dolinar et al., 2015). Another problem of the LS simulation is the overproduction of low cloud amount in polar regions (Figure 4.8g). For example, LS simulation produces more than 40% low cloud over the Arctic region.

In contrast, the cloud fractions in the FD and ALL simulations are adjusted by the freeze-dry method (see Section 4.2.1), which is mainly designed to reduce the unrealistic cloud amount in polar regions. Thus there is a reduction of low cloud amount over high latitudes in these two simulations (Figures 4.8h and 4.8i), although some positive biases still exist there. Compared with the LS simulation directly, the FD simulation can reduce the low cloud amount by more than 20% over polar regions (Figure 4.8e), showing a better agreement with the observations. The ALL simulation can further diagnose the marine stratus clouds off the west coast of continents through the predictor ELF, making the low clouds distribution closer to the observation (Figure 4.8c). It is noted that pronounced changes occur off the west coasts of Peru, California and Namibia in the ALL simulation, where the cloud fraction increases over 20% (Figure 4.8f) compared to the FD run. As shown in Table 4.3, the global mean low cloud amount decreases from 54.9% to 48.8% from the LS to ALL simulations with the linear RH scheme, which is closer to the observed value (40.4%). The changes of total cloud amount in these simulations (not shown here) are similar, and the global mean value decreases from 76.4% (the LS run) to 66.5% (the ALL run) for the linear RH scheme (Table 4.3).

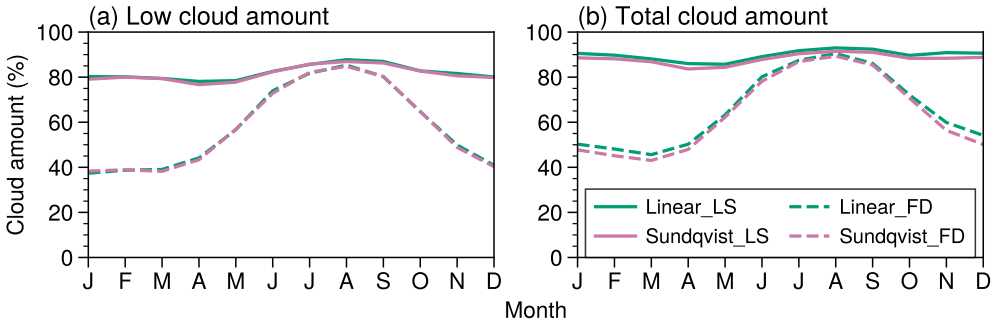

Figure 4.9 The seasonal cycle of (a) low and (b) total cloud amount (%) over the Arctic region (60°-90°N) from the LS (solid lines) and FD (dashed lines) simulations, where the freeze-dry adjustment method is applied in the FD simulations. The green and pink colors denote the experiments performed with the linear and Sundqvist cloud schemes respectively.

The above analyses have shown that the freeze-dry method can improve the spatial patterns of annual mean cloud amount, with these changes being especially pronounced during winter time (as also noted by Vavrus and Waliser, 2008). Figure 4.9 illustrates the annual cycle of low and total cloud amounts over the Arctic region from both linear RH and Sundqvist schemes. In the LS simulations, both the low and total cloud amounts are nearly at the same level throughout the year. However, a striking feature in the FD simulations is that the cloudiness declines rapidly during boreal winter but remains almost unchanged in warm and moist summer, which in fact is more realistic compared to observations as pointed by Vavrus and Waliser (2008).

4.4.2 Simulated cloud water path

The cloud water path (CWP) measures the total amount of cloud water within a column and is defined as the integral of cloud water content from surface ($p = p_s$) to TOA ($p = 0$) (Eq. 9.30 in Stensrud, 2007), and it can be expressed as follows if hydrostatic equilibrium is assumed:

$$\mathrm{CWP} = \int_{p=0}^{p=p_s} C \cdot w_l \frac{dp}{g}, \tag{4.14}$$

where w_l is the in-cloud liquid water mixing ratio specified in Equation (4.13), C is the cloud fraction within a grid box, g is the acceleration due to gravity and p is the pressure. The global and annual mean CWP in the LS simulation from the linear RH scheme is 142.1 gm^{-2}, which is larger than the observed global mean result (119.3 gm^{-2}, see Table 4.3). As displayed in Figure 4.10, one obvious bias in the spatial pattern in the LS simulation is the overestimation of CWP at high latitudes. For instance, these biases can be even more than 90 gm^{-2} in the polar

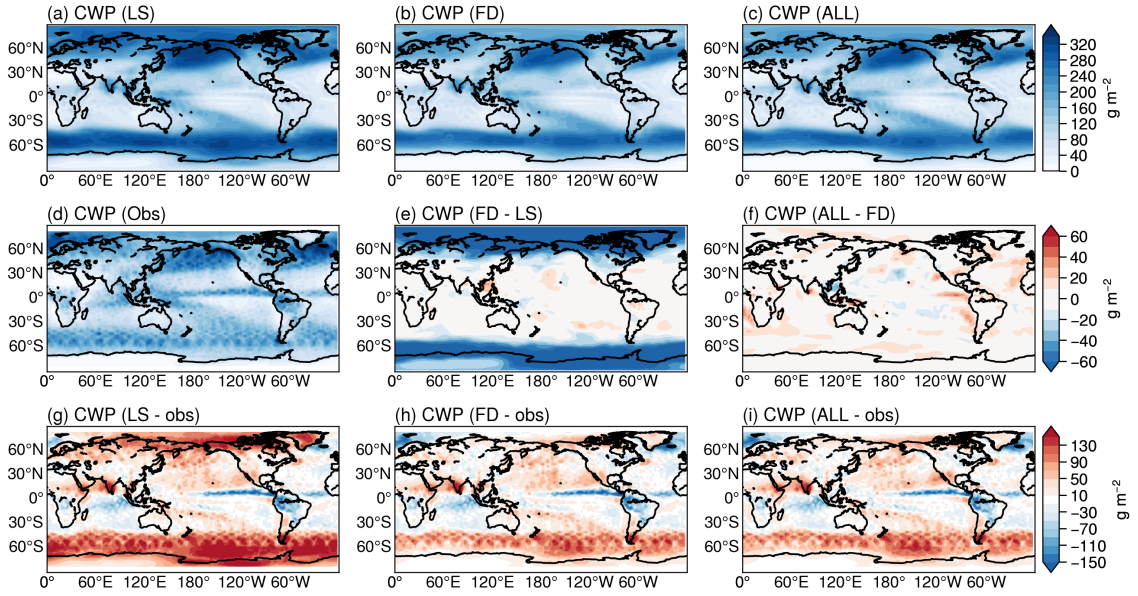

Figure 4.10 The same as Figure 4.8, but for the spatial patterns of total cloud water path (CWP; gm^{-2}). The observed climatology of CWP is derived from the CloudSat data set.

regions (Figures 4.10a and 4.10g). As the simple cloud scheme neglects the ice and mixed phase microphysics, this may contribute to the overestimate of CWP. Such an overestimation is also evident in cloud amount over polar regions (e.g. Figure 4.8g), suggesting that the adjustment of cloud fraction probably reduces the CWP biases there. Indeed, incorporating the freeze-dry method into the simulation produces a large change in the CWP spatial pattern, with a reduction over 60 gm^{-2} over polar regions (Figures 4.10b, 4.10e and 4.10h). The CWP biases off the west coast of continents are reduced in the ALL simulation due to the increase of the low cloud fraction there. For example, the CWP over Peruvian and Californian coasts in the ALL simulation increases at least 20 gm^{-2} when compared to the LS simulation (Figure 4.10e).

4.4.3 Simulated cloud radiative effect

The CRE is defined as the differences in TOA radiative fluxes between clear-sky and all-sky conditions (e.g., Ramanathan et al., 1989; Li et al., 2017). Specifically, the simulated LW CRE is derived from the difference between the outgoing longwave radiation flux under clear-sky and all-sky conditions, and the SW CRE is computed from the difference in reflected SW flux under clear-sky and all-sky conditions. The net CRE is defined as the sum of LW and SW CREs.

Spatial patterns of cloud radiative effect

The global mean SW CRE from the LS simulation is -60.0 Wm^{-2}, which is much larger than the observed value of -45.8 Wm^{-2} from CERES-EBAF (Table 4.3).

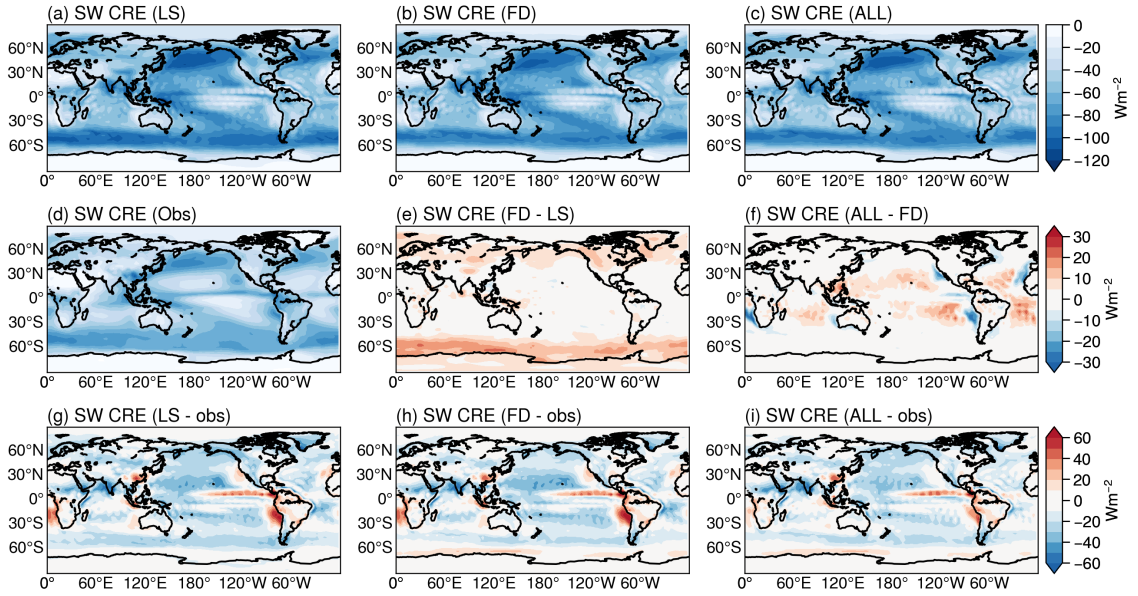

Figure 4.11 The same as Figure 4.8, but for shortwave (SW) cloud radiative effect (CRE) (Wm^{-2}) at TOA. The observed SW CRE is from CERES-EBAF data set.

Compared to the observed SW CRE (Figure 4.11d), the LS simulation can reproduce the general features of spatial patterns (Figure 4.11a), although it fails to grasp some key features. For example, SW CRE is underestimated by over 30 Wm^{-2} in eastern subtropical ocean basins off the west coast of Peru and over 15 Wm^{-2} off the west coast of California (Figure 4.11g), consistent with the insufficient low cloud amounts in these marine stratocumulus areas (Figure 4.8g). These biases also exist in the FD simulation (Figures 4.11b and 4.11h), as the freeze-dry method can only adjust the cloud amount over high latitudes. As shown in sections 4.4.1 and 4.4.2, the low cloud amount and CWP in these regions increase in the ALL simulation, which is thus expected to improve the SW CRE biases. In fact, the differences between the ALL and FD simulations show that the SW CREs reduce by more than 10 Wm^{-2} off the Californian, Peruvian and Namibian coasts (Figure 4.11f). Consequently, the positive biases in SW CRE over eastern subtropical ocean regions are reduced, although some smaller positive biases still remain (Figure 4.11i). The SW CRE biases from the FD and ALL simulations in the five marine stratocumulus clouds regions (defined in Figure 4.5) are quantified in Figure 4.12a. It is clear that these biases are reduced in all the locations, which is closely linked to the increase of low cloud amount over these regions (Figure 4.12b).

Another problem of the SW CRE in the LS simulation is that it is too negative in trade wind cumulus regions, Southern Ocean and northern Pacific Ocean (Figure 4.11g), which is associated with the excessive clouds over these regions (Figure 4.8g). The freeze-dry adjustment has reduced the cloud amount at high latitudes, making the SW CRE in the Southern Ocean less negative compared to the LS

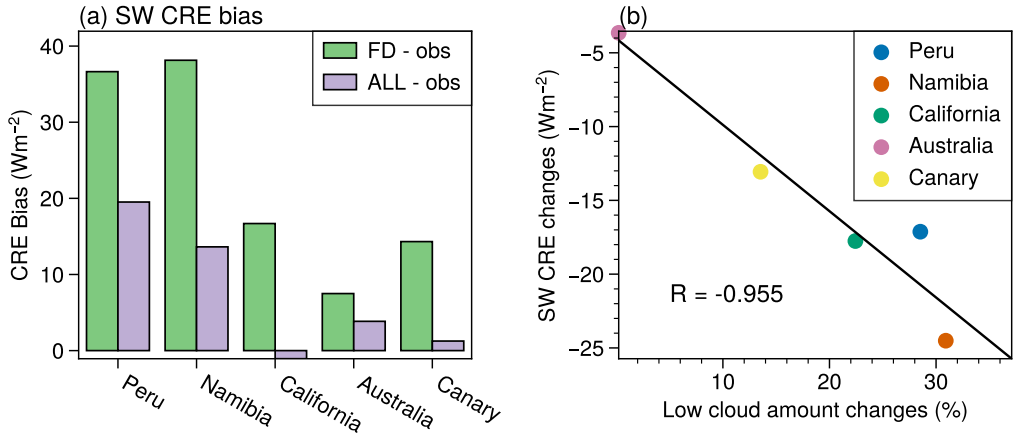

Figure 4.12 (a) The regional mean SW CRE biases from the FD and ALL simulations with with linear RH scheme in five different subtropical ocean regions off the west coast of continents, whose ranges are defined in the caption of Figure 4.5. (b) The relationship of regional mean SW CRE and low cloud amount changes in the FD and ALL simulations, and the changes are calculated as their differences (i.e., ALL-FD).

simulation (Figures 4.11e and 4.11h). In the end, the spatial pattern of SW CRE in the ALL simulation becomes more realistic compared to observations, but we also notice that the global mean SW CRE bias is still about 10 Wm^{-2} compared to the observed value (-45.8 Wm^{-2}) from CERES-EBAF (Table 4.3), implying that some errors still exist in microphysical properties (e.g., effective radius) and/or other processes in the model in addition to the macrophysical properties (e.g., cloud fraction).

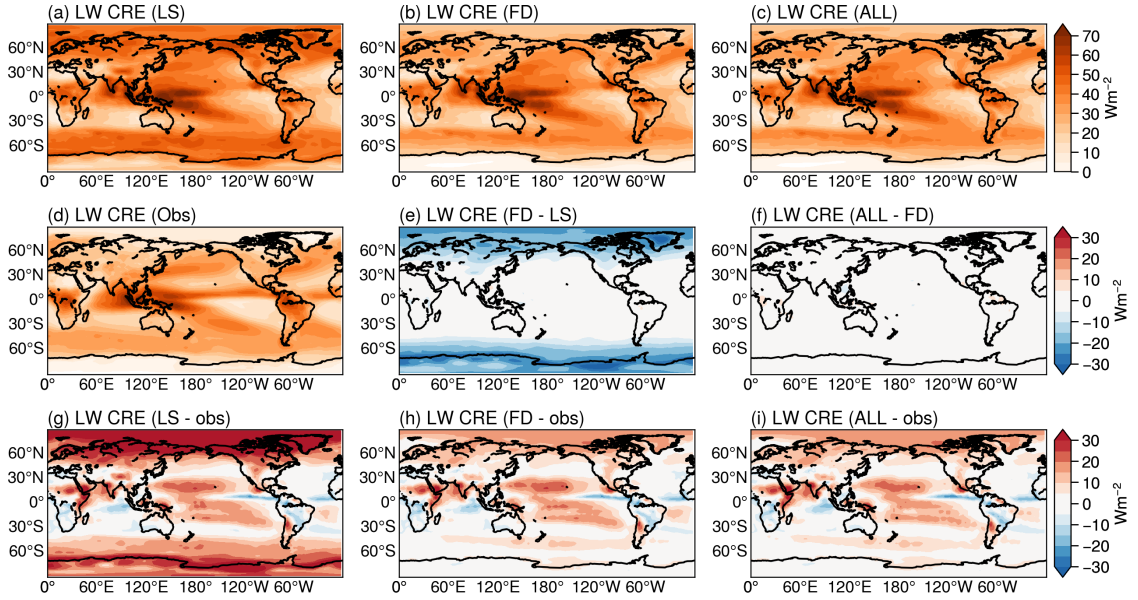

Figure 4.13 The same as Figure 4.11, but for LW CRE (Wm^{-2}) at TOA.

The LS simulation reproduces the general spatial pattern of the observed LW CRE (Figures 4.13a and 4.13d). However, the radiative effect is too strong, especially in the polar regions and also over the subtropical oceans located east of

the maritime continent (Figures 4.13a and 4.13d), which is also illustrated by the positive biases over these regions (Figure 4.13g). The LW CRE in the LS simulation is overestimated by over 30 Wm^{-2} in the Arctic and over 15 Wm^{-2} in the tropical regions. As discussed in previous sections, the cloud fraction, as well as the CWP in polar regions, decreases in the FD simulation compared to the LS run. Therefore, the LW CRE is improved over these regions (Figures 4.13b and 4.13h), where the bias in polar region is reduced by more than 15 Wm^{-2} (Figure 4.13e). Nevertheless, there is still a small positive bias over the Arctic and tropical regions. Compared to the FD simulation, the change in the ALL simulation has little effect on LW CRE (Figure 4.13f). After these improvements, the spatial patterns of LW CRE in the FD and ALL simulations become more similar to the observations, and the global mean CRE drops from 36.8 Wm^{-2} to 31.6 Wm^{-2}, much closer to global mean result from observations (Table 4.3).

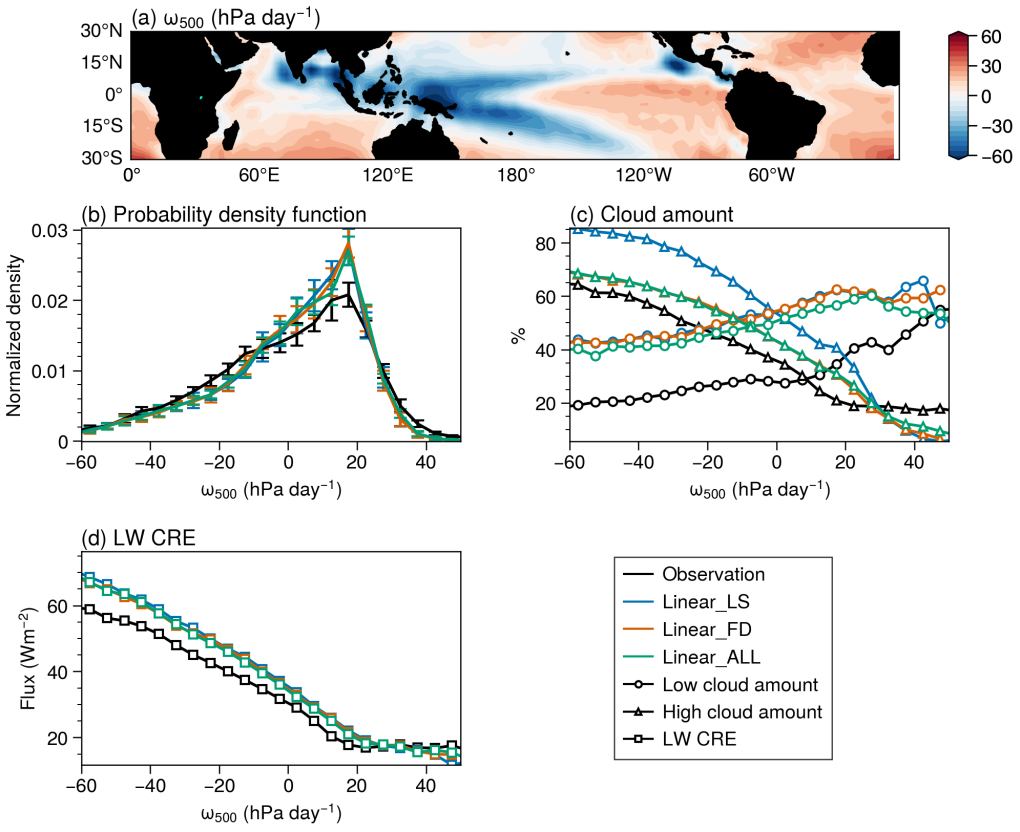

Figure 4.14 (a) The vertical pressure velocity field at 500 hPa (ω_{500}) over tropical oceans between 30°S and 30°N from the linear_LS simulation. (b) The probability density functions (PDFs) of the 500 hPa large-scale vertical velocity (ω_{500}) over the tropical ocean regions defined in (a), where the vertical bars indicate one standard deviation of the annual mean data. (c) The low, high cloud amounts and (d) the TOA LW CRE in different dynamical regimes binned by ω_{500}. The 9-year (2007-2015) observed cloud amounts from CALIPSO-GOCCP and the LW CRE from CERES-EBAF are binned by ω_{500} from ERA-Interim reanalysis data set (black lines). The results from the LS, FD and ALL simulations with the linear RH scheme are represented by blue, orange and green lines, respectively.

To further quantify the simulated LW CRE at TOA over the tropical ocean regions (30°S-30°N), following the method employed in Bony et al. (2004) and Bony and Dufresne (2005), we first define the upwelling and downwelling regimes based on the vertical pressure velocity at 500 hPa (ω_{500}, Figure 4.14a), and then evaluate the LW CRE over these regimes. ω_{500} is a measure of the large-scale atmospheric circulation, where the regions with positive ω_{500} are associated with the subsidence movement, while those with negative ω_{500} are related to large-scale atmospheric ascent. The PDFs of ω_{500} from the ERA-Interim reanalysis and Isca simulations (LS, FD and ALL runs) are displayed in Figure 4.14b. The PDFs of the Isca simulations generally follow the observations, albeit the Isca simulations have fewer weakly ascending regions and more weakly descending regions. The peak values of PDFs are located at 5-20 hPa day^{-1}, consistent with the results from Bony et al. (2004).

Figures 4.14c and 4.14d illustrate the high/low cloud amounts and LW CRE at the TOA over different dynamical regimes over tropical oceans, respectively. The observed cloud amount and LW CRE are from CALIPSO-GOCCP and CERES-EBAF data sets respectively, both covering the period from 2005 to 2014 with the regimes being defined by the ω_{500} from ERA-Interim. The regimes with stronger convective activity, related to the magnitude of ω_{500} in ascending regions ($\omega_{500} < 0$), usually have a larger amount of high clouds and thus stronger LW CREs. All the LW CREs from the three simulations are close to the observed values over the weak upwelling and subsidence regions. However, the LW CREs from the LS simulation deviate from the observations in strong ascending regions ($\omega_{500} < -20$ hPa day^{-1}). Furthermore, this discrepancy increases with the magnitude of ω_{500} in ascending regions ($\omega_{500} < 0$). It is noted that the large biases of LW CRE over ascending regions is reduced slightly in the FD and ALL simulations, associated with the decrease of high clouds over those regimes (Figure 4.14c). However, the positive biases still exist at the strong convection regions.

Finally, the spatial patterns of net CRE at the TOA are presented in Figure 4.15, where we can see that the positive biases in the LS simulation mainly occur in the polar regions and subtropical eastern ocean regions. There are also small negative biases in subtropical and extratropical regions. The positive biases in net CRE in the LS simulation are related to the cloud amount biases in these regions, as we have seen in the SW and LW CRE fields. Clearly, the biases in polar regions are reduced greatly in the FD simulations (Figures 4.15b, 4.15e and 4.15h) due to the freeze-dry method. Additionally, the positive biases off the west coasts of continents in subtropics can be mitigated in the ALL simulation (Figure 4.15i), making the spatial pattern closer to CERES-EBAF, although there are still slight positive biases in polar regions.

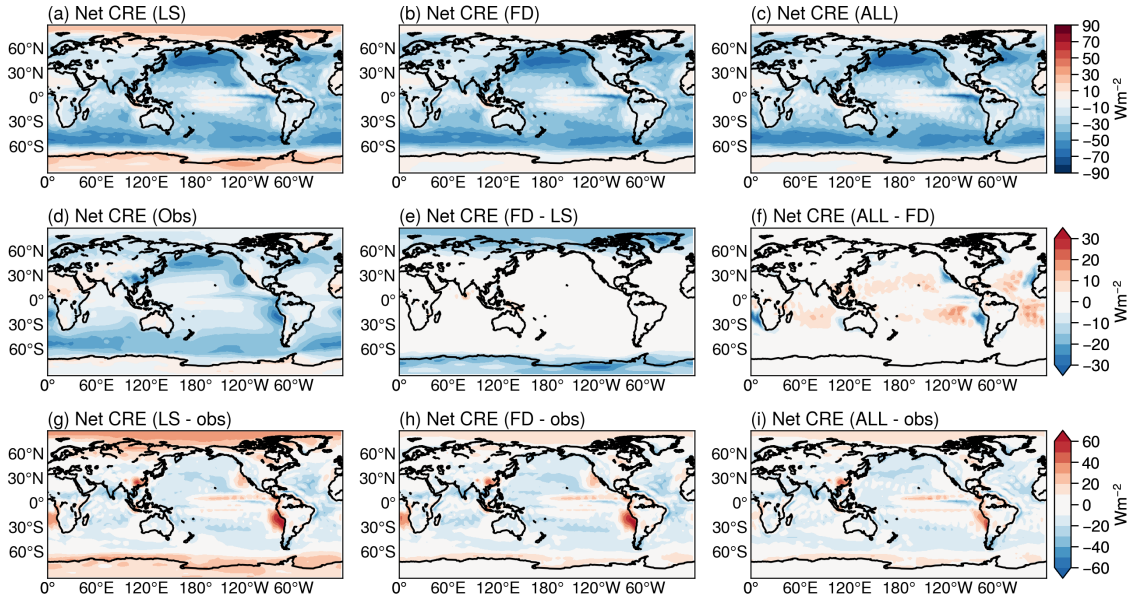

Figure 4.15 The same as Figure 4.11, but for net CRE (Wm^{-2}) at TOA.

Zonal mean structure

To further study their latitudinal variations, the zonally averaged SW, LW and net CREs from Isca simulations, CMIP5 simulations, satellite observation and reanalysis data set are shown in Figure 4.16. For the SW CRE (Figure 4.16a), the general latitudinal variations can be captured by all the Isca simulations, but the magnitude is larger than observations. The largest discrepancy in the LS simulations occurs in the mid-latitudes, especially in the Southern hemisphere, which is likely arising from the excessive cloud amount over these regions (Figure 4.8g). The improvement of cloud amount biases in the FD and ALL simulations contributes to the improvement of SW CRE over the extratropics. However, the difference of zonal mean SW CREs between the FD and ALL simulations is small, although the SW CRE biases over eastern subtropical ocean regions are reduced in the ALL run (Figure 4.11f). In addition, the remaining SW CRE biases, as well as the low cloud amount biases, in the ALL simulation over the subtropics and extratropics might be alleviated by an 'omega correction', namely a reduction of the low cloud fraction if subsidence is strong (e.g., Gordon, 1992), but the effects are mixed and we do not include that process in these results.

The LS simulations with both the linear RH and Sundqvist schemes agree well with observations of LW CRE at low latitudes (Figure 4.16b). However, there are large discrepancies from observation in the mid to high latitudes, which is consistent with the large biases of cloud amount at high latitudes (Figures 4.7d and 4.7g). It is striking that these biases can be largely reduced through the freeze-dry adjustment, as the LW CREs agree much better with the observation at high latitudes in the FD and ALL simulations. The remaining deviation from observation in Isca simulations over the Arctic region is possibly associated with the simple

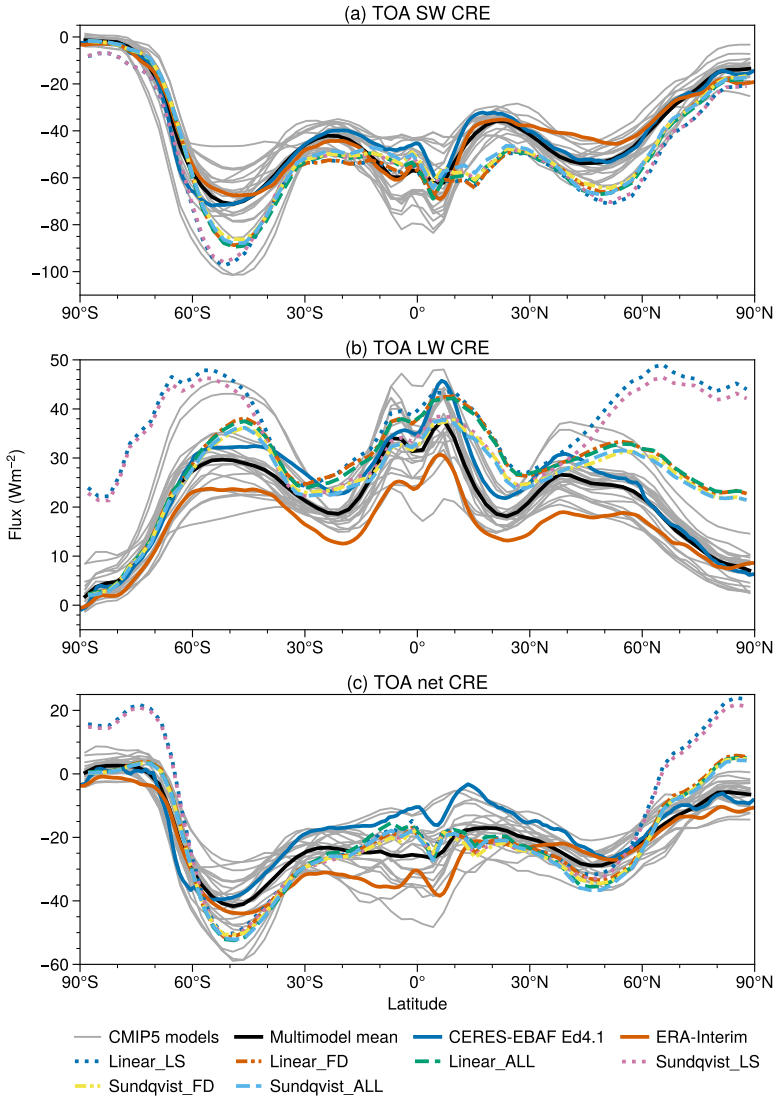

Figure 4.16 Zonally averaged distribution of the TOA (a) SW, (b) LW and (c) net CREs from CERES-EBAF Ed4.1 (blue solid line), ERA-Interim reanalysis (orange solid line), CMIP5 models (thin gray solid lines for each model and black solid line for multimodel mean) and different Isca simulations (dashed/dotted color lines, listed in legend).

sea ice setup in our model. Likewise, the disagreement between zonal mean net CRE at high latitudes between the LS run and the observations almost disappears in the FD and ALL runs (Figure 4.16c).

In addition, compared to the zonal mean variation of the SW, LW and net CREs from CMIP5 models, the Isca simulations are generally located within the spread of the CMIP5 simulations at each latitude, except the LW and net CREs over high latitudes in the LS simulations (Figures 4.16b and 4.16c). These biases are alleviated in the FD and ALL simulations, although there are still some discrepancies over the Arctic regions.

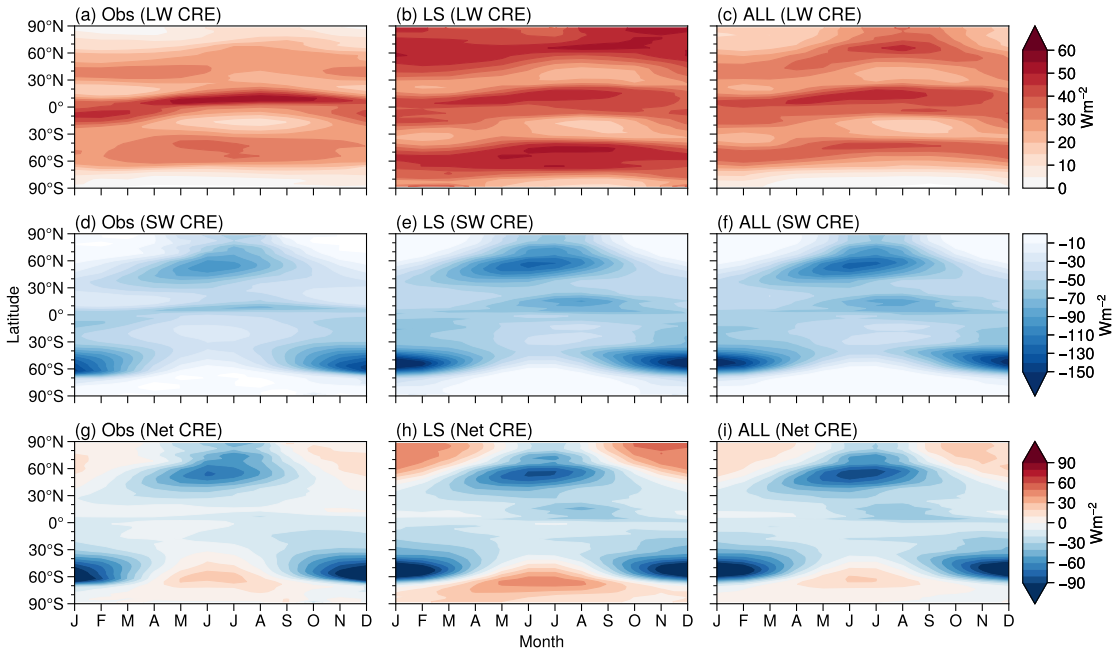

Figure 4.17 The zonal mean annual cycle of TOA LW (top), SW (middle) and net (bottom) CREs from observation (CERES-EBAF), LS and ALL simulations with the linear RH scheme in Isca.

Seasonal cycle

The zonal mean seasonal cycles of CRE from CERES-EBAF and Isca simulations (LS and ALL) with the linear RH scheme are displayed in Figure 4.17. In the Arctic region, the observed LW CRE is weak during boreal winter and early spring, and has a maximum in summer (Figure 4.17a). The simulated LW CRE tends to be overestimated throughout the year in the LS run (Figure 4.17b), but the biases are alleviated by the freeze-dry adjustment (in the ALL run), particularly in winter (also see Figure 4.9), leading to an overall improvement in the representation of the high-latitude seasonal cycle of the CRE. The existing problem for the seasonal cycle of LW CRE is that the band in the tropical region is too broad compared to the observations, which might relate to the too-broad high cloud pattern in the tropical and subtropical regions (see Figure 4.7f). The seasonal cycle of SW CRE in the LS simulation is realistic, except that it is too strong during boreal summer near 60°N (Figures 4.17d and 4.17e). This effect is slightly mitigated in the ALL simulation (4.17f) because of the improvement of cloud amount. Similar to the LW CRE, the positive biases of net CRE in winter over polar regions are also alleviated due to the improvement of LW CRE in winter (Figures 4.17h and 4.17i). In summary, the seasonal cycles of LW, SW and net CREs in simulations with freeze-dry and inversion-based adjustments compare well to observations (left and right columns of Figure 4.17), indicating that the cloud scheme does reproduce a reasonably realistic seasonal cycle of CRE.

4.4.4 Comparison with CMIP5 models

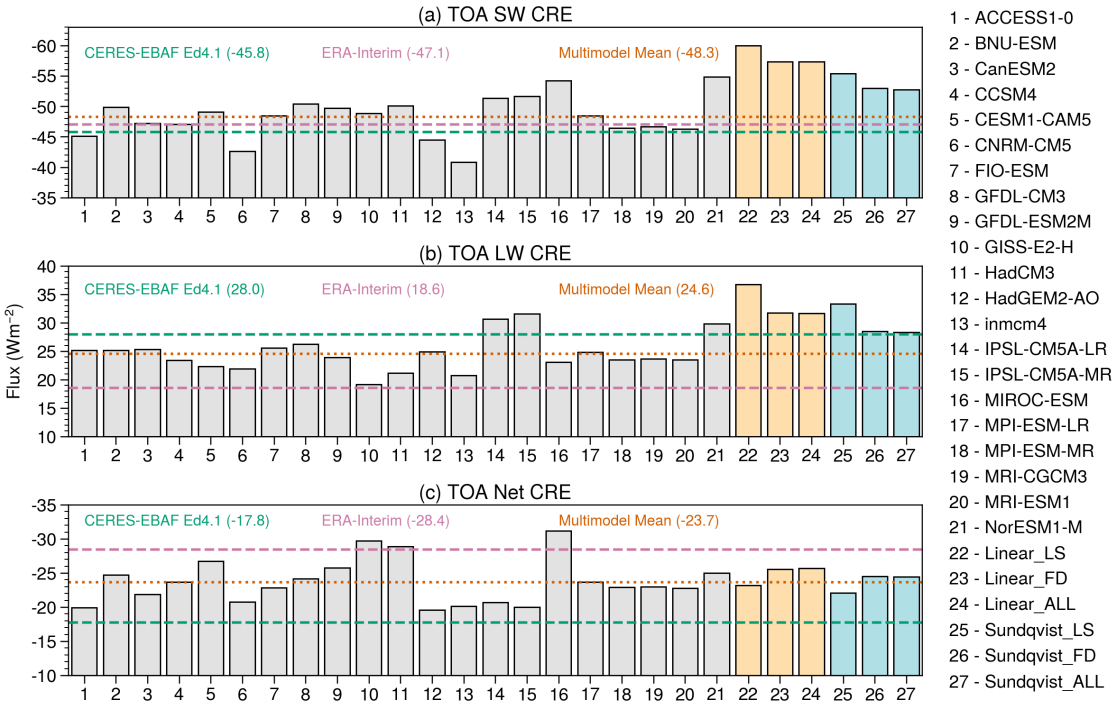

Figure 4.18 Globally averaged TOA (a) shortwave (SW), (b) longwave (LW) and (c) net cloud radiative effects (CREs, Wm^{-2}) from 21 CMIP5 models historical runs (1996-2005, gray bars) and Isca simulations with different setups (orange bars for linear scheme and cyan bars for the Sundqvist scheme). The horizontal lines are annual and global mean CREs from CERES-EBAF (green dashed lines, covering from 2001 to 2018) and the multimodel ensemble mean results (orange dotted lines) of CMIP5 models, whose names are listed on right for reference.

To evaluate the simulated CREs further, Isca simulations are compared with CMIP5 models. Figure 4.18 shows the global mean TOA SW, LW and net CREs from 21 CMIP5 models and Isca simulations with different cloud scheme setups. The observed SW CREs from CERES-EBAF and the multimodel mean of CMIP5 models are -45.8 Wm^{-2} and -48.3 Wm^{-2} respectively. While the multimodel mean SW CRE shows small difference from the observation, the spread among these CMIP5 models is large. Compared to the observation and CMIP5 models, the global mean SW CREs from the LS simulations with the linear RH and Sundqvist schemes are too strong, but they are more realistic in the FD and ALL simulations. With all components of our simple cloud scheme (ALL simulation), the global mean values are -57.3 and -52.8 Wm^{-2} for linear RH and Sundqvist schemes respectively, which are fairly close to the observed and multimodel mean values. The changes of LW CRE from the LS to ALL simulations are similar to SW CRE, where the LW CRE drops from 36.8 to 31.6 Wm^{-2} for linear RH scheme and decreases from 33.3 to 28.3 Wm^{-2} for the Sundqvist scheme, making the results from the simple cloud scheme closer to observations. These changes are likely due to the

decrease of cloud fraction and cloud liquid water path discussed in sections 4.4.1 and 4.4.2. The net CREs from all the Isca simulations are in a range that are comparable to the CMIP5 models, which are close to the multimodel mean but still over 6 Wm^{-2} larger than CERES-EBAF in magnitude.

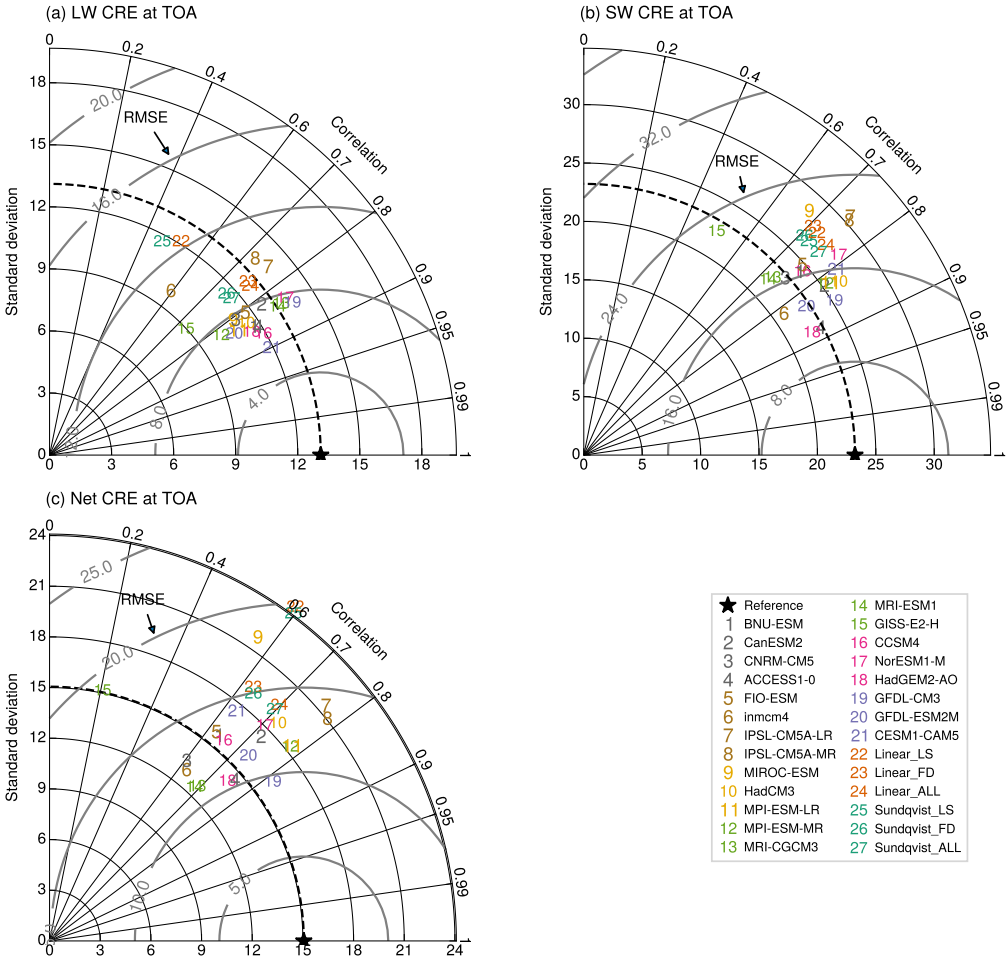

Figure 4.19 Taylor diagrams showing standard deviation (Wm^{-2}), root mean square error (RMSE; Wm^{-2}) and spatial pattern correlation for the observed and simulated (a) LW, (b) SW and (c) net CREs at TOA in CMIP5 models and Isca simulations (LS, FD and ALL). The statistics of these variables are calculated based on annual mean data, where the monthly data (1996-2005) from historical simulation is used for analysis of CMIP5 models. The observed field is as a reference and denoted by a black star. Contour of the standard deviation from observed field is shown by the black dashed line and contours of RMSE are displayed in gray with labels.

We can also use a Taylor diagram (Taylor, 2001) to compare Isca with other models, as this summarizes the standard deviation, pattern correlation and root mean square error (RMSE) in a single plot. Figure 4.19 shows the statistics of the observed and simulated LW, SW and net CREs from CMIP5 historical simulations (1996-2005) and Isca simulations. Compared to CMIP5 models, the LS runs from both the linear and Sundqvist schemes display large RMSEs and low spatial correlations for LW CRE field (Figure 4.19a), likely a consequence of too much cloud

Table 4.4 Global and annual mean climatology from parameter sensitivity tests. In each test, only the parameter listed in the table header (see Table 4.1) is changed from the default values. The units for cloud effective radius (r_e) and in-cloud liquid water mixing ratio (w_l) are μm and g kg^{-1} respectively.

	default	$r_{e\_\text{liq}} = 16$	$r_{e\_\text{liq}} = 12$	$r_{e\_\text{ice}} = 30$	$w_{l0} = 0.15$
TOA net SW flux (Wm^{-2})	230.6	240.3	234.7	238.9	241.4
TOA net LW flux (Wm^{-2})	227.1	229.0	228.6	229.8	229.7
TOA net flux (Wm^{-2})	3.6	11.3	6.0	9.1	11.7
TOA SW CRE (Wm^{-2})	-57.3	-47.8	-53.3	-49.1	-46.6
TOA LW CRE (Wm^{-2})	31.6	30.2	30.3	29.3	29.5
TOA net CRE (Wm^{-2})	-25.7	-17.5	-23.0	-19.7	-17.1
Cloud water path (gm^{-2})	127.8	116.3	116.2	115.4	96.4

in polar regions. Similarly, the net CREs in the LS runs also show larger RMSEs and standard deviations than most CMIP5 models (Figure 4.19c). The FD and ALL simulations improve matters: going from the LS to FD simulations the RMSE decreases from 12.1 to 9.0 Wm^{-2} and from 18.6 to 14.5 Wm^{-2} for LW and net CREs respectively. For the SW CREs (Figure 4.19b), compared to the LS runs, the RMSEs in the ALL runs have decreased slightly in both linear and Sundqvist schemes. By these metrics, the simple cloud scheme is performing similarly to a number of CMIP5 models.

4.4.5 Parameter sensitivity of the scheme

Thus far we have largely selected the various parameter values using observations. In order to test the sensitivity to these choices, a small number of simulations with different parameters are conducted. The simulations analyzed here are run for ten years and the last five years are used for analysis.

The parameters used in the simulation are the default values introduced previously; that is, the effective radii for liquid and ice clouds particles are $r_{e\_\text{liq}} = 14$ and $r_{e\_\text{ice}} = 25$ μm respectively, and the maximum in-cloud liquid water content one grid box can reach is $w_{l0} = 0.18$ g kg^{-1}. As displayed in Table 4.4, changing the value of the effective radius for liquid clouds has little impact on LW flux and CRE at TOA, but has a large impact on those fields associated with the SW flux. For instance, the net SW flux at TOA has reduced (increased) by about 4.1 Wm^{-2} (9.7 Wm^{-2}) when the effective radius of liquid cloud decreases (increases) from 14 μm to 12 μm (16 μm), which can be explained by the relationship between effective radius (r_e) and shortwave optical depth (τ) of clouds, as shown in Equation

(4.10), where LWP is the liquid water path of clouds (Stephens, 1978; Morcrette and Fouquart, 1986). Specifically, if the liquid water path remains unchanged, then τ increases (decreases) with the decrease (increase) of r_e (e.g., Slingo and Schrecker, 1982), implying that the reflected SW flux would increase (decrease), the net SW flux at TOA would decrease (increase) and the SW CRE would get more (less) negative.

As introduced in Section 4.2.2, ice clouds are treated as liquid clouds, except that the effective radius is different. Thus the increase of effective radius of ice clouds has a similar effect of the increase of effective radius of liquid clouds, resulting in the increase of net SW flux and less negative SW CRE at the TOA (see the fourth column in Table 4.4). However, what is different is that tuning the effective radius of ice clouds can also influence the LW related flux and CRE, as the ice clouds are usually located at high levels.

In addition, when decreasing the maximum value of in-cloud water mixing ratio that a grid box can reach (i.e., w_{l0}) from 0.18 g kg^{-1} to 0.15 g kg^{-1}, the global mean LWP decreases over 30 gm^{-2} (last column in Table 4.4). In this case, if the r_e is unchanged, then τ would decrease in response to the decrease of LWP. Hence, the atmosphere becomes less opaque, which has an opposite effect of reducing r_e and thus the net SW flux at TOA increases and the SW CRE becomes less negative. Therefore, these parameters can be used to adjust the radiative properties associated with SW. We note that tuning w_l can also impact LW radiative fluxes.

As mentioned in Section 4.2.1, the coefficient a in the linear scheme is related to the critical relative humidity. Therefore, the parameter a_s in Equation (4.2), which is related to the critical relative humidity at lower levels, can be used to tune the SW CRE. Changing the parameter a_t in Equation (4.2), which determines the coefficient profile (and the critical relative humidity) at high levels, impacts both the LW and SW CRE (the results not shown here). In general, all the parameters associated with the critical relative humidity (a_s or a_t), effective radius and cloud liquid water content can be used to tune the SW and LW CREs, and users can determine which one to use based on their research purpose.

4.5 Discussion and conclusions

In this chapter, the performance of the simple cloud scheme was evaluated in AMIP-type fixed-SST simulations under the Isca framework (Vallis et al., 2018). Prior to the implementation of this simple cloud scheme, Isca did not have a cloud scheme. By adding a simple cloud scheme to Isca, the simulated radiative properties is improved.

Simulations with large-scale clouds only (LS simulation) show that this method does capture the basic features of spatial patterns of cloud fraction and CREs at

TOA. Using the linear relation connecting cloud fraction to relative humidity gives similar results to those from the Sundqvist et al. (1989) scheme (which uses a square root dependency). However, both relative-humidity schemes were found to have two deficiencies. The first is that the cloud cover is generally too high in the high latitudes, especially over polar regions, which in turn leads to an overestimated CRE over these regions. These biases can be found not only in annual mean spatial patterns, but also in the seasonal cycles. The second issue is the underestimation of cloud fractions, and hence the SW and net CREs, in the marine stratocumulus regions off the west coast of continents; this has also been a long standing problem in CMIP3 and CMIP5 models (Dolinar et al., 2015).

In order to mitigate the biases of extra clouds over polar regions, a modified freeze-dry method from Vavrus and Waliser (2008) may be used, in which the cloud fractions over high latitudes are adjusted by a function of specific humidity. With this method, the seasonal cycle of cloud fraction over Arctic was found to be well simulated and the cloud fraction is more realistic, especially in winter. The improvement of the cloud fraction over high latitudes also decreases the CRE biases, contributing to the improvement of the seasonal cycle of LW CREs. We should note that in this adjustment the specific humidity threshold are derived according to current climate, but whether the threshold holds under global warming still needs further investigation. To alleviate the problem of the low cloud biases, a diagnostic low cloud scheme based on the estimated low-level cloud fraction (ELF) from Park and Shin (2019) was implemented, as the ELF shows a good linear relationship with low cloud fraction in the reanalysis data set. The simulation with both large-scale clouds and low clouds (the ALL simulation) reduced the SW and net CRE biases off the west continental regions over subtropics, by increasing both the cloud fraction and the cloud water path.

In summary, many of the basic features of observed cloud fraction and cloud radiative properties are captured by the cloud scheme. Using a simple cloud scheme, Isca is able to reasonably reproduce the observed spatial and temporal variability of clouds, comparable to a number of CMIP5 models that use more complicated schemes. This suggests that a simple cloud scheme might be suitable to study problems related to cloud feedback and cloud-circulation coupling. In addition, the scheme is relatively flexible and many aspects are optional or user-configurable, so the users can decide which one to use as per their own research interests or purposes. For example, if the users do not focus on the polar regions, they can omit the freeze-dry adjustment.

Certainly, the scheme has deficiencies. For example, the SW CREs are still a little weak off the west coast of continents and too strong over the extratropics compared to observations. The global mean CREs, including the LW and SW CREs, are too strong, and the TOA radiation imbalance is rather large compared

to the observations, which perhaps could be solved by further improvements of the cloud scheme, for example by including the microphysical processes. It should be noted that in addition to the cloud scheme, other physical processes such as precipitation are also important components in GCMs, and the improvements in these processes can also help to reduce GCM biases. For example, the incorporation of prognostic precipitation scheme in MIROC6-SPRINTARS model (Michibata et al., 2019) has improved some systematic biases in both the magnitude of aerosol-cloud interactions and in rain formation processes with more realistic cloud and radiation fields, indicating that the process-based model development is also important to help us better understand the climate system.

Finally, at a more general level, the diagnostic scheme presented here does not vary with model resolution and so is not 'scale aware'. Whereas this may be perfectly appropriate at low and modest resolutions, it would fail as the model resolution increases, for the distribution of relative humidity varies according to the resolution, and so the functional dependence of cloud fraction should properly be a function of grid size. This drawback is not, however, unique to our scheme. It could be overcome at an empirical level by re-tuning the coefficients as resolution changes. We have not found this to be an issue in practice at the resolutions we have used. If desired, it may be possible to address this using a more sophisticated treatment of the distribution properties of humidity, with the width of the moisture distribution, and hence the critical value of relative humidity, then becoming a function of grid size and/or being dynamically determined. Separate schemes to take into account the low-level inversion and polar effects would then ideally not be needed. It would also be of interest to further simplify the scheme so that it could, for example, be coupled to simpler (e.g., semi-gray) radiation schemes with less complicated treatments of scattering and absorption and which might be more appropriate for very different climate regimes. These are topics for future work.

Chapter 5

Simulated Cloud Feedbacks and Their Uncertainties

In Chapter 4, we introduced how the simple cloud scheme is constructed, and evaluated the simulated climatology when it is implemented in Isca. The simulations have shown that it can grasp the basic features of cloud climatology. In this chapter, the simulated cloud feedbacks under global warming are to be examined. Also, based on this simple cloud scheme, a series of perturbed parameter ensemble (PPE) experiments is carried out to investigate whether they can 'reproduce' the intermodel spread of cloud feedbacks among the Coupled Model Intercomparison Project (CMIP) models. Then the sensitivities of the corresponding parameters, components and processes are analyzed. The cloud controlling factor analysis is employed to identify the possible causes of the cloud response uncertainty under global warming. Finally, the implications for equilibrium climate sensitivity (ECS) are discussed.

The major findings of this chapter are:

1. The simple cloud scheme can capture the two positive cloud feedbacks found in the CMIP models, low cloud amount feedback and high cloud altitude feedback, but could not grasp the negative optical depth feedback in the Southern Ocean region, as the mixed-phase clouds are not explicitly represented in the scheme.

2. In the Isca PPE simulations, the low cloud amount feedback is the largest single contributor to the spread of global mean net cloud feedback, consistent with the conclusion drawn from CMIP models. For the regional contributions, the tropical low clouds over the subsidence region are at the heart of tropical cloud feedback uncertainties in the Isca PPE simulations.

3. The cloud controlling factor analysis suggests that the sea surface temperature (SST) and estimated inversion strength (EIS) have opposite effects on

marine low cloud amounts, but their responses to SST rather than EIS seem to bring larger uncertainty.

4. The perturbation related to marine low clouds produces the largest cloud feedback and ECS. At the same time, ECS and tropical cloud feedback over subsidence regimes show a robust linear relationship in the Isca PPE simulations and the models from sixth phase of the CMIP (CMIP6), suggesting that range of ECS perhaps can be constrained by these cloud feedbacks.

5.1 Introduction

As introduced in Chapter 1 and Chapter 4, clouds heat the Earth by absorbing and re-emitting the longwave radiation, and cool the Earth by reflecting the incoming solar radiation, the so called cloud radiative effect. In total, the net radiative effect of clouds is to cool the Earth at a magnitude about 20 Wm^2 (Figure 1.6). But the problem about how the cloud radiative effect would change under global warming (i.e., cloud feedback) has haunted the climate community for decades. For example, in early 1990s, Cess et al. (1990) evaluated the climate feedback processes in 19 Atmospheric General Circulation Models (AGCMs), and found that the broad spectrum of cloud feedbacks (from modest negative to strong positive) is the consequence of the models' different responses to sea surface temperature warming. Also, models may have similar responses if their net cloud feedbacks are similar, despite large difference in their compensating solar or infrared components. Later, an updated analysis from Cess et al. (1996) suggests that these AGCMs have moderate net cloud feedbacks compared to their predecessors, and the changes can be traced to different treatments of clouds in the respective models. In addition, the spread of the shortwave and longwave cloud feedback components in these AGCMs is still substantial, indicating that the models still have physical disagreements (Cess et al., 1996). Other studies such as Colman (2003), Webb et al. (2006) and Vial et al. (2013) also concluded that differences in cloud feedback make a large contribution to differences in climate sensitivity in general circulation models (GCMs). In recent CMIP6 models, the mutli-model mean net cloud feedback is positive (see Figure 1.3; Zelinka et al., 2020), meaning that the cloud would warm the planet as the planet warms. Nevertheless, the cloud feedback still has the largest uncertainty among all the climate feedback parameters, remaining the leading cause for the intermodel spread of ECS in climate models (Zelinka et al., 2020; Sherwood et al., 2020).

Over the years, the climate community has been focusing on understanding the underlying causes of the spread in cloud feedbacks among the models, and trying to reduce such spread so as to minimize the potential range of ECS. As

the frequencies of occurrence of different cloud types are unequal both in observation and models (e.g., Zhang et al., 2005), the behavior of certain clouds may matter than that of others in explaining the range of cloud feedbacks among models (Bony et al., 2006). For example, Wyant et al. (2006) showed that the responses of deep convective clouds and of low-level clouds differ among climate models. Furthermore, previous studies suggested that among all the cloud feedbacks, the tropical low cloud feedback is regarded as the major contributor to the intermodel spread (e.g., Bony and Dufresne, 2005; Webb et al., 2006; Webb and Lock, 2013; Vial et al., 2013; Zelinka et al., 2016). In a pioneering work from Bony and Dufresne (2005), the tropical ocean region was decomposed into different dynamical regimes by vertical velocity with the method proposed by Bony et al. (2004), showing that the cloud radiative effects differ most in the subsidence regimes among CMIP3 models, suggesting a dominant role of low clouds in driving the spread of tropical cloud feedbacks. Webb et al. (2006) also confirmed the role of low clouds by analyzing the cloud feedbacks in the doubling-CO_2 slab-ocean experiments from nine Cloud Feedback Model Intercomparison Project (CFMIP) models, and found that differences in cloud feedbacks in low cloud areas make the largest contribution to the spread in the global feedback. The findings are also confirmed in CMIP5 models. For instance, Vial et al. (2013) quantified the intermodel spread of climate sensitivity and decomposed it into contributions from individual adjustments and feedbacks, and into regional contributions (i.e., tropical, mid-latitude and polar regions). They estimated that about 70% of the intermodel spread in climate sensitivity stems from cloud feedbacks, among which tropical region plays the largest role. After breaking down the tropical changes into dynamical and thermodynamical components (method from Bony et al., 2004), they found the thermodynamic component is in fact the major source of the spread in tropical cloud feedbacks. In recent years, Zelinka et al. (2012a,b) proposed a refined decomposition of cloud feedbacks, the so called 'cloud radiative kernel method' (to be described in detail later; also in Section 2.4), in which the cloud feedback can be decomposed into cloud amount, altitude and optical depth feedbacks. Through this method, Zelinka et al. (2016) identified that low cloud amount feedback is the single largest contributor to the spread in net cloud feedback, although the non-low clouds also play certain roles in driving the spread of cloud feedbacks.

To understand the underlying causes for the spread of cloud feedbacks, we need to quantify the cloud feedbacks first, which is the necessary basis for the future analysis. As introduced in Section 2.4, several approaches have been used previously to calculate the cloud feedbacks in GCMs. The idea of these methods is to quantify the change of cloud radiative effect in response to unit change of global mean surface temperature. The intuitive way is to calculate the change

of cloud radiative effect under control and perturbed experiments, and normalize the changes by the global mean surface air temperature (e.g., Cess et al., 1990, 1996). However, this may be not an accurate estimate of the change of cloud radiative effect, as the non-cloud induced changes are also included (e.g., Soden et al., 2004). Of course, the so called cloud-masking effect can be removed using the all-sky and clear-sky radiative kernels (Details in Section 2.4; Shell et al., 2008). In addition, as pointed out by Soden et al. (2008) and Vial et al. (2013), this method in fact can reflect the spread of cloud feedbacks although the magnitude or sign may not be reasonable, and that is why it is still widely used in recent studies (e.g., Webb et al., 2015). Another possible problem of this approach is that it can obtain the total changes of cloud radiative fluxes at the top of the atmosphere (TOA), but could not identify from which type of clouds that these radiative fluxes changes arise. As the cloud location and optical properties (e.g., thin or thick) are essential to understand the possible changes in cloud longwave and shortwave radiative effects. Another type of approach employed in previous studies are the partial radiative perturbation (PRP) method (Wetherald and Manabe, 1988) and its variations such as two-way PRP (e.g., Colman and McAvaney, 1997) and radiative kernel method (e.g., Soden et al., 2008; Shell et al., 2008; Huang et al., 2017; Pendergrass et al., 2018; Smith et al., 2020). This kind of method quantifies the partial derivative of TOA radiation flux with respect model parameters such as temperature, water vapor and clouds. The traditional PRP method is quite computationally expensive, while the radiative kernel method can calculate the kernels in advance and be applied to many different GCM situations. The method is useful to decompose the climate feedbacks explicitly into various components, and can help us evaluate the cloud feedback alone (e.g., Soden et al., 2004; Soden and Held, 2006; Soden et al., 2008). Taking the masking effect into consideration, one can get the longwave and shortwave parts of cloud feedback from the radiative kernel method (e.g., Soden et al., 2008; Caldwell et al., 2016), but it is hard to decompose the cloud feedback further into refined constituents, as the radiative kernels provided by some GCMs such as Community Atmosphere Model version 5 (CAM5; Pendergrass et al., 2018) and Hadley Centre Global Environment Model version 3 (HadGEM3; Smith et al., 2020) are limited to all-sky and clear-sky temperature and water vapor, and surface albedo kernels. Of course, one can generate such kernels for cloud water and other components, but it is not easy to implement, which is a limitation of this approach. In recent years, a new technique called cloud radiative kernel method is proposed by Zelinka et al. (2012a,b), which can be regarded as a variation of PRP method applied to the joint histogram of cloud top pressure and optical depth from the International Satellite Cloud Climatology Project (ISCCP) simulator (Klein and Jakob, 1999; Webb et al., 2001). With this approach, the TOA radiative flux changes can be attributed to specific

cloud types, and can be partitioned into specific changes in amount, altitude and optical depth. Moreover, as the kernel is derived from the cloud related fields only, the calculation is not impacted by clear-sky changes that are irrelevant to cloud feedback, so the derived TOA flux changes are due to the change of clouds only. It has been shown that this refined decomposition can provide some insights for understanding the spread of cloud feedbacks in GCMs (e.g., Zelinka et al., 2016, 2020, 2021).

The cloud feedback calculation and decomposition methods mentioned above are used to answer the first question that we are going to explore in this chapter, that is whether the simple cloud scheme described in Chapter 4 could grasp the key mechanisms of cloud feedbacks. The results in Chapter 4 show that this simple cloud scheme could grasp a relatively reasonable cloud climatology, but as pointed out by Zelinka et al. (2021) that, better simulation of mean-state cloud properties does not necessarily guarantee the better simulation of cloud feedbacks. Thereby, the performance of the simple cloud scheme in simulating the cloud feedbacks are to be evaluated in this chapter and compared to CMIP5/6 GCMs and the expert assessments from Sherwood et al. (2020).

Another question is whether we could reproduce a certain level of spread in cloud feedback by perturbing a series of physical parameters in the simple cloud scheme. The PPE is a widely used method to understand the uncertainty of GCMs. For example, Murphy et al. (2004) performed a systematic attempt to determine the range of climate sensitivity based on a 53-member ensemble of model versions constructed by varying the subset of all the model physical parameters. Webb et al. (2013) investigated the origins of differences in climate sensitivity, forcing and climate feedbacks with the multi-model ensemble of CMIP3 models and 15 perturbed parameter ensemble members of HadGEM3 slab model, and they found that the cloud feedback uncertainty has a role about twice that of cloud forcing in determining the spread of climate sensitivity, and the low latitude ocean region contributes more than other areas. Inspired by these results, here we also seek to examine the uncertainty of cloud feedbacks by varying the physical parameters in the Isca model, and the only difference is that our perturbation is limited to the cloud scheme, while the parameters from other physical processes such as convection are kept unchanged. In doing so, we expect the spread of cloud feedback would be smaller compared to the intermodel range of CMIP models, and also likely smaller than the PPEs in which parameters from all the physical schemes are perturbed, but it could be easier for us to identify which parameter or process in the cloud scheme is most sensitive. Moreover, if the PPE of Isca simulations can produce a certain spread of cloud feedbacks, what are the underlying causes for this uncertainty? Are they similar to those of CMIP models? What are the implications for the ECS ranges? These are the problems we need to answer

through the PPE results in this chapter.

The outline of this chapter is as follows. Section 5.2 describes the basic simulation setups in this chapter, including the implementation of the observation satellite simulator package, the perturbed physics ensemble in Isca, and how the Q-flux is prescribed in the simulations. In Section 5.3, the behaviors of the satellite simulator is examined to make sure it is correctly implemented. In Section 5.4, changes in basic fields such as temperature and relative humidity under global warming are evaluated first to make sure their responses are relatively reasonable (Section 5.4.1). Then based on the satellite simulator outputs and the cloud radiative kernel method, several different methods to compute cloud feedbacks are compared in Section 5.4.2 to determine which manner to be employed in this study, which is also the basis for the future analysis. Next, we present the simulated spatial pattern (Section 5.4.3) and zonal mean structures (Section 5.4.4) of the cloud feedbacks from Isca PPE simulations, and explain the possible mechanisms for these feedbacks. Also, parts of the cloud feedback components are evaluated against the expert assessment based on multi-line evidence from Sherwood et al. (2020), and the reasons for the agreement and disagreement with these expert assessments are analyzed in Section 5.4.5. The spread of cloud feedbacks from PPE of Isca simulations and the underlying causes for the spread are investigated in Section 5.5. In this section, at first the global mean longwave, shortwave and net cloud feedbacks and their components decomposed by altitude and types are examined in Section 5.5.1, and the relative contributions of these components to spread of net cloud feedbacks are quantified. In addition to the global mean results, the regional contributions to the spread of cloud feedback are quantified in Section 5.5.2, and the possible reasons are explored by the cloud controlling factor analysis in Section 5.5.3. Finally, the relationship between cloud feedback and the equilibrium climate sensitivity is investigated briefly in Section 5.6.

5.2 Simulation setup

5.2.1 Implementation of the COSP

As introduced in Section 2.4.4, one possible way to calculate the cloud feedback is to use the cloud radiative kernel (Zelinka et al., 2012a,b), in which the joint-histogram between cloud top pressure and optical depth from ISCCP cloud simulator (Klein and Jakob, 1999; Webb et al., 2001) is needed. One can simply estimate the cloud feedback by the change of cloud radiative effect between control and perturbed experiments, but it also includes the masking effect of climatological cloudiness on non-cloud feedbacks (Soden et al., 2004). In addition, combining the histogram outputs from ISCCP cloud simulator with the cloud radiative kernel,

one can decompose the cloud feedback into different altitudes and different components (Zelinka et al., 2012b, 2016), which is a helpful tool for us to understand the causes of spread in multi-model spread of cloud feedback. As mentioned in Section 4, the cloud simulator has not previousl previously been implemented in Isca, and we could not employ the cloud radiative kernel method to calculate and decompose cloud feedback without it. Thus in this section, we try to implement the cloud simulator in Isca first in order for a refined look into cloud feedback.

As introduced in Chapter 2, the CFMIP Observational Simulator Package (COSP) version 2 (Swales et al., 2018) is a kind of diagnostic code applied to model variables, aiming to reduce the inconsistencies between the ways clouds are observed by satellites and the ways they are simulated in models (Bodas-Salcedo et al., 2011). From the satellite simulator, one can obtain what a satellite would retrieve if the atmosphere had the clouds of the model in the real world. In addition, it also facilitates intercomparison among GCMs by minimizing the impacts of how clouds are parameterized in models (e.g. Klein et al., 2013). The extremely thin clouds (i.e., $\tau < 0.3$) are excluded in the COSP analysis, as the models usually disagree largely with ISCCP observation in this category. One possible reason for this is the impact of the thin clouds on TOA radiation budget is usually difficult to detect by the passive sensors from the ISCCP satellites (Klein et al., 2013).

One key diagnostic output to be acquired from the COSP is the joint histogram of cloud-top pressure (CTP) and optical depth (*clisccp* in CFMIP variables). In the current setup, the histogram segments are first obtained separately for each CTP category (7 in total), and then the whole histogram is derived directly by concatenating these segments, as they are independent to each other. In the AMIP-type simulations or the ones performed with Q-flux (to be introduced in Section 5.2.2), the COSP is only run for the last five years, and the ISCCP simulator is enabled alone as its outputs are what we need here to calculate the cloud feedbacks. Note that the COSP is always active only in one simulation to get the kernel-derived cloud-induced radiation anomalies, so as to calculate cloud feedback through the Gregory (2004) method (see bottom right category of Table 5.2). The performance of the COSP is examined in Section 5.3.

5.2.2 Perturbed parameter ensemble

As introduced in Section 5.1, the PPE is a possible way to explore the sensitivity of a GCM and examine the plausible spread of climate feedbacks, so it is adopted in this chapter to investigate the possible uncertainty of cloud feedbacks simulated from the simple cloud scheme constructed in Chapter 4. Specifically, a subset of parameters of the simple cloud scheme (see Table 4.1) is perturbed to get the members of the PPE in Isca. There are many different options to vary the parameters to get the parameter space, but only one parameter is varied each

time in our current perturbation. The perturbed parameters are listed in Table 5.1.

Table 5.1 Design of the perturbed parameter experiments (PPEs). All simulations are run in T42 horizontal resolution.

Index	Experiment	Parameter change	Description
1	linear	Default values in Table 4.1	Simulations with Q-flux; Control ($1\times CO_2$) and perturbed ($4\times CO_2$) experiments
2	a_surf_20	a_s : 42 → 20	Equivalent to decrease the critical relative humidity at the surface
3	a_top_10	a_t : 13 → 10	Equivalent to decrease the critical relative humidity at the upper troposphere
4	sc_park_b_m0.3	c : −0.1 → −0.3	The added stratocumulus clouds should decrease
5	sc_park_a_1	b : 1.3 → 1	The added stratocumulus clouds should decrease
6	Tmax_0	T_{max} : −5 → 0 °C	Increase the temperature threshold of the fraction of liquid cloud (Reff would increase)
7	Tmin_m35	T_{min} : −40 → −35 °C	Increase the temperature threshold of the fraction of ice cloud
8	reffice_50	r_{e_ice} : 25 → 50 μm	Increase the default effective radius for ice cloud
9	reffliq_12	r_{e_liq} : 14 → 12 μm	Decrease the default effective radius for liquid cloud
10	freezedry	On	Use the freezedry method
11	sundqvist	On	Change the default cloud fraction scheme from linear to Sundqvist
12	qcl_T_0.2	$w_{l0} = 0.2$	Increase the maximum of in-cloud water mixing ratio a box can reach

The default parameters in Table 4.1 are used for the control run (*linear* in Table 5.1, but the freezedry adjustment introduced in Section 4.2.1 is turned off. We do this for two reasons: First, the low-latitude regions usually contribute most to the spread of global mean cloud feedbacks, as suggested from previous studies and as to be shown later in Section 5.5.2, and the simulated cloud radiative effect in low and middle latitudes is fine without this adjustment. Therefore, keeping the schemes used in the study to a minimalism does not have large impact on the study of spread of cloud feedback. Second, the 'freezedry' adjustment works well for the current climate (see Figure 4.16), but still needs some tests before it can be applied readily to the warming experiments. The perturbations for the cloud scheme alter either the cloud amount or cloud optical properties, as both are necessary components for radiation transfer calculation. Specifically, four experiments (i.e., *a_surf_20*, *a_top_10*, *sc_park_a_1* and *sc_park_b_m0.3*) listed in Table 5.1 are directly associated with the cloud amount, where *a_surf_20* and *a_top_10* adjust the cloud amount in large-scale cloud scheme (see Section 4.2.1), while *sc_park_a_1* and *sc_park_b_m0.3* have impacts on the correspond-

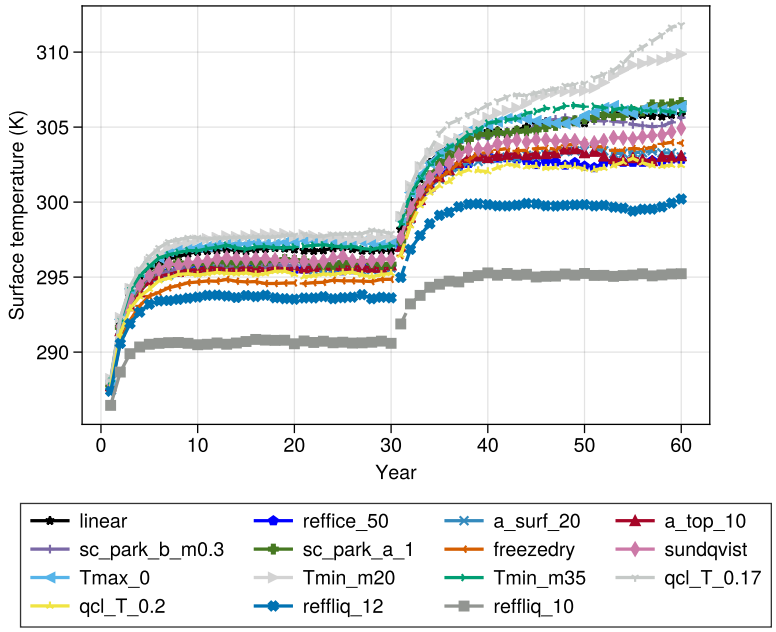

Figure 5.1 The simulated surface temperature from all the Isca perturbed parameter ensemble runs, both for control (CO_2 is 300 ppm; first 30 years) and 4×CO_2 (1200 ppm; last 30 years) runs. The perturbed parameters include the ones that are not used in the final analysis (see Table 5.1).

ing marine low cloud amount (see Section 4.2.1). The perturbed parameter in the *sundqvist* experiment is also related to the possible changes in large-scale cloud amount. The other perturbed parameters or corresponding experiments are associated directly with the optical properties of clouds, and these properties are altered by effective radius of cloud condensate (i.e., *reffice_50* and *reffliq_12*), temperature thresholds for liquid or ice water fraction (i.e. *Tmax_0* and *Tmin_m35*) or the maximum in-cloud water mixing ratio a box can reach (i.e. *qcl_T_0.2*). Of course, these perturbations could have impact on cloud amount once the background condition evolves. The *freezedry* experiment is also examined here for completeness, which can modify the behaviors of the cloud scheme over high-latitude regions.

For each simulation with perturbed parameter, two runs are performed: one with CO_2 level similar to current climate (300 ppm; control run for each parameter), and the other with quadruple CO_2 (1200 ppm; perturbed run for each parameter). The control run is performed for 30 years, and as mentioned in Section 5.2.1, the COSP is only active in the last 5 years. On the basis of the control run, the perturbed run is performed for another 30 years with CO_2 concentration quadrupled. Similarly, the satellite simulator is only enabled for the last 5 years in perturbed run. The spinup usually takes about 10 years to finish in both runs. Other Isca setups, such as the convection scheme, large-scale condensation scheme and radiation scheme, are the same as those described in Section 4.3. The only difference is that the simulations in Chapter 4 are the AMIP-type

fixed-SST experiments, while here the ocean heat flux (the 'Q-flux') is prescribed. In the fixed-SST experiments, the changes in atmosphere could not feedback into the SST changes, but the Q-flux can make the simulation more realistic, as SST can respond to forcing changes (see Figure 5.1). Here we prescribe the derived 'Q-flux' from a given distribution of SSTs (Durack et al., 2018) following the method from Russell et al. (1985), so that the SST can respond freely to the CO_2 forcing. The detailed description of how Q-flux is calculated can be found in Section 2.2.4.

As a final note of this section, the perturbation strategy for the parameters is discussed briefly as follows. As shown in Figure 5.1, beyond the perturbed values in Table 5.1, some parameters are also perturbed in a larger range, but the basic states (surface temperature) of control simulations changed a lot, or the global warming simulations could not reach new balances, so they are not included in the final ensemble. For example, when the liquid cloud effective radius r_{e_liq} is perturbed to 10 μm (default is 14 μm), the global mean surface temperature is about 5 K lower than most simulations, as indicated by label *reffliq_10* in Figure 5.1. In addition, when the in-cloud liquid water content related parameter w_{l0} in Equation (4.13) uses 0.17 g kg^{-1}, or the liquid cloud fraction related variable $T_{\min}$ in Equation (4.11) uses -20°C, we find the simulations (*Tmin_m20* and *qcl_T_0.17*) under 4×CO_2 could not reach new balances. Therefore, both perturbations are not included in the final ensemble. Note that the surface temperature in both runs is also higher than the majority of simulations in the first 30 years (i.e., control runs), because the cloud optical depth from both runs decreases under the perturbations according to Equation (4.10). We have kept the *reffliq_12* run in the PPE, as when r_{e_liq} is perturbed to 12 μm, its surface temperature in control run is much closer to the other runs and could reach new balance under global warming, although the surface temperature under global warming simulation has a gap from other runs (Note the gap is nearly halved compared to the *reffliq_10* run).

5.3 COSP evaluation

The implementation of COSP provides a new tool to compare Isca simulation results with observations. For the Isca simulation with COSP, only ISCCP simulator (Klein and Jakob, 1999; Webb et al., 2001) is activated. One key output from ISCCP simulator is the joint histogram of cloud-top pressure and optical depth, as shown in Figure 5.2a, which bins the cloud fields into seven CTP and seven optical depth categories. The value in each bin represents the cloud fraction of that category. To make sure the COSP is correctly implemented in Isca, the diagnostics from COSP are compared to the native Isca outputs. Specifically, following the method from Zelinka et al. (2012a) and Klein et al. (2013), the sum of cloud cover over all bins of the joint histogram (Figure 5.2 b) is compared with the diag-

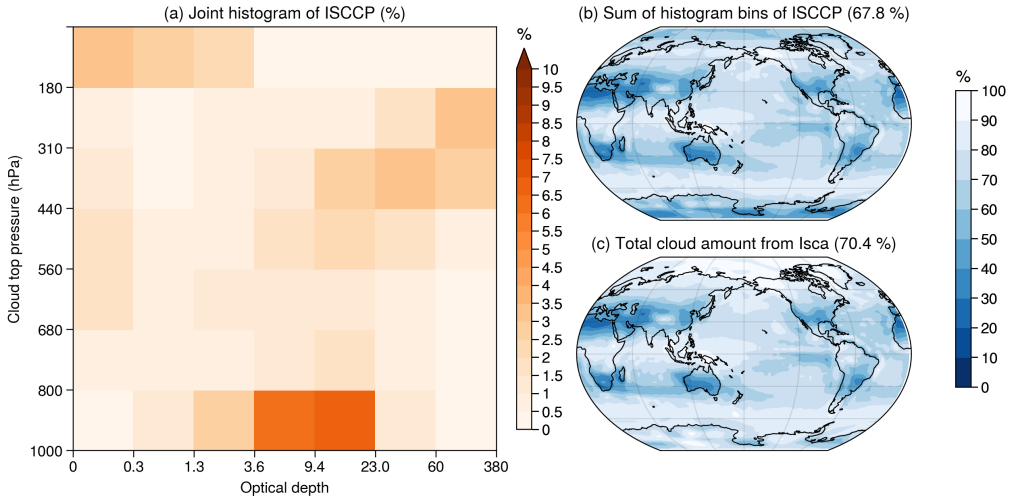

Figure 5.2 (a) The annual mean cloud fraction (%) binned by the joint histogram of cloud top pressure and optical depth from ISCCP simulator implemented in Isca. (b) The sum of the histogram bins for each location from the ISCCP simulator of Isca. (c) The annual mean native total cloud amount from Isca simulations based on max-random overlap assumption.

nostic of total cloud cover (Figure 5.2 c) from Isca that is computed without using the ISCCP simulator. It is noted that the global mean values of the two cloud covers are quite close, and the spatial patterns also match with each other, although we notice that some discrepancies appear over polar regions. This comparison suggests that the COSP is correctly implemented in Isca, and its output can be employed for the later analysis.

Here we also compared the ISCCP simulator outputs from Isca with observation directly. The Isca simulation is run with Q-flux with linear and low cloud scheme (shown in Table 5.1), while the observed cloud amount frequency distribution product is derived from the ISCCP D1 data set (Rossow and Schiffer, 1999) (available at `https://climserv.ipsl.polytechnique.fr/cfmip-obs/data/ISCCP`, last access: June 10, 2021), which is binned into six optical thickness categories, and each of these bins is further divided into seven cloud-top pressure groups. As shown in Figure 5.3, the annual mean cloud frequency from GCM simulator-oriented ISCCP product (covering the period from 1998 to 2007; top panels) and Isca simulation (bottom panels) is compared by sorting them into categories of different optical depth, namely thin ($0.3 \leq \tau < 3.6$), intermediate ($3.6 \leq \tau < 23$), thick ($\tau \geq 23$), and and all optical depths. As this comparison is for the tropical region (30°S–30°N) only, we further break them down into different dynamic regimes by vertical velocity at 500 hPa (ω_{500}), similar to Wyant et al. (2006) (see their Figs. 7–9). The observed ISCCP product is binned by ω_{500} from ERA-Interim reanalysis of the same period. In ISCCP observation product, the thin clouds (Figure 5.3a) are a major contributor to the total cloud fraction (Figure 5.3d) at all heights and all the dynamic regimes, especially near the surface over the subsidence regions

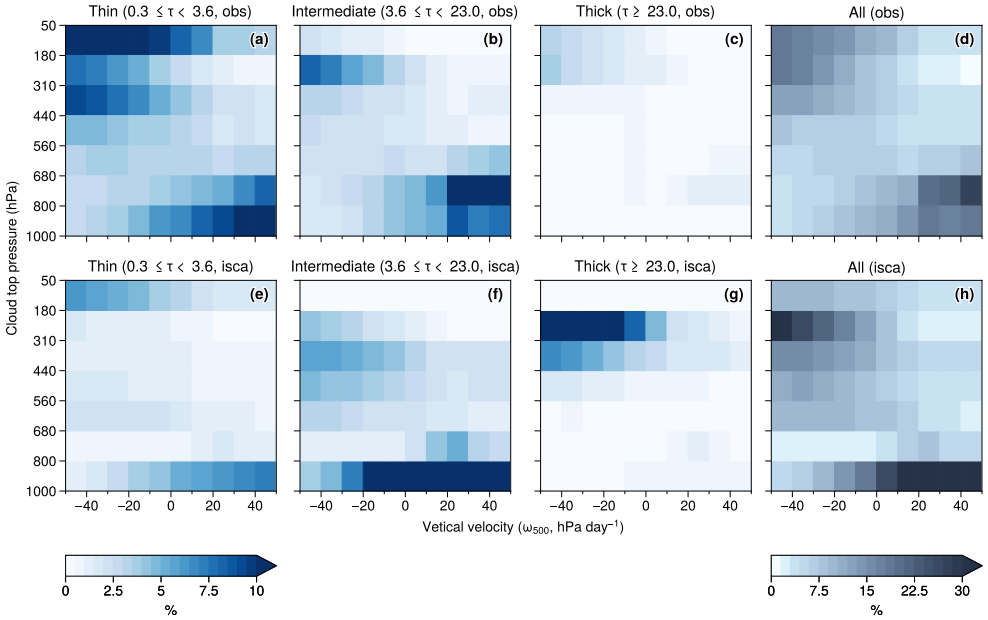

Figure 5.3 Annual mean cloud frequency from (top row) GCM simulator-oriented ISCCP product (1998-2007) and (bottom row) one Isca simulation, sorted by vertical velocity at 500 hPa (ω_{500}, units: hPa day^{-1}) and divided into different cloud thickness categories: (a, e) thin ($0.3 \leq \tau < 3.6$), (b, f) intermediate ($3.6 \leq \tau < 23$), (c, g) thick ($\tau \geq 23$), and (d, h) all optical depths. For ISCCP, the ω_{500} is from ERA-Interim reanalysis (1998-2007).

and in the upper troposphere over the ascent regimes. The intermediate clouds (Figure 5.3b) are prevalent at the similar locations as the thin clouds, but the levels of maximum cloud fraction is different. The fraction of thick clouds (Figure 5.3c) is the smallest among the three categories, and they are concentrated at the upper troposphere of ascending regions. Compared to the observation, the simulator diagnostics from Isca have have less thin clouds both in the upper troposphere of upwelling region and in the lower troposphere of the subsidence regimes (Figure 5.3e). With regard to the intermediate clouds, the Isca diagnostics have a very similar pattern to observations, except that clouds concentrate near the bottom of CTP-bins over the subsidence regimes (Figure 5.3f). The thick cloud fraction is overestimated in Isca at the ascent regimes near the tropopause (Figure 5.3g). In total, Isca diagnostics have qualitatively similar CTP and optical depth histograms to observations (Figure 5.3h), though the biases mentioned in the thin, intermediate and thick categories. These results suggest again that the COSP has run successfully in Isca.

5.4 Simulated cloud feedbacks

One goal of this chapter is to investigate the underlying causes of the uncertainty in cloud feedbacks, but the first step is to evaluate the cloud feedbacks from Isca simulations. Therefore, this section is arranged as follows: the simulated basic

fields, such as temperature, relative humidity and cloud-related variables such as cloud fraction and cloud water content, and their possible changes under global warming in Isca simulations are examined in Section 5.4.1, which could help us to understand the possible mechanisms of cloud feedback. The different diagnostics and methods that could be employed for the cloud feedback computation are compared in Section 5.4.2 and from this section we will conclude which method and diagnostic to be used for the future cloud feedback analysis. The spatial pattern and zonal mean structure of cloud feedbacks and their components are presented in Section 5.4.3 and Section 5.4.4, respectively. Parts of the cloud feedback components from Isca simulations are compared with the expert assessment in Section 5.4.5.

5.4.1 Basic fields

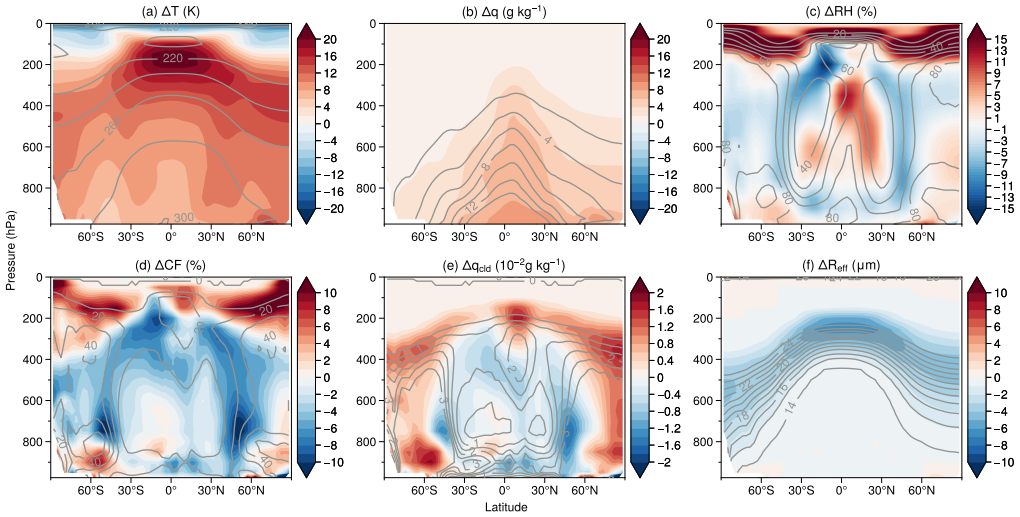

Figure 5.4 Zonal mean profiles (contour) for (a) temperature, (b) specific humidity, (c) relative humidity, (d) cloud fraction, (e) cloud water content and (f) effective radius and their responses (shading) to warming due to quadruple of CO_2 from Isca perturbed parameter ensemble.

The mean and range of simulations of both present-day zonal mean profiles of some basic fields and their responses to global warming are exhibited in Figure 5.4). Focusing on the cloud fraction (Figure 5.4d), the ensemble mean results show an upward shift of clouds near the tropopause, and a decrease in clouds in most of the troposphere (cf. Fig. 5a of Sherwood et al. 2020). The changes in cloud fraction field basically reflect the changes in relative humidity (Figure 5.4c) (also see Fig. 2 of Sherwood et al., 2010), although there are some discrepancies in the tropical and subtropical regions. This is a problem of the relative humidity based cloud scheme, as it is possible that the relative humidity increases but the diagnosed cloud fraction decreases, if the increased relative humidity is still less

than the threshold for the cloud formation (e.g., Ming and Held, 2018). The fraction of liquid cloud fraction increases under global warming, so the effective radius, which is the weighted sum of liquid and ice cloud effective radii based on their each fraction, decreases accordingly (Figure 5.4f).

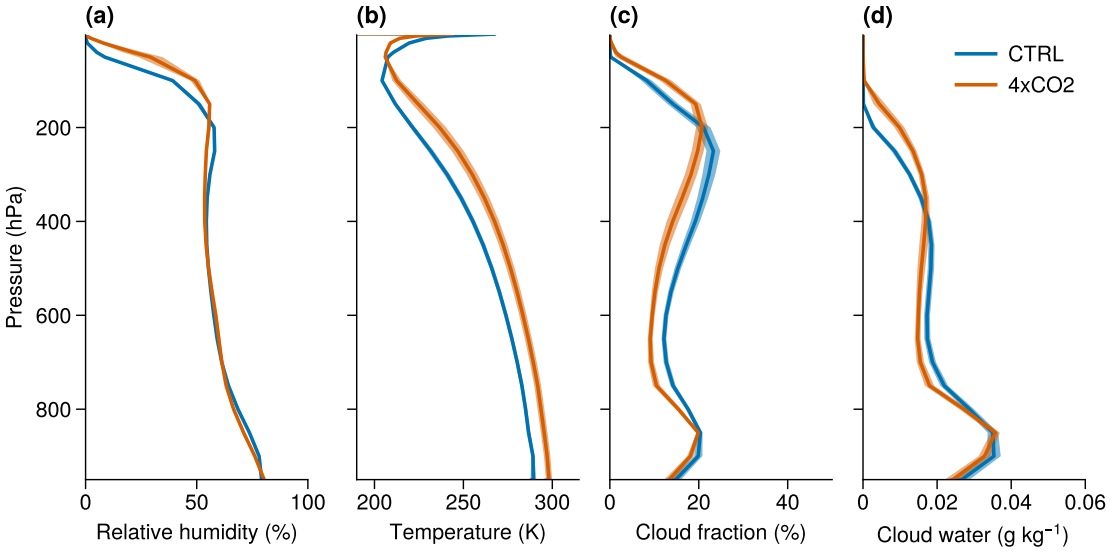

Figure 5.5 The ensemble and global mean profiles for (a) relative humidity, (b) temperature, (c) cloud fraction and (d) cloud water content in control ($1\times CO_2$) and global warming ($4\times CO_2$) experiments in Isca perturbed parameter ensemble.

To have a clear look at the changes of the simulated fields under global warming in Isca simulations, the ensemble and global mean profiles from the PPE are shown in Figure 5.5. There is a clear reduction of cloud fraction in the lower and middle troposphere and an upward shift of cloud fraction at the upper troposphere in the global warming experiment of Isca (Figure 5.5c). The latter change can be inferred from the relative humidity changes under global warming (Figure 5.5a), but we also notice that there are some discrepancies in the middle troposphere between the relative humidity and cloud fraction fields, as shown in Figure 5.4. The cloud water content changes under global warming in Figure 5.5d follow the changes in cloud fraction field. All these changes could assist us in understanding the changes in cloud radiative effect under global warming (i.e., cloud feedback) in Section 5.4.3.

5.4.2 Comparison of cloud feedback calculation

One goal of this chapter is to evaluate the cloud feedbacks from Isca simulations. The methods used in previous studies to estimate cloud feedback are introduced in Section 2.4, including the estimation from cloud radiative effect (CRE; i.e. the all-sky minus clear-sky downward radiative flux at TOA) and the PRP method. An alternative to the PRP method is the kernel method, which is more efficient than

the PRP method, and can be widely used among different models (Soden and Held, 2006; Soden et al., 2008). The traditional radiative kernel method can account for the masking effect of clouds via the difference between the all-sky and clear-sky kernels when calculating the cloud feedback, but it is hard to decompose the bulk cloud feedback into different components. The cloud kernel method proposed by Zelinka et al. (2012a,b) calculates the cloud feedback in the space of the ISCCP joint histogram of CTP and cloud optical depth, which facilitates the diagnosis of cloud changes consistently across the different models and can track the cloud feedback to the changes in cloud altitude, amount or optical thickness, and thus to different cloud types (Siebesma et al., 2020).

Here we compute and compare the cloud feedback from Isca simulations with various diagnostics and methods. As summarized by Zelinka et al. (2013a) (see their Table 1), based on the CRE or the kernel derived cloud-induced radiation anomalies diagnostics, there still two ways using them to estimate the cloud feedback. One is to calculate the cloud feedback by normalizing the CRE or cloud-induced radiation anomalies by the change of surface temperature between perturbed and control simulations; The other is to use the Gregory method (Gregory, 2004), which regresses the time series of radiation anomalies against the surface temperature changes and the slope is the feedback we wanted. The advantage of the Gregory method is that it accounts for the rapid adjustments, which is usually considered as part of radiative forcing (Andrews et al., 2012a; Siebesma et al., 2020). In addition, the CRE based diagnostic is affected by the cloud masking effect, while the cloud-induced radiation anomalies derived from cloud radiative kernel method is not affected by the masking effect (Zelinka et al., 2013a).

Figure 5.6 shows the Gregory plot of the global and annual mean anomalies in cloud-induced TOA radiative flux against the change in global mean surface temperature (ΔT_s). These flux anomalies are estimated from CRE and cloud radiative kernel respectively, so they are corresponding to II and IV categories in Table 5.2. The cloud-induced radiative flux anomalies at TOA (ΔR_C) is computed as follows:

$$\Delta R_C = \sum_{p=1}^{7} \sum_{\tau=1}^{7} \left(K_{p\tau} \Delta C_{p\tau} \right), \tag{5.1}$$

where $K_{p\tau}$ is the cloud radiative kernel at each CTP-optical depth bin of ISCCP histogram, in which both the CTP and optical depth (τ) categories have 7 bins. In this calculation, the cloud radiative kernels are multiplied by changes in ISCCP simulator-diagnosed cloud fraction $\Delta C_{p\tau}$ between a perturbed and control climate and summed over all CTP and optical depth categories. It is clear that there is a sign change in the slope of longwave cloud feedback (Figure 5.6a), where the slope changed from -0.25 $Wm^{-2}K^{-1}$ in category II (CRE + Gregory) to 0.42 $Wm^{-2}K^{-1}$ in category IV (kernel + Gregory). The longwave forcing term in

category II is more negative than that in category IV due to the cloud masking effect. For example, Andrews et al. (2012a) found that the instantaneous cloud masking effect for longwave CRE is about -0.62 Wm^{-2} in response to doubling CO_2 (see their Table 2). Similarly, Soden et al. (2004) got a better estimation of cloud longwave feedback by assuming the cloud-masking effect is uniform and about 0.69 Wm^{-2}.

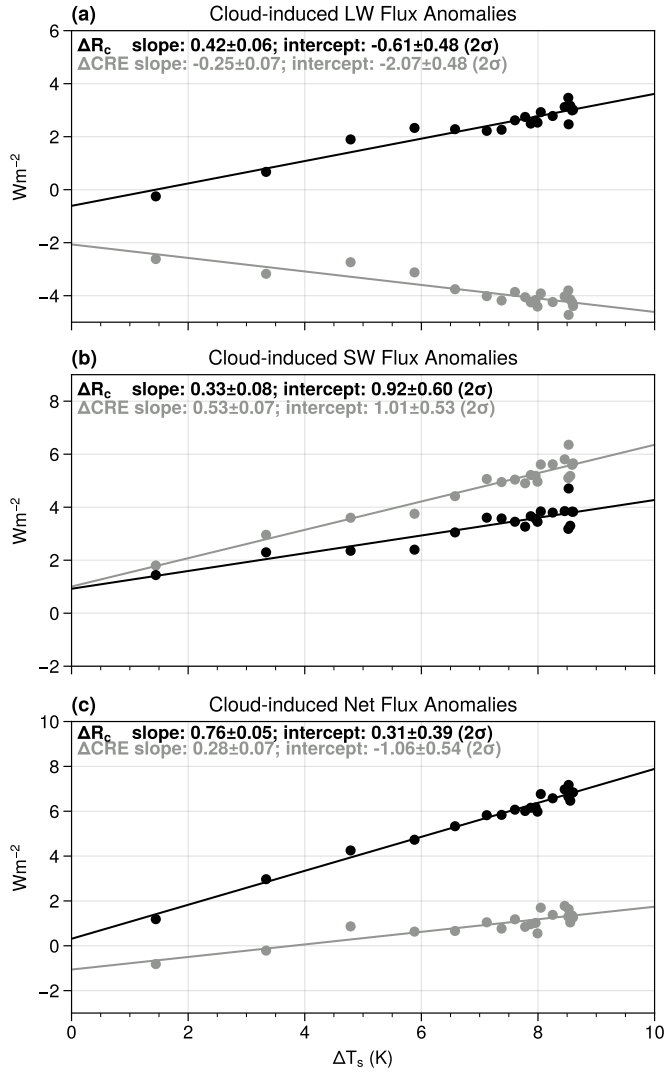

Figure 5.6 Global and annual mean anomalies in cloud-induced TOA (a) longwave (LW), (b) shortwave (SW) and (c) net radiative flux against global mean surface temperature change (ΔT_s). The black dots and lines are fluxes derived from cloud radiative kernel method (Zelinka et al., 2012a), while the gray ones are for the cloud radiative effect (CRE).

The cloud feedback is also calculated by the change of CRE directly, as shown in the categories I and III in Table 5.2. Focusing on the second row (the radiative kernel based diagnostic), we can find that the cloud feedback parameters from the categories III and IV are very similar, indicating that neglecting the rapid cloud adjustments has relatively little impact on cloud feedback when using the kernel-based diagnostic. In contrast, comparing the results in the first and second

Table 5.2 Comparison of longwave (LW), shortwave (SW) and net cloud feedbacks estimated from different methods and diagnostics as summarized in Table 1 (categories I–IV) of Zelinka et al. (2013a) (units: $Wm^{-2}K^{-1}$).

Diagnostic	$\Delta R/\Delta T_s$			Slope of ΔR against ΔT_s (Gregory method)		
	LW	SW	Net	LW	SW	Net
CRE anomalies	-0.45	0.61	0.16 (I)	-0.25	0.53	0.28 (II)
Kernel-derived cloud-induced radiation anomalies	0.40	0.41	0.81 (III)	0.42	0.33	0.76 (IV)

rows of Table 5.2, we can find the cloud masking effect do have a large impact on the cloud feedback calculation, especially for the longwave cloud feedbacks. For instance, the sign of longwave cloud feedback parameter changed when using kernel-derived diagnostic rather than CRE related diagnostic in Table 5.2 (category I to III or II to IV).

In summary, from this comparison we conclude that the CRE based diagnostics can be impacted by the cloud masking effect, especially for the longwave components; while the kernel-derived diagnostics are nearly not impacted by the masking effect. Also, comparing the $\Delta R/\Delta T_s$ method with the Gregory method, we find the rapid adjustment has little influence on the feedback calculation when using kernel-based diagnostics. As the COSP needs to be active from the start of the simulation when employing the Gregory method, it is time consuming if all the simulations in PPE use this method. Therefore we adopt the kernel-derived diagnostics but estimate the cloud feedback from $\Delta R/\Delta T_s$ in the current study.

5.4.3 Spatial pattern

The comparisons in Section 5.4.2 have shown that the cloud radiative kernel based diagnostics and the $\Delta R/\Delta T_s$ method can provide a relatively accurate calculation of cloud feedback, and thus in this section all the feedbacks are calculated in this way. Another advantage of using this method is that it can break down the total cloud feedback into various components according to cloud altitude and types. The ensemble and annual mean spatial pattern of the cloud feedbacks from the Isca PPE are displayed in Figure 5.7.

The net cloud feedback simulated in Isca is positive in most locations (Figure 5.7a), and the global mean quantity is about 0.86 $Wm^{-2}K^{-1}$, a value larger than the multi-model ensemble mean (~0.5 $Wm^{-2}K^{-1}$) but still within the range of net cloud feedbacks among all the CMIP5/6 models (Figure 1.3; see also Fig. 1 of Zelinka et al. 2020). The decomposition of the net cloud feedback based on cloud radiative kernel method could provide some insights to understand the cloud feed-

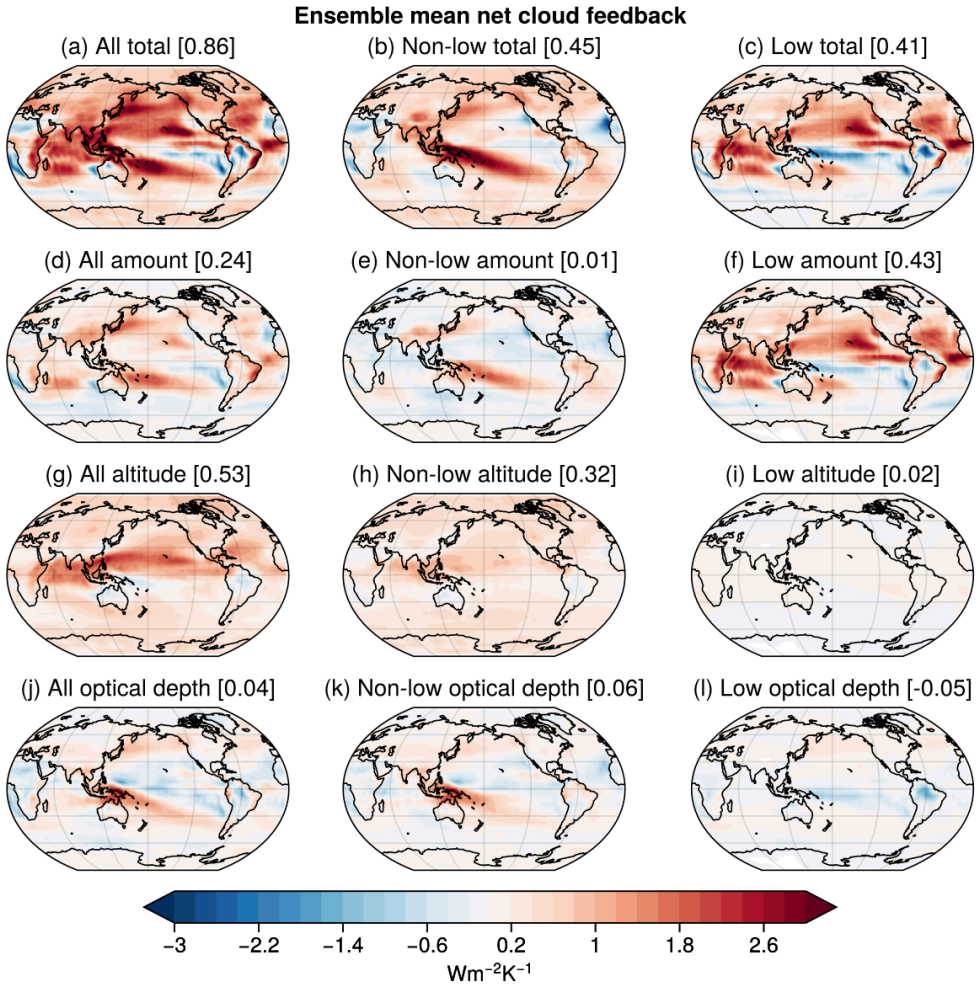

Figure 5.7 The ensemble and annual mean net cloud feedback and its amount, altitude, and optical depth components from Isca perturbed parameter ensemble for all clouds (left), non-low clouds (cloud top pressure, CTP $\leq$ 680 hPa; middle), and only low clouds (CTP > 680 hPa; right). Global mean values (in $Wm^{-2}K^{-1}$) are shown in brackets in the title of each panel.

backs. In Figure 5.7, the total cloud feedback is broken down into amount (second row), altitude (third row) and optical depth (fourth row) ingredients, repeated for all (left column), non-low (CTP $\leq$ 680 hPa; middle column) and low (CTP > 680 hPa; right column) clouds, respectively. In terms of the cloud amount feedback, the global mean low cloud component is strongly positive (Figure 5.7f), while the non-low component is close to zero (Figure 5.7e). The positive low cloud amount feedback is probably due to the reduction of cloud amount in the lower troposphere, as shown in Figures 5.4d and 5.5c. The low cloud amount feedback is strongly positive over northern Pacific and equatorial eastern Pacific regions. However, the ensemble mean low cloud amount feedback in the Isca PPE is negative in the subtropical east Pacific regions off the west coast of Peru, which is due to the increase of low cloud amount in these regions under global warming (not shown here) and is not consistent with the positive low cloud amount feedback over these locations

in CFMIP models (see the Fig. 2 of Zelinka et al. 2016). One plausible explanation for this is that the low cloud scheme (see Section 4.2.1) depends too strongly on the inversion strength, thereby inducing more low clouds under global warming (to be discussed in Section 5.5.3). The other low cloud feedback components such as altitude (Figure 5.7i) and optical depth (Figure 5.7l) feedbacks are quite weak globally. Regarding the non-low cloud amount, the altitude feedback is positive universally (Figure 5.7h), with the global mean value being 0.32 $Wm^{-2}K^{-1}$. This is associated to the upward shift the free tropospheric clouds under global warming (Figure 5.5c), and could be explained by the fixed anvil temperature assumption (e.g., Hartmann and Larson, 2002; Ceppi et al., 2017). Under this assumption, the CTP temperature does not warming in step with the surface warming, implying that more longwave radiation is trapped in the atmosphere. The global mean value of other components of non-low cloud feedbacks is not as evident as the altitude feedback, as indicated in Figures 5.7e and 5.7k. One plausible reason is that the longwave and shortwave radiative effects of high clouds nearly cancel with each other (Kiehl, 1994), so the change of non-low cloud amount leads to a near-zero net amount feedback (also see Figure 5.10b). Similarly, as pointed out by Zelinka et al. (2016), the increase in optical depth for non-low clouds would induce the reduction of incoming solar radiation and outgoing longwave radiation due to the increase of cloud albedo and emissivity, respectively, so the offset results in near-zero global mean optical depth feedback for non-low clouds.

In fact, compared to the cloud feedback in CFMIP1/2 models (see Fig. 2 of Zelinka et al. 2016), the feature of strong negative cloud feedback in the extratropics, particular over the Southern Ocean, is missing in Isca simulations (Figure 5.7a). This negative feedback in CFMIP models is from the negative optical depth feedback, which likely arises from two reasons: The first is that the adiabatic cloud water content increases with temperature, and increases more strongly at lower temperature (Betts, 1987); The second is the phase change in mixed-phase clouds under global warming, as there is more liquid condensate that usually has smaller particle size, reduced precipitation efficiency and longer life time than ice clouds (Ceppi et al., 2017). However, this is not well represented in the simple cloud scheme due to lack of microphysical processes and the direct interaction between cloud and convection schemes.

5.4.4 Zonal mean structure

The ensemble and zonal mean longwave, shortwave and net cloud feedbacks from the PPE of Isca are displayed in Figure 5.8. If the total cloud feedback is decomposed into non-low (above 680 hPa) and low (below 680 hPa) components, it is evident that the non-low clouds dominate the zonal mean structure of longwave feedback (Figure 5.8a), while the low cloud component is quite close to zero. This

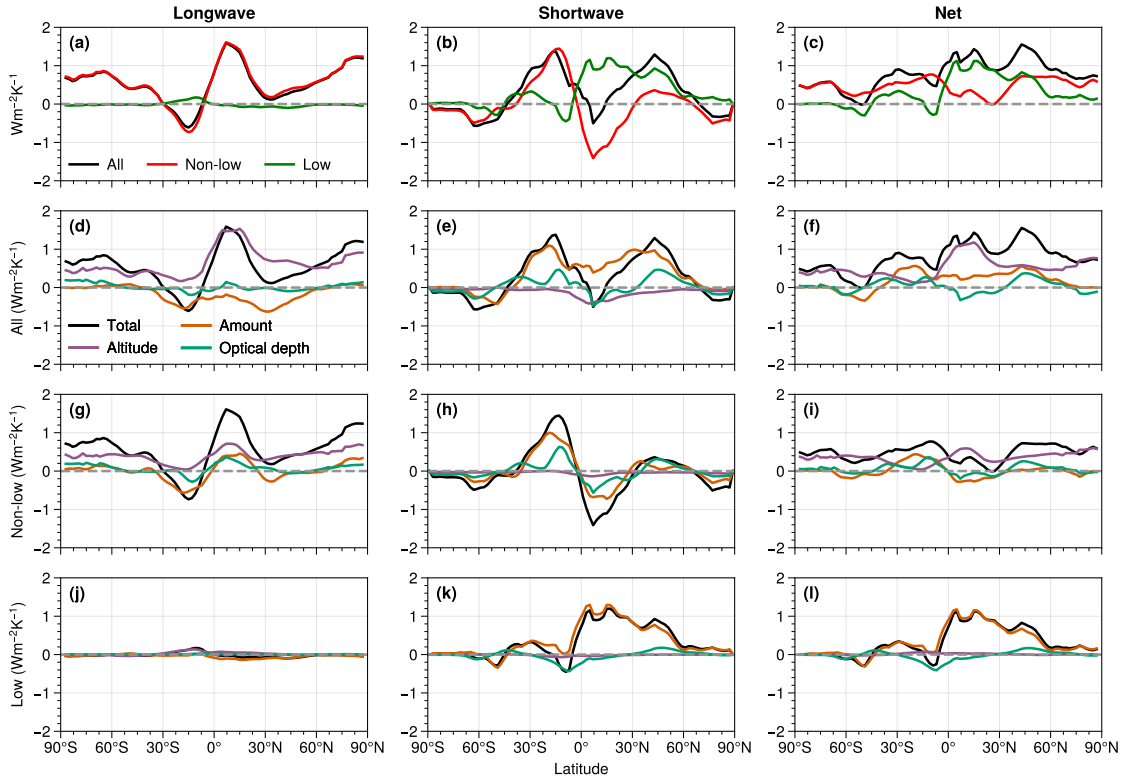

Figure 5.8 Zonal and ensemble mean (left column) longwave, (middle column) shortwave, and (right column) net cloud feedbacks from Isca perturbed parameter ensemble. (a-c) Total cloud feedbacks and their separate contributions from non-low (red) and low (green) clouds. Total cloud feedbacks (black) and their amount (orange), altitude (purple), and optical depth (green) components for (d-f) all clouds, (g-i) non-low clouds only, and (j-l) low clouds only.

is reasonable as the temperature difference between low clouds and Earth surface is small compared to that of high clouds, so the longwave feedback is not significant (Figure 5.8j). The longwave feedback of high clouds in fact is dominated by its altitude component, as shown in Figures 5.8d and 5.8g. As discussed in Section 5.4.3, this could be explained by the fixed-anvil temperature assumption (Hartmann and Larson, 2002). In terms of the shortwave cloud feedback (middle column of Figure 5.8), both low and non-low clouds have large impact on the zonal structure of cloud feedback (Figure 5.8b).

For shortwave cloud feedback, in the tropical and subtropical region, the low cloud feedback is usually positive, possibly due to the reduction of low cloud amount, as indicated by the positive low cloud amount feedback in Figure 5.8k. The non-low cloud feedback (Figure 5.8h) from Isca simulation shows the asymmetrical pattern in the subtropical regions, in which the positive feedbacks in 0–40°S and 30°–60°N are due to the reduction of high cloud amount and negative feedback in 0–30°N is due to the increase in high cloud amount.

The net cloud feedback (right column of Figure 5.8) is the sum of longwave and shortwave components. For the low clouds, the positive cloud feedback in the

tropical and subtropical regions is dominated by cloud amount changes (Figure 5.8l), but there is no clear negative optical depth feedback in midlatitudes, which disagrees with the CMIP models (see Fig. 5 of Sherwood et al. 2020 and Fig. S7 of Zelinka et al. 2016). This missing feature in Isca simulations arises from its absent representation of microphysical processes of mixed-phase clouds over those regions. For the middle and high clouds, the overall positive feedback among all the latitudes is major from the altitude feedback (Figure 5.8i). In sum, the positive low cloud amount feedback and high cloud altitude feedback are two basic features that account for the positive cloud feedback in Isca simulations (Figures 5.8c and 5.8f).

5.4.5 Comparison with WCRP assessment

Zelinka et al. (2021) evaluated the cloud feedbacks from CMIP5 and CMIP6 models and compared them to the latest World Climate Research Programme (WCRP) assessment of cloud feedbacks reported in Sherwood et al. (2020). Note that only 9 CMIP5 and 10 CMIP6 models are used, as only those that have successfully implemented the COSP (Bodas-Salcedo et al., 2011) are adopted. Based on the analysis from Zelinka et al. (2021), here the perturbed parameter ensemble simulations from Isca simulations are also added to this comparison, as shown in Figure 5.9 (produced using the package developed by Zelinka et al. (2021), available at `https://github.com/mzelinka/assessed-cloud-fbks`). In this figure, the feedback values from each category are weighted averaged according to their area fractions, so that the values shown in the last row of the figure are the direct sum of these categories.

All the simulated cloud feedbacks from Isca are within the *very likely* (90%, or 5%–95%; thin black line of WCRP assessment) confidence intervals of expert assessment, except the ones related to tropical anvil cloud area and tropical marine low cloud. In Isca simulations, the tropical anvil cloud area feedback (third row) is computed as the sum of non-altitude related feedbacks from both low and high clouds in the tropical deep convection region. Specifically, the sum includes low and high cloud mount and optical depth feedbacks. This feedback is strongly positive with the mean value larger than 0.3 $Wm^{-2}K^{-1}$, while the mean value of expert assessment is -0.2 $Wm^{-2}K^{-1}$ (1-σ uncertainty is 0.2 $Wm^{-2}K^{-1}$). This feature makes the total cloud feedback from Isca simulations very positive, and located at the right end of expert assessment (last row). Note that the CMIP5 and CMIP6 models also underestimate the magnitude of tropical anvil cloud area feedback, and some also produce the positive feedback parameters for this category. Nevertheless, their ensemble mean has the same negative sign as the expert assessment, although we notice it is very weak and close to zero. Regarding the tropical marine low cloud feedback, the ensemble mean feedback from Isca simulation

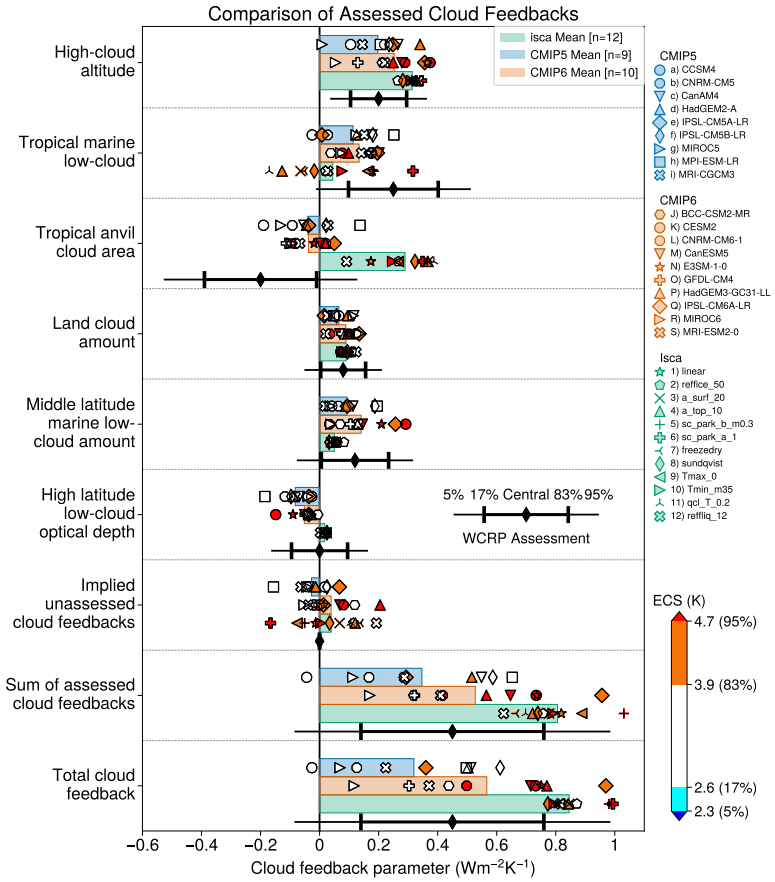

Figure 5.9 Cloud feedback components estimated from climate model simulations and as assessed in Sherwood et al. (2020). For each component, the individual model values are indicated with symbols, the multi-model means are indicated with blue (CMIP5), orange (CMIP6) and green (Isca) bars, and the expert assessed *likely* (66%, or 17%–83%) and *very likely* (90%, or 5%–95%) confidence intervals are indicated with thick and thin black errorbars, respectively. Model symbols (only for CMIP5/6) are color-coded by equilibrium climate sensivity (ECS) with color boundaries corresponding to the edges of the *likely* (17%–83%) and *very likely* (5%–95%) ranges of the Baseline posterior probability density function (PDF) of ECS from Sherwood et al. (2020). The results from Isca simulation are added to original Fig. 1 of Zelinka et al. (2021).

is much weaker than the expert assessed, and also weaker than the ensemble mean of CMIP5/6 models. Another feature of Isca simulation for this category is that the spread is quite large, and some members even produce negative marine low cloud feedback.

5.5 Spread of cloud feedback

Section 5.4 has introduced the simulated cloud feedback from Isca simulations. In this section, the spread of simulated cloud feedback is to be investigated. As introduced in Section 5.4, the simulated cloud feedback is decomposed physically into cloud amount, altitude and optical depth components through the cloud radia-

tive kernel method (Zelinka et al., 2012a,b). Also, this method can be performed separately for the decomposition of low (CTP > 680 hPa) and non-low (CTP < 680 hPa) clouds, which considers the probability that the boundary layer clouds may behave differently from the clouds in the free troposphere and can make the analysis of the change in the free-tropospheric clouds more coherently (Zelinka et al., 2016). As suggested by Zelinka et al. (2016), this refined decomposition can provide some insights for us to understand the underlying causes of spread in cloud feedback. Here we employ the cloud radiative kernel method to repeat the decomposition for Isca simulations, intending to investigate the possible reasons for cloud feedback spread in the Isca PPE. In Section 5.5.1, the global mean cloud feedbacks, including their longwave/shortwave and low/non-low cloud components, are examined. In addition, the contributions from different regions are discussed in Section 5.5.2. The cloud controlling factor analysis is used in Section 5.5.3 to analyze the influence of large-scale climatological factors on cloud changes.

5.5.1 Spread of global mean cloud feedbacks

The global mean longwave (light blue symbols), shortwave (oragne symbols), and net (black symbols) cloud feedbacks, and their non-low and low cloud components, are shown in Figure 5.10. For each cloud feedback, it is further broken down into amount, altitude and optical depth parts. As pointed out by Zelinka et al. (2012b), one can get total cloud feedback by summing its longwave and shortwave counterparts, which, however, does not hold for the feedback components. For example, you could not get the total cloud amount feedback by adding the low and non-low cloud amount feedbacks directly.

In the runs of Isca PPE, the net non-low cloud altitude and net low cloud amount feedbacks are robustly positive (Figures 5.10b and 5.10c, black symbols), and the contributions are almost from one band (longwave or shortwave). Specifically, the positive low cloud amount feedback is due to its shortwave component, while the positive longwave part contributes most to the net non-low cloud altitude feedback. The former can be explained by the fact that the temperature difference between the cloud top of low clouds and surface is small, so the longwave effect of low clouds is insignificant compared to its shortwave counterpart. In contrast, for the non-low cloud altitude feedback, if the cloud amount and optical depth are fixed, the change of the altitude mainly effects the cloud top temperature, indicating that longwave effect plays an important role, which explains why the longwave component dominates the net non-low cloud feedback. Except for these two components, the ensemble mean of other net cloud feedback components are close to zeros in the Isca PPE simulations (Figure 5.10), including the low cloud optical depth, a robust non-zero negative component in CMIP models (e.g., Zelinka et al.,

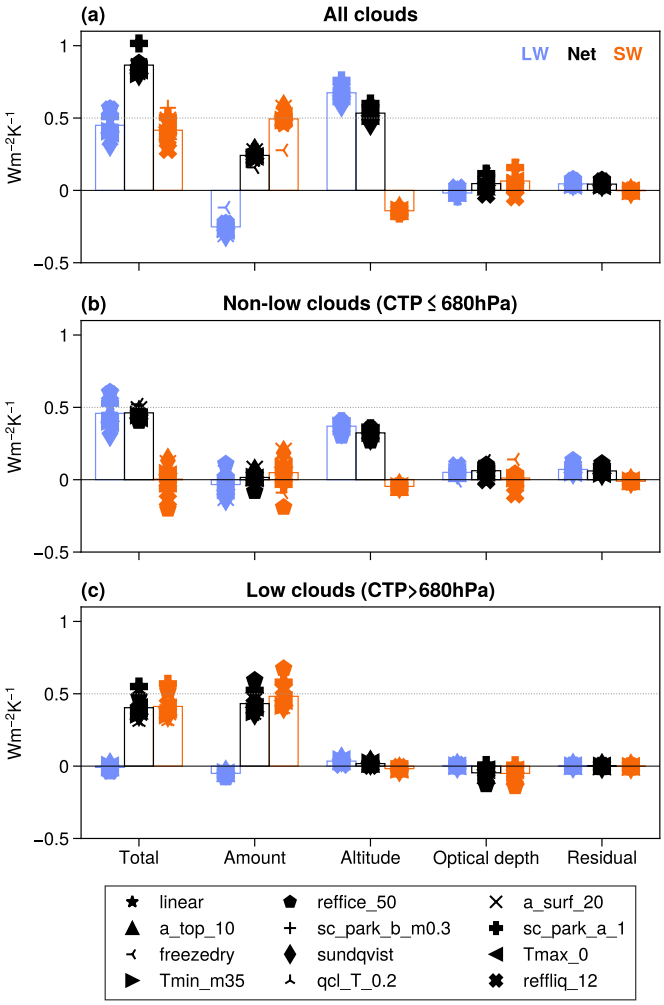

Figure 5.10 Global mean (orange) shortwave (SW), (blue) longwave (LW), and (black) net cloud feedbacks decomposed into amount, altitude, optical depth, and residual components for (a) all clouds, (b) non-low clouds (cloud top pressure, CTP $\leq$ 680 hPa), and (c) low clouds (CTP > 680hPa). The mean feedbacks of perturbed parameter ensemble are shown as empty bars.

2016; Ceppi et al., 2017; Zelinka et al., 2020). The reason for this missing feature is discussed in Section 5.4.3.

The spread of net cloud feedback in the Isca PPE is about 0.076 $Wm^{-2}K^{-1}$ (1σ), which is about 1/3 of the intermodel spread of CFMIP models (Zelinka et al., 2016). There are two possible reasons to explain why the spread in the Isca PPE is less than the CFMIP intermodel uncertainty: First, the perturbation is limited to one parameter each time, and the parameter is limited within the simple cloud scheme itself. The range of the parameter space is rather narrow in the current PPE of Isca. Second, only one model, Isca, is employed for the PPE, which is different from the CFMIP where models from multiple institutions are involved. In this case, the cloud schemes and other parameterization schemes may also contribute to the potential spread of cloud feedbacks. As previous study has pointed out that the responses in cloud fields under global warming are different for models with

different cloud scheme (e.g., Qu et al., 2014), and replacing the cloud scheme in GCMs can reduce the intermodel spread of cloud feedback for CMIP5 models (Geoffroy et al., 2017). The net low cloud amount feedback exhibits greater uncertainty than the net cloud feedback, and the standard deviation is 0.077 $Wm^{-2}K^{-1}$. Although the non-low cloud altitude feedback is robust non-zero, its spread is relatively small (standard deviation is 0.018 $Wm^{-2}K^{-1}$). In addition, the spread in non-low cloud amount feedback is about 0.041 $Wm^{-2}K^{-1}$, in spite of its ensemble mean being quite close to zero due to the cancellation between shortwave and longwave components (Figure 5.10b). Next, we will evaluate their contributions quantitatively.

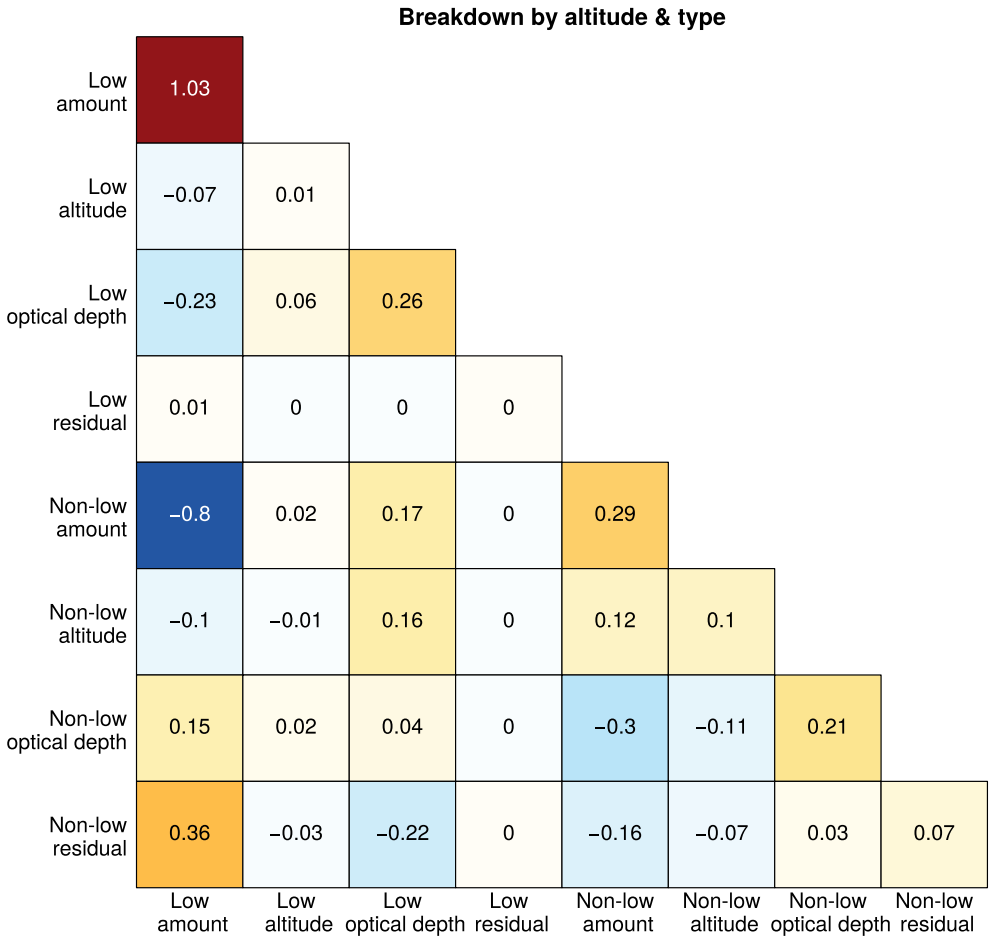

Figure 5.11 The fractional contributions to the Isca perturbed physical ensemble variance in net cloud feedback are broken down to different altitudes and types, including low/non-low cloud amount, altitude, optical depth feedbacks and residuals.

Following Caldwell et al. (2016) and Zelinka et al. (2016), the contribution of cloud types to the spread of net cloud cloud feedback is quantified as follows:

$$\begin{aligned} \mathrm{var}\left(\sum_{i=1}^{N} X_i\right) &= \sum_{i=1}^{N}\sum_{j=1}^{N} \mathrm{cov}\left(X_i, X_j\right) \\ &= \sum_{i=1}^{N} \mathrm{var}\left(X_i\right) + 2\sum_{j=1}^{N}\sum_{k=j+1}^{N} \mathrm{cov}\left(X_i, X_j\right), \end{aligned} \tag{5.2}$$

where X_i are low/non-low cloud amount, altitude, optical depth feedbacks and residuals in the decomposition. Then the ratios of these components to total variance are obtained and plotted in Figure 5.11. The variance terms of each component are on the main diagonal, while the values below the diagonal are for the covariance terms. Here the covariance terms are multiplied by 2, so the section above the diagonal in Figure 5.11 is omitted. This is reasonable as the covariance matrix is symmetric and each covariance should be included twice, as indicated by Equation (5.2). Covariance terms can be positive or negative while variances are always non-negative.

The low cloud amount feedback is by far the largest single contributor to the spread of net cloud feedback in the Isca PPE, as indicated by the greatest variance ratio in Figure 5.11. It seems that the variance of low cloud amount feedback is even larger than that of total net cloud feedback in the Isca PPE. This conclusion is qualitatively consistent with the results from CFMIP models that low cloud amount feedback contributes most to the net cloud feedback (Zelinka et al., 2016). The second largest contributor is the non-low cloud amount feedback, which accounts for 29% of the total variance of the net cloud feedback. But it also appears that there is a strong anticorrelation between the low cloud amount and non-low cloud amount feedbacks ($r = -0.73$), which reduces the spread of net cloud feedbacks, but the physical mechanism still needs further investigation. This anti-correlation is also found in CFMIP models, but Zelinka et al. (2016) thought it might be "entirely fortuitous" as it is uncorrelated with non-low cloud fraction changes and there is no strong correlation between low and non-low cloud amount changes in the CFMIP models. The contribution from low-cloud optical depth feedback is also a relatively important contributor to the spread of net cloud feedbacks, despite its ensemble mean being close to zero in Isca simulations.

5.5.2 Regional contributions

Section 5.5.1 has found that the low cloud amount feedback is the largest single contributor to the spread of Isca PPE, but the analyses are based on the global mean values. This section extends the analysis to regional scales, and intends to identify which region has the largest uncertainty for low cloud feedback. Figure 5.12 shows the low cloud feedbacks and their various components in different regions, including the tropics (30°S–30°N), midlatitudes (30°–60°S/N)

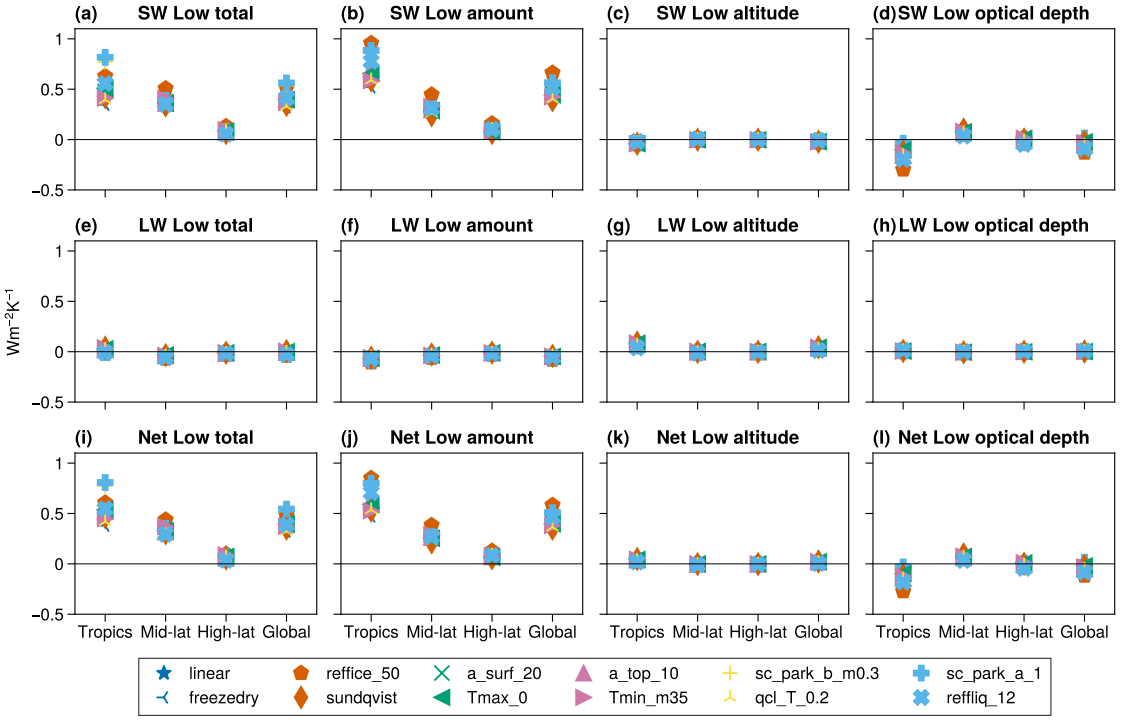

Figure 5.12 The scatter plot of total low cloud feedback (first column) and its amount (second column), altitude (third column) and optical depth (fourth column) components for different regions from Isca perturbed parameter ensemble. The top, middle and bottom rows are for the shortwave, longwave and net cloud feedbacks, respectively.

and high latitudes (60°–90°S/N). Basically no matter in which region, the longwave cloud feedback components (Figures 5.12e–h) and the shortwave altitude feedback component (Figure 5.12c) are nearly zero and contribute little to the spread of low cloud feedbacks in the Isca PPE. In contrast, the shortwave cloud amount (Figure 5.12b) and optical depth (Figure 5.12c) feedbacks, especially the former, are the major sources of spread in low cloud feedbacks (see Figures 5.12a and i). Focusing on the spread in different regions, we find the tropical region in fact plays the greatest part in determining the spread for global mean values of cloud feedbacks, both for cloud amount and optical depth components. As the spread in cloud amount feedback is larger than in optical depth, we can conclude that the tropical low cloud amount feedback (shortwave part) is the biggest contributor to the uncertainty of cloud feedback in the Isca PPE, which is consistent with previous studies (e.g., Bony et al., 2006).

A further step from the above analysis is to divide the tropical region into different dynamical regimes. For example, Bony et al. (2004) proposed a method to decompose the tropical ocean region into ascending and subsidence regimes with the vertical velocity at 500 hPa (ω_{500}), as these two regimes have distinctive dynamical and thermodynamical properties for cloud formation. This composite analysis has been used in Chapter 4 to evaluate the simulated longwave cloud radiative effect from simple cloud scheme in the tropical regions. Here we apply

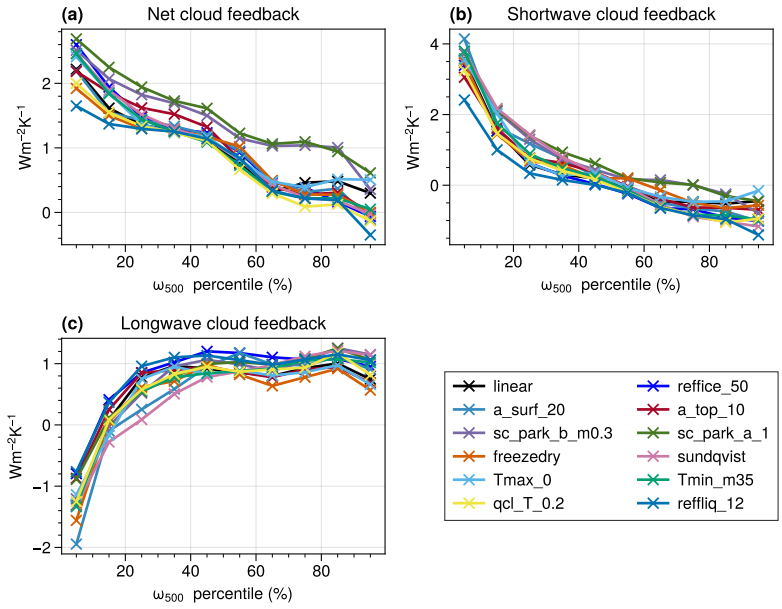

Figure 5.13 Composites of (a) net, (b) shortwave and (c) longwave cloud feedbacks over low-latitude oceans (30°S–30°N) in the Isca perturbed parameter ensemble, sorted by percentiles of the vertical velocity at 500 hPa (ω_{500}).

this composite analysis again to assess the simulated cloud feedback in the tropical regions, and seek to find which dynamical regime has the largest uncertainty in cloud feedbacks.

Figure 5.13 shows composites of cloud feedback over the low-latitude (30°S–30°N) oceans in the Isca PPE simulations, sorted by the percentiles of vertical velocity at 500 hPa (ω_{500}). Note that the percentile rather than actual ω_{500} is used for analysis. Larger percentiles represent the subsidence regimes over tropical and subtropical regions, while lower percentiles represent the deep convection areas. The spread of net cloud feedback is large in large percentile regimes (Figure 5.13a), which is from the shortwave component (Figure 5.13b; Note the scales of y-axis are different in Figure 5.13). As previous studies such as Bony and Dufresne (2005) have found that the marine boundary layer clouds are at the heart of tropical cloud feedback uncertainties in climate models, we further carry out the composite analysis for low cloud feedback in the tropical ocean regions (Figure 5.14). It is noteworthy that the low cloud amount feedback shows the largest difference over subsidence regions (percentiles greater than 50%) among the Isca PPE (Figure 5.14b), while the uncertainty in low cloud altitude and optical depth feedbacks is relatively low (Figures 5.14c and d). This finding confirms the results from Figure 5.12 that tropical low cloud amount feedback is one of the largest sources of uncertainty in net cloud feedback, and also identifies that the subsidence regime in fact plays a major role for low cloud feedback uncertainty, consistent with the findings from Bony and Dufresne (2005).

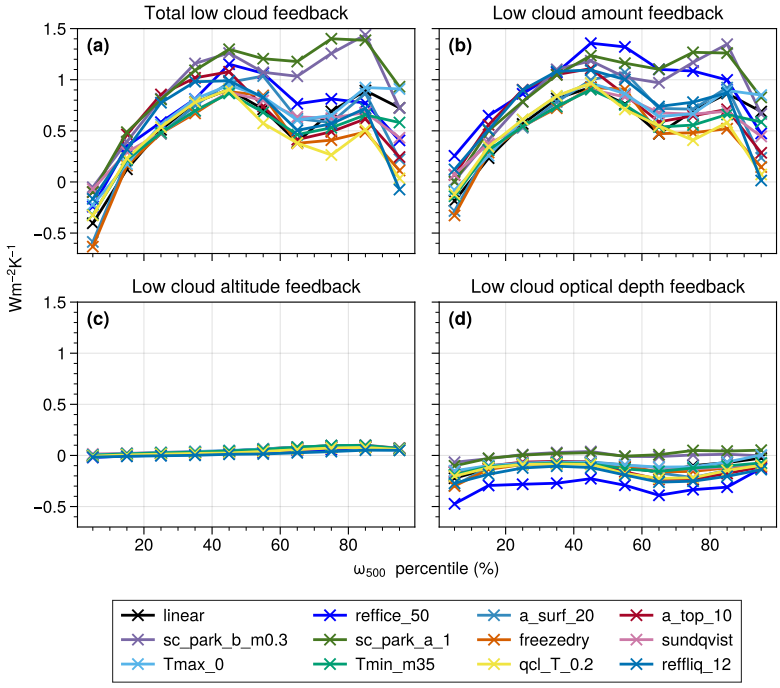

Figure 5.14 Similar to Figure 5.13, but the composites for (a) the total low cloud feedback and its (b) amount, (c) altitude and (d) optical depth components.

5.5.3 Cloud controlling factor analysis

Why does the low cloud amount feedback have the largest uncertainty over the subsidence regions in the Isca PPE simulations? To answer this question, the cloud controlling factor analysis (e.g., Qu et al., 2015b; Myers and Norris, 2016; McCoy et al., 2017; Klein et al., 2017; Scott et al., 2020; Myers et al., 2021; Cesana and Del Genio, 2021; Ceppi and Nowack, 2021) is employed in this section to analyze the sensitivity of low cloud amount to various large-scale meteorological conditions.

In the tropical and subtropical regions, climate regimes usually contain different cloud types. To this end, it is better to partition the whole region into different cloud regimes. In fact, several metrics have been proposed to partition the cloud regimes. For example, Medeiros and Stevens (2011) combined the vertical velocity at 500/700 hPa (ω_{500} or ω_{700}) and lower tropospheric stability (LTS) to partition the trade-wind cumulus clouds (Cu) and stratocumulus (Sc) over topical oceans. Recently, the metric such as estimate inversion strength (EIS) is also adopted for same purpose in latest studies (Scott et al., 2020; Myers et al., 2021; Cesana and Del Genio, 2021). In a similar manner as Scott et al. (2020), the criterion to partition the low cloud regimes over tropical oceans are as follows: the regimes are trade-wind cumulus clouds if $\omega_{700} > 15$ hPa and EIS < 4 K, and the regimes are stratocumulus clouds if $\omega_{700} > 15$ hPa and EIS ≥ 4 K. The first criterion (ω_{700}) is to make sure the clouds are in the subsidence regime and the second one (EIS) is to distinguish different low cloud types. An example of this partition is shown

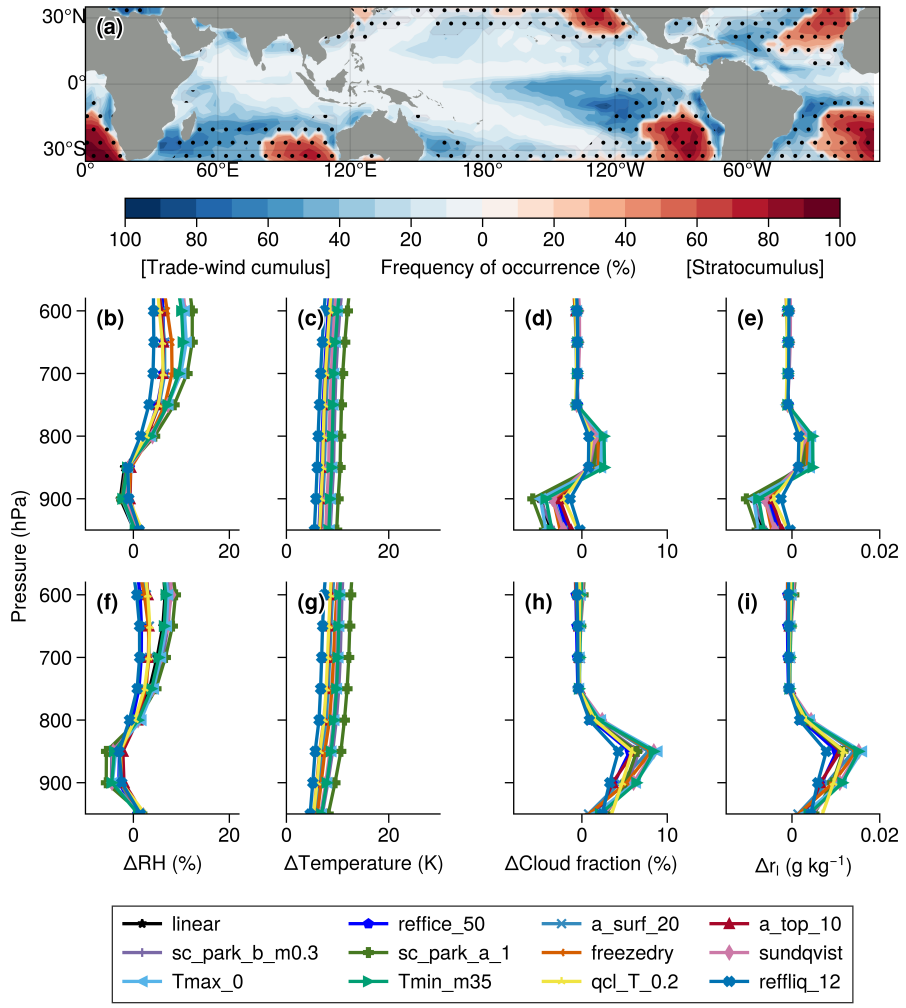

Figure 5.15 (a) The frequency of occurrence for (blue) trade-wind cumulus clouds and (red) stratocumulus clouds in low-latitude (35°S–35°N) ocean regions. Stippled regions indicate both types of cloud regimes can occur, but the color is chosen as the more frequent one. (b–e) The vertical profile changes in (b) relative humidity, (c) temperature, (d) cloud fraction and (e) cloud water content in the trade-wind cumulus cloud regions under global warming in Isca perturbed parameter ensemble simulations. (f–i) As in (b–e), but for stratocumulus regions.

in Figure 5.15a, in which blue denotes the frequency of occurrence of trade-wind cumulus clouds, while red represents the frequency of occurrence of stratocumulus clouds. Stippled regions indicate both types of cloud regimes can occur, but the color is chosen as the more frequent one. As we have discussed in Chapter 4, the stratocumulus clouds are abundant in the subtropical oceans off the west coast of continents (Figure 5.15a).

Under global warming, the changes of lower tropospheric cloud fraction profiles over trade-wind cumulus and stratocumulus cloud regimes in low-latitude oceans are different in the Isca PPE control and 4×CO_2 simulations (Figures 5.15d and 5.15h). The cloud fractions in the lower troposphere show clear reduction in the trade-wind cumulus cloud region (Figure 5.15d), which is consistent with the de-

crease in relative humidity at the same locations (Figure 5.15b). In contrast, the cloud fractions over the stratocumulus cloud regime increase in the lower troposphere (Figure 5.15h), in despite of the reduction in relative humidity (Figure 5.15f). The inconsistency in the stratocumulus cloud regime is due to the fact that the marine low clouds, particularly the stratocumulus clouds, are not directly diagnosed from relative humidity, but also from the inversion strength related variable. As introduced in Section 4.2.1, the maximum of the two diagnoses is regarded as the cloud fraction over the stratocumulus cloud region. Therefore, the increase of cloud fraction over the stratocumulus regime may reflect the strengthened inversion strength there (e.g., Webb et al., 2013, 2018).

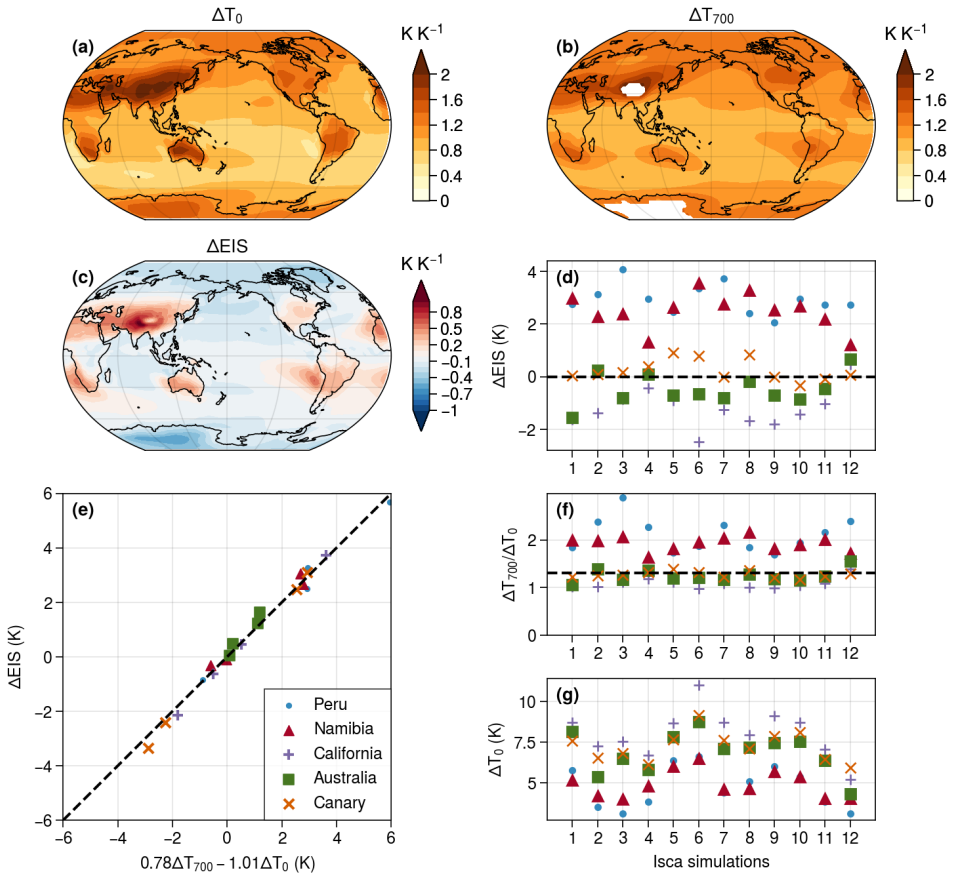

Figure 5.16 The annual and ensemble mean changes in (a) surface air temperature (T_0), (b) temperature at 700 hPa (T_{700}) and (c) estimate inversion strength (EIS) in Isca perturbed parameter ensemble (PPE) simulations, and these changes are normalized by the global mean surface air temperature. (e) The seasonal mean changes in EIS are estimated by the changes in surface temperature and temperature at 700 hPa for five marine low cloud regions in Isca simulation. The annual and regional mean EIS changes, the ratio between changes in T_{700} and T_0, and surface temperature changes for each member of Isca PPE are shown in (d), (f) and (g), respectively. The ranges of the five locations are the same as those used in Figure 4.5.

To check the changes of EIS under global warming, the ensemble mean spatial patterns of changes in surface temperature, temperature at the free tropo-

sphere, and EIS in the Isca PPE simulations are shown in Figures 5.16a, b and c, respectively, and these changes are normalized by the global mean surface air temperature changes. Focusing on the stratocumulus regimes over the subtropical eastern Pacific region, we can find the surface warming (Figure 5.16a) is lower than the warming at 700 hPa (Figure 5.16b), and this perhaps could explain the increase of EIS there (Figure 5.16c). The reason is that the change of EIS can be approximately explained by the changes of surface temperature (ΔT_0) and temperature at 700 hPa (ΔT_{700}), as pointed out by Qu et al. (2014) (see the analytical expression for EIS change in their Appendix 2). Basically, following the moist adiabatic assumption and with some simplifications, the change of EIS can be written as:

$$\Delta\text{EIS} = \alpha\Delta T_{700} - \beta\Delta T_0, \tag{5.3}$$

where the linear coefficients α and β are positive values and can be derived theoretically or obtained by regressing the model data. In this case, EIS increases if the ratio between the warming at 700 hPa and surface ($\Delta T_{700}/\Delta T_0$) is larger than certain threshold (i.e., β/α). In other words, $\Delta\text{EIS} \geq 0$ if $\Delta T_{700}/\Delta T_0 \geq \beta/\alpha$. To verify this relationship, the seasonal changes of EIS, T_{700} and T_0 from five marine low cloud regions (Klein and Hartmann, 1993; Qu et al., 2014) in a pair of control and 4×CO_2 Isca simulations are selected to derive their relationship and linear coefficients in Equation (5.3), with the result displayed in Figure 5.16e (Note that the constant, or the y-axis intercept, in the relationship is neglected in plotting). Thus, the change of EIS in Isca simulations can be estimated by $\Delta\text{EIS} \approx 0.78\Delta T_{700} - 1.01\Delta T_0$, and $\Delta\text{EIS} > 0$ if it is greater than $1.01/0.78 \approx 1.29$, close to the theoretical ratio (1.18) in Qu et al. (2014). This conclusion holds if the derived relationship is applied to all the Isca PPE simulations (Figures 5.16d, f and g). It is clear that the annual mean changes of EIS are positive (Figure 5.16d) if the temperature warming ratio between 700 hPa and surface is larger than 1.29, as denoted by the horizontal dashed line in Figure 5.16f.

According to Wood and Bretherton (2006), ΔEIS is close to zero if the vertical profile of tropospheric warming follows a moist adiabat from the subtropical surface ($\Delta T_{700}/\Delta T_0 \approx 1.2$). Therefore, it is the greater-than-adiabatic warming in the subtropical free troposphere that leads to the more stable environment (Qu et al., 2014). There are two possible reason for this: The first is the uneven warming pattern in the tropical and subtropical regions, as indicated by the surface temperature warming pattern in Figure 5.16a, in which the warming in the tropical west Pacific is enhanced relative to the subtropical low cloud regions. Based on the weak-temperature gradient approximation (Sobel et al., 2001), the low-latitude free troposphere temperature is largely set by the warm pool region, so the enhanced warming in the west Pacific could lead to the free tropospheric temperature warming in the subtropical low cloud regions (e.g. Zhou et al., 2016, 2017;

Mauritsen, 2016; McCoy et al., 2017; Andrews and Webb, 2018; Dong et al., 2019). The second is probably due to the rapid warming over nearby land (Qu et al., 2014, 2015a). As indicated in Figure 5.16b, in the marine low cloud regions, the land temperature changes are larger than the nearby ocean region in the free troposphere.

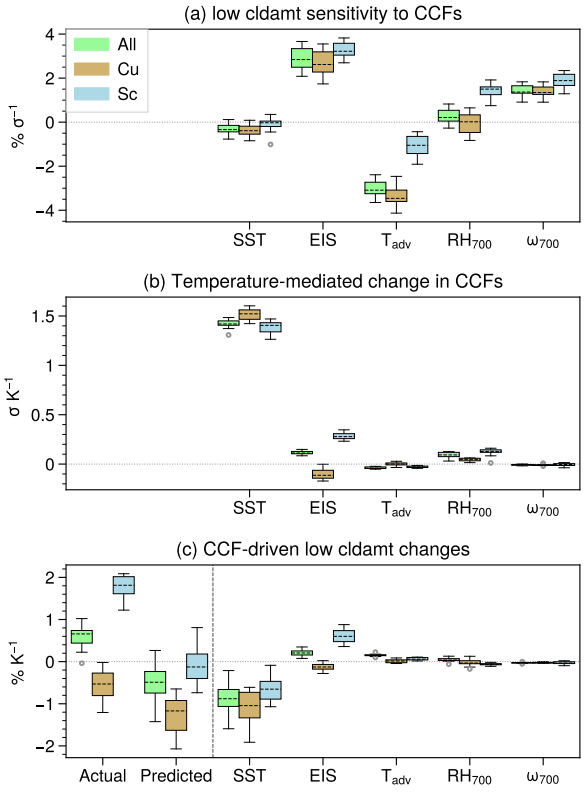

Figure 5.17 (a) Sensitivities of trade-wind cumulus (Cu; brown box), stratocumulus (Sc; blue box) and all low cloud amounts (green box) to cloud controlling factors (CCF), including sea surface temperature (SST), estimated inversion strength (EIS), surface temperature advection (T_{adv}), relative humidity at 700 hPa (RH_{700}), and vertical velocity at 700 hPa (ω_{700}) estimated from climate variability over low-latitude oceans (35°S–35°N) the in the control simulations of Isca perturbed parameter ensemble. (b) The changes in these factors per unit global warming from the 4xCO2 simulations of Isca. (c) Predicted and actual changes in low cloud amount due to each cloud controlling factor. Boxes extend from the 25th to 75th percentiles of the model values, with a dashed line at the median value. Outliers are denoted by gray empty circles. Anomalies in cloud controlling factors are normalized by the standard deviation of their interannual variations in ERA5 data set and are therefore expressed in σ units.

The above analyses put emphasis on EIS, which is one of the key meteorological factors that could help us understand low cloud changes. As EIS increases, the strengthened inversion inhibits the mixing between moist boundary with the drying free troposphere, in favor of more low clouds (e.g., Qu et al., 2014, 2015a; Ceppi et al., 2017; Webb et al., 2018; Scott et al., 2020). Actually, the other cloud controlling factors such as sea surface temperature (SST) also contribute to the

low cloud field changes, and may have opposite effects from EIS (e.g., Bretherton, 2015; Myers and Norris, 2016; Scott et al., 2020; Myers et al., 2021; Cesana and Del Genio, 2021). As summarized in Klein et al. (2017), many different predictor variables have been used in previous studies. In this section, following the analysis in Myers and Norris (2016) and Zelinka et al. (2020), we use the SST, EIS, temperature advection (T_{adv}), relative humidity in the free troposphere at 700 hPa (RH_{700}) and vertical velocity at 700 hPa (ω_{700}) to build the multiple linear regression model, with the results displayed in Figure 5.17. The analyses are performed over the trade-wind cumulus, stratocumulus and all low cloud regimes over tropical ocean regions (35°S/N), respectively. The anomalies of the meteorological factors in Isca outputs are normalized by the standard deviation of climatology data set from ERA5 (Copernicus Climate Change Service (C3S), 2017), covering the period from 1979 to 2018. Moreover, we need to keep in mind that some of the meteorological factors might co-vary and not be independent with each other, such as SST and EIS (McCoy et al., 2017), which might bring some problems in explaining the predicted results.

In Isca simulations, the dependence of low cloud amount on SST is negative (Figure 5.17a) for both trade-wind cumulus and stratocumulus cloud regimes, although the sensitivity of stratocumulus region is much weaker. This negative dependence is consistent with previous large-eddy simulation (LES) studies (e.g., Bretherton, 2015), observational studies (e.g., Qu et al., 2015b; Seethala et al., 2015; Scott et al., 2020; Myers et al., 2021) and GCM studies (e.g., Myers and Norris, 2016). The mechanism for this negative sensitivity is as follows: warmer SST increases the moisture in the boundary layer, which releases more latent heat flux and thus enhances the mixing with the free tropospheric dry air, thereby favoring fewer low clouds (Qu et al., 2015b; Scott et al., 2020). As the SST increases under global warming for both two cloud regimes (SST column in Figure 5.17b), the final SST-driven low cloud amount changes are negative for all the cloud regimes (SST column in Figure 5.17c).

In contrast, the effect of EIS on low cloud amount is opposite to SST, as shown in the EIS column of Figure 5.17a. This is because the stronger inversion strength of the boundary layer inhibits the entrainment drying at the cloud top and thus favors the formation of low clouds (e.g., Bretherton, 2015; Scott et al., 2020). The positive dependence of low cloud amount on EIS in Isca simulation is also consistent with previous studies (Qu et al., 2015b; Myers et al., 2021; Cesana and Del Genio, 2021), and this positive dependence holds for both trade-wind cumulus and stratocumulus regimes. However, we find the EIS changes in these two cloud regimes are different under global warming in Isca simulations. EIS increases in the stratocumulus cloud regime while decreases in the trade-wind cumulus cloud regime, which can be inferred from the EIS changes in Figure 5.16c. Therefore, low cloud

amount changes driven by EIS are opposite for these two regimes (see EIS column in Figure 5.17c). For all the low clouds, the EIS-driven amount changes are weakly positive.

In terms of the other factors such as T_{adv}, RH_{700} and ω_{700}, their changes under global warming in Isca simulations are small (the last three columns in Figure 5.17b), and thus the final contributions to low cloud amount change are neglected compared to the contributions from SST and EIS, as shown in Figure 5.17c. The negative sensitivity of low cloud amount to T_{adv} is well simulated in Isca (third column in Figure 5.17a), as positive T_{adv} brings relatively warm and moist air over cooler water, which stabilizes the boundary layer and cuts off clouds from the surface moisture supply (Scott et al., 2020). But we should note that Isca does not seem to be able to grasp the dependence of low cloud amount changes on ω_{700}, showing positive dependence on it, while other studies show a negative dependence (e.g., Scott et al., 2020; Zelinka et al., 2020), as the LES simulation shows the thinning of low clouds under strong subsidence (Bretherton, 2015). However, we find this negative dependence of low cloud amount on ω_{700} can be simulated well for total cloud amount in Isca (not shown). It is possible that the simple diagnostic cloud scheme introduced in Chapter 4 could not grasp the physical mechanisms found in LES. But as pointed out by McCoy et al. (2017), this mechanism also seems to be regime and model dependent, and also given the contributions from ω_{700} to final low cloud amount change in Isca simulation are tiny, we do not need to worry too much about this problem in the simple cloud scheme of Isca.

For the sum of the low cloud amount changes under global warming in Isca simulations (first two columns of Figure 5.17c), we find the SST and EIS are the major contributors to these changes, in agreement with previous studies (Myers and Norris, 2015, 2016; Qu et al., 2015b; Seethala et al., 2015; Zhou et al., 2015; McCoy et al., 2016). For trade-wind cumulus cloud regime, the sum of CCF-driven cloud amount changes is negative, suggesting the reduction of cumulus clouds under global warming. Also, the predicted changes of cumulus clouds is close to the actual changes in Isca simulation (first column in Figure 5.17c), in agreement with the reduction of cloud fraction in the lower troposphere shown in Figure 5.16d. For the stratocumulus clouds, the mean value of the sum of CCF-driven cloud amount changes is close to zero (second column in Figure 5.17c), while the actual changes in Isca simulations are very positive (first column in Figure 5.17c). This discrepancy is probably because the simple cloud scheme for stratocumulus regime is too strongly dependent on the inversion strength, while the multiple linear model overestimates its dependence on SST. We notice that such prediction among GCMs is also not so good, and thus some studies try to use observation to constrain the predictions (Myers and Norris, 2016; Myers et al., 2021).

In fact, despite the prediction from the multiple linear regression model being not

as good as expected, we still can get some useful ideas on the uncertainty of cloud feedback among Isca PPE simulations. It is noted that compared to the low cloud amount changes driven by EIS and other cloud controlling factors, the responses to SST show the largest spread (Figure 5.17c). This implies that the spread of low cloud amount changes is probably largely determined by SST-related changes.

5.6 Implications for equilibrium climate sensitivity

Table 5.3 Effective radiative forcing ($ERF_{2\times}$, Wm^{-2}), equilibrium climate sensitivity (ECS, K) and climate feedback parameters (λ, $Wm^{-2}K^{-1}$) for Isca perturbed parameter ensemble simulations.

PPE	$ERF_{2\times}$	λ	λ_{cld}	λ_{cld_SW}	λ_{cld_LW}	ECS
linear	3.09	-0.68	0.81	0.39	0.42	4.54
reffice_50	2.79	-0.80	0.88	0.32	0.56	3.50
a_surf_20	2.69	-0.70	0.85	0.48	0.37	3.83
a_top_10	2.64	-0.71	0.85	0.41	0.44	3.74
sc_park_b_m0.3	3.14	-0.66	0.98	0.54	0.45	4.77
sc_park_a_1	2.82	-0.57	1.00	0.50	0.50	4.91
freezedry	3.21	-0.74	0.81	0.31	0.50	4.34
sundqvist	3.04	-0.75	0.78	0.46	0.32	4.05
Tmax_0	2.65	-0.60	0.82	0.43	0.39	4.45
Tmin_m35	2.63	-0.58	0.80	0.39	0.41	4.52
qcl_T_0.2	2.79	-0.76	0.81	0.42	0.39	3.68
reffliq_12	2.63	-0.85	0.82	0.29	0.53	3.08

The Isca PPE simulations have produced a certain range in cloud feedbacks, as discussed in Section 5.5 and also in Table 5.3, so what are the implications for the ECS? To answer this question, we first evaluate the ECS from Isca simulations based on the method proposed by Gregory (2004). That is to say, the TOA radiation imbalances are plotted versus the surface air temperature anomalies between control and quadruple CO_2 simulations, in which the half of the x-axis intercept is the ECS, as the effective radiative forcing is defined in double CO_2 situation. The other derived parameters, climate feedback parameter (λ; slope) and effective radiative forcing (half of the y-axis intercept), are shown in Table 5.3. The Gregory type calculation is possible in the current Q-flux setup as the SST can vary in response to the changes in radiative forcing. In Isca PPE, the estimated effective forcing and climate feedback parameters vary due to the changes in the parameters of the cloud scheme, and thus the derived ECS values also show certain spread. The smallest ECS is 3.08 K in *reffliq_12* run, while the largest is 4.91 K in

sc_park_a_1 run. The later is not surprising as the parameter perturbed associated with the marine low cloud amount. The decrease of this parameter leads to the reduction of marine stratiform clouds, thus inducing more incoming solar radiation to warm the Earth. Similarly, the second highest cloud feedback and ECS is also from the perturbation of the marine low cloud parameter (*sc_park_b_m0.3*), as shown in Table 5.3. The mean ECS of the Isca PPE is 4.12 ± 0.54 K (1σ), within the 5%–95% percentile range of the expert assessed range (Sherwood et al., 2020). But as the cloud feedbacks of Isca PPE simulations are located at the right-hand end of the very-likely range (5%–95%) of expert assessed cloud feedback (see bottom row of Figure 5.9), the PPE mean ECS is also larger than the multi-model mean of CMIP5/6 models (see Fig. 1 of Zelinka et al., 2020).

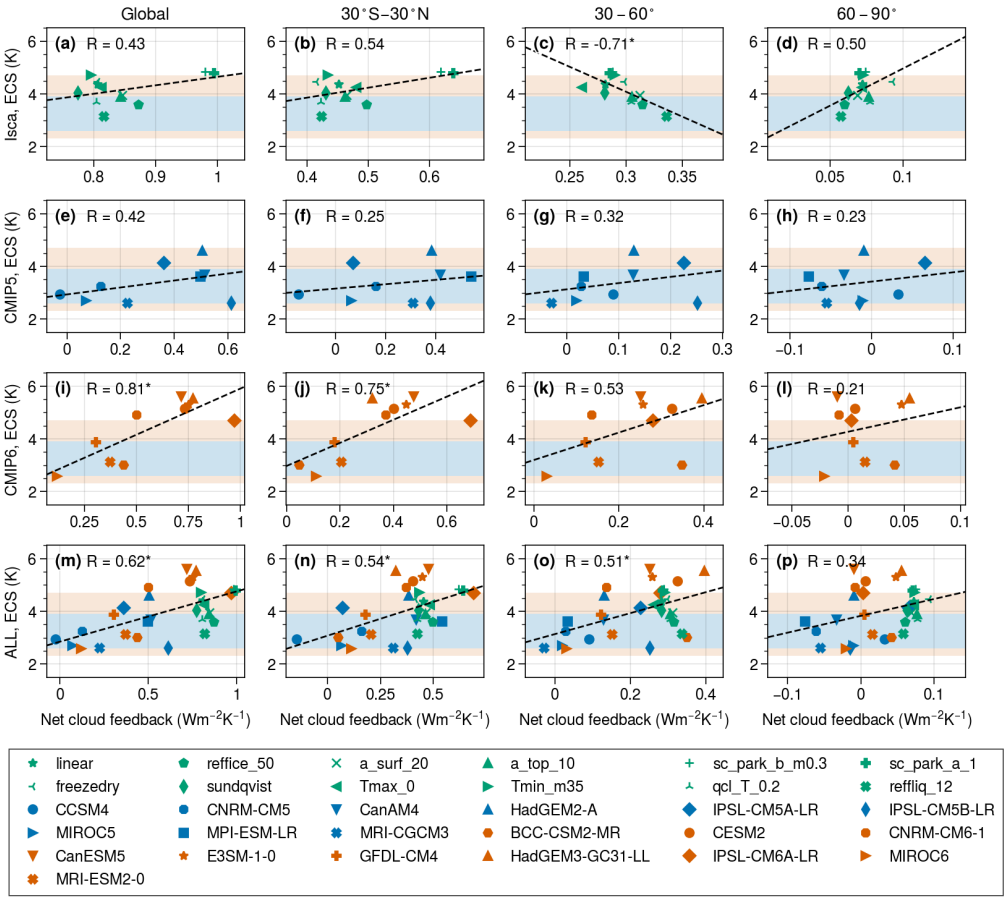

Figure 5.18 The scatter plot of equilibrium climate sensitivity (ECS; K) against the net cloud feedbacks ($Wm^{-2}K^{-1}$) from different models and different regions. Rows from top to bottom are for Isca (green), CMIP5 (blue), CMIP6 (orange) models and all of them, respectively. From left to right, the columns are for global, tropical (30°S–30°N), midlatitude (30–60°), and high latitude (60–90°) regions, respectively. The blue shaded indicates the 17th and 83rd percentile range of the Baseline probability density function of ECS from Sherwood et al. (2020), while the orange shaded indicates the 5th to 95th percentile range. The dashed lines are liner regression of ECS against cloud feedbacks, and the correlation coefficient (R) with asterisk is above 95% confidence interval.

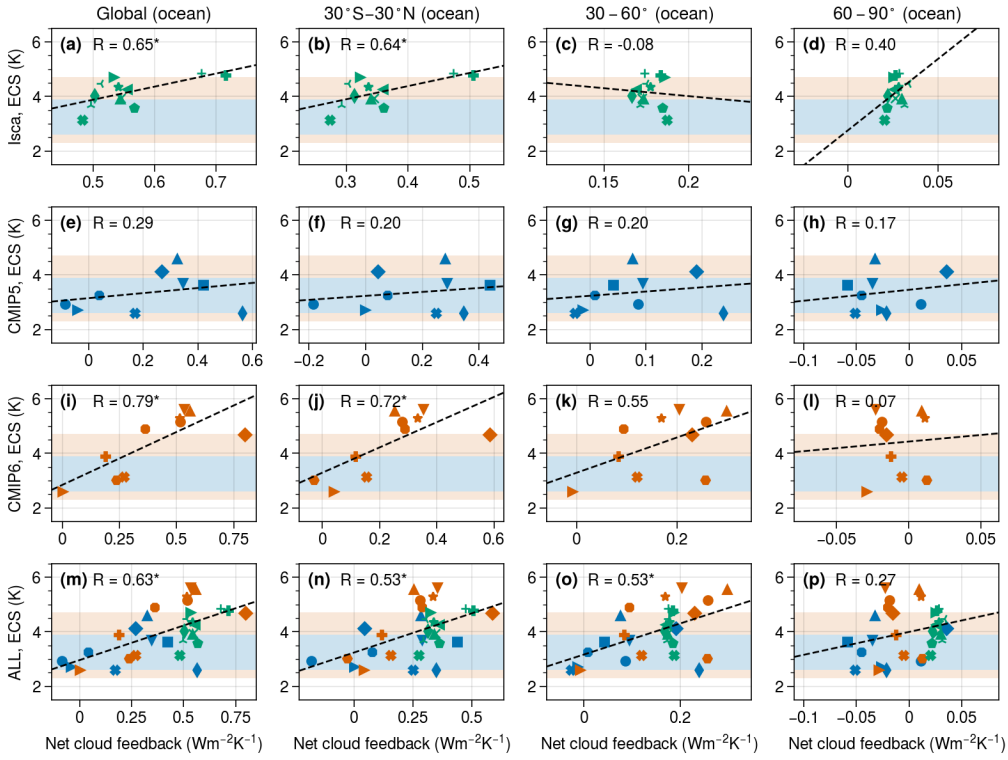

Figure 5.19 As in Figure 5.18, but for cloud feedbacks from ocean regions only. Symbols are the same as Figure 5.18.

As both feedbacks and ECS display a certain range (Table 5.3), is there any relationship between the spread in ECS and the spread in cloud feedbacks in the Isca PPE simulations? Previous studies have confirmed that the cloud feedback uncertainty is the largest source of intermodel spread of ECS in CMIP models (e.g., Ceppi et al., 2017; Zelinka et al., 2020). In addition, Zelinka et al. (2020) find the intermodel spread of ECS in CMIP5/6 models is well related the spread of global mean cloud feedbacks (see their Fig. S4). However, this linear relationship may not be robust across all the regions or across models with different ECS (Lutsko et al., 2021). Therefore, here we check the relationship between the spread of ECS and cloud feedback in the Isca PPE simulations. As shown in Figure 5.18, the ECS of Isca PPE did not show a robust linear relationship against cloud feedback for global and tropical (30°S–30°N) and high latitude (60–90°) regions (first row). The anticorrelation of ECS and cloud feedback in the midlatitude region (30–60°) of Isca (Figure 5.18c) could be fortuitous or artifacts of the PPE, as the perturbations are limited to a very narrow range. Another reason saying so is because we find the Isca PPE does display a relative narrow scope at the midlatitude when combining with part of CMIP5/6 models (Figure 5.18o). We also find such linear relationships are not robust among CMIP5 models both globally and for different regions (Figures 5.18e–h), but it is robust for global in CMIP5 (see Fig. S4 in Zelinka et al., 2020). The discrepancy is perhaps due to the fact that only the 9 CMIP5 models that are implemented with the COSP are used in

this research (Zelinka et al., 2021), while almost all the models are employed in Zelinka et al. (2020). With regard to CMIP6 models, it is the same that only the ones implemented with COSP are selected, but they still show a robust linear relationship between ECS and cloud feedback both for global and tropical regions (Figures 5.18i and j). Nevertheless, when all the Isca and CMIP models are used for the regression, the ECS and cloud feedbacks are linearly correlated with each other for global, tropical and midlatitude regions (last row of Figure 5.18).

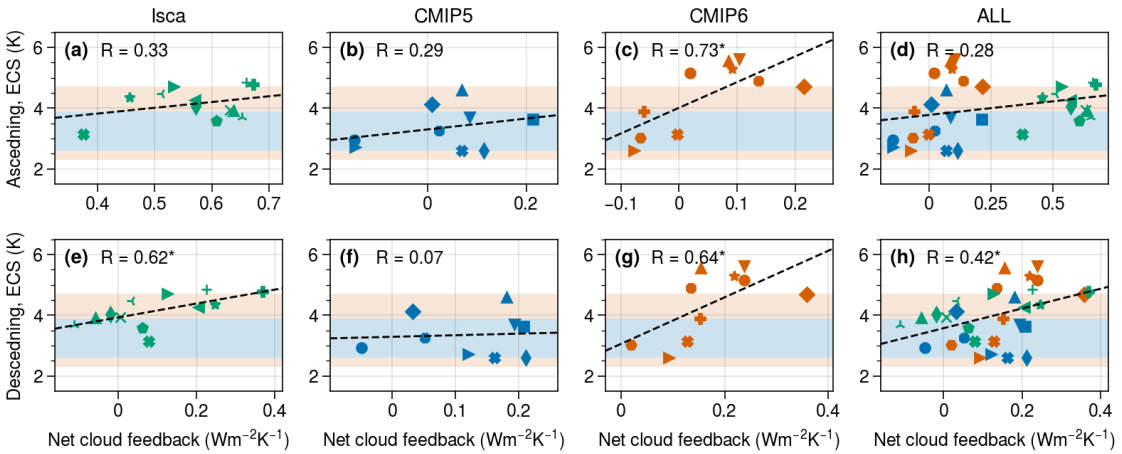

Figure 5.20 As in Figure 5.18, but for cloud feedbacks from tropical (top) ascending and (bottom) descending regions respectively, and the regimes are decomposed based on vertical velocity at 500 hPa. Symbols keep the same as Figure 5.18.

Similarly, when the analysis is repeated for the ocean region only, we find that the linear relationship is robust in global and tropical regions for Isca, CMIP6 and when all the models are used, but not robust for CMIP5 models (Figure 5.19). It is noted that this relationship is not robust for Isca when both land and ocean are involved (first row of Figure 5.18), indicating that the cloud feedbacks from ocean regions, especially tropical oceans, are more relevant to the spread of ECS. Inspired by this, after decomposing the tropical ocean region into ascending and descending regimes according to vertical velocity at 500 hPa (Bony et al., 2004; Bony and Dufresne, 2005) and reiterating the analysis, we find the linear relationship of ECS and cloud feedback is only robust in the descending regime for Isca simulations (Figures 5.20a and e). Also considering the whole tropical ocean region shows a robust correlation in Figure 5.19b, this implies that the cloud feedback in the subsidence regime is key to understanding the spread of ECS in Isca, consistent with the conclusions in Section 5.5.2. The CMIP5 models used in this study did not show a robust linear relationship for both dynamical regimes, while CMIP6 models show robust results for both regimes. When all the models are involved in the regression, the linear relationship is only robust in the descending regime, reflecting that low cloud feedback in the subsidence regime plays an important role in determining the spread of total cloud feedback (Section 5.5.2) and

ECS.

5.7 Summary and discussion

Cloud feedback has the largest intermodel spread among all the feedback parameters in CMIP5/6 models (Zelinka et al., 2020), one of the largest sources of uncertainty in ECS among GCMs (Stocker et al., 2013; Ceppi et al., 2017; Zelinka et al., 2020), but the underlying causes for cloud feedback uncertainty are still not fully understood (e.g., Bony and Dufresne, 2005; Vial et al., 2013; Qu et al., 2014, 2015b; Webb et al., 2015; Zelinka et al., 2016; Geoffroy et al., 2017; Zelinka et al., 2020). Narrowing down the cloud feedback uncertainty is key to constraining the range of ECS (e.g., Myers et al., 2021; Ceppi and Nowack, 2021) and to help us better understand the responses of the climate system to global warming. In this chapter, we intend to use the simple cloud scheme developed in Chapter 4 to understand the spread of cloud feedbacks. In doing so, a series of perturbed parameter ensemble (PPE) simulations under control (CO_2 =300 ppm) and global warming (CO_2 =1200 ppm) situations are performed in Isca, but the perturbation is limited to the simple cloud scheme and only a single parameter is perturbed for each simulation (Table 5.1). In addition, Q-flux is prescribed in the simulations to make the SST more realistic.

Based on the Isca PPE simulations, the first question we try to answer is whether the simple cloud scheme in Isca can grasp the mechanisms and basic features of cloud feedbacks. As summarized in Section 2.4, several methods have been employed in previous studies to estimate the cloud feedbacks simulated from GCMs, and one method using the cloud radiative kernel method (Zelinka et al., 2012a,b) requires that the COSP (Bodas-Salcedo et al., 2011; Swales et al., 2018) to be implemented. Therefore at the beginning, the COSP was implemented in Isca to get the necessary outputs for the cloud feedback calculation and decomposition Section 5.2.1). Then the diagnosis from COSP was compared with the Isca native outputs to make sure it has been successfully implemented (Section 5.3). Based on these results, different diagnostics and methods to compute cloud feedbacks were compared in Section 5.4.2, and we found the following two conclusions: First the diagnostics, the CRE based diagnostic can be impacted by the non-cloud effects, while the cloud radiative kernel derived diagnostics can overcome this caveat; Second for the method, although the Gregory (2004) method (i.e., calculate the slope of radiative imbalance at TOA against surface temperature change) is more accurate in computing the feedback than the method directly normalizing the changes of TOA imbalance by the global mean surface temperature changes, it is more computing expensive as it requires the COSP to be enabled all the time during the simulation. Thus in the later analyses, the kernel derived cloud-induced

TOA imbalance is normalized by the change of global mean surface temperature to compute the cloud feedback directly (type III in Table 5.2).

The next task is to evaluate the cloud feedbacks in the Isca PPE simulations. Combining the ISCCP outputs and cloud radiative kernel method, the net cloud feedback is broken down into longwave/shortwave cloud amount, altitude and optical depth components for low and non-low clouds, which provides a good opportunity to inspect the spatial pattern (Section 5.4.3) and zonal mean structure (Section 5.4.4) of these various cloud feedback components. Basically, the simple cloud scheme can grasp the two robust positive cloud feedbacks found in CMIP models (e.g., Zelinka et al., 2016): the low cloud amount feedback and the high cloud altitude feedback. However, the negative optical depth feedback in the midlatitude regions such as the Southern ocean, was missing in the current configuration of the simple cloud scheme, perhaps due to the fact that there is no physical representation of ice and liquid cloud fraction and lack of microphysical process of mixed phase clouds. The negative optical depth feedback is a feature seen in many GCMs (e.g., Zelinka et al., 2016; Ceppi et al., 2017; Zelinka et al., 2020) and observations (e.g., Tan et al., 2016), but the related processes still have many uncertainties. For example, the improvement of the supercooled liquid water representation in CMIP6 models induces a weaker negative cloud optical depth feedback compared to their predecessors, resulting in a higher climate sensitivity in CMIP6 models (Zelinka et al., 2020). However, Mülmenstädt et al. (2021) suggests that the negative cloud feedback due to cloud lifetime changes may be underestimated in CMIP6 models, hinting there should be a more moderate ECS. In addition, the cloud feedback components are also compared to the expert assessed values (Sherwood et al., 2020) and CMIP5/6 models (Section 5.4.5), in which all the components are within the very-likely range of expert assessment except the tropical anvil cloud feedback.

As the simple cloud scheme can grasp the two robust features of cloud feedbacks found in the CMIP models, we still use it to investigate the underlying causes of spread in cloud feedbacks in the Isca PPE, although the negative optical depth feedback is missing. In Section 5.5.1, through the scatter plot of the global mean cloud feedback components, we find there is a certrain spread of net cloud feedback among the Isca PPE simulations, but the spread is smaller than the inter-model spread in CMIP5/6 models (Ceppi et al., 2017; Zelinka et al., 2020). The possible reasons are that the perturbations are limited to the cloud scheme itself and only one model framework is used in the simulations, so naturally the possible range of cloud feedback is narrower than multiple models. Nevertheless, we still find that the low cloud amount feedback is the largest single contributor to the spread of cloud feedback in the Isca PPE, consistent with the results from CMIP models (Zelinka et al., 2016). Moreover, the regional analyses also identify the

tropical region, particularly the subsidence regime, is the most uncertain part of the cloud feedback (Section 5.5.2), in agreement with Bony and Dufresne (2005).

To investigate the sensitivity of low cloud amount to the large-scale meteorological factors, the cloud controlling factor analysis is carried out in the tropical marine low cloud regions (Section 5.5.3). In general, SST and EIS have the dominant roles in controlling cloud amount changes, but they have opposite effects (e.g., Qu et al., 2014, 2015b; Klein et al., 2017; Scott et al., 2020; Cesana and Del Genio, 2021). In Isca simulations, the cloud fraction responses under global warming are different for two cloud regimes: the cloud fraction decreases in the trade-wind cumulus cloud regime while it increases in the stratocumulus cloud regime, despite both regimes showing the reduction of relative humidity in the lower troposphere. These changes are likely linked to the configuration of the cloud scheme itself, as the marine low cloud amount, especially the amount of stratocumulus, is parameterized as the maximum of relative humidity diagnosed value and the inversion strength diagnosed value, as introduced in Section 4.2.1. We do find the inversion strength increases under global warming in the stratocumulus cloud regimes (Figure 5.16), which accounts for the changes of cloud fraction in that regime. While in the trade-wind cumulus clouds, the SST changes dominate the EIS changes, thus the mixing between the drier free troposphere with the boundary layer dissipate the clouds. Another point we got from the cloud controlling factor analysis is that the spread in cloud amount feedback is largely arsing from the response to SST rather than EIS.

Regarding the ECS of Isca with the simple cloud scheme (Section 5.6), the Isca PPE simulations have produce a certain range of ECS, mostly within the *very likely* (5%–95%) range of Baseline PDF from Sherwood et al. (2020), as shown in Figure 5.9. Furthermore, the largest ECS values (as well as the cloud feedback) in the Isca PPEs are from the perturbations associated with the marine low cloud scheme (*sc_park_b_m0.3* and *sc_park_a_1* in Table 5.3), suggesting that the low cloud amount feedback is highly correlated with the ECS in Isca simulations. Indeed, this has been confirmed by the regression of ECS against the net cloud feedback for different regions and among different models, where the cloud feedback from tropical subsidence ocean region show a robust linear relationship with ECS in the Isca PPE simulations and CMIP6 models, while the relationship is not robust for ascending regions.

In summary, the simple cloud scheme of Isca can grasp the two major positive cloud feedback mechanisms found in CMIP models and can be used to study the cloud feedback uncertainties through perturbing a series of physical parameters. However, we should also notice that the range of the cloud feedbacks and ECS is relatively narrow, due to the perturbation strategy used in this study. In this case, it is hard to quantify the sensitivity of cloud feedback to these parameters.

In the future, perhaps we can perturb parameter in a wider range, perturb more parameters each time, and/or perturb the parameters from different parameterization schemes so as to produce a larger range of ECS, which would be useful to constrain the climate sensitivity. In addition, the ice cloud and mixed phase cloud, as well as the microphysical processes are missing in the simple cloud scheme, so that it is impossible to simulate the corresponding cloud properties and feedbacks, such as the phase change in mixed phase clouds and cloud lifetime process. Such modules could be added to the simple cloud scheme to make it more realistic in the future.

Chapter 6

Conclusions and Future Work

6.1 Conclusions

The global mean surface temperature change in response to increased greenhouse gas (i.e., climate sensitivity) is one of the key problems in current climate studies (e.g., Bony et al., 2006; Stocker et al., 2013; Sherwood et al., 2020), and the estimates of climate sensitivity depend on the climate feedbacks (Bony et al., 2006; Soden and Held, 2006). The aim of this thesis is to understand the climate feedbacks with simple climate models and the following problems are addressed:

1. What roles do the climate feedback processes play in the polar amplification of surface temperature change in idealized aquaplanet simulations?

2. Could we build a cloud scheme for idealized general circulation models (GCMs) that is simple enough but could grasp the key features of cloud fields?

3. If so, could the scheme be used to investigate the underlying causes of the intermodel spread of cloud feedback in climate models?

To answer the first question, a series of Isca (Vallis et al., 2018) aquaplanet simulations (without sea ice and clouds) with different surface albedos and with a hierarchy of radiation schemes were performed (see Chapter 3). In the simulations, the climate feedbacks are quantified through the radiative kernel method, derived from the offline calculation with the radiation codes (Liu, 2020). When the total temperature response is decomposed into different components, we find that the increase in poleward heat transport, the lapse rate and Planck feedbacks contribute to the polar amplification most, while the water vapor feedback dominates the tropical temperature change.

The second and the third problems were to understand the cloud feedback with a simple cloud scheme. The reason to use a simple scheme rather than the existing ones is that previous studies have suggest that the spread does not decrease

even if the convection schemes are off (Webb et al., 2015) and the cloud scheme itself might play a role in it (e.g., Qu et al., 2014; Geoffroy et al., 2017). Therefore, a simple scheme that interacts directly with the radiation scheme only might be helpful. As the idealized climate model involved in this study is Isca, which has no cloud scheme at the beginning, the first step is to construct a simple cloud scheme for it. As introduced in Chapter 4, the scheme (Liu et al., 2021) is inspired by the phase II of Selected Process On/Off Klima Intercomparison Experiment (SPOOKIE II) project, which intends to explore the role of cloud scheme in the intermodel spread of cloud feedback. In the scheme, the large-scale clouds are diagnosed from relative humidity, and the marine low stratus clouds, typically found off the west coast of continents over subtropical oceans, are determined largely as a function of inversion strength. A "freeze-dry" adjustment based on a simple function of specific humidity is also available to reduce an excessive cloud bias in polar regions. The cloud optical related properties, such as the effective radius of cloud droplet and cloud liquid water content, are specified as simple functions of temperature. All of these features are user-configurable. The Atmospheric Model Intercomparion Project (AMIP) fixed sea surface temperature (SST) simulations show the scheme can capture the spatial pattern, zonal mean structure and seasonal cycle of climatologies of cloud radiative effect, and hence could be a useful tool for clouds related study.

To answer the third question, a series of perturbed parameter ensemble (PPE) simulations under control (CO_2 level is 300 ppm) and global warming (quadruple CO_2) situations are performed in Isca (see Chapter 5). In the PPE simulations, the perturbed parameters are limited to cloud scheme and the runs are performed with realistic continents and with prescribed Q-flux. We find the simple cloud scheme can capture two robust positive cloud feedbacks, low cloud amount feedback and high cloud altitude feedback, but fails to grasp the strong negative optical depth feedback in midlatitudes, as the mixed-phase clouds are not explicitly represented in the simple cloud scheme. The PPE simulations could reproduce part of the intermodel uncertainty of cloud feedback in GCMs by perturbing its key parameters, and the low cloud amount feedback, especially in the subsidence regime of tropical and subtropical oceans, is the largest contributor to the net cloud uncertainty. The cloud controlling factor analysis suggests that the SST and estimated inversion strength (EIS) have opposite effects on marine low cloud amounts, but their responses to SST rather than EIS seem to bring larger uncertainty. As for the climate sensitivity, we find the perturbation related to marine low clouds produces the largest cloud feedback and equilibrium climate sensitivity (ECS), and the range of ECS perhaps can be constrained by the tropical cloud feedback over subsidence regimes, as they show a robust linear relationship in the Isca PPE and the sixth phase of Coupled Model Intercomparison Project (CMIP6) models.

6.2 Future work

In this thesis, we have investigated the roles of climate feedbacks in climate system with a series of idealized simulations, but in fact there is still lots of work that can be done in the future.

In Chapter 3, we have explored the roles of different climate feedbacks in amplified change of surface temperature in polar regions. However, due to the limitation of our setup, the roles of sea ice and clouds in polar amplification have not been studied. As suggested by Screen and Simmonds (2010), the retreat of sea ice may play a central role in Arctic temperature amplification. As there is no sea ice model in Isca, perhaps in the future we can set up a simple sea ice model to explore the roles of sea ice in polar amplification. Alternatively, we can use the current aquaplanet setup, but just modify the albedo in polar regions to mimic the diminishing of sea ice, so as to investigate the role of sea ice in a simple way. Note that the simple cloud scheme has not been constructed when the simulations described in Chapter 3 were run, so the roles of clouds are ignored. But as the simple cloud scheme is ready now, we could rerun the same simulations with the simple cloud scheme to examine the role of clouds in the same problem, and to see whether other feedbacks would change when clouds are present.

The work presented in Chapter 4 and Chapter 5 is based on the simple cloud scheme described in Liu et al. (2021). At first, we should keep in mind that the scheme is a diagnostic scheme, and the cloud fraction and cloud water are diagnosed from different variables in the scheme, which could lead to the inconsistency between cloud fraction and cloud condensate (e.g., Gregory et al., 2002; Tompkins, 2005). Also, cloud fraction and relative humidity might show opposing changes at some locations under global warming in RH scheme (Ming and Held, 2018). Therefore, in the future, perhaps we could build a statistical scheme or even a prognostic scheme in Isca, so as to improve the simulations of cloud fields. As we discussed in Section 5.4.3, the negative optical depth feedback is too weak in the current simple cloud scheme, due to the poor representation of mixed-phase clouds and lack of mircophysical processes, which makes the global mean cloud feedback larger than the ensemble mean of CMIP5/6 models. In future studies, we consider introducing the microphysical processes in the simple cloud scheme, so as to better simulate the transition between ice and liquid cloud and to improve the simulation of cloud lifetime and its optical depth feedback.

For the Isca PPE simulations in Chapter 5, currently only the parameters within the cloud scheme are perturbed, and only one parameter is perturbed each time, so the parameter space is narrow compared to the intermodel differences. In addition, the PPE results might be biased due to the perturbations being within a small scale. To solve these potential problems, it would be worthwhile to perturb more parameters to generate a wider parameter space in the future. For example,

we can perturb the parameters from other parameterization schemes, or can perturb several parameters at the same time. In this way we can explore the possible ranges of ECS.

Moreover, it is noteworthy that not only the cloud scheme itself, but other factors such as SST warming pattern (e.g., Zhou et al., 2016; Dong et al., 2019, 2020) or the coupling between clouds and circulation (e.g., Bony et al., 2004; Vial et al., 2013) can also have impacts on cloud feedbacks, but these issues are not explored in this study. In the future, we could design a series of experiments to test these problems with the simple cloud scheme. For example, we could run the simulations with different warming patterns to examine the influences on climate feedbacks. And we can investigate the cloud-circulation coupling with the cloud-locking method (e.g., Voigt et al., 2020). All these efforts will help us better understand cloud feedbacks in the climate system.

Appendices

Appendix A

Code and data availability

A.1 The simple cloud scheme

A.1.1 Introduction

The simple cloud scheme diagnoses cloud fraction based on relative humidity (RH) and specifies the in-cloud water mixing ratio and effective radius of the cloud condensate as function of temperature. It has been implemented and tested under Isca framework (Vallis et al., 2018) and can be ported to other climate models if needed.

A.1.2 Code structure

The simple cloud scheme code can be accessed at `https://doi.org/10.5281/zenodo.4382536`, and the updates can be found at `https://github.com/lqxyz/Isca/tree/simple_clouds`. It will be merged with the Isca master repository (`https://github.com/ExeClim/Isca`) in the future. Specifically, they are in `src/atmos_param/cloud_simple` directory and are called by the file `src/atmos_spectral/driver/solo/idealized_moist_phys.F90`.

The major files in *src/atmos_param/cloud_simple* directory include:

- *cloud_simple.F90*
  The main module of the SimCloud scheme, which specifies the in-cloud water mixing ratio and effective radius of cloud condensate, and calls the following modules to diagnose cloud fraction.

- *large_scale_cloud.F90*
  The module that diagnoses large-scale clouds based on RH. In this module, several different schemes are provided, such as *linear* and *Sundqvist et al. (1989)* schemes, which can be set through *large_scale_cloud_nml* namelist by specifying the method name (*cf_diag_formula_name*).

- *marine_strat_cloud.F90*
  This module diagnoses the marine stratus clouds based on low-level cloud proxy *ELF* (estimated low-level cloud fraction) from Park and Shin (2019).

- *cloud_cover_diags.F90*
  This module diagnoses the 2D cloud cover based on different overlap assumptions, including *'maximum-random'*, *'maximum'* and *'random'*.

A.2 Data and scripts

Chapter 3

The derived radiative kernels for three radiation schemes of Isca are availabel at https://doi.org/10.5281/zenodo.4282681, namely two gray radiation schems, Frierson (Frierson et al., 2006) and Byrne and O'Gorman (BOG; Byrne and O'Gorman, 2013), and a full radiation scheme, the multiband correlated-*k* Rapid Radiative Transfer Model (RRTM; Clough et al., 2005). The scripts to calculate the offline radiative kernels can be found at https://github.com/lqxyz/Isca_kernels (last access: 31 July 2021). The input basic state data sets are available at https://doi.org/10.5281/zenodo.4071837, and they are generated from Isca simulations (T42, 25 vertical levels) without sea ice and clouds.

Chapter 4

The Isca model outputs are available on Zenodo: https://doi.org/10.5281/zenodo.4573610, generated from the AMIP-type fixed SST simulations with realistic continents, SOCRATES radiation scheme and the simple cloud scheme with different setups. An archive of the scripts used to process data and generate figures/tables is available at https://doi.org/10.5281/zenodo.4597263 and the updates can be found at https://github.com/lqxyz/cloud_scheme_manuscript_figs (last access: 31 July 2021).

Chapter 5

The Isca perturbed parameter ensemble (PPE) simulation outputs under 1×CO_2 and 4×CO_2 scenarios are available on Zenodo: https://doi.org/10.5281/zenodo.5150241 and https://doi.org/10.5281/zenodo.5188175. The scripts for processing data and plotting figures can be found at https://github.com/lqxyz/cloud_feedback_from_Isca_PPE (last access: 3 August 2021).

Bibliography

Alexeev, V., P. Langen, and J. Bates, 2005: Polar amplification of surface warming on an aquaplanet in “ghost forcing” experiments without sea ice feedbacks. *Climate Dynamics*, **24 (7-8)**, 655–666, doi:10.1007/s00382-005-0018-3.

Andrews, T., J. M. Gregory, P. M. Forster, and M. J. Webb, 2012a: Cloud adjustment and its role in CO_2 radiative forcing and climate sensitivity: A review. *Surveys in geophysics*, **33 (3-4)**, 619–635, doi:10.1007/s10712-011-9152-0.

Andrews, T., J. M. Gregory, M. J. Webb, and K. E. Taylor, 2012b: Forcing, feedbacks and climate sensitivity in CMIP5 coupled atmosphere-ocean climate models. *Geophysical research letters*, **39 (9)**, doi:10.1029/2012GL051607.

Andrews, T., and M. J. Webb, 2018: The dependence of global cloud and lapse rate feedbacks on the spatial structure of tropical Pacific warming. *Journal of Climate*, **31 (2)**, 641–654, doi:10.1175/JCLI-D-17-0087.1.

Armour, K. C., C. M. Bitz, and G. H. Roe, 2013: Time-varying climate sensitivity from regional feedbacks. *Journal of Climate*, **26 (13)**, 4518–4534, doi:10.1175/JCLI-D-12-00544.1.

Austin, R. T., A. J. Heymsfield, and G. L. Stephens, 2009: Retrieval of ice cloud microphysical parameters using the CloudSat millimeter-wave radar and temperature. *Journal of Geophysical Research: Atmospheres*, **114 (D8)**, doi:10.1029/2008JD010049.

Barker, H., A. Korolev, D. Hudak, J. Strapp, K. Strawbridge, and M. Wolde, 2008: A comparison between CloudSat and aircraft data for a multilayer, mixed phase cloud system during the Canadian CloudSat-CALIPSO Validation Project. *Journal of Geophysical Research: Atmospheres*, **113 (D8)**, doi:10.1029/2008JD009971.

Betts, A., and M. Miller, 1986: A new convective adjustment scheme. Part II: Single column tests using GATE wave, BOMEX, ATEX and Arctic air-mass data sets. *Quarterly Journal of the Royal Meteorological Society*, **112 (473)**, 693–709, doi:10.1002/qj.49711247308.

Betts, A. K., 1986: A new convective adjustment scheme. Part I: Observational and theoretical basis. *Quarterly Journal of the Royal Meteorological Society*, **112 (473)**, 677–691, doi:10.1002/qj.49711247307.

Betts, A. K., 1987: Thermodynamic constraint on the cloud liquid water feedback in climate models. *Journal of Geophysical Research: Atmospheres*, **92 (D7)**, 8483–8485, doi:10.1029/JD092iD07p08483.

Bjordal, J., T. Storelvmo, K. Alterskjær, and T. Carlsen, 2020: Equilibrium climate sensitivity above 5°C plausible due to state-dependent cloud feedback. *Nature Geoscience*, **13 (11)**, 718–721, doi:10.1038/s41561-020-00649-1.

Bodas-Salcedo, A., and Coauthors, 2011: COSP: Satellite simulation software for model assessment. *Bulletin of the American Meteorological Society*, **92 (8)**, 1023–1043, doi:10.1175/2011bams2856.1.

Bohren, C. F., 1987: Multiple scattering of light and some of its observable consequences. *American Journal of Physics*, **55 (6)**, 524–533, doi:10.1119/1.15109.

Bony, S., and J.-L. Dufresne, 2005: Marine boundary layer clouds at the heart of tropical cloud feedback uncertainties in climate models. *Geophysical Research Letters*, **32 (20)**, doi:10.1029/2005GL023851.

Bony, S., J. L. Dufresne, H. Le Treut, J. J. Morcrette, and C. Senior, 2004: On dynamic and thermodynamic components of cloud changes. *Climate Dynamics*, **22 (2-3)**, 71–86, doi:10.1007/s00382-003-0369-6.

Bony, S., and K. a. Emanuel, 2001: A parameterization of the cloudiness associated with cumulus convection; evaluation using TOGA COARE data. *Journal of the Atmospheric Sciences*, **58 (21)**, 3158–3183, doi:10.1175/1520-0469(2001)058<3158:APOTCA>2.0.CO;2.

Bony, S., and Coauthors, 2006: How well do we understand and evaluate climate change feedback processes? *Journal of Climate*, **19 (15)**, 3445–3482, doi:10.1175/jcli3819.1.

Boville, B. A., P. J. Rasch, J. J. Hack, and J. R. McCaa, 2006: Representation of clouds and precipitation processes in the Community Atmosphere Model version 3 (CAM3). *Journal of Climate*, **19 (11)**, 2184–2198, doi:10.1175/JCLI3749.1.

Bretherton, C. S., 2015: Insights into low-latitude cloud feedbacks from high-resolution models. *Philosophical Transactions of the Royal Society A: Mathematical, Physical and Engineering Sciences*, **373 (2054)**, 20140 415, doi:10.1098/rsta.2014.0415.

Brient, F., T. Schneider, Z. Tan, S. Bony, X. Qu, and A. Hall, 2016: Shallowness of tropical low clouds as a predictor of climate models' response to warming. *Climate Dynamics*, **47 (1-2)**, 433–449, doi:10.1007/s00382-015-2846-0.

Byrne, M. P., and P. A. O'Gorman, 2013: Land–Ocean warming contrast over a wide range of climates: Convective quasi-equilibrium theory and idealized simulations. *Journal of Climate*, **26 (12)**, 4000–4016, doi:10.1175/jcli-d-12-00262.1.

Cai, M., 2005: Dynamical amplification of polar warming. *Geophysical Research Letters*, **32 (22)**, L22 710, doi:10.1029/2005gl024481.

Cai, M., 2006: Dynamical greenhouse-plus feedback and polar warming amplification. Part I: A dry radiative-transportive climate model. *Climate Dynamics*, **26 (7-8)**, 661–675, doi:10.1007/s00382-005-0104-6.

Caldwell, P. M., M. D. Zelinka, K. E. Taylor, and K. Marvel, 2016: Quantifying the sources of intermodel spread in equilibrium climate sensitivity. *Journal of Climate*, **29 (2)**, 513–524, doi:10.1175/JCLI-D-15-0352.1.

Ceppi, P., F. Brient, M. D. Zelinka, and D. L. Hartmann, 2017: Cloud feedback mechanisms and their representation in global climate models. *Wiley Interdisciplinary Reviews: Climate Change*, **8 (4)**, e465, doi:10.1002/wcc.465.

Ceppi, P., and J. M. Gregory, 2017: Relationship of tropospheric stability to climate sensitivity and Earth's observed radiation budget. *Proceedings of the National Academy of Sciences*, **114 (50)**, 13 126–13 131, doi:10.1073/pnas.1714308114.

Ceppi, P., D. L. Hartmann, and M. J. Webb, 2016: Mechanisms of the negative shortwave cloud feedback in middle to high latitudes. *Journal of Climate*, **29 (1)**, 139–157, doi:10.1175/JCLI-D-15-0327.1.

Ceppi, P., and P. Nowack, 2021: Observational evidence that cloud feedback amplifies global warming. *Proceedings of the National Academy of Sciences of the United States of America (PNAS)*, **118 (30)**, e2026290 118, doi:10.1073/pnas.2026290118.

Cesana, G. V., and A. D. Del Genio, 2021: Observational constraint on cloud feedbacks suggests moderate climate sensitivity. *Nature Climate Change*, **11 (3)**, 213–218, doi:10.1038/s41558-020-00970-y.

Cess, R., and Coauthors, 1990: Intercomparison and interpretation of climate feedback processes in 19 atmospheric general circulation models. *J. Geophys. Res.*, **95 (D10)**, 16 601, doi:10.1029/jd095id10p16601.

Cess, R., and Coauthors, 1996: Cloud feedback in atmospheric general circulation models: An update. *Journal of Geophysical Research: Atmospheres*, **101 (D8)**, 12 791–12 794, doi:10.1029/96JD00822.

Chepfer, H., S. Bony, D. Winker, G. Cesana, J. Dufresne, P. Minnis, C. Stubenrauch, and S. Zeng, 2010: The GCM-oriented calipso cloud product (CALIPSO-GOCCP). *Journal of Geophysical Research: Atmospheres*, **115 (D4)**, doi:10.1029/2009JD012251.

Clough, S., M. Shephard, E. Mlawer, J. Delamere, M. Iacono, K. Cady-Pereira, S. Boukabara, and P. Brown, 2005: Atmospheric radiative transfer modeling: A summary of the AER codes. *Journal of Quantitative Spectroscopy and Radiative Transfer*, **91 (2)**, 233–244, doi:10.1016/j.jqsrt.2004.05.058.

Collins, W. D., and Coauthors, 2004: Description of the NCAR community atmosphere model (CAM 3.0). *NCAR Tech. Note NCAR/TN-464+ STR*, **226**, URL http://www.cesm.ucar.edu/models/atm-cam/docs/description/description.pdf.

Colman, R., 2003: A comparison of climate feedbacks in general circulation models. *Climate Dynamics*, **20 (7-8)**, 865–873, doi:10.1007/s00382-003-0310-z.

Colman, R., and B. McAvaney, 1997: A study of general circulation model climate feedbacks determined from perturbed sea surface temperature experiments. *Journal of Geophysical Research: Atmospheres*, **102 (D16)**, 19 383–19 402, doi:10.1029/97JD00206.

Colman, R., and B. McAvaney, 2011: On tropospheric adjustment to forcing and climate feedbacks. *Climate dynamics*, **36 (9-10)**, 1649, doi:10.1007/s00382-011-1067-4.

Copernicus Climate Change Service (C3S), 2017: ERA5: Fifth generation of ECMWF atmospheric reanalyses of the global climate, Copernicus Climate Change Service Climate Data Store (CDS). URL https://cds.climate.copernicus.eu/cdsapp#!/home.

Dee, D. P., and Coauthors, 2011: The ERA-Interim reanalysis: Configuration and performance of the data assimilation system. *Quarterly Journal of the Royal Meteorological Society*, **137 (656)**, 553–597, doi:10.1002/qj.828.

Dolinar, E. K., X. Dong, B. Xi, J. H. Jiang, and H. Su, 2015: Evaluation of CMIP5 simulated clouds and TOA radiation budgets using NASA satellite observations. *Climate Dynamics*, **44 (7-8)**, 2229–2247, doi:10.1007/s00382-003-0369-6.

Dong, Y., K. C. Armour, M. D. Zelinka, C. Proistosescu, D. S. Battisti, C. Zhou, and T. Andrews, 2020: Intermodel spread in the pattern effect and its contribution to climate sensitivity in CMIP5 and CMIP6 models. *Journal of Climate*, **33 (18)**, 7755–7775, doi:10.1175/JCLI-D-19-1011.1.

Dong, Y., C. Proistosescu, K. C. Armour, and D. S. Battisti, 2019: Attributing historical and future evolution of radiative feedbacks to regional warming patterns using a Green's function approach: The preeminence of the western Pacific. *Journal of Climate*, **32 (17)**, 5471–5491, doi:10.1175/JCLI-D-18-0843.1.

Dufresne, J.-L., and S. Bony, 2008: An assessment of the primary sources of spread of global warming estimates from coupled atmosphere–ocean models. *Journal of Climate*, **21 (19)**, 5135–5144, doi:10.1175/2008JCLI2239.1.

Durack, P., and Coauthors, 2018: Toward standardized data sets for climate model experimentation. *Eos*, **99 (10.1029)**, doi:10.1029/2018EO101751.

Edwards, J. M., and A. Slingo, 1996: Studies with a flexible new radiation code. I: Choosing a configuration for a large-scale model. *Quarterly Journal of the Royal Meteorological Society*, **122 (531)**, 689–719, doi:10.1002/qj.49712253107.

Eyring, V., S. Bony, G. A. Meehl, C. A. Senior, B. Stevens, R. J. Stouffer, and K. E. Taylor, 2016: Overview of the Coupled Model Intercomparison Project Phase 6 (CMIP6) experimental design and organization. *Geoscientific Model Development*, **9 (5)**, 1937–1958, doi:10.5194/gmd-9-1937-2016.

Feldl, N., B. T. Anderson, and S. Bordoni, 2017a: Atmospheric eddies mediate lapse rate feedback and arctic amplification. *Journal of Climate*, **30 (22)**, 9213–9224, doi:10.1175/jcli-d-16-0706.1.

Feldl, N., and S. Bordoni, 2016: Characterizing the hadley circulation response through regional climate feedbacks. *Journal of Climate*, **29 (2)**, 613–622, doi:10.1175/jcli-d-15-0424.1.

Feldl, N., S. Bordoni, and T. M. Merlis, 2017b: Coupled high-latitude climate feedbacks and their impact on atmospheric heat transport. *Journal of Climate*, **30 (1)**, 189–201, doi:10.1175/JCLI-D-16-0324.1.

Feldl, N., and G. Roe, 2013a: Four perspectives on climate feedbacks. *Geophysical Research Letters*, **40 (15)**, 4007–4011, doi:10.1002/grl.50711.

Feldl, N., and G. H. Roe, 2013b: The nonlinear and nonlocal nature of climate feedbacks. *Journal of Climate*, **26 (21)**, 8289–8304, doi:10.1175/jcli-d-12-00631.1.

Frey, W. R., and J. E. Kay, 2018: The influence of extratropical cloud phase and amount feedbacks on climate sensitivity. *Climate dynamics*, **50 (7)**, 3097–3116, doi:10.1007/s00382-017-3796-5.

Frierson, D. M., I. M. Held, and P. Zurita-Gotor, 2006: A gray-radiation aquaplanet moist GCM. part i: Static stability and eddy scale. *Journal of the Atmospheric Sciences*, **63 (10)**, 2548–2566, doi:10.1175/jas3753.1.

Frierson, D. M. W., 2007: The dynamics of idealized convection schemes and their effect on the zonally averaged tropical circulation. *Journal of the Atmospheric Sciences*, **64 (6)**, 1959–1976, doi:10.1175/JAS3935.1.

Fröhlich, C., and J. Lean, 2004: Solar radiative output and its variability: evidence and mechanisms. *The Astronomy and Astrophysics Review*, **12 (4)**, 273–320, doi:10.1007/s00159-004-0024-1.

Gates, W. L., and Coauthors, 1999: An overview of the results of the Atmospheric Model Intercomparison Project (AMIP I). *Bulletin of the American Meteorological Society*, **80 (1)**, 29–56, doi:10.1175/1520-0477(1999)080<0029:AOOTRO>2.0.CO;2.

Geen, R., A. Czaja, and J. D. Haigh, 2016: The effects of increasing humidity on heat transport by extratropical waves. *Geophysical Research Letters*, **43 (15)**, 8314–8321, doi:10.1002/2016gl070214.

Geen, R., F. Lambert, and G. Vallis, 2018: Regime change behavior during Asian monsoon onset. *Journal of Climate*, **31 (8)**, 3327–3348, doi:10.1175/JCLI-D-17-0118.1.

Geen, R., F. H. Lambert, and G. K. Vallis, 2019: Processes and timescales in onset and withdrawal of “aquaplanet monsoons”. *Journal of the Atmospheric Sciences*, **76 (8)**, 2357–2373, doi:10.1175/JAS-D-18-0214.1.

Geoffroy, O., S. Sherwood, and D. Fuchs, 2017: On the role of the stratiform cloud scheme in the inter-model spread of cloud feedback. *Journal of Advances in Modeling Earth Systems*, **9 (1)**, 423–437, doi:10.1002/2016MS000846.

Gettelman, A., J. Kay, and K. Shell, 2012: The evolution of climate sensitivity and climate feedbacks in the Community Atmosphere Model. *Journal of Climate*, **25 (5)**, 1453–1469, doi:10.1175/JCLI-D-11-00197.1.

Giorgetta, M. A., and Coauthors, 2018: ICON-A, the atmosphere component of the ICON earth system model: I. Model description. *Journal of Advances in Modeling Earth Systems*, **10 (7)**, 1613–1637, doi:10.1029/2017MS001242.

Goosse, H., P.-Y. Barriat, M.-F. Loutre, and V. Zunz, 2010: *Introduction to climate dynamics and climate modeling*. Centre de recherche sur la Terre et le climat Georges Lemaître-UCLouvain, URL http://www.climate.be/textbook.

Goosse, H., and Coauthors, 2018: Quantifying climate feedbacks in polar regions. *Nature Communications*, **9 (1)**, doi:10.1038/s41467-018-04173-0.

Gordon, C. T., 1992: Comparison of 30-day integrations with and without cloud-radiation interaction. *Monthly Weather Review*, **120 (7)**, 1244–1277, doi:10.1175/1520-0493(1992)120<1244:CODIWA>2.0.CO;2.

Graversen, R. G., P. L. Langen, and T. Mauritsen, 2014: Polar amplification in CCSM4: Contributions from the lapse rate and surface albedo feedbacks. *Journal of Climate*, **27 (12)**, 4433–4450, doi:10.1175/jcli-d-13-00551.1.

Graversen, R. G., and M. Wang, 2009: Polar amplification in a coupled climate model with locked albedo. *Climate Dynamics*, **33 (5)**, 629–643, doi:10.1007/s00382-009-0535-6.

Gregory, D., D. Wilson, and A. Bushell, 2002: Insights into cloud parametrization provided by a prognostic approach. *Quarterly Journal of the Royal Meteorological Society*, **128 (583)**, 1485–1504, doi:10.1002/qj.200212858305.

Gregory, J., 2004: A new method for diagnosing radiative forcing and climate sensitivity. *Geophysical Research Letters*, **31 (3)**, L03 205, doi:10.1029/2003gl018747.

Guo, Z., and T. Zhou, 2014: An improved diagnostic stratocumulus scheme based on estimated inversion strength and its performance in GAMIL2. *Science China Earth Sciences*, **57 (11)**, 2637–2649, doi:10.1029/2005GL023851.

Hall, A., 2004: The role of surface albedo feedback in climate. *Journal of Climate*, **17 (7)**, 1550–1568, doi:10.1175/1520-0442(2004)017<1550:trosaf>2.0.co;2.

Hansen, J., A. Lacis, D. Rind, G. Russell, P. Stone, I. Fung, R. Ruedy, and J. Lerner, 1984: Climate sensitivity: Analysis of feedback mechanisms. *Climate Processes and Climate Sensitivity, Geophysical Monograph*, **29**, 130–163, doi:10.1029/GM029p0130.

Hansen, J., M. Sato, and R. Ruedy, 1997: Radiative forcing and climate response. *Journal of Geophysical Research: Atmospheres*, **102 (D6)**, 6831–6864, doi:10.1029/96jd03436.

Hansen, J., and Coauthors, 2005: Efficacy of climate forcings. *Journal of Geophysical Research D: Atmospheres*, **110 (18)**, 1–45, doi:10.1029/2005JD005776.

Hansen, J. E., and L. D. Travis, 1974: Light scattering in planetary atmospheres. *Space science reviews*, **16 (4)**, 527–610, doi:10.1007/BF00168069.

Hartmann, D. L., 2016: *Global physical climatology*. 2nd ed., Elsevier, Boston, 485 pp., doi:10.1016/C2009-0-00030-0.

Hartmann, D. L., and K. Larson, 2002: An important constraint on tropical cloud-climate feedback. *Geophysical research letters*, **29 (20)**, 12–1, doi:10.1029/2002GL015835.

Held, I. M., and K. M. Shell, 2012: Using relative humidity as a state variable in climate feedback analysis. *Journal of Climate*, **25 (8)**, 2578–2582, doi:10.1175/JCLI-D-11-00721.1.

Held, I. M., and B. J. Soden, 2000: Water vapor feedback and global warming. *Annual review of energy and the environment*, **25 (1)**, 441–475, doi:10.1146/annurev.energy.25.1.441.

Hersbach, H., and Coauthors, 2020: The ERA5 global reanalysis. *Quarterly Journal of the Royal Meteorological Society*, **146 (730)**, 1999–2049, doi:10.1002/qj.3803.

Heymsfield, A. J., and L. M. Miloshevich, 1993: Homogeneous ice nucleation and supercooled liquid water in orographic wave clouds. *Journal of the Atmospheric Sciences*, **50 (15)**, 2335–2353, doi:10.1175/1520-0469(1993)050<2335:HINASL>2.0.CO;2.

Holloway, J. L., and S. Manabe, 1971: Simulation of climate by a global general circulation model. *Monthly Weather Review*, **99 (5)**, 335–370, doi:10.1175/1520-0493(1971)099<0335:>2.3.CO;2.

Hourdin, F., and Coauthors, 2017: The art and science of climate model tuning. *Bulletin of the American Meteorological Society*, **98 (3)**, 589–602, doi:10.1175/BAMS-D-15-00135.1.

Houze, R. A., 2014: *Cloud dynamics*, International Geophysics, Vol. 104. 2nd ed., Academic Press, San Diego, 432 pp., URL https://www.sciencedirect.com/bookseries/international-geophysics/vol/104.

Huang, Y., Y. Xia, and X. Tan, 2017: On the pattern of CO2 radiative forcing and poleward

energy transport. *Journal of Geophysical Research: Atmospheres*, **122 (20)**, 10,578–10,593, doi:10.1002/2017jd027221.

IPCC, 2007: *Fourth Assessment Report: Climate Change 2007: The AR4 Synthesis Report*. Geneva: IPCC, URL https://www.ipcc.ch/report/ar4/syr.

Johannessen, O. M., and Coauthors, 2004: Arctic climate change: Observed and modelled temperature and sea-ice variability. *Tellus A*, **56 (4)**, 328–341, doi:10.1111/j.1600-0870.2004.00060.x.

Jones, C. G., K. Wyser, A. Ullerstig, and U. Willén, 2004: The Rossby Centre regional atmospheric climate model part II: Application to the Arctic climate. *AMBIO: A Journal of the Human Environment*, **33 (4)**, 211–220, doi:10.1579/0044-7447-33.4.211.

Joshi, M., M. Stringer, K. Wiel, A. O'Callaghan, and S. Fueglistaler, 2015: IGCM4: a fast, parallel and flexible intermediate climate model. *Geoscientific Model Development*, **8 (4)**, 1157–1167, doi:10.5194/gmd-8-1157-2015.

Kawai, H., and T. Inoue, 2006: A simple parameterization scheme for subtropical marine stratocumulus. *SOLA*, **2**, 17–20, doi:10.2151/sola.2006-005.

Kawai, H., T. Koshiro, and M. J. Webb, 2017: Interpretation of factors controlling low cloud cover and low cloud feedback using a unified predictive index. *Journal of Climate*, **30 (22)**, 9119–9131, doi:10.1175/JCLI-D-16-0825.1.

Kawai, H., S. Yukimoto, T. Koshiro, N. Oshima, T. Tanaka, H. Yoshimura, and R. Nagasawa, 2019: Significant improvement of cloud representation in the global climate model MRI-ESM2. *Geoscientific Model Development*, **12 (7)**, 2875–2897, doi:10.5194/gmd-12-2875-2019.

Kay, J., and Coauthors, 2012: Exposing global cloud biases in the Community Atmosphere Model (CAM) using satellite observations and their corresponding instrument simulators. *Journal of Climate*, **25 (15)**, 5190–5207, doi:10.1175/JCLI-D-11-00469.1.

Kiehl, J., 1994: On the observed near cancellation between longwave and shortwave cloud forcing in tropical regions. *Journal of Climate*, **7**, 559–565, doi:10.1175/1520-0442(1994)007<0559:OTONCB>2.0.CO;2.

Kim, D., S. M. Kang, Y. Shin, and N. Feldl, 2018: Sensitivity of polar amplification to varying insolation conditions. *Journal of Climate*, **31 (12)**, 4933–4947, doi:10.1175/jcli-d-17-0627.1.

Klein, S. A., A. Hall, J. R. Norris, and R. Pincus, 2017: Low-cloud feedbacks from cloud-controlling factors: A review. *Shallow clouds, water vapor, circulation, and climate sensitivity*, **38**, 135–157, doi:10.1007/s10712-017-9433-3.

Klein, S. A., and D. L. Hartmann, 1993: The seasonal cycle of low stratiform clouds. *Journal of Climate*, **6 (8)**, 1587–1606, doi:10.1175/1520-0442(1993)006<1587:TSCOLS>2.0.CO;2.

Klein, S. A., and C. Jakob, 1999: Validation and sensitivities of frontal clouds simulated by the ECMWF model. *Monthly weather review*, **127 (10)**, 2514–2531, doi:10.1175/1520-0493(1999)127<2514:VASOFC>2.0.CO;2.

Klein, S. A., Y. Zhang, M. D. Zelinka, R. Pincus, J. Boyle, and P. J. Gleckler, 2013: Are climate model simulations of clouds improving? An evaluation using the IS-

CCP simulator. *Journal of Geophysical Research: Atmospheres*, **118 (3)**, 1329–1342, doi:10.1002/jgrd.50141.

Korolev, A., and Coauthors, 2017: Mixed-phase clouds: Progress and challenges. *Meteorological Monographs*, **58**, 5–1, doi:10.1175/AMSMONOGRAPHS-D-17-0001.1.

Kuang, Z., and D. L. Hartmann, 2007: Testing the fixed anvil temperature hypothesis in a cloud-resolving model. *Journal of Climate*, **20 (10)**, 2051–2057, doi:10.1175/JCLI4124.1.

Kuma, P., and Coauthors, 2020: Evaluation of Southern Ocean cloud in the HadGEM3 general circulation model and MERRA-2 reanalysis using ship-based observations. *Atmospheric Chemistry and Physics*, **20 (11)**, 6607–6630, doi:10.5194/acp-20-6607-2020.

Langen, P. L., and V. A. Alexeev, 2007: Polar amplification as a preferred response in an idealized aquaplanet GCM. *Climate Dynamics*, **29 (2-3)**, 305–317, doi:10.1007/s00382-006-0221-x.

Langen, P. L., R. G. Graversen, and T. Mauritsen, 2012: Separation of contributions from radiative feedbacks to polar amplification on an aquaplanet. *Journal of Climate*, **25 (8)**, 3010–3024, doi:10.1175/jcli-d-11-00246.1.

Lauer, A., and K. Hamilton, 2013: Simulating clouds with global climate models: A comparison of CMIP5 results with CMIP3 and satellite data. *Journal of Climate*, **26 (11)**, 3823–3845, doi:10.1175/JCLI-D-12-00451.1.

Le Treut, H., and Z.-X. Li, 1991: Sensitivity of an atmospheric general circulation model to prescribed SST changes: feedback effects associated with the simulation of optical properties. *Climate Dynamics*, **5**, 175–187, doi:10.1007/BF00251808.

Lenaerts, J. T., K. Van Tricht, S. Lhermitte, and T. S. L'Ecuyer, 2017: Polar clouds and radiation in satellite observations, reanalyses, and climate models. *Geophysical Research Letters*, **44 (7)**, 3355–3364, doi:10.1002/2016GL072242.

Li, J., J. Mao, and F. Wang, 2017: Comparative study of five current reanalyses in characterizing total cloud fraction and top-of-the-atmosphere cloud radiative effects over the Asian monsoon region. *International Journal of Climatology*, **37 (15)**, 5047–5067, doi:10.1002/joc.5143.

Liou, K., S. Ou, Y. Takano, F. Valero, and T. Ackerman, 1990: Remote sounding of the tropical cirrus cloud temperature and optical depth using 6.5 and 10.5 μm radiometers during STEP. *Journal of Applied Meteorology and Climatology*, **29 (8)**, 716–726, doi:10.1175/1520-0450(1990)029<0716:RSOTTC>2.0.CO;2.

Liu, Q., 2020: Radiative kernels for Isca v1.0. Zenodo, URL https://github.com/lqxyz/Isca_kernels, doi:10.5281/zenodo.4282681.

Liu, Q., M. Collins, P. Maher, S. I. Thomson, and G. K. Vallis, 2021: SimCloud version 1.0: a simple diagnostic cloud scheme for idealized climate models. *Geoscientific Model Development*, **14 (5)**, 2801–2826, doi:10.5194/gmd-14-2801-2021.

Liu, R., H. Su, K. Liou, J. H. Jiang, Y. Gu, S. C. Liu, and C. Shiu, 2018: An assessment of tropospheric water vapor feedback using radiative kernels. *Journal of Geophysical Research: Atmospheres*, **123 (3)**, 1499–1509, doi:10.1002/2017jd027512.

Loeb, N. G., B. A. Wielicki, D. R. Doelling, G. L. Smith, D. F. Keyes, S. Kato, N. Manalo-Smith, and T. Wong, 2009: Toward optimal closure of the Earth's top-of-atmosphere radiation budget. *Journal of Climate*, **22 (3)**, 748–766, doi:10.1175/2008JCLI2637.1.

Loeb, N. G., and Coauthors, 2018: Clouds and the earth's radiant energy system (CERES) energy balanced and filled (EBAF) top-of-atmosphere (TOA) edition-4.0 data product. *Journal of Climate*, **31 (2)**, 895–918, doi:10.1175/JCLI-D-17-0208.1.

Lutsko, N. J., M. Popp, R. H. Nazarian, and A. L. Albright, 2021: Emergent constraints on regional cloud feedbacks. *Geophysical Research Letters*, e2021GL092934, doi:10.1029/2021GL092934.

Maher, P., and Coauthors, 2019: Model hierarchies for understanding atmospheric circulation. *Reviews of Geophysics*, **57**, doi:10.1029/2018RG000607.

Manabe, S., and R. T. Wetherald, 1975: The effects of doubling the CO2 concentration on the climate of a general circulation model. *Journal of the Atmospheric Sciences*, **32 (1)**, 3–15, doi:10.1175/1520-0469(1975)032<0003:TEODTC>2.0.CO;2.

Manners, J., J. M. Edwards, P. Hill, and J.-C. Thelen, 2015: SOCRATES (Suite Of Community RAdiative Transfer codes based on Edwards and Slingo) Technical Guide. Met Office, UK, URL https://code.metoffice.gov.uk/trac/socrates.

Mauritsen, T., 2016: Clouds cooled the Earth. *Nature Geoscience*, **9 (12)**, 865–867, doi:10.1038/ngeo2838.

Mauritsen, T., and Coauthors, 2012: Tuning the climate of a global model. *Journal of advances in modeling Earth systems*, **4 (3)**, doi:10.1029/2012MS000154.

McCoy, D. T., R. Eastman, D. L. Hartmann, and R. Wood, 2017: The change in low cloud cover in a warmed climate inferred from AIRS, MODIS, and ERA-Interim. *Journal of Climate*, **30 (10)**, 3609–3620, doi:10.1175/JCLI-D-15-0734.1.

McCoy, D. T., I. Tan, D. L. Hartmann, M. D. Zelinka, and T. Storelvmo, 2016: On the relationships among cloud cover, mixed-phase partitioning, and planetary albedo in GCMs. *Journal of Advances in Modeling Earth Systems*, **8 (2)**, 650–668, doi:10.1002/2015MS000589.

Medeiros, B., and B. Stevens, 2011: Revealing differences in gcm representations of low clouds. *Climate dynamics*, **36 (1-2)**, 385–399, doi:10.1007/s00382-009-0694-5.

Merlis, T. M., and M. Henry, 2018: Simple estimates of polar amplification in moist diffusive energy balance models. *Journal of Climate*, **31 (15)**, 5811–5824, doi:10.1175/jcli-d-17-0578.1.

Michibata, T., K. Suzuki, M. Sekiguchi, and T. Takemura, 2019: Prognostic precipitation in the MIROC6-SPRINTARS GCM: description and evaluation against satellite observations. *Journal of Advances in Modeling Earth Systems*, **11 (3)**, 839–860, doi:10.1029/2018MS001596.

Ming, Y., and I. M. Held, 2018: Modeling water vapor and clouds as passive tracers in an idealized GCM. *Journal of Climate*, **31 (2)**, 775–786, doi:10.1175/JCLI-D-16-0812.1.

Moorthi, S., and M. J. Suarez, 1992: Relaxed Arakawa-Schubert. A parameterization of moist convection for general circulation models. *Monthly Weather Review*, **120 (6)**, 978–1002, doi:10.1175/1520-0493(1992)120<0978:RASAPO>2.0.CO;2.

Morcrette, J.-J., and Y. Fouquart, 1986: The overlapping of cloud layers in shortwave radiation parameterizations. *Journal of the Atmospheric Sciences*, **43 (4)**, 321–328, doi:10.1175/1520-0469(1986)043<0321:TOOCLI>2.0.CO;2.

Morcrette, J.-J., and C. Jakob, 2000: The response of the ECMWF model to changes in the cloud overlap assumption. *Monthly Weather Review*, **128 (6)**, 1707–1732, doi:10.1175/1520-0493(2000)128<1707:TROTEM>2.0.CO;2.

Mülmenstädt, J., and Coauthors, 2021: An underestimated negative cloud feedback from cloud lifetime changes. *Nature Climate Change*, **11 (6)**, 508–513, doi:10.1038/s41558-021-01038-1.

Murphy, D., S. Solomon, R. Portmann, K. Rosenlof, P. Forster, and T. Wong, 2009: An observationally based energy balance for the Earth since 1950. *Journal of Geophysical Research: Atmospheres*, **114 (D17)**, doi:10.1029/2009JD012105.

Murphy, J. M., D. M. Sexton, D. N. Barnett, G. S. Jones, M. J. Webb, M. Collins, and D. A. Stainforth, 2004: Quantification of modelling uncertainties in a large ensemble of climate change simulations. *Nature*, **430 (7001)**, 768–772, doi:10.1038/nature02771.

Myers, T. A., and J. R. Norris, 2015: On the relationships between subtropical clouds and meteorology in observations and CMIP3 and CMIP5 models. *Journal of Climate*, **28 (8)**, 2945–2967, doi:10.1175/JCLI-D-14-00475.1.

Myers, T. A., and J. R. Norris, 2016: Reducing the uncertainty in subtropical cloud feedback. *Geophysical Research Letters*, **43 (5)**, 2144–2148, doi:10.1002/2015GL067416.

Myers, T. A., R. C. Scott, M. D. Zelinka, S. A. Klein, J. R. Norris, and P. M. Caldwell, 2021: Observational constraints on low cloud feedback reduce uncertainty of climate sensitivity. *Nature Climate Change*, **11**, 501–507, doi:10.1038/s41558-021-01039-0.

Nam, C., S. Bony, J.-L. Dufresne, and H. Chepfer, 2012: The 'too few, too bright' tropical low-cloud problem in CMIP5 models. *Geophysical Research Letters*, **39 (21)**, doi:10.1029/2012GL053421.

Ose, T., 1993: An examination of the effects of explicit cloud water in the UCLA GCM. *Journal of the Meteorological Society of Japan. Ser. II*, **71 (1)**, 93–109, doi:10.2151/jmsj1965.71.1_93.

O'Gorman, P. A., and T. Schneider, 2008: The hydrological cycle over a wide range of climates simulated with an idealized GCM. *Journal of Climate*, **21 (15)**, 3815–3832, doi:10.1175/2007JCLI2065.1.

Painemal, D., and P. Minnis, 2012: On the dependence of albedo on cloud microphysics over marine stratocumulus clouds regimes determined from Clouds and the Earth's Radiant Energy System (CERES) data. *Journal of Geophysical Research: Atmospheres*, **117 (D6)**, doi:10.1029/2011JD017120.

Park, K., S. M. Kang, D. Kim, M. F. Stuecker, and F.-F. Jin, 2018: Contrasting local and remote impacts of surface heating on polar warming and amplification. *Journal of Climate*, **31 (8)**, 3155–3166, doi:10.1175/jcli-d-17-0600.1.

Park, S., C. S. Bretherton, and P. J. Rasch, 2014: Integrating cloud processes in the Community Atmosphere Model, version 5. *Journal of Climate*, **27 (18)**, 6821–6856, doi:10.1175/JCLI-D-14-00087.1.

Park, S., and J. Shin, 2019: Heuristic estimation of low-level cloud fraction over the globe based on a decoupling parameterization. *Atmospheric Chemistry and Physics*, **19 (8)**, 5635–5660, doi:10.5194/acp-19-5635-2019.

Parkinson, C. L., A. Ward, and M. D. King, 2006: *Earth science reference handbook: a guide to NASA's earth science program and earth observing satellite missions*. National Aeronautics and Space Administration, URL https://eospso.gsfc.nasa.gov/sites/default/files/publications/2006ReferenceHandbook.pdf.

Pendergrass, A. G., A. Conley, and F. M. Vitt, 2018: Surface and top-of-atmosphere radiative feedback kernels for CESM-CAM5. *Earth System Science Data*, **10 (1)**, 317–324, doi:10.5194/essd-10-317-2018.

Pietschnig, M., F. Lambert, M. Saint-Lu, and G. Vallis, 2019: The presence of Africa and limited soil moisture contribute to future drying of South America. *Geophysical Research Letters*, **46 (21)**, 12 445–12 453, doi:10.1029/2019GL084441.

Pithan, F., and T. Mauritsen, 2014: Arctic amplification dominated by temperature feedbacks in contemporary climate models. *Nature Geoscience*, **7 (3)**, 181–184, doi:10.1038/ngeo2071.

Po-Chedley, S., K. C. Armour, C. M. Bitz, M. D. Zelinka, B. D. Santer, and Q. Fu, 2018: Sources of intermodel spread in the lapse rate and water vapor feedbacks. *Journal of Climate*, **31 (8)**, 3187–3206, doi:10.1175/JCLI-D-17-0674.1.

Polyakov, I. V., and Coauthors, 2002: Observationally based assessment of polar amplification of global warming. *Geophysical Research Letters*, **29 (18)**, 25–1–25–4, doi:10.1029/2001gl011111.

Pope, V., M. Gallani, P. Rowntree, and R. Stratton, 2000: The impact of new physical parametrizations in the Hadley Centre climate model: HadAM3. *Climate Dynamics*, **16 (2-3)**, 123–146, doi:10.1007/s003820050009.

Qin, Y., and Y. Lin, 2018: Alleviated double ITCZ problem in the NCAR CESM1: A new cloud scheme and the working mechanisms. *Journal of Advances in Modeling Earth Systems*, **10 (9)**, 2318–2332, doi:10.1029/2018MS001343.

Qin, Y., Y. Lin, S. Xu, H. Y. Ma, and S. Xie, 2018: A diagnostic PDF cloud scheme to improve subtropical low clouds in NCAR Community Atmosphere Model (CAM5). *Journal of Advances in Modeling Earth Systems*, **10 (2)**, 320–341, doi:10.1002/2017MS001095.

Qu, X., A. Hall, S. A. Klein, and P. M. Caldwell, 2014: On the spread of changes in marine low cloud cover in climate model simulations of the 21st century. *Climate Dynamics*, **42 (9-10)**, 2603–2626, doi:10.1007/s00382-013-1945-z.

Qu, X., A. Hall, S. A. Klein, and P. M. Caldwell, 2015a: The strength of the tropical inversion and its response to climate change in 18 CMIP5 models. *Climate Dynamics*, **45 (1-2)**, 375–396, doi:10.1007/s00382-014-2441-9.

Qu, X., A. Hall, S. A. Klein, and A. M. DeAngelis, 2015b: Positive tropical marine low-cloud cover feedback inferred from cloud-controlling factors. *Geophysical Research Letters*, **42 (18)**, 7767–7775, doi:10.1002/2015GL065627.

Quaas, J., 2012: Evaluating the critical relative humidity as a measure of subgrid-scale variability of humidity in general circulation model cloud cover parameteri-

zations using satellite data. *Journal of Geophysical Research*, **117 (D9)**, D09 208, doi:10.1029/2012JD017495.

Ramanathan, V., R. Cess, E. Harrison, P. Minnis, B. Barkstrom, E. Ahmad, and D. Hartmann, 1989: Cloud-radiative forcing and climate: Results from the Earth Radiation Budget Experiment. *Science*, **243 (4887)**, 57–63, doi:10.1126/science.243.4887.57.

Ramanathan, V., P. Crutzen, J. Kiehl, and D. Rosenfeld, 2001: Aerosols, climate, and the hydrological cycle. *science*, **294 (5549)**, 2119–2124, doi:10.1126/science.1064034.

Randall, D., M. Khairoutdinov, A. Arakawa, and W. Grabowski, 2003: Breaking the cloud parameterization deadlock. *Bulletin of the American Meteorological Society*, **84 (11)**, 1547–1564, doi:10.1175/BAMS-84-11-1547.

Randall, D. A., 1989: Cloud parameterization for climate modeling: Status and prospects. *Atmospheric Research*, **23**, 345–361, doi:10.1016/0169-8095(89)90025-2.

Ricketts, J., 1973: An investigation into a relationship between upper-air relative humidity and cloud cover. *Meteor. Mag*, **102**, 146–153.

Rieck, M., L. Nuijens, and B. Stevens, 2012: Marine boundary layer cloud feedbacks in a constant relative humidity atmosphere. *Journal of the Atmospheric Sciences*, **69 (8)**, 2538–2550, doi:10.1175/JAS-D-11-0203.1.

Roehrig, R., and Coauthors, 2020: The CNRM global atmosphere model ARPEGE-Climat 6.3: description and evaluation. *Journal of Advances in Modeling Earth Systems*, e2020MS002075, doi:10.1029/2020MS002075.

Rossow, W. B., and R. A. Schiffer, 1991: ISCCP Cloud Data Products. *Bulletin of the American Meteorological Society*, **72 (1)**, 2–20, doi:10.1175/1520-0477(1991)072<0002:ICDP>2.0.CO;2.

Rossow, W. B., and R. A. Schiffer, 1999: Advances in understanding clouds from ISCCP. *Bulletin of the American Meteorological Society*, **80 (11)**, 2261–2288, doi:10.1175/1520-0477(1999)080<2261:AIUCFI>2.0.CO;2.

Russell, G. L., J. R. Miller, and L.-C. Tsang, 1985: Seasonal oceanic heat transports computed from an atmospheric model. *Dynamics of atmospheres and Oceans*, **9 (3)**, 253–271, doi:10.1016/0377-0265(85)90022-3.

Ryan, B., 1996: On the global variation of precipitating layer clouds. *Bulletin of the American Meteorological Society*, **77 (1)**, 53–70, doi:10.1175/1520-0477(1996)077<0053:OTGVOP>2.0.CO;2.

Schiffer, R. A., and W. B. Rossow, 1983: The International Satellite Cloud Climatology Project (ISCCP): The First Project of the World Climate Research Programme. *Bulletin of the American Meteorological Society*, **64 (7)**, 779–784, doi:10.1175/1520-0477-64.7.779.

Schneider, E. K., B. P. Kirtman, and R. S. Lindzen, 1999: Tropospheric water vapor and climate sensitivity. *Journal of the Atmospheric Sciences*, **56 (11)**, 1649–1658, doi:10.1175/1520-0469(1999)056<1649:twvacs>2.0.co;2.

Schneider, T., C. M. Kaul, and K. G. Pressel, 2019: Possible climate transitions from breakup of stratocumulus decks under greenhouse warming. *Nature Geoscience*, **12 (3)**, 163, doi:10.1038/s41561-019-0310-1.

Scott, R. C., T. A. Myers, J. R. Norris, M. D. Zelinka, S. A. Klein, M. Sun, and D. R. Doelling, 2020: Observed sensitivity of low-cloud radiative effects to meteorological perturbations over the global oceans. *Journal of Climate*, **33 (18)**, 7717–7734, doi:10.1175/JCLI-D-19-1028.1.

Screen, J., C. Deser, and I. Simmonds, 2012: Local and remote controls on observed arctic warming. *Geophysical Research Letters*, **39 (10)**, L10 709, doi:10.1029/2012gl051598.

Screen, J. A., and I. Simmonds, 2010: The central role of diminishing sea ice in recent arctic temperature amplification. *Nature*, **464 (7293)**, 1334–1337, doi:10.1038/nature09051.

Seethala, C., J. R. Norris, and T. A. Myers, 2015: How has subtropical stratocumulus and associated meteorology changed since the 1980s? *Journal of Climate*, **28 (21)**, 8396–8410, doi:10.1175/JCLI-D-15-0120.1.

Serreze, M. C., and R. G. Barry, 2011: Processes and impacts of arctic amplification: A research synthesis. *Global and Planetary Change*, **77 (1-2)**, 85–96, doi:10.1016/j.gloplacha.2011.03.004.

Serreze, M. C., and J. A. Francis, 2006: The arctic amplification debate. *Climatic Change*, **76 (3-4)**, 241–264, doi:10.1007/s10584-005-9017-y.

Shell, K. M., J. T. Kiehl, and C. A. Shields, 2008: Using the radiative kernel technique to calculate climate feedbacks in NCAR's community atmospheric model. *Journal of Climate*, **21 (10)**, 2269–2282, doi:10.1175/2007jcli2044.1.

Sherwood, S., and Coauthors, 2020: An assessment of Earth's climate sensitivity using multiple lines of evidence. *Reviews of Geophysics*, **58 (4)**, e2019RG000 678, doi:10.1029/2019RG000678.

Sherwood, S. C., S. Bony, and J.-L. Dufresne, 2014: Spread in model climate sensitivity traced to atmospheric convective mixing. *Nature*, **505 (7481)**, 37–42, doi:10.1038/nature12829.

Sherwood, S. C., W. Ingram, Y. Tsushima, M. Satoh, M. Roberts, P. L. Vidale, and P. A. O'Gorman, 2010: Relative humidity changes in a warmer climate. *Journal of Geophysical Research: Atmospheres*, **115 (D9)**, doi:10.1029/2009JD012585.

Siebesma, A. P., S. Bony, C. Jakob, and B. Stevens, 2020: *Clouds and Climate: Climate Science's Greatest Challenge*. Cambridge University Press, doi:10.1017/9781107447738.

Slingo, A., 1990: Sensitivity of the Earth's radiation budget to changes in low clouds. *Nature*, **343 (6253)**, 49, doi:10.1038/343049a0.

Slingo, A., and H. Schrecker, 1982: On the shortwave radiative properties of stratiform water clouds. *Quarterly Journal of the Royal Meteorological Society*, **108 (456)**, 407–426, doi:10.1002/qj.49710845607.

Slingo, J. M., 1980: A cloud parametrization scheme derived from GATE data for use with a numerical model. *Quarterly Journal of the Royal Meteorological Society*, **106 (450)**, 747–770, doi:10.1002/qj.49710645008.

Slingo, J. M., 1987: The development and verification of a cloud prediction scheme for

the ECMWF model. *Quarterly Journal of the Royal Meteorological Society*, **113 (477)**, 899–927, doi:10.1002/qj.49711347710.

Smagorinsky, J., 1960: On the dynamical prediction of large-scale condensation by numerical methods. *Geophys. Monogr.*, H. Weickmann, Ed., Vol. 5, American Geophysical Union, 71–78, doi:10.1029/GM005p0071.

Smith, C. J., R. J. Kramer, and A. Sima, 2020: The hadgem3-ga7.1 radiative kernel: the importance of a well-resolved stratosphere. *Earth System Science Data*, **12 (3)**, 2157–2168, doi:10.5194/essd-12-2157-2020.

Smith, R. N. B., 1990: A scheme for predicting layer clouds and their water content in a general circulation model. *Quarterly Journal of the Royal Meteorological Society*, **116 (492)**, 435–460, doi:10.1002/qj.49711649210.

Sobel, A. H., J. Nilsson, and L. M. Polvani, 2001: The weak temperature gradient approximation and balanced tropical moisture waves. *Journal of the atmospheric sciences*, **58 (23)**, 3650–3665, doi:10.1175/1520-0469(2001)058<3650:TWTGAA>2.0.CO;2.

Soden, B. J., A. J. Broccoli, and R. S. Hemler, 2004: On the use of cloud forcing to estimate cloud feedback. *Journal of Climate*, **17 (19)**, 3661–3665, doi:10.1175/1520-0442(2004)017<3661:OTUOCF>2.0.CO;2.

Soden, B. J., and I. M. Held, 2006: An assessment of climate feedbacks in coupled Ocean–Atmosphere models. *Journal of Climate*, **19 (14)**, 3354–3360, doi:10.1175/jcli3799.1.

Soden, B. J., I. M. Held, R. Colman, K. M. Shell, J. T. Kiehl, and C. A. Shields, 2008: Quantifying climate feedbacks using radiative kernels. *Journal of Climate*, **21 (14)**, 3504–3520, doi:10.1175/2007jcli2110.1.

Sommeria, G., and J. W. Deardorff, 1977: Subgrid-scale condensation in models of nonprecipitating clouds. *Journal of the Atmospheric Sciences*, **34**, 344–355, doi:10.1175/1520-0469(1977)034<0344:SSCIMO>2.0.CO;2.

Stensrud, D. J., 2007: *Parameterization schemes: Keys to understanding numerical weather prediction models*. Cambridge University Press, Cambridge, doi:10.1017/cbo9780511812590.

Stephens, G. L., 1978: Radiation profiles in extended water clouds. II: Parameterization schemes. *Journal of Atmospheric Sciences*, **35 (11)**, 2123–2132, doi:10.1175/1520-0469(1978)035<2123:RPIEWC>2.0.CO;2.

Stephens, G. L., 2005: Cloud feedbacks in the climate system: A critical review. *Journal of climate*, **18 (2)**, 237–273, doi:10.1175/JCLI-3243.1.

Stephens, G. L., and Coauthors, 2012: An update on Earth's energy balance in light of the latest global observations. *Nature Geoscience*, **5 (10)**, 691–696, doi:10.1038/ngeo1580.

Stocker, T. F., and Coauthors, 2013: *Climate change 2013: The physical science basis*. Cambridge University Press, Cambridge, 1535 pp., doi:10.1017/CBO9781107415324.

Storelvmo, T., I. Tan, and A. V. Korolev, 2015: Cloud phase changes induced by CO_2 warming–A powerful yet poorly constrained cloud-climate feedback. *Current climate change reports*, **1 (4)**, 288–296, doi:10.1007/s40641-015-0026-2.

Stubenrauch, C., and Coauthors, 2013: Assessment of global cloud datasets from satellites: Project and database initiated by the GEWEX radiation panel. *Bulletin of the American Meteorological Society*, **94 (7)**, 1031–1049, doi:10.1175/BAMS-D-12-00117.1.

Sundqvist, H., 1978: A parametrization scheme for non-convective condenstion including prediction of cloud water content. *Quarterly Journal of the Royal Meteorological Society*, **104**, 677–690, doi:10.1002/qj.49710444110.

Sundqvist, H., E. Berge, and J. E. Kristjánsson, 1989: Condensation and cloud parameterization studies with a mesoscale numerical weather prediction model. *Monthly Weather Review*, **117 (8)**, 1641–1657, doi:10.1175/1520-0493(1989)117<1641:CACPSW>2.0.CO;2.

Swales, D. J., R. Pincus, and A. Bodas-Salcedo, 2018: The Cloud Feedback Model Intercomparison Project Observational Simulator Package: Version 2. *Geoscientific Model Development*, **11 (1)**, 77–81, doi:10.5194/gmd-11-77-2018.

Tan, I., T. Storelvmo, and M. D. Zelinka, 2016: Observational constraints on mixed-phase clouds imply higher climate sensitivity. *Science*, **352 (6282)**, 224–227, doi:10.1126/science.aad5300.

Taylor, K., D. Williamson, and F. Zwiers, 2000: The sea surface temperature and sea-ice concentration boundary concentrations for AMIP II simulations. *PMCDI Report*, **60**, URL https://pcmdi.llnl.gov/report/pdf/60.pdf?id=84.

Taylor, K. E., 2001: Summarizing multiple aspects of model performance in a single diagram. *Journal of Geophysical Research: Atmospheres*, **106 (D7)**, 7183–7192, doi:10.1029/2000JD900719.

Taylor, K. E., R. J. Stouffer, and G. A. Meehl, 2012: An overview of CMIP5 and the experiment design. *Bulletin of the American meteorological Society*, **93 (4)**, 485–498, doi:10.1175/BAMS-D-11-00094.1.

Taylor, P. C., M. Cai, A. Hu, J. Meehl, W. Washington, and G. J. Zhang, 2013: A decomposition of feedback contributions to polar warming amplification. *Journal of Climate*, **26 (18)**, 7023–7043, doi:10.1175/jcli-d-12-00696.1.

Thomson, S. I., and G. K. Vallis, 2018: Atmospheric response to SST anomalies. Part I: Background-state dependence, teleconnections, and local effects in winter. *Journal of the Atmospheric Sciences*, **75 (12)**, 4107–4124, doi:10.1175/JAS-D-17-0297.1.

Thomson, S. I., and G. K. Vallis, 2019: Hierarchical modeling of solar system planets with Isca. *Atmosphere*, **10 (12)**, 803, doi:10.3390/atmos10120803.

Tiedtke, M., 1993: Representation of clouds in large-scale models. *Monthly Weather Review*, **121**, 3040–3061, doi:10.1175/1520-0493(1993)121<3040:ROCILS>2.0.CO;2.

Tompkins, A. M., 2002: A prognostic parameterization for the subgrid-scale variability of water vapor and clouds in large-scale models and its use to diagnose cloud cover. *Journal of the Atmospheric Sciences*, **59 (12)**, 1917–1942, doi:10.1175/1520-0469(2002)059<1917:APPFTS>2.0.CO;2.

Tompkins, A. M., 2005: The parametrization of cloud cover. *ECMWF Moist Processes Lecture Note Series*, URL https://www.ecmwf.int/node/16958.

Tsang, Y.-K., and G. K. Vallis, 2018: A stochastic Lagrangian basis for a probabilistic parameterization of moisture condensation in Eulerian models. *J. Atmos. Sci.*, **75 (11)**, 3925–3941, doi:10.1175/jas-d-18-0065.1.

Vallis, G. K., and Coauthors, 2018: Isca, v1.0: A framework for the global modelling of the atmospheres of earth and other planets at varying levels of complexity. *Geoscientific Model Development*, **11 (3)**, 843–859, doi:10.5194/gmd-11-843-2018.

Vavrus, S., 2004: The impact of cloud feedbacks on Arctic climate under greenhouse forcing. *Journal of Climate*, **17 (3)**, 603–615, doi:10.1175/1520-0442(2004)017<0603:tiocfo>2.0.co;2.

Vavrus, S., and D. Waliser, 2008: An improved parameterization for simulating Arctic cloud amount in the CCSM3 climate model. *Journal of Climate*, **21 (21)**, 5673–5687, doi:10.1175/2008JCLI2299.1.

Vial, J., S. Bony, J.-L. Dufresne, and R. Roehrig, 2016: Coupling between lower-tropospheric convective mixing and low-level clouds: Physical mechanisms and dependence on convection scheme. *Journal of Advances in Modeling Earth Systems*, **8 (4)**, 1892–1911, doi:10.1002/2016MS000740.

Vial, J., J.-L. Dufresne, and S. Bony, 2013: On the interpretation of inter-model spread in CMIP5 climate sensitivity estimates. *Climate Dynamics*, **41 (11-12)**, 3339–3362, doi:10.1007/s00382-013-1725-9.

Voigt, A., N. Albern, P. Ceppi, K. Grise, Y. Li, and B. Medeiros, 2020: Clouds, radiation, and atmospheric circulation in the present-day climate and under climate change. *WIREs Climate Change*, **12 (2)**, e694, doi:10.1002/wcc.694.

Walker, C. C., and T. Schneider, 2006: Eddy influences on Hadley circulations: Simulations with an idealized GCM. *Journal of the atmospheric sciences*, **63 (12)**, 3333–3350, doi:10.1175/JAS3821.1.

Wall, C. J., D. L. Hartmann, and J. R. Norris, 2019: Is the net cloud radiative effect constrained to be uniform over the tropical warm pools? *Geophysical Research Letters*, **46 (21)**, 12 495–12 503, doi:10.1029/2019GL083642.

Walters, D., and Coauthors, 2019: The Met Office Unified Model Global Atmosphere 7.0/7.1 and JULES Global Land 7.0 configurations. *Geoscientific Model Development*, **12 (5)**, 1909–1963, doi:10.5194/gmd-12-1909-2019.

Webb, M., C. Senior, S. Bony, and J.-J. Morcrette, 2001: Combining ERBE and ISCCP data to assess clouds in the Hadley Centre, ECMWF and LMD atmospheric climate models. *Climate Dynamics*, **17 (12)**, 905–922, doi:10.1007/s003820100157.

Webb, M. J., F. H. Lambert, and J. M. Gregory, 2013: Origins of differences in climate sensitivity, forcing and feedback in climate models. *Climate Dynamics*, **40 (3)**, 677–707, doi:10.1007/s00382-012-1336-x.

Webb, M. J., and A. P. Lock, 2013: Coupling between subtropical cloud feedback and the local hydrological cycle in a climate model. *Climate dynamics*, **41 (7-8)**, 1923–1939, doi:10.1007/s00382-012-1608-5.

Webb, M. J., A. P. Lock, and F. H. Lambert, 2018: Interactions between hydrological sensitivity, radiative cooling, stability, and low-level cloud amount feedback. *Journal of Climate*, **31 (5)**, 1833–1850, doi:10.1175/JCLI-D-16-0895.1.

Webb, M. J., and Coauthors, 2006: On the contribution of local feedback mechanisms to the range of climate sensitivity in two GCM ensembles. *Climate dynamics*, **27 (1)**, 17–38, doi:10.1007/s00382-006-0111-2.

Webb, M. J., and Coauthors, 2015: The impact of parametrized convection on cloud feedback. *Philosophical Transactions of the Royal Society A: Mathematical, Physical and Engineering Sciences*, **373 (2054)**, 20140 414, doi:10.1098/rsta.2014.0414.

Webb, M. J., and Coauthors, 2017: The cloud feedback model intercomparison project (CFMIP) contribution to CMIP6. *Geoscientific Model Development*, **10 (1)**, 359–384, doi:10.5194/gmd-10-359-2017.

Wetherald, R., and S. Manabe, 1988: Cloud feedback processes in a general circulation model. *Journal of Atmospheric Sciences*, **45 (8)**, 1397–1416, doi:10.1175/1520-0469(1988)045<1397:CFPIAG>2.0.CO;2.

Wielicki, B. A., B. R. Barkstrom, E. F. Harrison, R. B. Lee III, G. L. Smith, and J. E. Cooper, 1996: Clouds and the Earth's Radiant Energy System (CERES): An earth observing system experiment. *Bulletin of the American Meteorological Society*, **77 (5)**, 853–868, doi:10.1175/1520-0477(1996)077<0853:CATERE>2.0.CO;2.

Wild, M., and Coauthors, 2015: The energy balance over land and oceans: an assessment based on direct observations and CMIP5 climate models. *Climate Dynamics*, **44 (11-12)**, 3393–3429, doi:10.1007/s00382-014-2430-z.

Winton, M., 2006a: Amplified arctic climate change: What does surface albedo feedback have to do with it? *Geophysical Research Letters*, **33 (3)**, 1–4, doi:10.1029/2005gl025244.

Winton, M., 2006b: Surface albedo feedback estimates for the AR4 climate models. *Journal of Climate*, **19 (3)**, 359–365, doi:10.1175/jcli3624.1.

Wood, R., 2012: Stratocumulus clouds. *Monthly Weather Review*, **140 (8)**, 2373–2423, doi:10.1175/MWR-D-11-00121.1.

Wood, R., and C. S. Bretherton, 2006: On the relationship between stratiform low cloud cover and lower-tropospheric stability. *Journal of Climate*, **19 (24)**, 6425–6432, doi:10.1175/JCLI3988.1.

Wyant, M. C., C. S. Bretherton, J. T. Bacmeister, J. T. Kiehl, I. M. Held, M. Zhao, S. A. Klein, and B. J. Soden, 2006: A comparison of low-latitude cloud properties and their response to climate change in three AGCMs sorted into regimes using mid-tropospheric vertical velocity. *Climate Dynamics*, **27 (2)**, 261–279, doi:10.1007/s00382-006-0138-4.

Xu, K.-M., and D. A. Randall, 1996: A semiempirical cloudiness parameterization for use in climate models. *Journal of the Atmospheric Sciences*, **53 (21)**, 3084–3102, doi:10.1175/1520-0469(1996)053<3084:ASCPFU>2.0.CO;2.

Yoshimori, M., F. H. Lambert, M. J. Webb, and T. Andrews, 2020: Fixed anvil temperature feedback: Positive, zero, or negative? *Journal of Climate*, **33 (7)**, 2719–2739, doi:10.1175/JCLI-D-19-0108.1.

Young, A. H., K. R. Knapp, A. Inamdar, W. Hankins, and W. B. Rossow, 2018: The International Satellite Cloud Climatology Project H-Series climate data record product. *Earth System Science Data*, **10 (1)**, 583–593, doi:10.5194/essd-10-583-2018.

Zelinka, M. D., and D. L. Hartmann, 2010: Why is longwave cloud feedback positive? *Journal of Geophysical Research: Atmospheres*, **115 (D16)**, doi:10.1029/2010JD013817.

Zelinka, M. D., S. A. Klein, and D. L. Hartmann, 2012a: Computing and partitioning cloud feedbacks using cloud property histograms. Part I: Cloud radiative kernels. *Journal of Climate*, **25 (11)**, 3715–3735, doi:10.1175/JCLI-D-11-00248.1.

Zelinka, M. D., S. A. Klein, and D. L. Hartmann, 2012b: Computing and partitioning cloud feedbacks using cloud property histograms. Part II: Attribution to changes in cloud amount, altitude, and optical depth. *Journal of Climate*, **25 (11)**, 3736–3754, doi:10.1175/JCLI-D-11-00249.1.

Zelinka, M. D., S. A. Klein, and Y. Qin, 2021: Evaluating climate models' cloud feedbacks against expert judgement. *Earth and Space Science Open Archive*, 31, doi:10.1002/essoar.10506979.1.

Zelinka, M. D., S. A. Klein, K. E. Taylor, T. Andrews, M. J. Webb, J. M. Gregory, and P. M. Forster, 2013a: Contributions of different cloud types to feedbacks and rapid adjustments in CMIP5. *Journal of Climate*, **26 (14)**, 5007–5027, doi:10.1175/JCLI-D-12-00555.1.

Zelinka, M. D., S. A. Klein, K. E. Taylor, T. Andrews, M. J. Webb, J. M. Gregory, and P. M. Forster, 2013b: Contributions of different cloud types to feedbacks and rapid adjustments in CMIP5. *Journal of Climate*, **26 (14)**, 5007–5027, doi:10.1175/JCLI-D-12-00555.1.

Zelinka, M. D., T. A. Myers, D. T. McCoy, S. Po-Chedley, P. M. Caldwell, P. Ceppi, S. A. Klein, and K. E. Taylor, 2020: Causes of higher climate sensitivity in cmip6 models. *Geophysical Research Letters*, **47 (1)**, e2019GL085 782, doi:10.1029/2019GL085782.

Zelinka, M. D., D. A. Randall, M. J. Webb, and S. A. Klein, 2017: Clearing clouds of uncertainty. *Nature Climate Change*, **7 (10)**, 674–678, doi:10.1038/nclimate3402.

Zelinka, M. D., C. Zhou, and S. A. Klein, 2016: Insights from a refined decomposition of cloud feedbacks. *Geophysical Research Letters*, **43 (17)**, 9259–9269, doi:10.1002/2016GL069917.

Zhang, M., J. Hack, J. Kiehl, and R. Cess, 1994: Diagnostic study of climate feedback processes in atmospheric general circulation models. *Journal of Geophysical Research: Atmospheres*, **99 (D3)**, 5525–5537, doi:10.1029/93JD03523.

Zhang, M., W. Lin, C. S. Bretherton, J. J. Hack, and P. J. Rasch, 2003: A modified formulation of fractional stratiform condensation rate in the NCAR Community Atmospheric Model (CAM2). *Journal of Geophysical Research: Atmospheres*, **108 (D1)**, ACL–10, doi:10.1029/2002JD002523.

Zhang, M., and Coauthors, 2005: Comparing clouds and their seasonal variations in 10 atmospheric general circulation models with satellite measurements. *Journal of Geophysical Research: Atmospheres*, **110 (D15)**, doi:10.1029/2004JD005021.

Zhang, M., and Coauthors, 2013: CGILS: Results from the first phase of an international project to understand the physical mechanisms of low cloud feedbacks in single column models. *Journal of Advances in Modeling Earth Systems*, **5 (4)**, 826–842, doi:10.1002/2013MS000246.

Zhao, M., 2014: An investigation of the connections among convection, clouds, and climate sensitivity in a global climate model. *Journal of Climate*, **27 (5)**, 1845–1862, doi:10.1175/JCLI-D-13-00145.1.

Zhou, C., M. D. Zelinka, A. E. Dessler, and S. A. Klein, 2015: The relationship between interannual and long-term cloud feedbacks. *Geophysical Research Letters*, **42 (23)**, 10–463, doi:10.1002/2015GL066698.

Zhou, C., M. D. Zelinka, and S. A. Klein, 2016: Impact of decadal cloud variations on the Earth's energy budget. *Nature Geoscience*, **9 (12)**, 871–874, doi:10.1038/ngeo2828.

Zhou, C., M. D. Zelinka, and S. A. Klein, 2017: Analyzing the dependence of global cloud feedback on the spatial pattern of sea surface temperature change with a Green's function approach. *Journal of Advances in Modeling Earth Systems*, **9 (5)**, 2174–2189, doi:10.1002/2017MS001096.

Index